FHWA/IN/JTRP-2008/11

Final Report

EARTHQUAKE RESISTANCE OF INTEGRAL ABUTMENT BRIDGES

Robert J. Frosch
Michael E. Kreger
Aaron M. Talbott

May 2009

INDOT Research

TECHNICAL *Summary*

Technology Transfer and Project Implementation Information

TRB Subject Code: 25-1 Bridges *May 2009*
Publication No. FHWA/IN/JTRP-2008/11, SPR-2867 *Final Report*

Earthquake Resistance of Integral Abutment Bridges

Introduction

Integral abutment construction has become an increasingly popular alternative to conventional construction in recent years. In conventional construction, the superstructure typically consists of a series of simply supported spans separated by expansion joints and resting on bearings at the abutments and intermediate piers. In integral construction, the superstructure and abutments form a continuous, monolithic structure. The structure may be made integral with the intermediate piers or may rest on elastomeric bearings. Integral construction has increased in popularity because it eliminates maintenance associated with joints and bearings. However, in the absence of the joints and bearings used in conventional construction, the abutments and foundations must accommodate the movements associated with both thermal and seismic movements.

One of the most common problems in the seismic resistance of traditional bridge construction is unseating of the superstructure from the support bearings. This problem is eliminated in integral abutment construction as there are no support bearings. However, the system of joints and bearings used in traditional construction allows superstructure movements during a seismic event which result in a decreased demand on the foundation. In integral abutment construction, the foundation piles and abutment must be able to accommodate these increased demands. There has been a general agreement that integral abutment construction provides increased seismic resistance with respect to traditional construction through increased redundancy and continuity. However, detailed analysis of the earthquake resistance of this type of construction has not been conducted. Further, no work has been conducted to determine the displacement capacity of the abutment-pile connection using INDOT design details or the displacement demand of the connection considering the seismic hazard associated with Indiana. The objective of this research program is to evaluate the earthquake resistance of integral abutment bridges. The abutment-pile connection was identified as a critical detail and was considered to control the displacement capacity of the structure.

Findings

Four major tasks were performed as part of this research program: (1) development of a series of design ground motions representing current estimates of the seismic hazard in Indiana, (2) evaluation of field data collected during an existing long-term integral abutment bridge monitoring project to estimate the relationship between abutment movements and earth pressures, (3) laboratory testing of current and proposed details of the abutment-pile connection to estimate displacement capacity, and (4) construction of analytical models to estimate seismic displacements of the abutment. Based on the research program, it is recommended that current INDOT integral abutment bridge details are sufficient to provide seismic resistance for bridges up to 500 ft in length. This length was selected considering actual seismic records as well as design based on the MCE (Maximum Considered Earthquake) for Indiana. The following additional recommendations are provided:

- A pile embedment length of 24 in. in the abutment should be used. While the current embedment length of 15 in. was

determined to be adequate based on laboratory tests, the specimen with a 24 in. embedment length had significantly improved performance at larger displacement levels. This length was also demonstrated analytically to be sufficient for the range of H-pile sections used in construction. This embedment length is recommended for all bridge construction as it provides enhanced behavior for both thermal and seismic considerations.

- Integral abutment bridges can be used for lengths up to 1000 ft. For bridge lengths greater than 500 ft, confining reinforcement must be provided around the pile head. As a minimum, it is recommended that a #4 spiral with a 2.5 in. pitch be specified.
- The use of a "pin" detail is not recommended for seismic applications. Although this detail performed adequately in laboratory tests, its performance under dynamic loading is uncertain. There is considerable benefit of continuity of the abutment and pile from both a vertical load path point of view and the lateral resistance provided by this connection.

Implementation

The recommendations provided in this study can easily be implemented to improve the performance of integral abutment bridges subjected to seismic motions. It is suggested that the recommendations provided be incorporated into the INDOT Design Manual. Through incorporation of these recommendations, integral bridges across the state can be constructed with inherent seismic resistance. This increased seismic resistance not only provides enhanced safety to the traveling public in the event of a seismic event, it also allows for the preservation of transportation routes which are essential for emergency response, public welfare, and economic security.

Contacts

For more information:

Prof. Robert J. Frosch
Principal Investigator
School of Civil Engineering
Purdue University
West Lafayette IN 47907
Phone: (765) 494-5904
Fax: (765) 496-1105
E-mail: frosch@purdue.edu

Prof. Michael E. Kreger
Principal Investigator
School of Civil Engineering
Purdue University
West Lafayette IN 47907
Phone: (765) 494-9340
Fax: (765) 496-1105
E-mail: kreger@purdue.edu

Indiana Department of Transportation
Office of Research & Development
1205 Montgomery Street
P.O. Box 2279
West Lafayette, IN 47906
Phone: (765) 463-1521
Fax: (765) 497-1665

Purdue University
Joint Transportation Research Program
School of Civil Engineering
West Lafayette, IN 47907-1284
Phone: (765) 494-9310
Fax: (765) 496-7996
E-mail: jtrp@ecn.purdue.edu
http://www.purdue.edu/jtrp

Final Report

FHWA/IN/JTRP-2008/11

EARTHQUAKE RESISTANCE OF INTEGRAL ABUTMENT BRIDGES

by

Robert J. Frosch
Principal Investigator
Professor of Civil Engineering

Michael E. Kreger
Principal Investigator
Professor of Civil Engineering

and

Aaron M. Talbott
Graduate Research Assistant

School of Civil Engineering
Purdue University

Joint Transportation Research Program
Project No. C-36-56TTT
File No. 7-4-71
SPR-2867

Conducted in Cooperation with the
Indiana Department of Transportation
and the Federal Highway Administration

Purdue University
West Lafayette, IN 47907
May 2009

TECHNICAL REPORT STANDARD TITLE PAGE

1. Report No.	2. Government Accession No.	3. Recipient's Catalog No.
FHWA/IN/JTRP-2008/11		

4. Title and Subtitle	5. Report Date
Earthquake Resistance of Integral Abutment Bridges	May 2009
	6. Performing Organization Code
7. Author(s)	8. Performing Organization Report No.
Robert J. Frosch, Michael E. Kreger, Aaron M. Talbott	FHWA/IN/JTRP-2008/11
9. Performing Organization Name and Address Joint Transportation Research Program 550 Stadium Mall Drive Purdue University West Lafayette, IN 47907-2051	10. Work Unit No.
	11. Contract or Grant No. SPR-2867
12. Sponsoring Agency Name and Address Indiana Department of Transportation State Office Building 100 North Senate Avenue Indianapolis, IN 46204	13. Type of Report and Period Covered Final Report
	14. Sponsoring Agency Code

15. Supplementary Notes

Prepared in cooperation with the Indiana Department of Transportation and Federal Highway Administration.

16. Abstract

Integral abutment construction has become a popular alternative to conventional bridge construction for short and intermediate length bridges. Integral abutment construction eliminates joints and bearings which reduce long-term maintenance costs. However, in the absence of joints and bearings, the bridge abutments and foundations must be able to accommodate lateral movements from thermal expansion and contraction of the superstructure and from seismic events. Previous research has focused on the response to thermal expansion and contraction. The current research examines the response of integral abutment bridges to seismic loading. A field investigation was conducted to examine the response of an integral abutment to lateral loading from thermal expansion and contraction. The results were used to calibrate analytical bridge models used to estimate displacements of the abutment during design seismic events. A laboratory investigation was conducted to estimate the lateral displacement capacity of the abutment based on the performance of the abutment-pile connection. Results of the field, analytical, and laboratory investigations were used to evaluate allowable bridge lengths based on seismic performance. Finally, design recommendations are provided to enhance the seismic performance of integral abutment bridges.

17. Key Words	18. Distribution Statement
Bridge, Bridge Design, Integral Abutment, Earthquake Resistance.	No restrictions. This document is available to the public through the National Technical Information Service, Springfield, VA 22161

19. Security Classif. (of this report)	20. Security Classif. (of this page)	21. No. of Pages	22. Price
Unclassified	Unclassified	217	

Form DOT F 1700.7 (8-69)

ACKNOWLEDGEMENTS

This work was supported by the Joint Transportation Research Program (JTRP) administered by the Indiana Department of Transportation (INDOT) and Purdue University through contract SPR-2867 and SPR-3377. The support of the Indiana Department of Transportation (INDOT) and the Federal Highway Administration (FHWA) are gratefully acknowledged. The authors would like to thank Dr. Tommy Nantung from the INDOT Division of Research for serving as Project Administrator and for his support throughout the project. In addition, thanks are extended to members of the Study Advisory Committee for their participation and thoughtful comments throughout the project. These members include Randy Strain, Mir Zaheer, John McCrary, Tony McClellan, and Keith Hoernschemeyer. Finally, thanks are extended to Steel Dynamics for donating the H-piles used during the experimental phase of this research study.

TABLE OF CONTENTS

Page

LIST OF TABLES

LIST OF FIGURES

CHAPTER 1: INTRODUCTION AND BACKGROUND

1.1 Integral Abutment Construction

Integral abutment construction has become an increasingly popular alternative in recent years to conventional construction. A recent survey indicates that there are over 13,000 integral abutment bridges in service in the United States (Maruri 2004). In conventional construction (Figure 1.1a), the superstructure typically consists of a series of simply supported spans separated by expansion joints and resting on bearings at the abutments and intermediate piers. In integral construction (Figure 1.1b), the superstructure and abutments form a continuous, monolithic structure. The structure may be made integral with the intermediate piers or may rest on elastomeric bearings. Integral construction has increased in popularity because it eliminates maintenance associated with joints and bearings (Wasserman 1996). However, in the absence of the joints and bearings used in conventional construction, the abutments and foundations must accommodate the movements associated with both thermal and seismic movements.

1.2 Previous Research

Previous research by Chovichien (2004) focused on the foundation piles and their ability to accommodate lateral displacements associated with thermal expansion and contraction of the bridge. Bonczar and Brena (2005) also focused on the thermal response of an integral abutment through field monitoring and analytical modeling. Burdette (2005) performed laboratory tests of the abutment-pile connection to observe its performance under lateral loading. These previous efforts focused primarily on the response to thermal loading. The current work focuses on the ability of the abutment and foundation piles to accommodate lateral displacements associated with a seismic event.

1.3 INDOT Standards

Details of integral abutment construction vary significantly from state to state. This study will focus on construction practices in Indiana. The limits of integral abutment bridge construction are addressed by the Indiana Department of Transportation (INDOT) in Bridge Design Memoranda #233 and #244 (INDOT 1992a,b). These memoranda limit the skew angle of integral abutment bridges to 30° and set the maximum bridge length to 250 ft for steel construction and 300 ft for prestressed concrete construction. Foundation piles are limited to steel HP sections or concrete-filled steel tubes. Steel H-piles are to be oriented with the weak axis perpendicular to the longitudinal axis of the bridge. Design Memorandum #05-07 (INDOT 2005) requires that all H-piles be ASTM A572 Grade 50 steel and sets the corresponding maximum allowable stress in the pile design as $0.25F_y$ or 12.5 ksi.

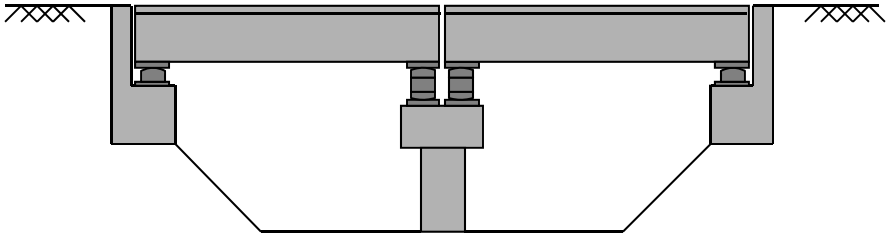

(a) Conventional Construction

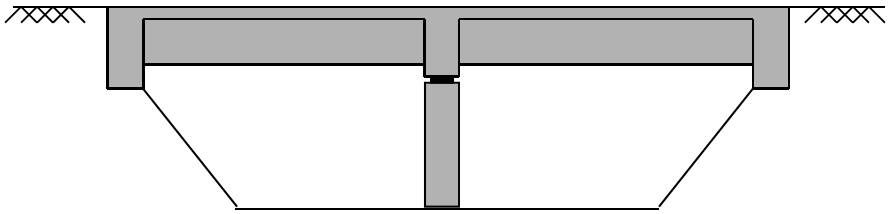

(b) Integral Construction

Figure 1.1: Integral Abutment Construction

INDOT provides two suggested integral abutment details (Figure 1.2, Figure 1.3). In detail "A" (Figure 1.2), the superstructure beams rest directly on the foundation piles prior to the final concrete casting operation. In detail "B" (Figure 1.3) a pile cap is constructed. The superstructure beams rest on a bearing assembly prior to the final concrete casting operation. The advantage of detail "B" is that the superstructure beams do not have to align directly with the foundation piles.

1.4 Seismic Resistance of Integral Abutment Bridges

One of the most common problems associated with seismic resistance of traditional bridge construction is unseating of the superstructure from the support bearings. This problem is eliminated in integral abutment construction because there are no support bearings (Wasserman 1996). However, the system of joints and bearings used in traditional construction allows superstructure movements during a seismic event which result in a decreased demand on the foundation. In integral abutment construction, the foundation piles and abutment must be able to accommodate these increased demands. There has been a general agreement that integral abutment construction provides increased seismic resistance relative to traditional construction through increased redundancy and continuity (Wasserman 1996). The behavior of integral piers has been studied by Patty et. al. (2001). However, detailed analysis of the earthquake resistance of this type of construction has not been conducted. Further, no work has been conducted to determine the displacement capacity of the abutment-pile connection incorporating INDOT design details or the displacement demand of the connection considering the seismic hazard associated with Indiana.

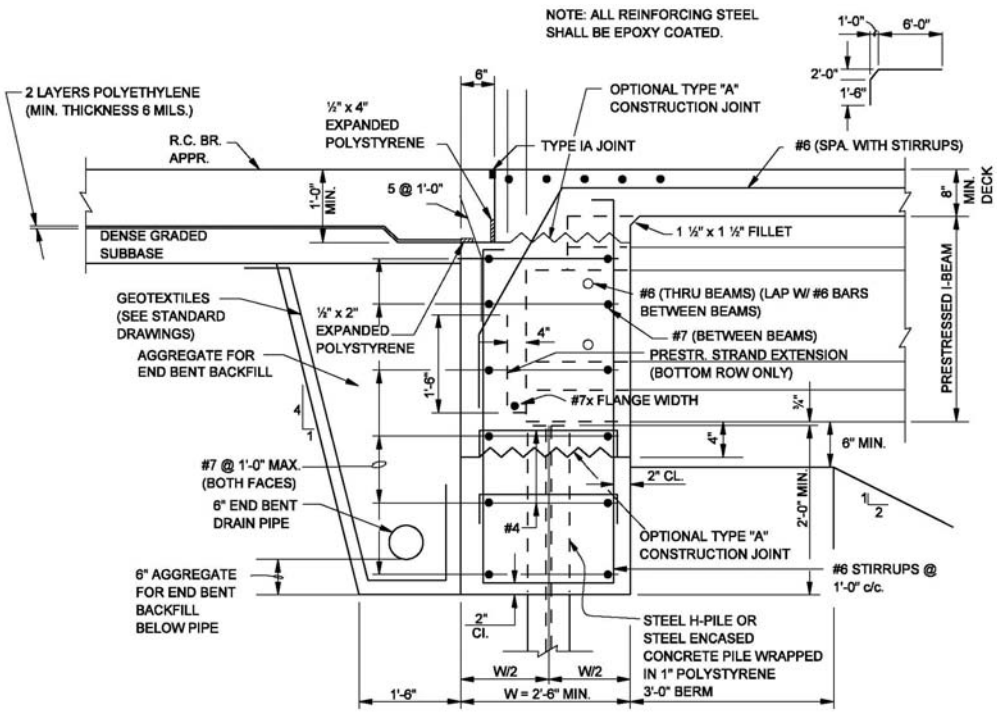

PRESTRESSED CONCRETE I-BEAM

SUGGESTED INTEGRAL END BENT DETAILS
(Beams Attached Directly to Piling, Method A)
Figure 67-1B

Figure 1.2: INDOT Suggested Detail "A"

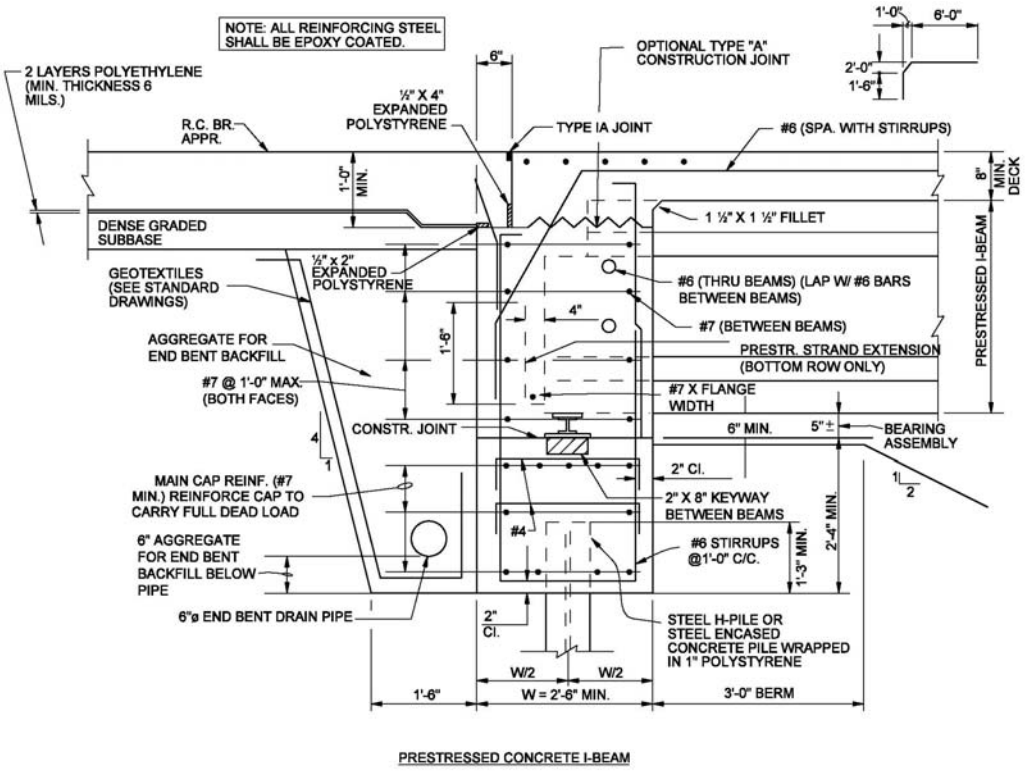

SUGGESTED INTEGRAL END BENT DETAILS
(Beams Attached toConcrete Cap, Method B)
Figure 67-1C

Figure 1.3: INDOT Suggested Detail "B"

1.5 Research Objectives and Scope

The objective of this research program is to evaluate the earthquake resistance of integral abutment bridges. The abutment-pile connection was identified as a critical detail and is assumed to control the displacement capacity of the structure. The research scope consists of the following tasks:

1. The development of a series of design ground motions meeting the requirements of the design specifications under consideration.
2. The evaluation of field data from an existing long-term integral abutment bridge monitoring project to estimate the relationship between abutment movements and earth pressures.
3. Laboratory testing of current and proposed abutment-pile connection details to evaluate displacement capacity.
4. Analytical modeling of integral abutment bridge structures up to 1000 ft in length to estimate displacements of the abutment using the design ground motions developed in Task 1.
5. The development of design recommendations and suggested details.

CHAPTER 2: DESIGN GROUND MOTIONS

2.1 Introduction

A set of design ground motions representing the seismic hazard in Indiana was developed to assess the seismic behavior of integral abutments. This task was complicated by the fact that few strong ground motion recordings exist for Indiana. In lieu of recorded Indiana ground motions, a set of eight strong ground motions from both the Eastern and Western United States was selected. These ground motions were then scaled to match the applicable design spectra. This chapter discusses the development of these design ground motions. The sources of seismic hazard in Indiana are reviewed and the methodology used to develop the USGS Seismic Hazard Maps (Frankel et al 1996, 2002) is discussed. Design response spectra are developed according to the AASHTO Standard Specifications (AASHTO 2002), the AASHTO LRFD Specifications (AASHTO 2006) including the 2008 interims, the Recommended LRFD Guidelines (ATC 2002), and the recently approved Guide Specifications for LRFD Seismic Bridge Design (2009). Finally, each set of scaled ground motions and response spectra is presented.

2.2 Seismic Hazard in Indiana

Indiana is located near two seismic zones: the New Madrid Seismic Zone and the Wabash Valley Seismic Zone (Figure 2.1). Figure 2.2 shows earthquakes in the Central United States from 1699-2002 (Wheeler et. al. 2002). The majority of the seismic hazard assigned to Indiana is due to the 1811-1812 sequence of earthquakes in the New Madrid Zone (Figure 2.2) and paleoliquefaction features which suggest powerful, pre-historic earthquakes occurred throughout Indiana and Illinois. Paleoliquefaction features are

discussed in detail by Wesnousky and Leffler (1992), Obermeier (1998), and Munson, et al. (1992). Liquefaction features may occur when a liquefiable layer of material is trapped beneath a non-liquefiable layer of material during a seismic event. During the event, the pore pressures in the liquefiable layer may increase to the point that the liquefiable layer penetrates the non-liquefiable layer and erupts to the surface. The deposit of material on the ground surface is referred to as a sand boil (Figure 2.3). Liquefaction features which have occurred in the distant past are referred to as paleoliqufaction features (Figure 2.4). By dating these features in the geologic record, it is possible to determine the approximate time of past seismic events. Estimates of earthquake magnitude are sometimes made based on the characteristics of the liquefaction feature (size, depth, etc.). The existence of paleoliquefaction features coupled with the 1811-1812 sequence of events demonstrates that the New Madrid region has had very large seismic events in the past. However, the relationship between current New Madrid seismicity and the 1811-1812 sequence is uncertain. It is unclear whether post-1811 earthquakes are essentially aftershocks of the 1811-1812 sequence or represent a new accumulation of elastic strain (Johnston and Shedlock 1992).

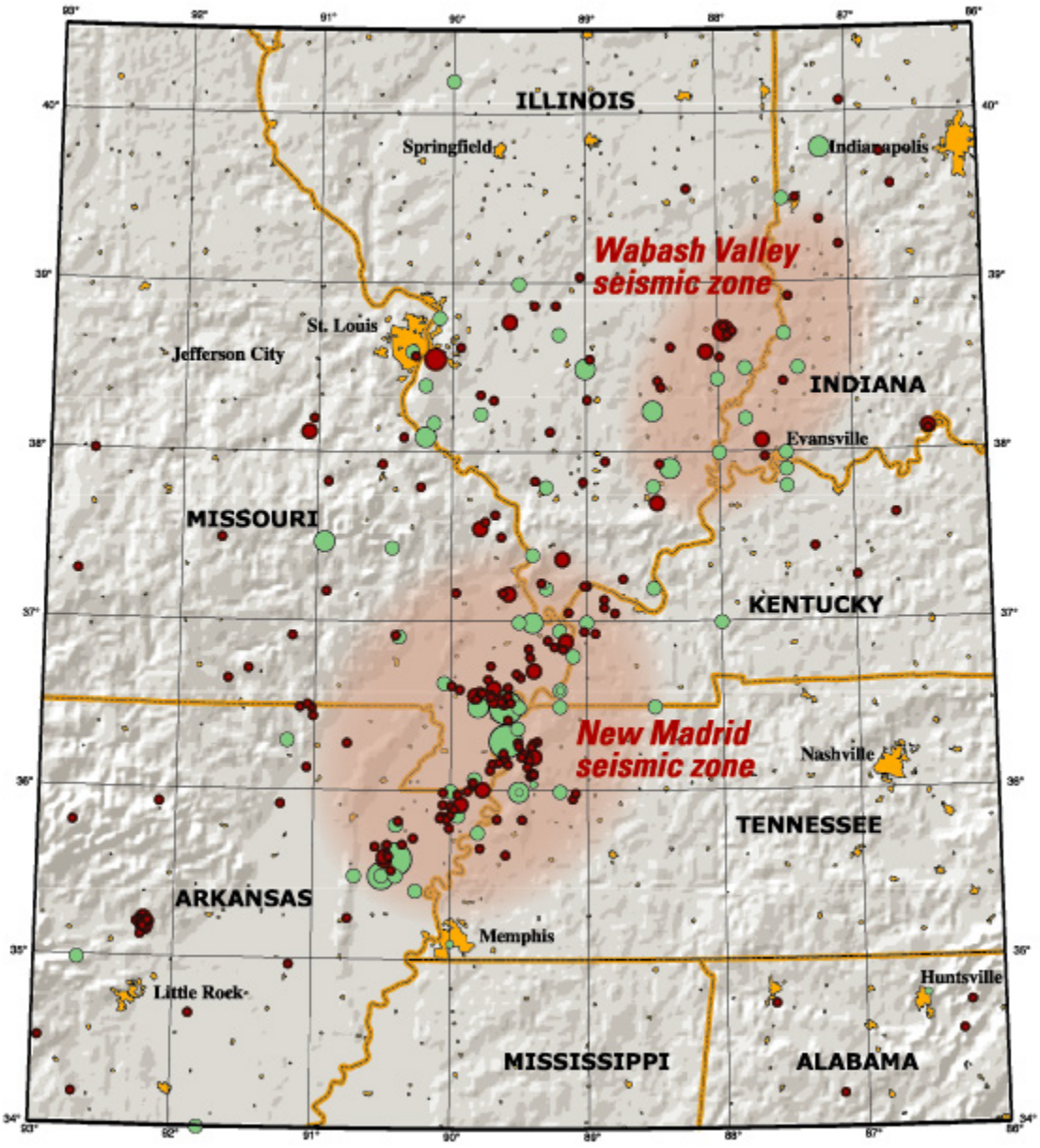

Figure 2.1: New Madrid and Wabash Valley Seismic Zones (USGS 2002)

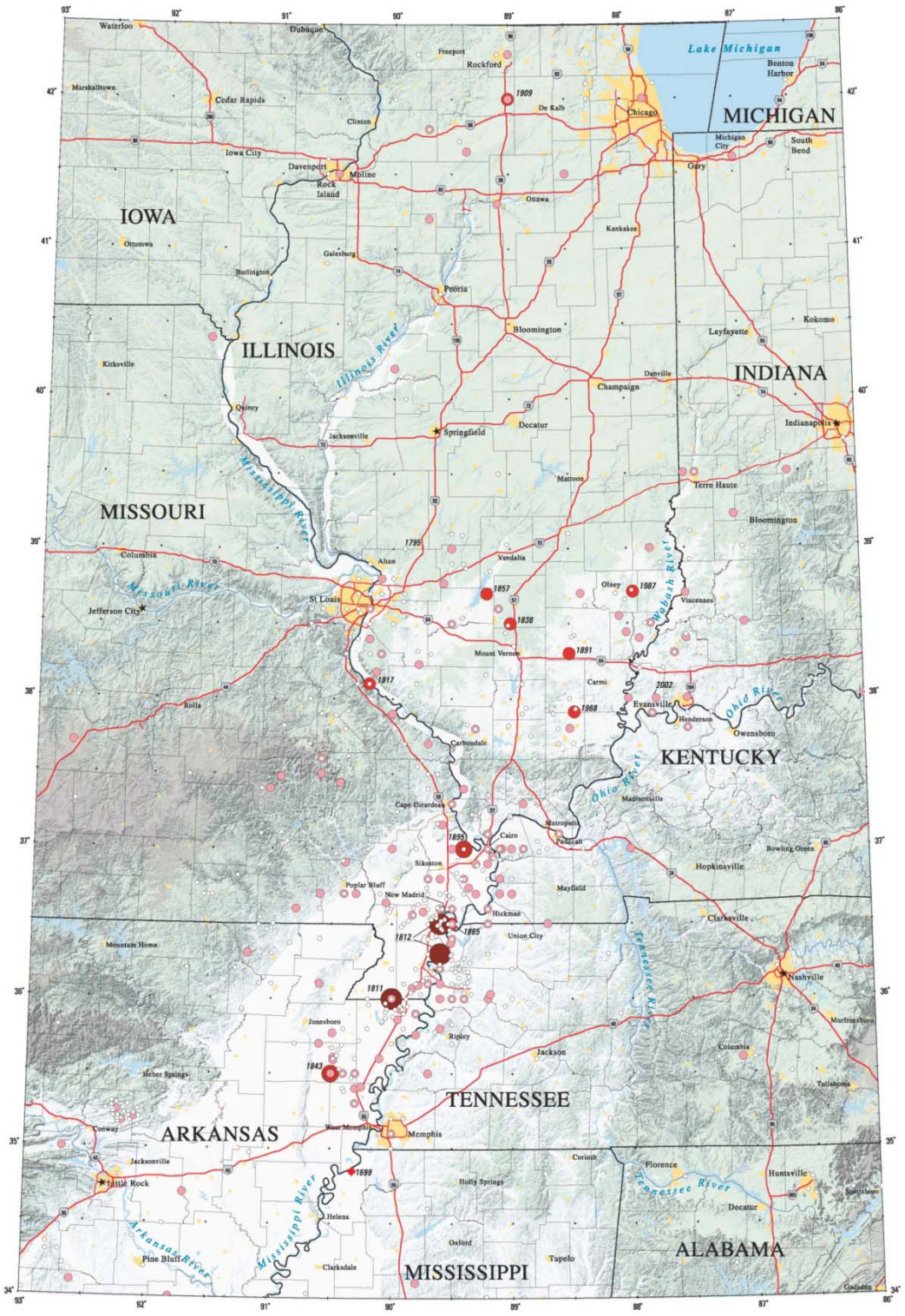

Figure 2.2: Earthquakes in the Central United States 1699-2002 (Wheeler et al 2002)

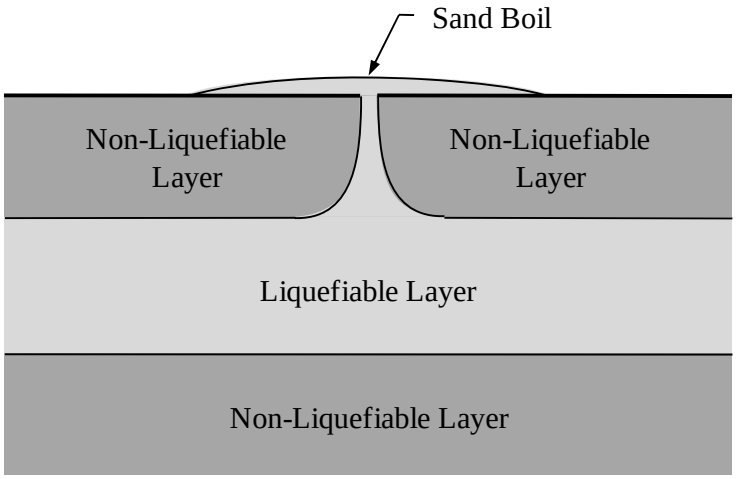

Figure 2.3: Liquefaction Feature

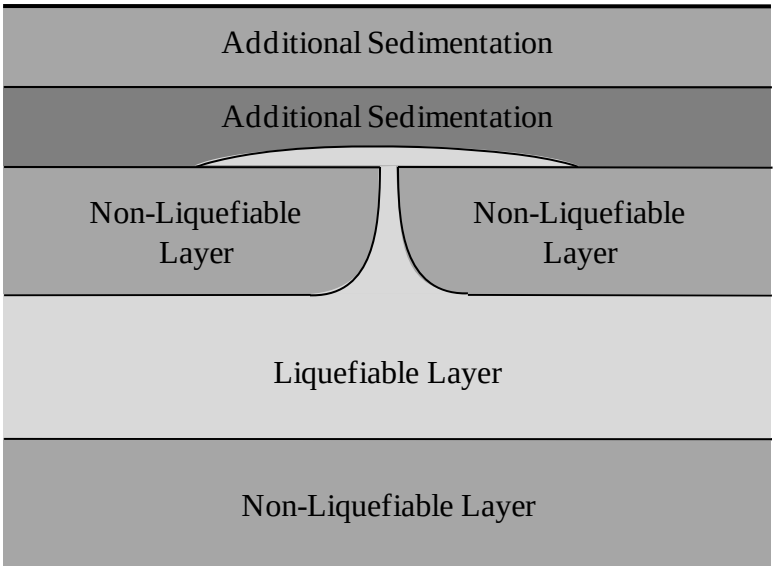

Figure 2.4: Paleoliquefaction Feature

2.2.1 USGS Seismic Hazard Maps

This report will make use of seismic hazard mapping performed by the United States Geologic Survey (USGS) National Seismic Hazard Mapping Program (NSHMP). The development of these maps has been documented by Frankel (1995) and Frankel et al (1996, 2002). These maps are based on a probabilistic seismic hazard analysis (PSHA). A PSHA consists of four steps (Reiter, 1990):

1. Earthquake sources, including the probability distribution of potential rupture locations within each source, are identified and characterized.
2. Recurrence relationships representing the temporal distribution of earthquakes for each source zone are developed.
3. Ground motions at the site resulting from earthquakes of any possible size at any possible location within each source zone are determined using predictive relationships.
4. The uncertainties in earthquake location, size, and ground motion parameter prediction are combined to obtain the probability that a ground motion parameter will be exceeded during a given period.

The USGS has performed this analysis for the entire United States. Hazard maps for Indiana were created using custom mapping tools available from the USGS. These maps are presented as Figure 2.5 through Figure 2.12 and include both the 1996 and 2002 versions of each map. Each map shows a particular ground motion parameter with a specified probability of exceedance (P.E.). For example, Figure 2.5 shows the 0.2 sec Spectral Acceleration with a 10% probability of exceedance in 50 years. In other words, there is a 10% chance that the 0.2 sec spectral accelerations given by the contours of Figure 2.5 will be exceeded in a given 50 year period. These ground motion parameters are used by building codes to generate site-specific design response spectra. The construction of design response spectra is discussed in the following sections.

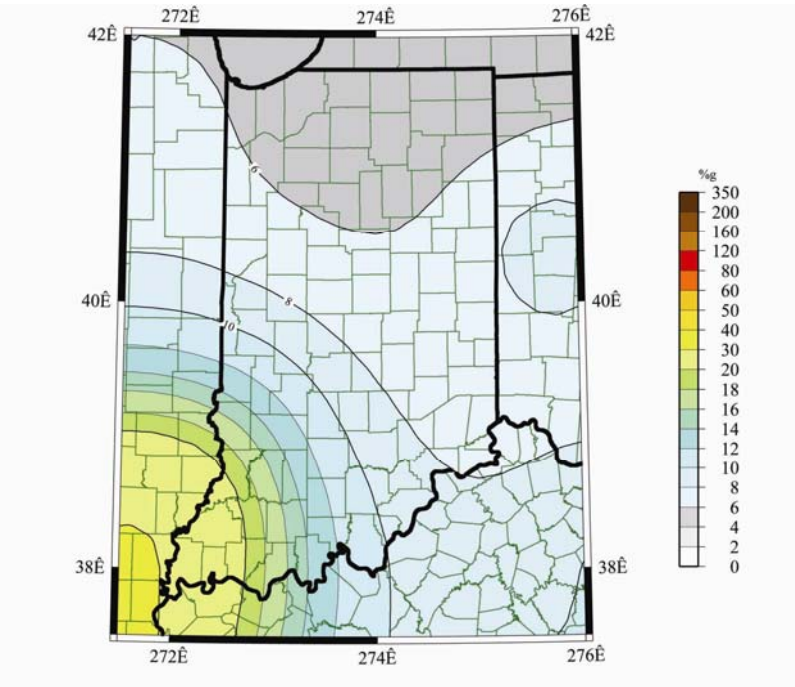

Figure 2.5: 0.2 sec Spectral Acceleration with 10% Probability of Exceedance in 50 years (1996)

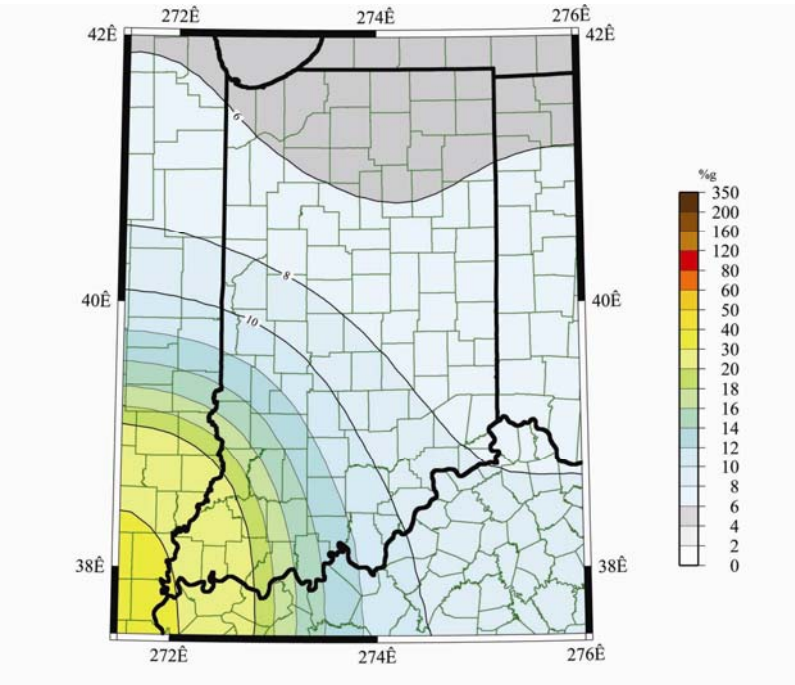

Figure 2.6: 0.2 sec Spectral Acceleration with 10% Probability of Exceedance in 50 years (2002)

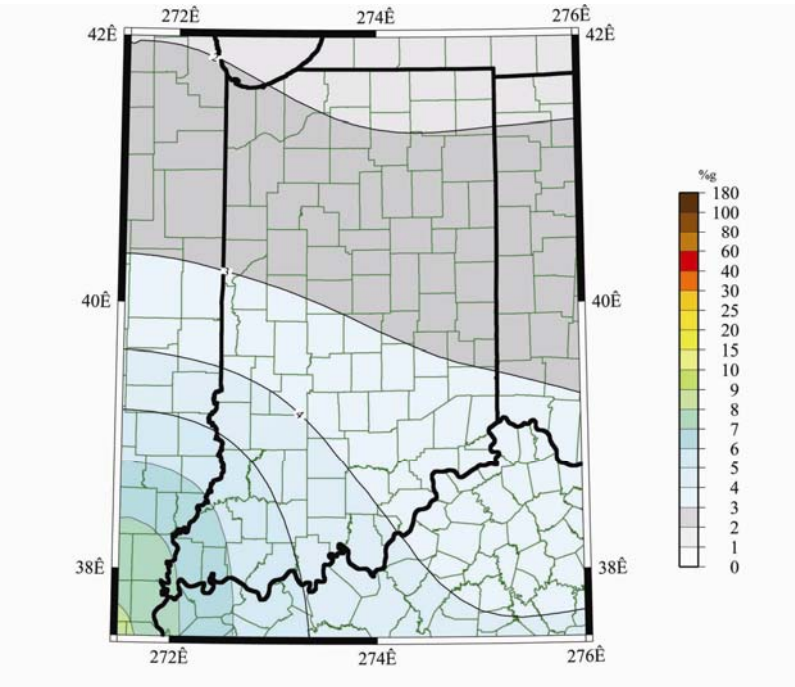

Figure 2.7: 1.0 sec Spectral Acceleration with 10% Probability of Exceedance in 50 years (1996)

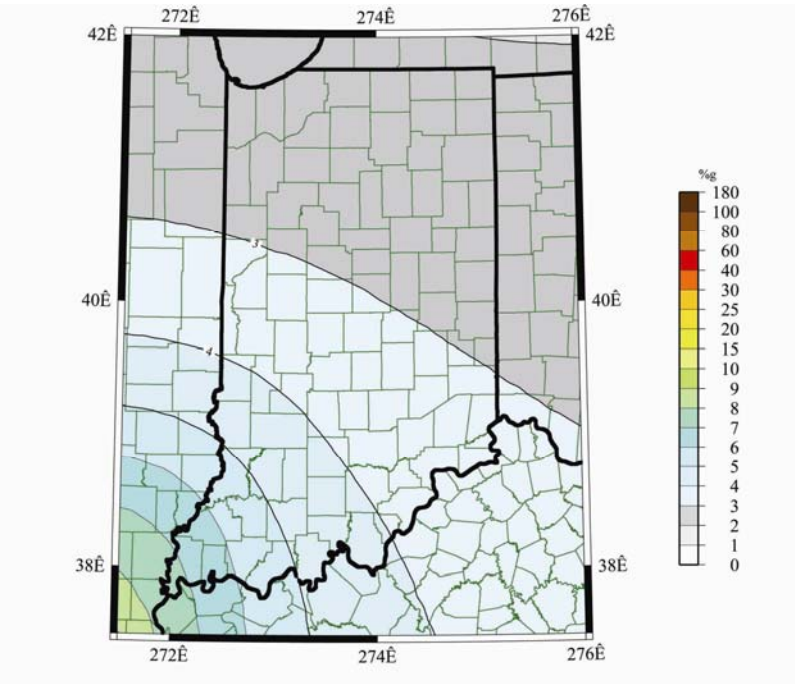

Figure 2.8: 1.0 sec Spectral Acceleration with 10% Probability of Exceedance in 50 years (2002)

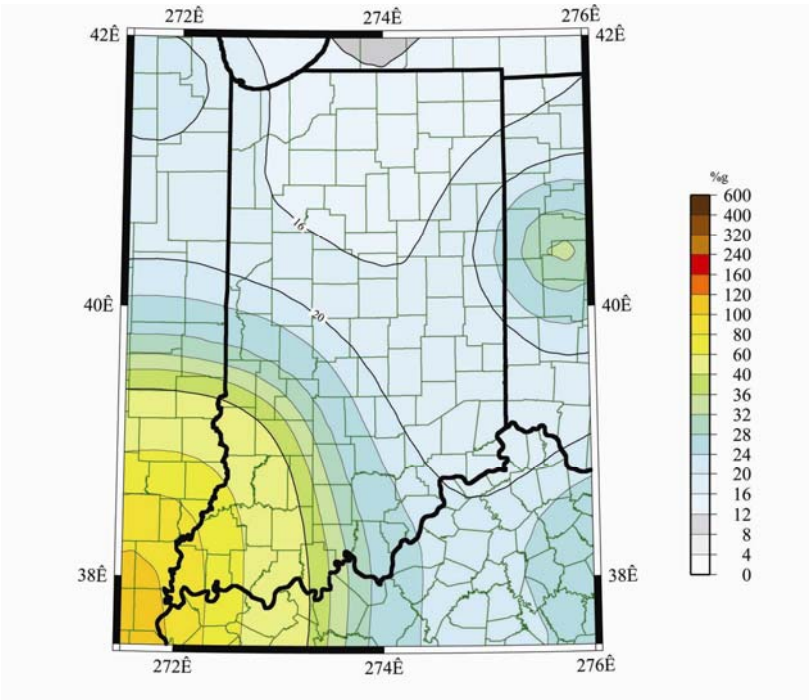

Figure 2.9: 0.2 sec Spectral Acceleration with 2% Probability of Exceedance in 50 years (1996)

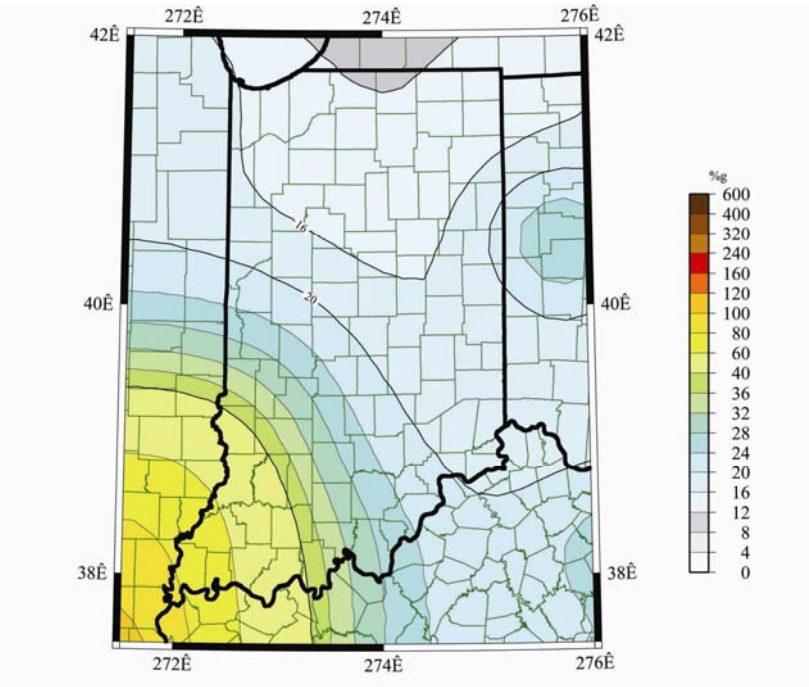

Figure 2.10: 0.2 sec Spectral Acceleration with 2% Probability of Exceedance in 50 years (2002)

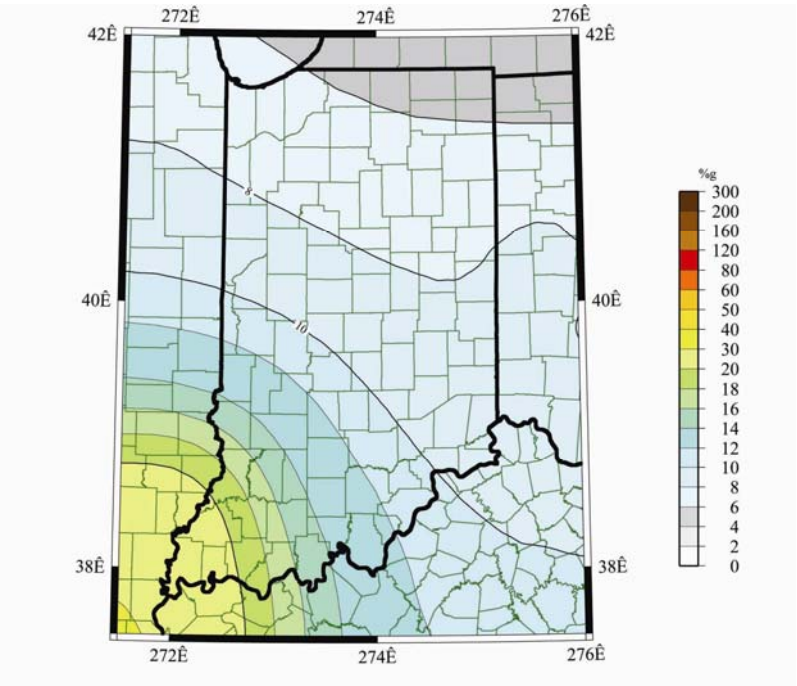

Figure 2.11: 1.0 sec Spectral Acceleration with 2% Probability of Exceedance in 50 years (1996)

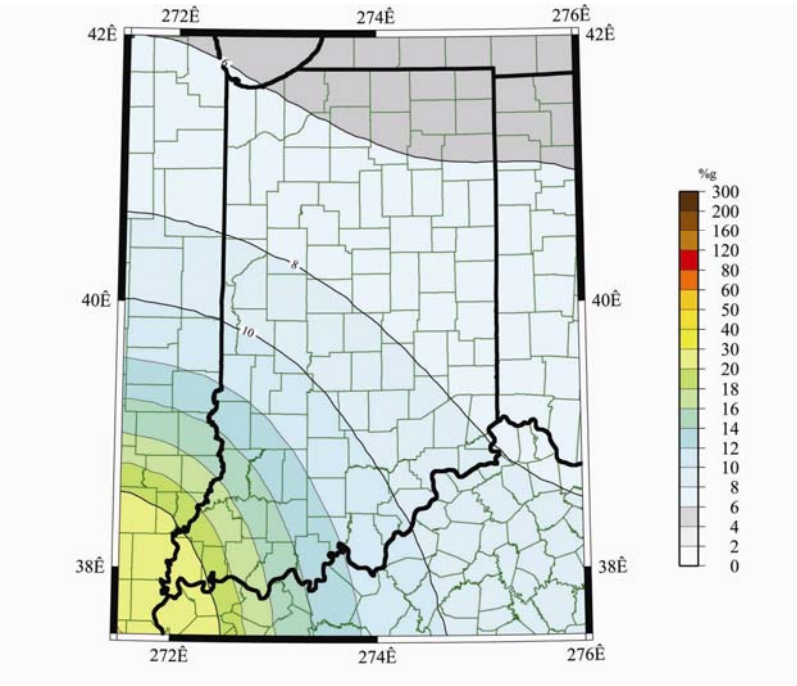

Figure 2.12: 1.0 sec Spectral Acceleration with 2% Probability of Exceedance in 50 years (2002)

2.3 Design Response Spectra

Design response spectra were constructed for three cities in Indiana (Figure 2.13). For reference, design response spectra were also constructed for Los Angeles, CA and San Francisco, CA. These spectra were developed using the 17th Edition AASHTO Standard Specifications for Highway Bridges (AASHTO 2002), the 4th Edition AASHTO LRFD Bridge Design Specifications (AASHTO 2006) including the 2008 interims, the Recommended LRFD Guidelines for the Seismic Design of Highway Bridges (ATC 2002), and the recently published AASHTO Guide Specifications for LRFD Seismic Bridge Design (2009). A variety of specifications and recommendations were considered because the current state of design is in flux due to the transition from the Standard to LRFD Specifications as well as recent movement in the adoption of updated provisions originally proposed by the Recommended LRFD Guidelines. The method used in each specification is briefly described, and the resulting spectra are presented in the following sections.

Figure 2.13: Select Indiana Cites

2.3.1 AASHTO Standard Specifications, 17th Edition

Using the 17th Edition of the AASHTO Standard Specifications for Highway Bridges (AASHTO 2002), design acceleration response spectra are defined by the elastic seismic response coefficient, C_s, given in Article 3.6 of Division I-A Seismic Design:

$$C_s = \frac{1.2AS}{T^{2/3}} \leq 2.5A \tag{2.1}$$

where:

A = Acceleration Coefficient (Article 3.2)

S = Site Coefficient (Article 3.5)

T = Period of Vibration

The acceleration coefficient, A, is determined for a given location from the contour map provided in Article 3.2 of the Design Specifications. An enlarged version of this map for Indiana is presented in Figure 2.14. These coefficients represent a 10% probability of exceedance in 50 years based on the 1988 edition of the NEHRP Recommended Provisions. The site coefficient, S, depends on the local soil conditions. The AASHTO specifications define four general soil profiles (I – IV) which are used to determine the site coefficient. The specifications state that Soil Profile II, which is described as a stiff soil, is to be used when no detailed site information exists. Therefore, Soil Profile II was assumed for purposes of this discussion and S = 1.2. The spectrum resulting from Equation 2.1 is presented as Figure 2.15. The specific design spectra for several cities are provided in Figure 2.16.

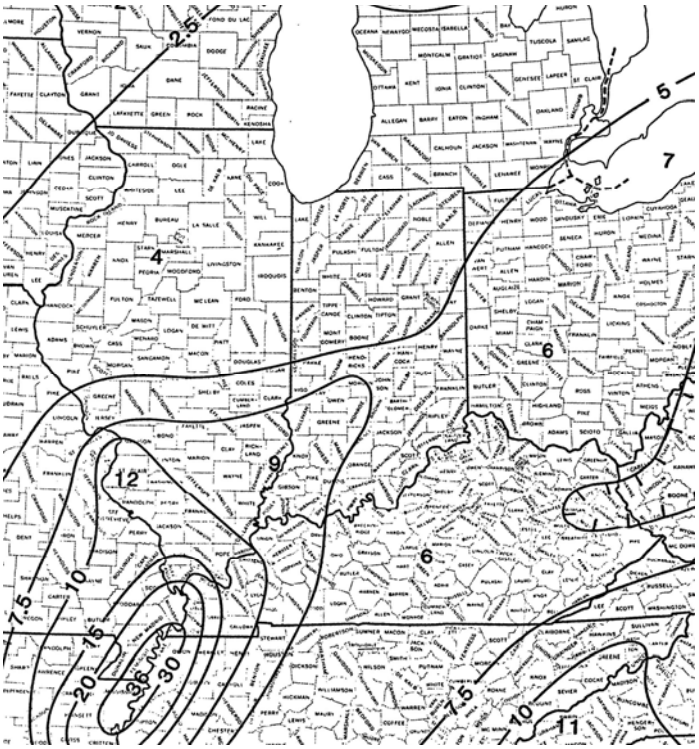

Figure 2.14: AASHTO Acceleration Coefficient (based on NEHRP, 1988)

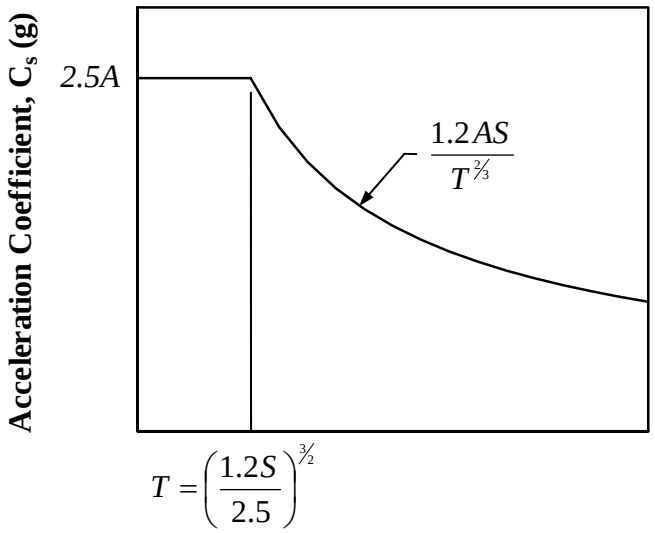

Figure 2.15: Typical Acceleration Response Spectrum (AASHTO Standard Spec., 17th Ed.)

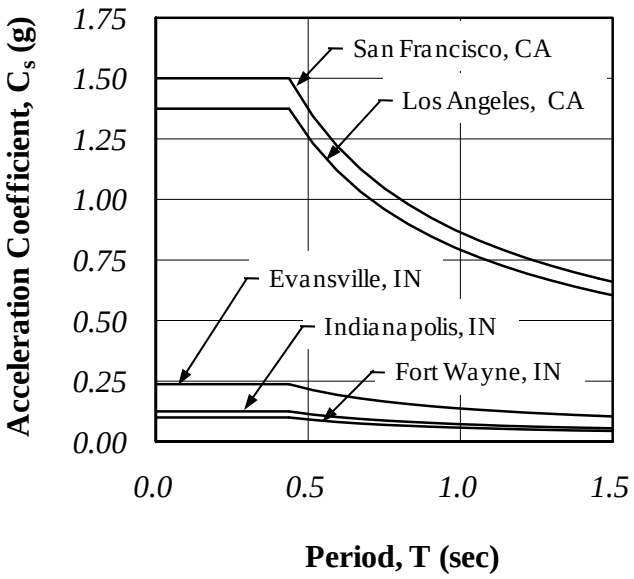

Figure 2.16: Acceleration Response Spectra for Select Cities (AASHTO Standard Spec., 17th Ed.)

2.3.2 AASHTO LRFD Specifications, 4th Edition

Apart from minor differences in terminology, the design acceleration spectrum defined in the AASHTO LRFD Specifications, 4th Edition (2006) is identical to that in the Standard Specifications (AASHTO 2002). The same equation is used for C_s, and the same maps are used for determining the acceleration coefficient, *A*. It should be noted that the seismic provisions discussed in this section consider the 4th Edition without the 2008 interims. The 2008 interims have introduced significant changes to the provisions which are discussed later.

2.3.3 Recommended LRFD Guidelines

Two design seismic events are defined in the Recommended LRFD Guidelines for Seismic Design of Highway Bridges (ATC 2002): the expected earthquake (EE) and the maximum considered earthquake (MCE). Each event has different performance objectives. The EE has a 50% probability of exceedance in 75 years. The MCE has a 3%

probability of exceedance in 75 years. It should be noted that the time interval was increased to 75 years to be consistent with the LRFD Specifications (AASHTO 2006) which consider a 75-year design life. The older Standard Specifications (AASHTO 2002) consider a 50-year design life. The design acceleration spectrum for each event is constructed as shown in Figure 2.17. The required parameters are given by:

$$S_{DS} = F_a S_s \tag{2.2}$$

$$S_{D1} = F_v S_1 \tag{2.3}$$

The spectral accelerations for a 0.2 second and 1.0 second period are S_s and S_1, respectively. These values may be obtained from the maps provided in Section 3.4.1 of the Recommended Guidelines (ATC 2002) or from the Seismic Design Parameters CD-ROM (ATC 2002). The spectral accelerations used in the recommended guidelines are based on the 1996 Seismic Hazard Maps prepared by the United States Geologic Survey (USGS).

The terms F_a and F_v are site coefficients. The site coefficient is a function of the site class and spectral acceleration. Numerical values may be obtained from Tables 3.4.2.3-1 and 3.4.2.3-2 of the Recommended Guidelines. According to Section 3.4.2.1, Site Class D, which represents a stiff soil, shall be used if soil properties are not known in detail. Therefore, acceleration response spectra for select cities were constructed assuming Site Class D. These spectra are presented as Figure 2.18 and Figure 2.19 for the MCE and EE, respectively.

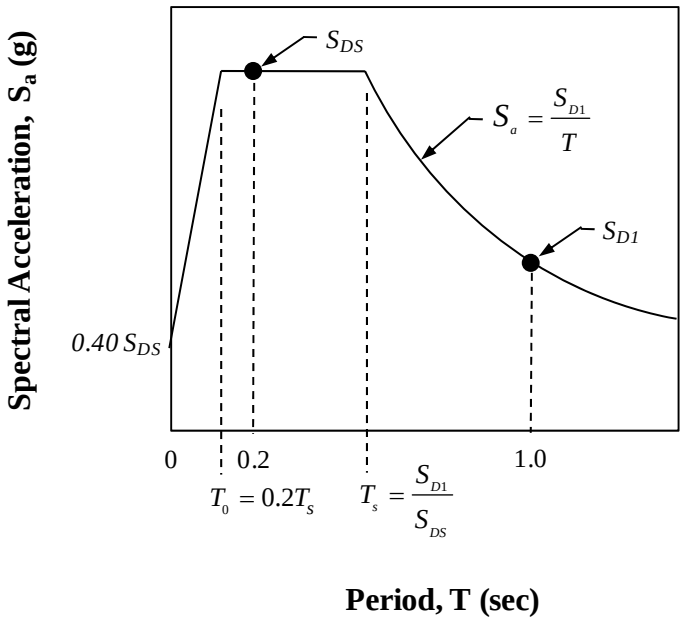

Figure 2.17: Typical Acceleration Spectrum (Recommended LRFD Guidelines)

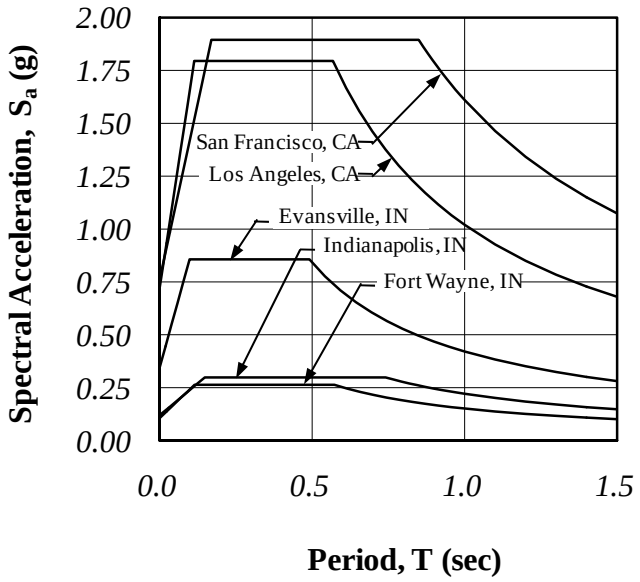

Figure 2.18: MCE Acceleration Response Spectra for Select Cities (Recommended LRFD Guidelines)

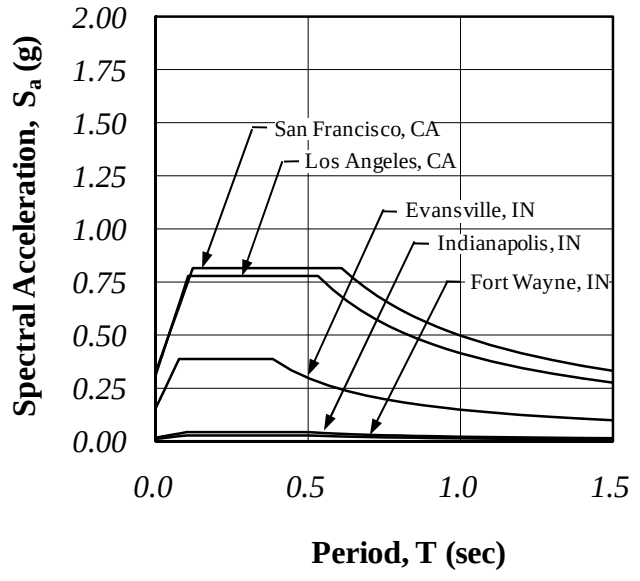

Figure 2.19: EE Acceleration Response Spectra for Select Cities (Recommended LRFD Guidelines)

2.3.4 AASHTO LRFD Specifications, 4th Edition (Including 2008 Interims)

With the issue of the 2008 interim revisions (AASHTO 2008), significant changes were made to the seismic design provision in the LRFD Specifications. Many of the provisions included in the Recommended LRFD Guidelines (ATC 2002) were adopted. However, two primary changes were made. The 2008 interims adopted a 7% probability of exceedance in 75 years which is less severe than the MCE recommended in the Guidelines (3% in 75 years). Second, the shape of the design spectrum was slightly modified by changing the acceleration at a period of zero as shown in Figure 2.20. The value was changed to $A_s = F_{pga}PGA$ rather than $0.4S_{DS}$.

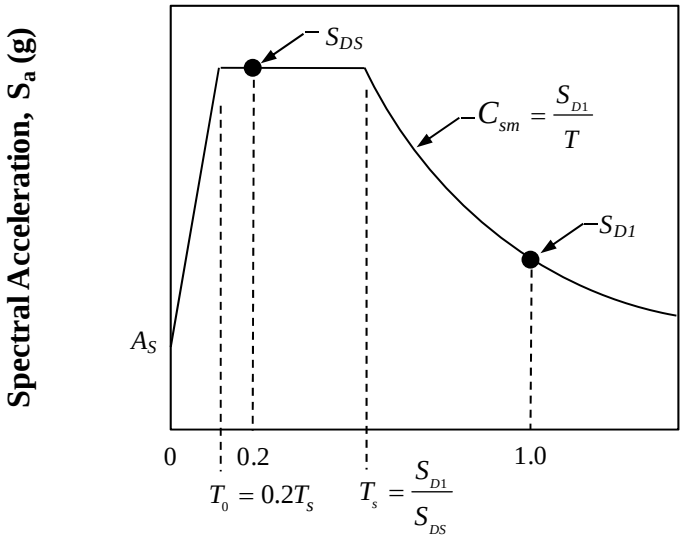

Figure 2.20: Typical Acceleration Spectrum (2008 Interim Revisions)

As for the Recommended Guidelines (ATC 2002), the required parameters are given by:

$$S_{DS} = F_a S_s \tag{2.4}$$

$$S_{D1} = F_v S_1 \tag{2.5}$$

The spectral accelerations for a 0.2 second and 1.0 second period are S_s and S_1, respectively. These values may be obtained from the maps provided in Section 3.20.2.1 of the interim revisions or from the USGS 2007 Seismic Parameters CD. The spectral accelerations used in the interim specifications for the 48 conterminous states are based on the 2002 Seismic Hazard Maps prepared by the United States Geologic Survey (USGS).

Ther terms F_a and F_v are site coefficients. The site coefficient is a function of the site class and spectral acceleration. Numerical values may be obtained from Tables 3.10.3.2-1 through 3.10.3.2-3 of the 2008 interims. The site class definitions are identical to those in the Recommended Guidelines.

Figure 2.21 presents a comparison of the design spectra provided by the 2008 interims and the MCE provided by the Recommended Guidelines for Evansville, IN. Site Class D is assumed in both cases for consistency. It should be noted that the primary difference is due to the change in the probability of exceedance (7% for the 2008 interims versus 3% for the Recommended Guidelines). While the USGS maps are also different (the interim revisions use the 2002 rather than the 1996 USGS maps), the changes made to the maps for Indiana are relatively minor with very little increase in hazard assigned to the State. As evident from Figure 2.21, the demand is significantly lower in the 2008 interims than that provided by the MCE from the Recommended Guidelines.

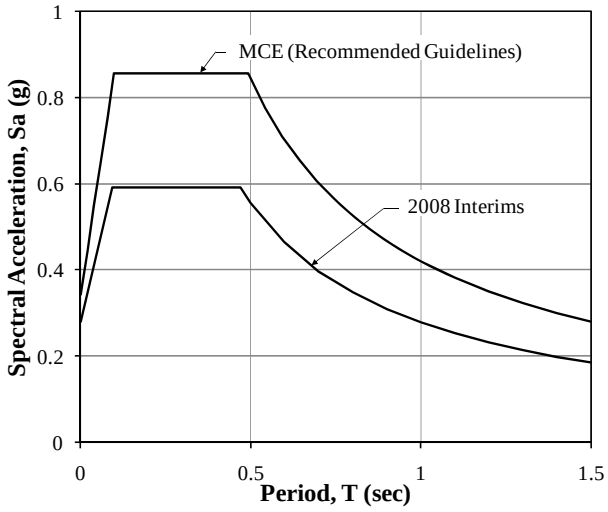

Figure 2.21: Comparison of Acceleration Response Spectra for Evansville

2.3.5 AASHTO Guide Specifications for LRFD Seismic Bridge Design

AASHTO has recently published a Guide Specification for LRFD Seismic Bridge Design (2009). The design acceleration spectrum defined in the Guide Specifications is identical to that adopted in the 2008 interims with only a slight change in notation. In addition to the spectra, the ground acceleration coefficients, spectral acceleration coefficients, site factors, and site classification system are identical. Identical seismic hazard maps are used which are based on the 2002 Seismic Hazard Maps prepared by the USGS.

2.3.6 Selection of Design Spectra

It can be observed from Figure 2.16, Figure 2.18, and Figure 2.19 that the AASHTO Specifications (Standard and LRFD (exclusive of 2008 interims)) and the Recommended Guidelines (ATC 2002) deal with three different levels of design event. To illustrate this difference more clearly, the design spectra for the provisions are shown for Evansville, IN in Figure 2.22. Examining Figure 2.22, it is demonstrated that the AASHTO Specifications (Standard and LRFD (exclusive of 2008 interims)) generally have the lowest design values. The Expected Event (EE) spectrum values are larger than

the AASHTO design spectrum values (10% in 50 years) even though the EE has a much larger probability of exceedance (50% in 75 years). This difference is due to the fact that the AASHTO Specifications are based on the 1988 NEHRP Hazard Maps while the Recommended Guidelines are based on the 1996 USGS Hazard Maps. Finally, the MCE values spectrum are substantially higher than those for both the AASHTO design spectrum and the EE spectrum.

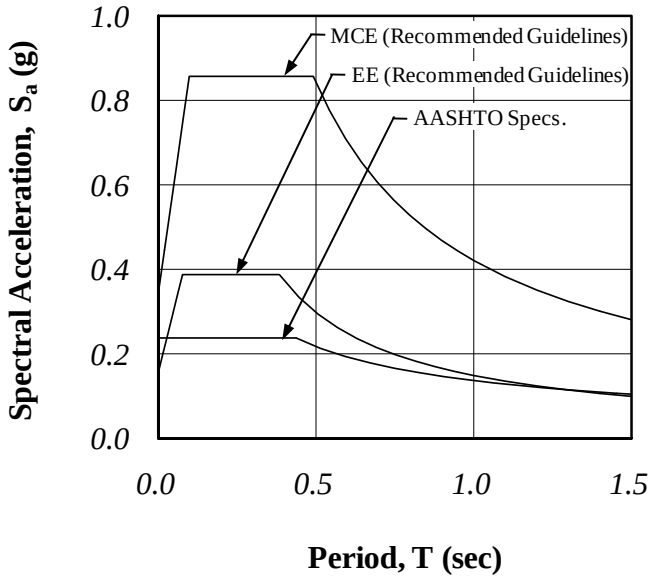

Figure 2.22: Comparison of Evansville Design Spectra

The Recommended Guidelines were developed as part of a National Cooperative Highway Research Program (NCHRP) project to update the seismic design specifications considering the current state of knowledge and practice. While significant differences in philosophy resulted, such as considering multiple design events (EE and MCE), the hazard map update (1988 to 1996) produced significant differences in design. The Recommended Guidelines were used as a basis for moving forward with revisions to the seismic design bridge specifications, and the recommendations for the most part have been recently adopted in the 2008 interims to the LRFD specifications as well as the recently published Guide Specifications for LRFD Seismic Bridge Design (2009). It should be noted that while the Recommended Guidelines included a 3% probability of

exceedance in 75 years for the MCE, the 2008 interims and the Guide Specifications adopted a reduced event defined by a 7% probability of exceedance in 75 years. This difference is illustrated in Figure 2.21.

While the 7% probability of exceedance in 75 years has been adopted, which relates to an approximately 1000 year event, there is merit in considering a very rare event defined by a 3% probability of exceedance in 75 years (approximately a 2500 year event). Furthermore, the spectra previously presented are based on Site Class D. If a Site Class E is considered using the 2008 interims, an increase in the spectral accelerations results as illustrated in Figure 2.23. As shown, the spectrum developed for Site Class E using the 2008 interims is approximately the same as that using the MCE for the default Site Class D. Because the spectrum is very similar, all future analyses will consider only the MCE spectrum. This spectrum is considered an upper bound of response and will produce conservative results over an extremely wide range of soil types for both the 2008 interims to the LRFD Design Specifications and for the Guide Specifications.

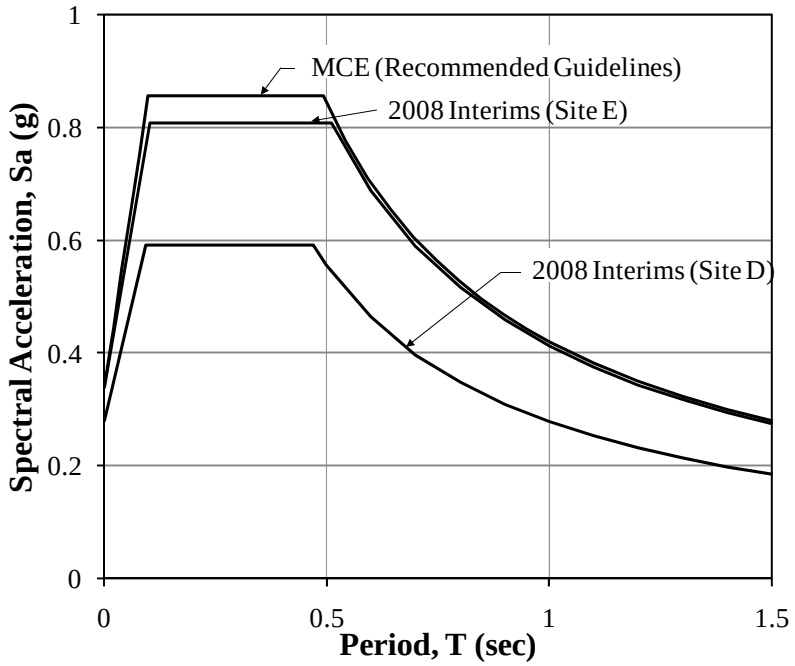

Figure 2.23: Comparison of Site Class

Considering the various levels of seismic demand as provided by the various design specifications and guidelines, three design spectra were selected to bracket the response: the "AASHTO design spectrum," as defined by the Standard Specifications and LRFD Specifications (exclusive of 2008 interims) which serve as the lower bound and the two design spectra defined in the Recommended LRFD Design Guidelines (ATC 2002) that represent the Expected Event (EE) and Maximum Considered Event (MCE) which serves as the upper bound. Using these design spectra, ground motions were developed which consider the range of expected seismic response.

2.3.6.1 *Probability of Exceedance*

The probability of an earthquake occurring in a given time period is commonly modeled as a Poisson process. For a Poisson process, the probability of an event occurring *N* times during an interval of time *t* can be shown to be

$$P[N = n] = \frac{(\lambda t)^n e^{-\lambda t}}{n!} \tag{1.1}$$

where λ is the average rate of occurrence of the event. The probability of at least one event occurring during an interval of time t (the probability of exceedance) is then

$$\begin{aligned} P[N \geq 1] &= P[N = 1] + P[N = 2] + P[N = 3] + \cdots \\ &+P[N = \infty] = 1 - P[N = 0] = 1 - e^{-\lambda t} \end{aligned} \tag{1.2}$$

Solving for λ:

$$\lambda = -\frac{\ln(1 - P[N \geq 1])}{t} \tag{1.3}$$

The return period T_R of an event is the reciprocal of the average rate of occurrence:

$$T_R = \frac{1}{\lambda} = -\frac{t}{\ln(1 - P[N \geq 1])} \tag{1.4}$$

The AASHTO specifications (Standard and LRFD (exclusive of 2008 interims)) consider one design earthquake corresponding to a 10% probability of exceedance in 50 years. The corresponding return period is

$$T_R = -\frac{50\ years}{\ln(1 - 0.10)} = 475\ years$$

The Recommended LRFD Guidelines consider two events: the maximum considered earthquake (MCE) and the expected earthquake (EE). The MCE corresponds to 3% probability of exceedance in 75 years. The EE corresponds to a 50% probability of exceedance in 75 years. The return periods computed as shown above are approximately 2462 years and 108 years for the MCE and EE, respectively. In addition, the 2008 interims and the AASHTO Guide Specifications consider a 7% probability of exceedance in 75 years which corresponds to a 1033 year return period. These values are tabulated in Table 2.1.

Table 2.1: Return Period for Various Probabilities of Exceedance

Source	Prob. of Exceedance (%)	t (yrs)	T_R (yrs)
AASHTO Specifications			
Standard Specifications, 17th Ed.	10	50	475
LRFD Specifications, 4th Ed.	10	50	475
LRFD Specifications, 2008 Interims	7	75	1033
Recommended LRFD Guidelines			
Maximum Considered Earthquake (MCE)	3	75	2462
Expected Earthquake (EE)	50	75	108
AASHTO Guide Specifications			
1st Ed.	7	75	1033

It is helpful for comparison purposes to compute the probability of exceedance for each case based on the same time interval. It can be shown that a 10% probability of exceedance in 50 years is approximately equivalent to a 15% probability of exceedance in 75 years:

$$P[N \geq 1] = 1 - e^{-\left(\frac{1}{475}\right)(75)} = 0.146 \approx 15\%$$

2.4 Representative Ground Motions

A group of eight ground motions was considered for use in the analytical portion of this study. Because few recorded strong ground motions exist for Indiana, additional ground motions from other regions were used. Three motions were selected from the Eastern United States and Canada and five from the Western United States. The epicenters of the selected events are presented in Figure 2.24. The details of each event are listed Table 2.2. The recorded ground motions are presented in the next section.

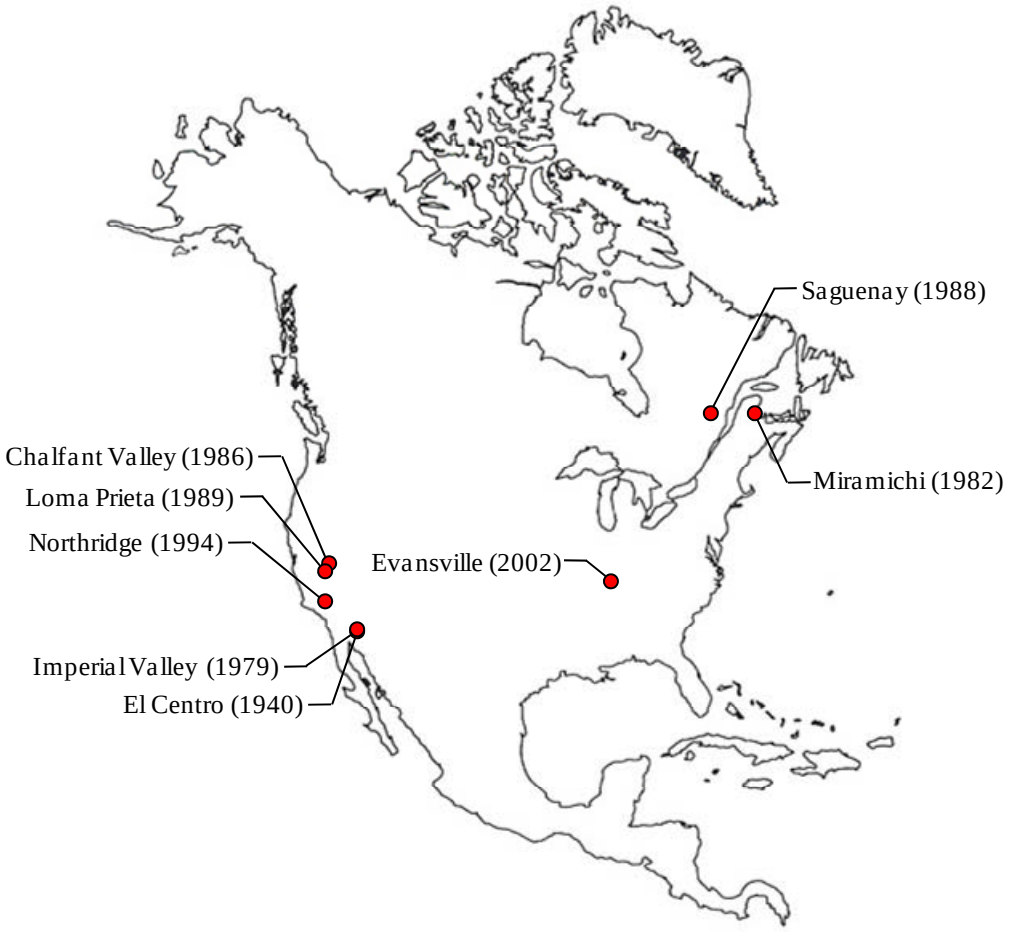

Figure 2.24: Epicenters of Representative Ground Motions

Table 2.2: Ground Motion Details

	Event Num.	Date	Event Name	Event Mag.	Event Location	Recording Station	Instrument Orientation (deg.)	Distance From Event (km)	Data Source
Eastern U.S.	1	04/31/1982	Miramichi	5.0 m_b (2)	N 47° W 66° 36'	GSC Station IB2	231	5.1 (6)	(8)
	2	11/25/1988	Saguenay	6.0 M_s (3)	N 48° 7' 15.6" W 71° 11' 9.6"	NCEER Station DCKY	90	194.7 (6)	(8)
	3	06/18/2002	Evansville	5.0 M_n (4)	N 38° 4' 8.4" W 87° 40' 48"	USGS Station 2491	16	228.0 (5)	(8)
Western U.S.	4	05/18/1940	El Centro	6.9 M_L (1)	N 32° 45' 36.36" W 115° 24' 58.32"	Array Sta. 9: Imperial Valley Irrigation Dist.	180	12.2 (6)	(8)
	5	10/15/1979	Imperial Valley	6.5 M_L (1)	N 32° 38' 4.2" W 115° 18' 31.68"	USGS Station 0955	220	8.3 (7)	(8)
	6	07/21/1986	Chalfant Valley	6.4 M_L (1)	N 37° 32' 17.88" W 118° 26' 34.8"	CSMIP Station 54428	270	18.5 (6)	(8)
	7	10/19/1989	Loma Prieta	7.0 M_L (1)	N 37° 2' 26.52" W 121° 52' 58.44"	USGS Station 1571	322	21.1 (7)	(8)
	8	01/17/1994	Northridge	6.4 M_L (1)	N 34° 12' 20.52" W 118° 33' 14.04"	USC Station 5303	180	12.9 (7)	(8)

(1) M_L = Richter local magnitude
(2) m_b = body wave magnitude
(3) M_s = surface wave magnitude
(4) M_n = Nuttli magnitude
(5) Epicentral Distance
(6) Hypocentral Distance
(7) Closest Distance to Fault
(8) Cosmos Virtual Data Center (http://db.cosmos-eq.org)

2.4.1 Unscaled Ground Motions

Elastic response spectra computed for the unscaled ground motions are presented in Figure 2.25. The unscaled ground motions are presented in Figure 2.26. K_a represents the amplitude scaling factor. The value of K_a equal to 1.00 in Figure 2.26 indicates that the ground motions are unaltered. The K_a factor is defined in detail in Section 2.4.2.

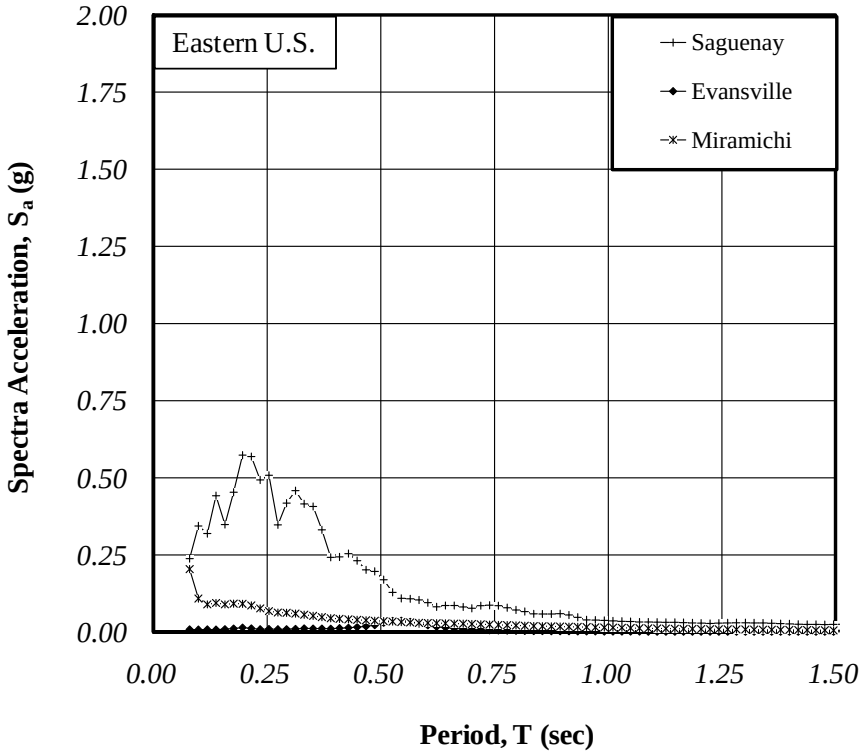

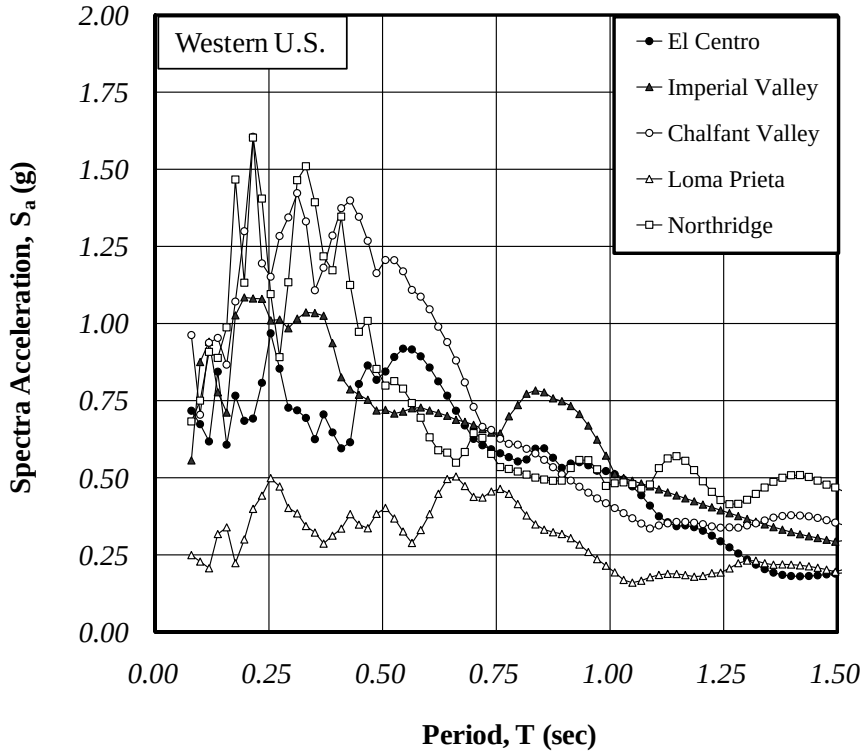

Figure 2.25: Unscaled Response Spectra

Eastern U.S.

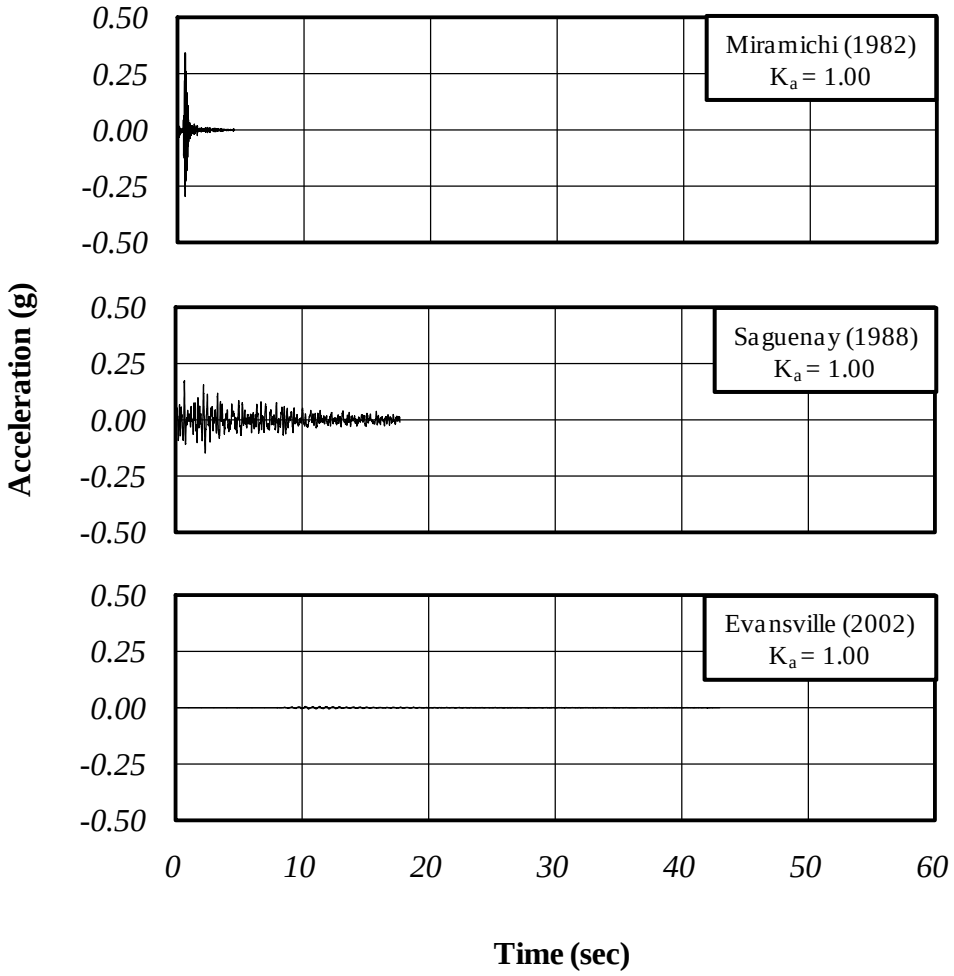

Figure 2.26: Unscaled Ground Motions

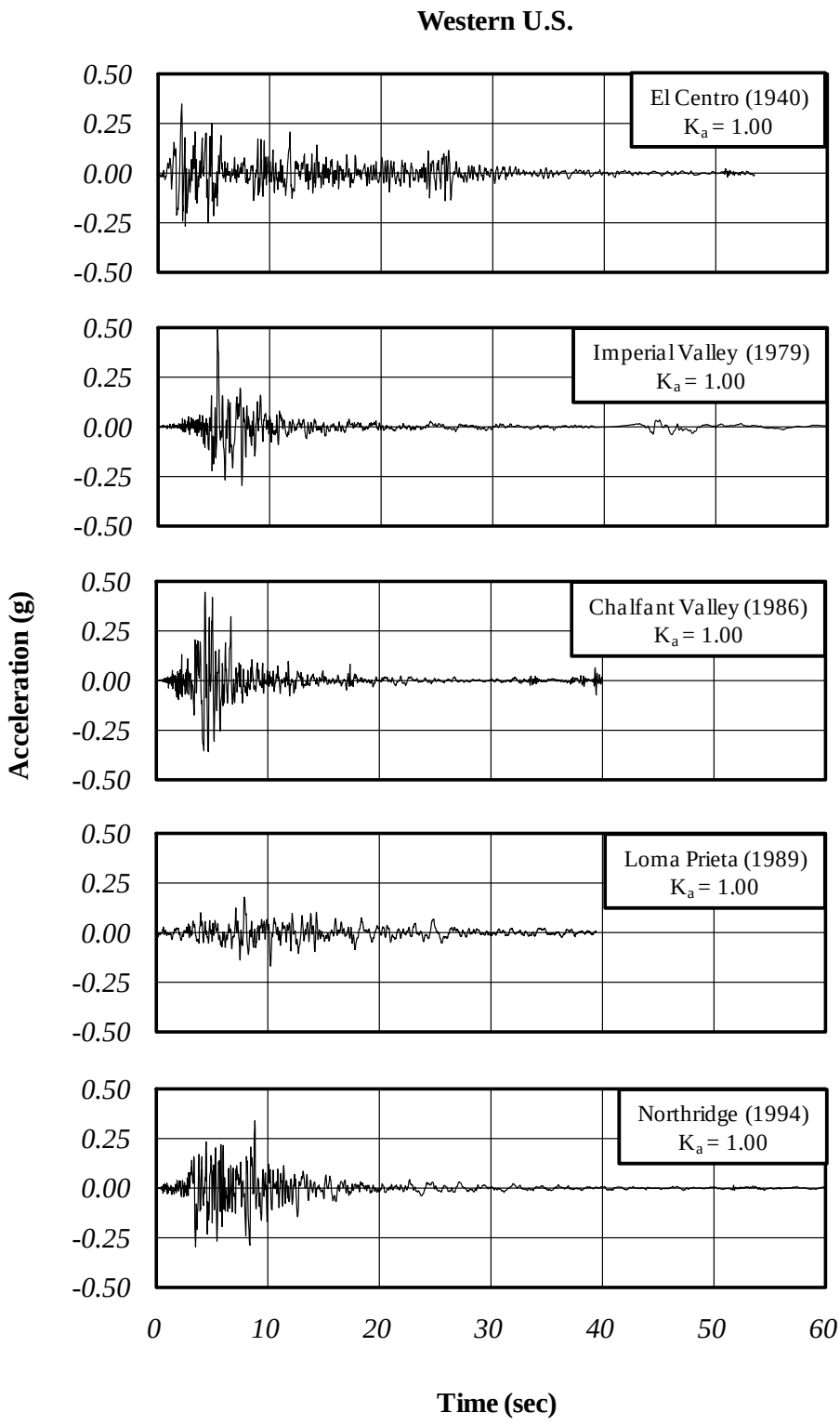

Figure 2.26 (continued): Unscaled Ground Motions

2.4.2 Scaled Ground Motions

The unscaled ground motions vary considerably in amplitude and duration. Many approaches exist for scaling ground motions (Karuma and Farrow 2003). For the purposes of this study a scaling factor, K_a, was used to scale the input acceleration record so that the acceleration response spectrum fit the applicable design spectrum as closely as possible. Because of their relatively small magnitude, the Evansville and Miramichi ground motions were not scaled. Significant scaling would be required for these events resulting in an unrealistic record. The scaling factor K_a is shown in Figure 2.27.

The acceleration records were scaled to match the design spectra as closely as possible. The Western U.S. ground motions matched the design spectra reasonably well across the entire range of periods under consideration. However, the lone Eastern U.S. ground motion that was scaled did not follow the design spectra as well. This ground motion was scaled to match the short period plateau of the design spectra. Consequently, the longer-period response spectra for the Eastern U.S. motion are significantly lower than the design spectra. The design spectra for Evansville , IN (Figure 2.22) were used as the basis for scaling the ground motions. Evansville spectra were selected because of this city's location in the Southwest corner of the state where the seismic hazard is highest. These spectra were constructed using default soil conditions (stiff soil) as defined by the respective specifications. The scaled ground motions for the three design spectra (AASHTO, EE, and MCE) are presented in the following sections and are illustrated in Figure 2.28, Figure 2.30, and Figure 2.32.

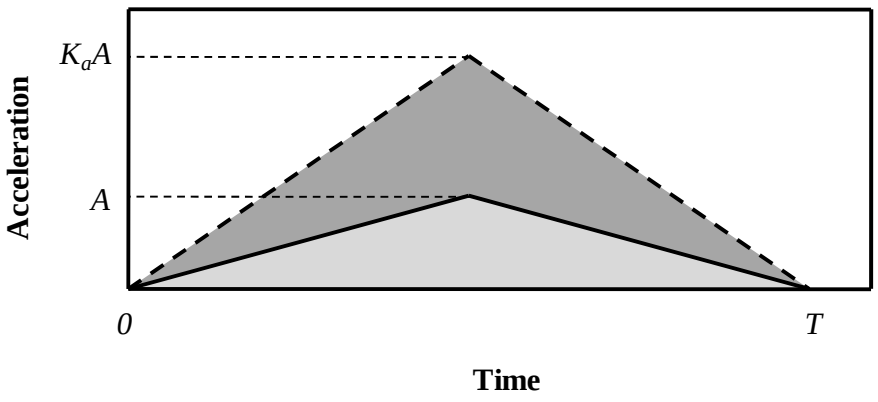

Figure 2.27: Ground Motion Scaling Parameters

2.4.2.1 AASHTO Specifications (Standard and LRFD)

The design ground motions were scaled to fit the AASHTO design spectrum for Evansville, IN (Figure 2.22). The resulting response spectra are presented in Figure 2.28. The scaled ground motions are presented in Figure 2.29.

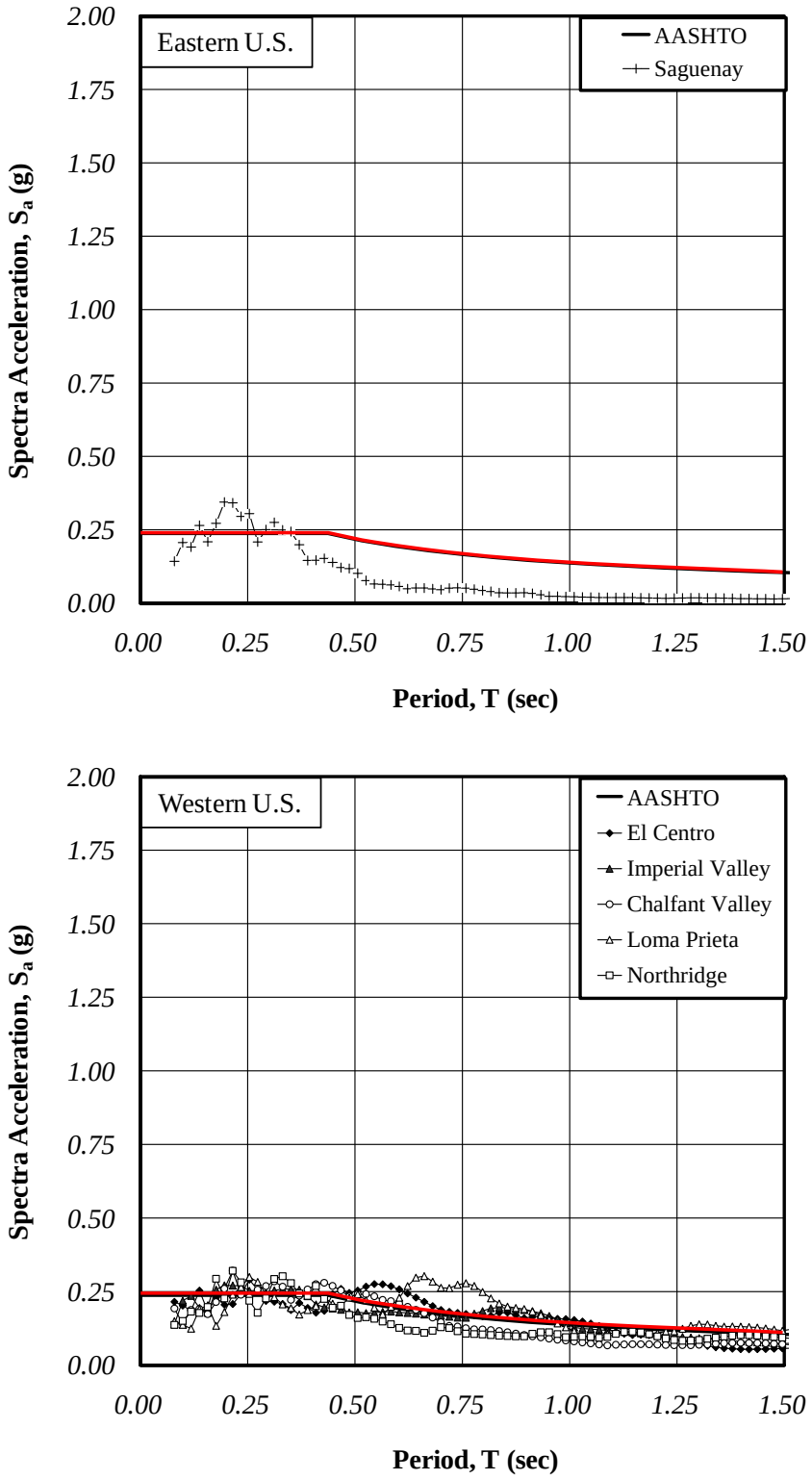

Figure 2.28: Scaled Response Spectra - AASHTO

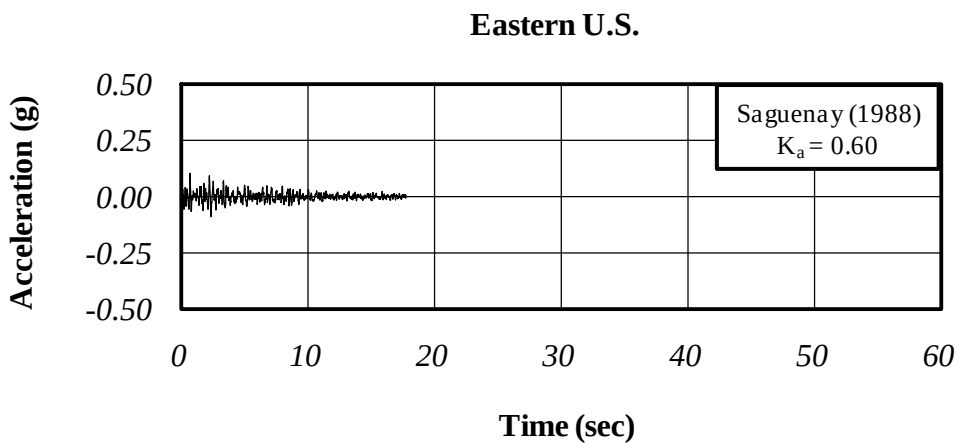

Figure 2.29: AASHTO Scaled Ground Motions

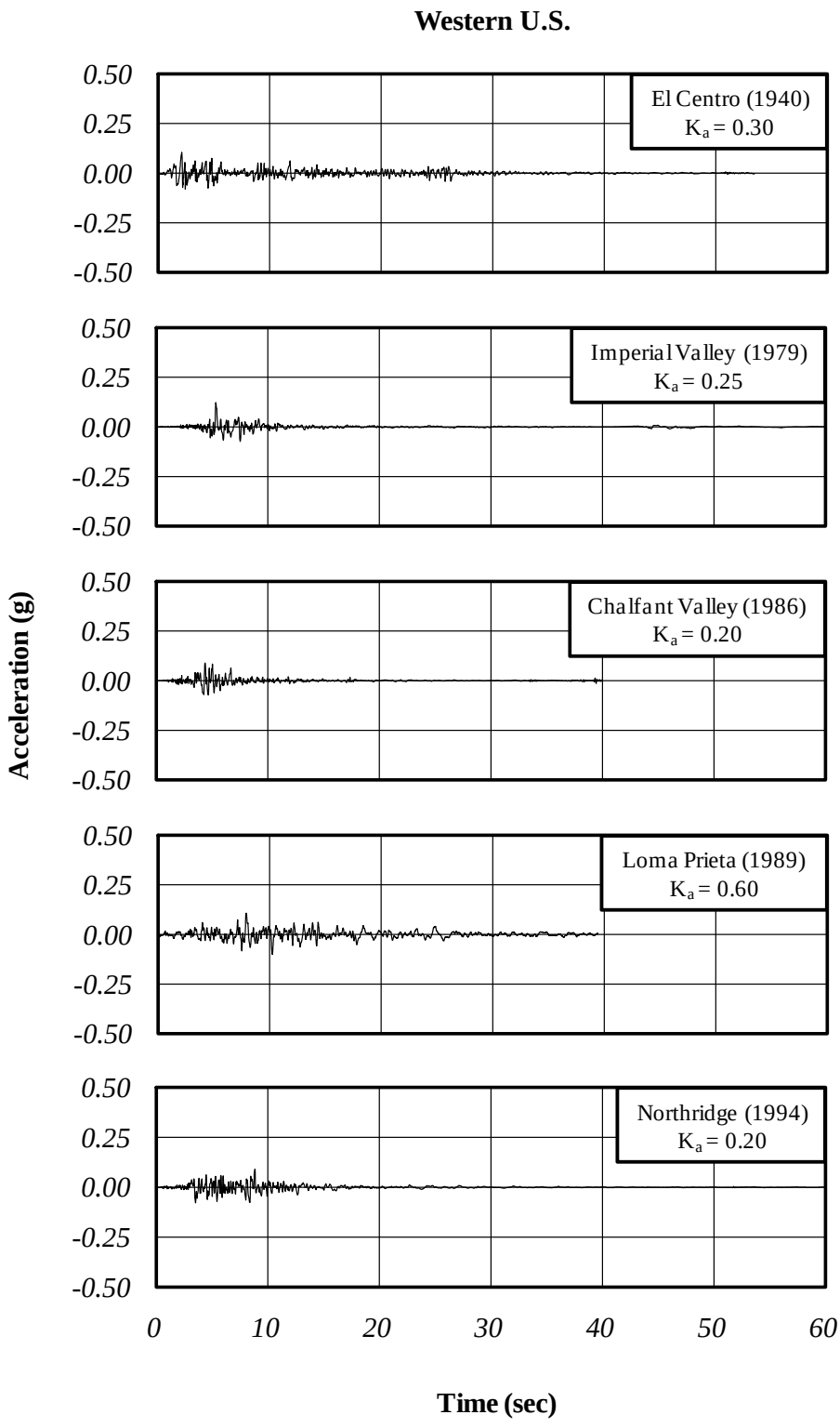

Figure 2.29 (continued): AASHTO Scaled Ground Motions

2.4.2.2 Recommended Guidelines: EE

The design ground motions were scaled to fit the Expected Event (EE) design spectrum for Evansville, IN (Figure 2.22) as defined in the Recommended LRFD Guidelines (ATC 2002). The resulting response spectra are presented in Figure 2.30. The EE scaled ground motions are presented in Figure 2.31.

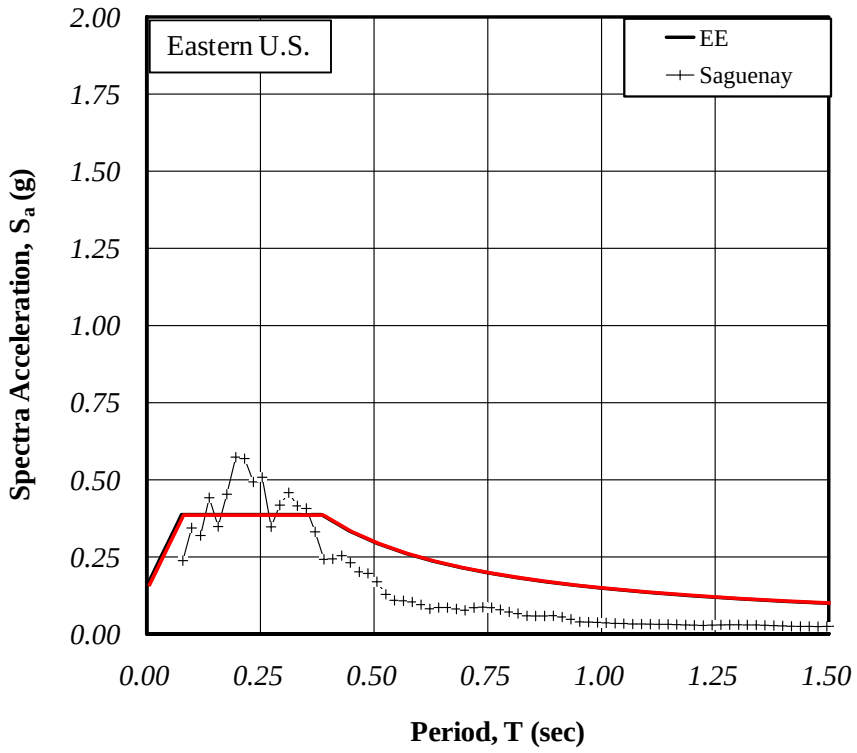

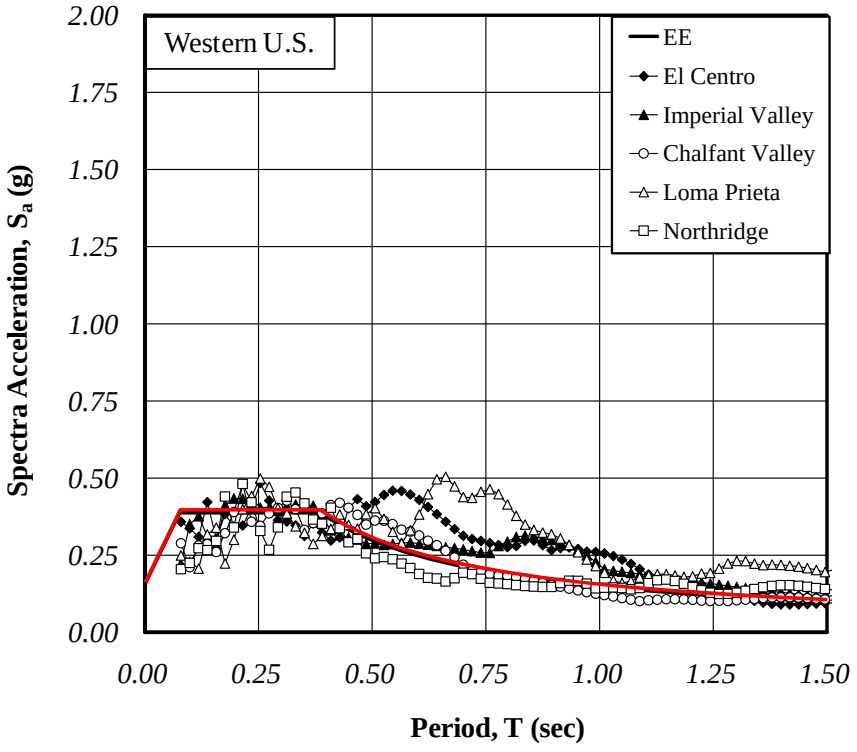

Figure 2.30: Scaled Response Spectra - EE

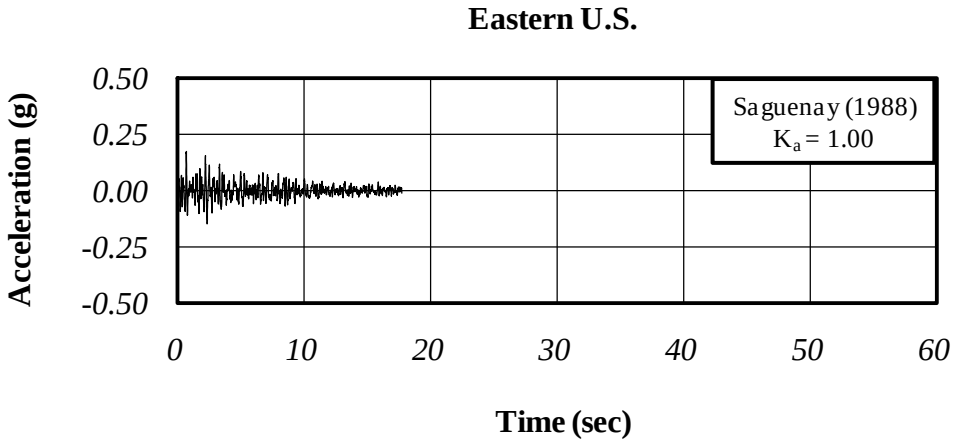

Figure 2.31: EE Scaled Ground Motions

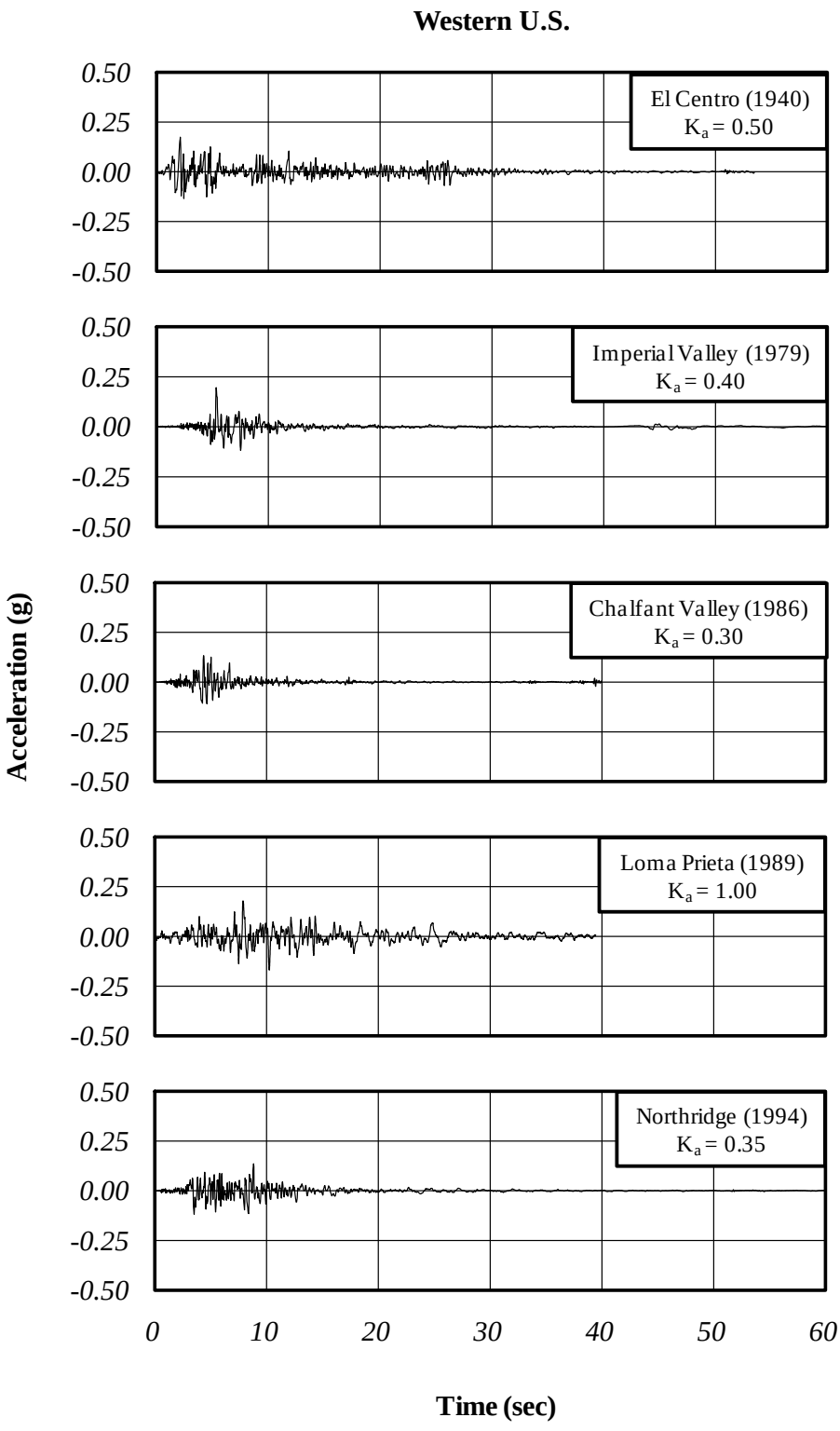

Figure 2.31 (continued): EE Scaled Ground Motions

2.4.2.3 Recommended Guidelines: MCE

The design ground motions were scaled to fit the Maximum Considered Event (MCE) design spectrum for Evansville, IN (Figure 2.22) as defined in the Recommended LRFD Guidelines (ATC 2002). The resulting response spectra are presented in Figure 2.32. The MCE scaled ground motions are presented in Figure 2.33.

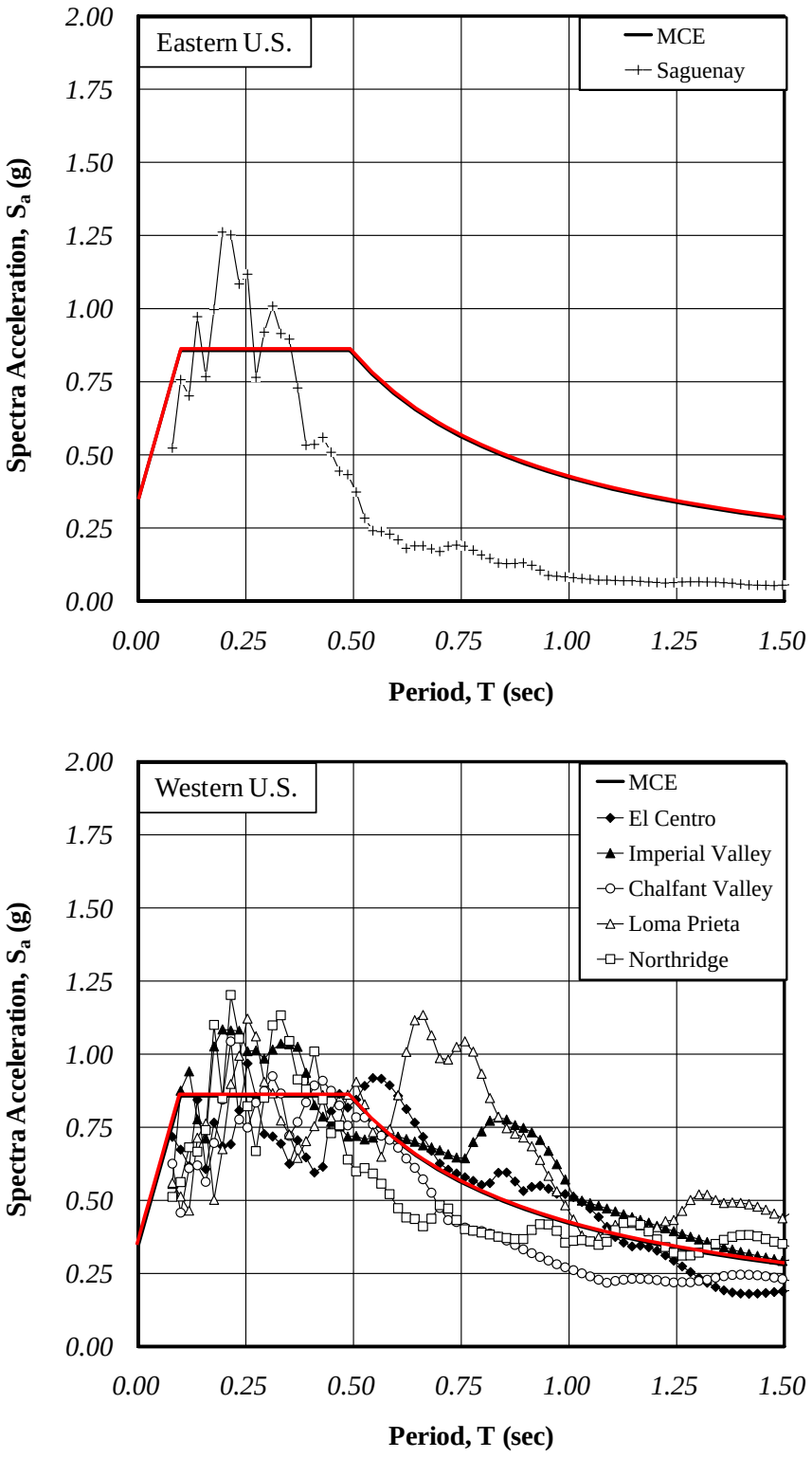

Figure 2.32: Scaled Response Spectra - MCE

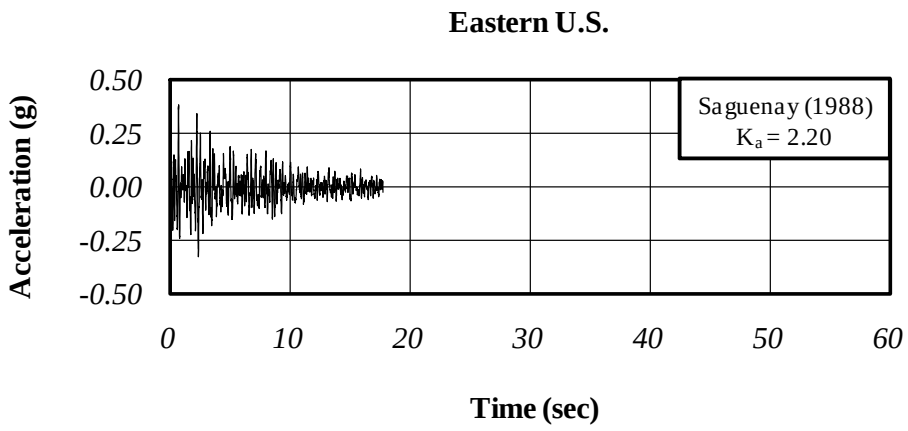

Figure 2.33: MCE Scaled Ground Motions

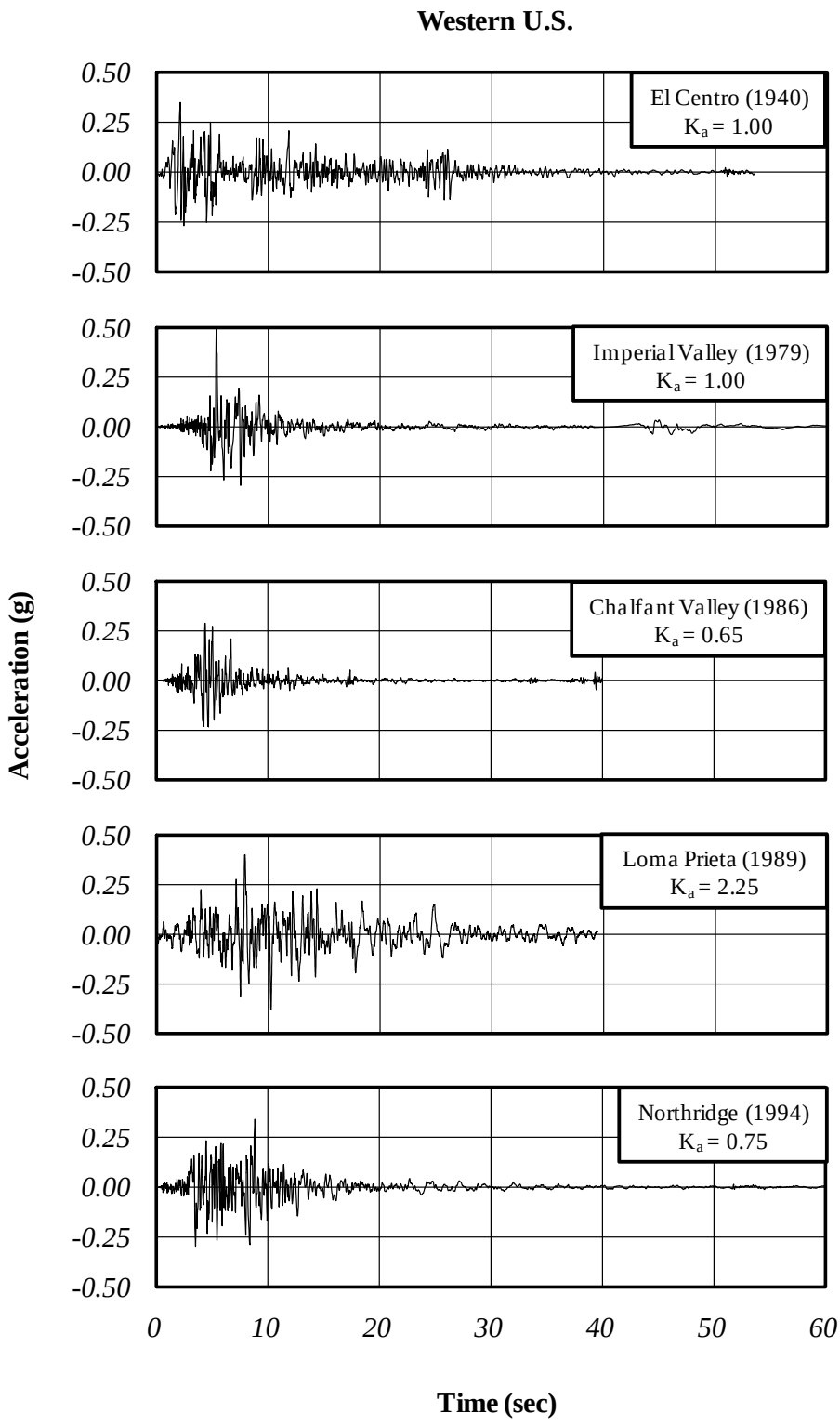

Figure 2.33 (continued): MCE Scaled Ground Motions

2.5 Conclusions

As illustrated in the preceding sections, the Recommended LRFD Guidelines consider a much larger ground motion than previous AASHTO requirements. In addition, current requirements as provided by the 2008 interims and the recently published Guide Specifications for LRFD Seismic Bridge Design, while producing significantly larger motions than past practice, are not as severe as originally proposed in the Recommended LRFD Guidelines due to the increase in the probability of exceedance from 3% to 7% in 75 years. The requirements of both the Recommended LRFD Guidelines and the prior AASHTO Design Specifications will be considered to evaluate the range of design levels and provide perspective on both past and future design practice. Therefore three sets of design ground motions were developed. The ground motions developed in this section will be used to estimate seismic displacements of integral bridge abutments.

CHAPTER 3: FIELD INVESTIGATION

3.1 Introduction

The force-displacement characteristics of integral abutments are critical to understanding the response of integral abutment bridges to seismic loading. In traditional construction, the bearings are typically the controlling feature of a seismic design and the abutments are assumed to remain fixed. However, in integral abutment construction, there are no bearings and the superstructure and abutment form a continuous, monolithic system. Integral abutments have been observed in the field to move significantly under thermal expansion and contraction of the superstructure. Data related to the thermal movements of one particular Indiana bridge are analyzed in this chapter. An approximate force-displacement relationship for the integral abutment is developed. This relationship is important as it can be used to estimate the soil-structure interaction and be integrated into analytical models used to estimate displacement demand.

3.2 Structure

The structure under consideration in this chapter is the SR18 Bridge over the Mississinewa River located in Marion, Indiana (Figure 3.1, Figure 3.2). The overall bridge dimensions are presented in Figure 3.3. The bridge is a 5-span, continuous, integral abutment structure with a skew angle of 8º and a total length of 367 ft. A typical cross-section of the superstructure is shown in Figure 3.4. The superstructure consists of five prestressed concrete bulb tee girders and an 8-in. thick concrete deck. The superstructure is integral with the two abutments (Bents 1 and 6) and rests on elastomeric bearings at each intermediate pier (Piers 2-5). Each abutment is supported by a single row of ten concrete filled steel tube piles (CFT14x0.312).

Figure 3.1: Bridge Location

Figure 3.2: SR18 Bridge

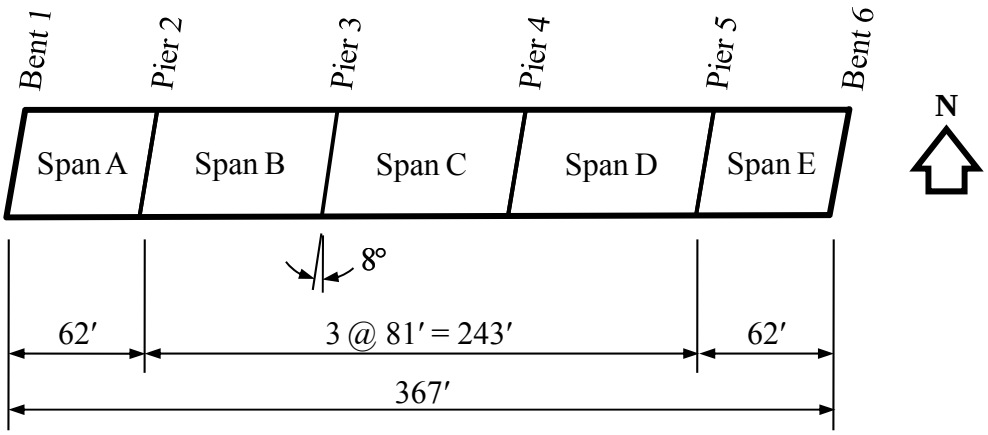

Figure 3.3: SR18 Overall Plan

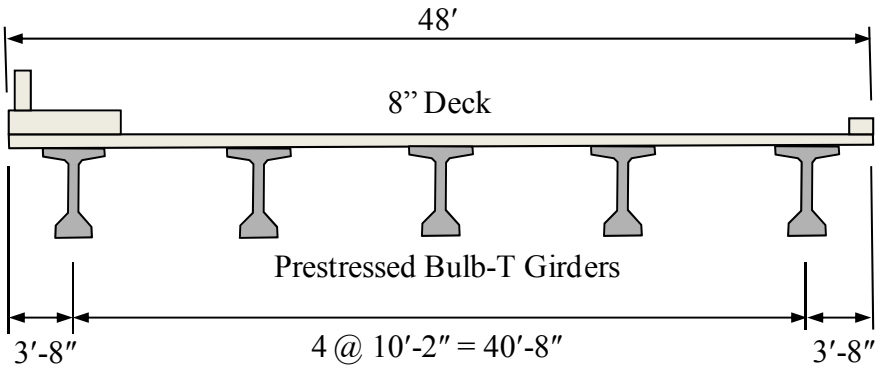

Figure 3.4: Typical Cross-Section

3.3 Instrumentation

The bridge was instrumented extensively in 2003 during a reconstruction project. Only the instrumentation relevant to movements of the abutment are discussed here. A full description of the installed instrumentation is provided by Chovichien (2004). Bent 6 instrument locations are shown in Figure 3.5 and Figure 3.6. Longitudinal displacements of Bent 6 were measured with convergence meters attached to reference piles driven 10 ft behind the centerline of the abutment. One convergence meter is located at the centerline of the abutment (referred to as CV6NE). A second convergence meter was installed near

the south end of Bent 6 (referred to as CV6SE). Two earth pressure cells were installed in the abutment during casting. These pressure cells are located at the same height as the convergence meters and, as closely as possible, near the point where the convergence meter attaches to the abutment. The earth pressure cells are referred to as EP6NE and EP6SE corresponding to CV6NE and CV6SE, respectively. These four instruments produce a relationship between earth pressure and displacement at two points on the abutment. In addition to the instruments shown in Figure 3.5 and Figure 3.6, an ambient temperature gage was installed at Pier 5. The temperature gage is mounted to the underside of the deck between two girders to minimize the effects of direct sunlight and wind chill. All gages used in this study were vibrating-wire type instruments. Data were collected hourly by an on-site datalogger and were accessible remotely via a telephone modem.

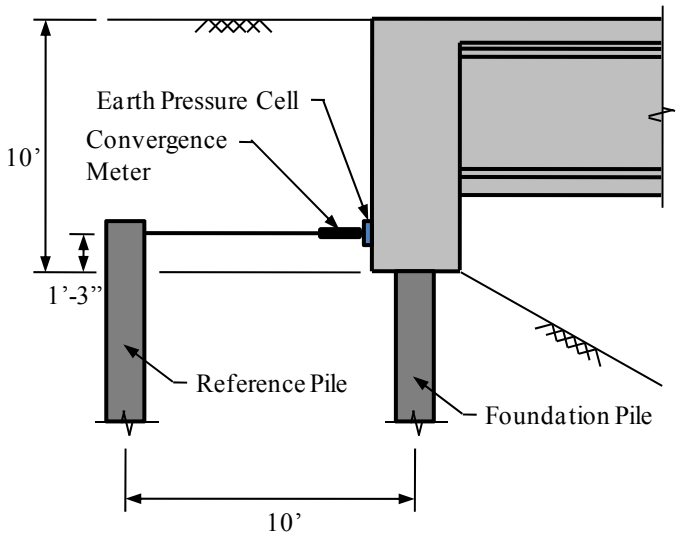

Figure 3.5: SR18 East Abutment Instrumentation (Elevation View)

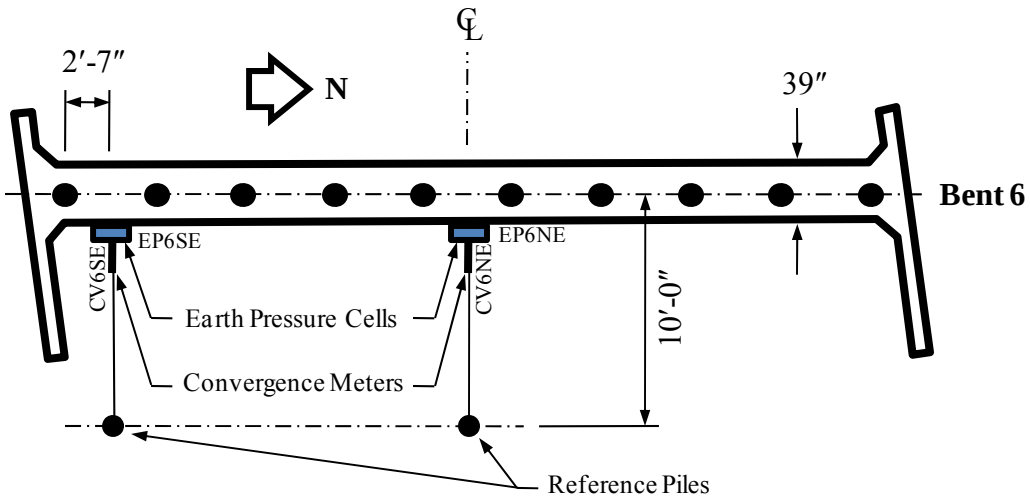

Figure 3.6: SR18 East Abutment Instrumentation (Plan View)

3.4 Results

Data collected by the instruments discussed in the previous section are presented as a series of annual plots in Figure 3.7- Figure 3.11 from 2003 – 2007. The entire record for each instrument is shown in Figure 3.12. The gage records are continuous except for a brief period in mid 2004 when no data are available due to power failure of the data collection system.

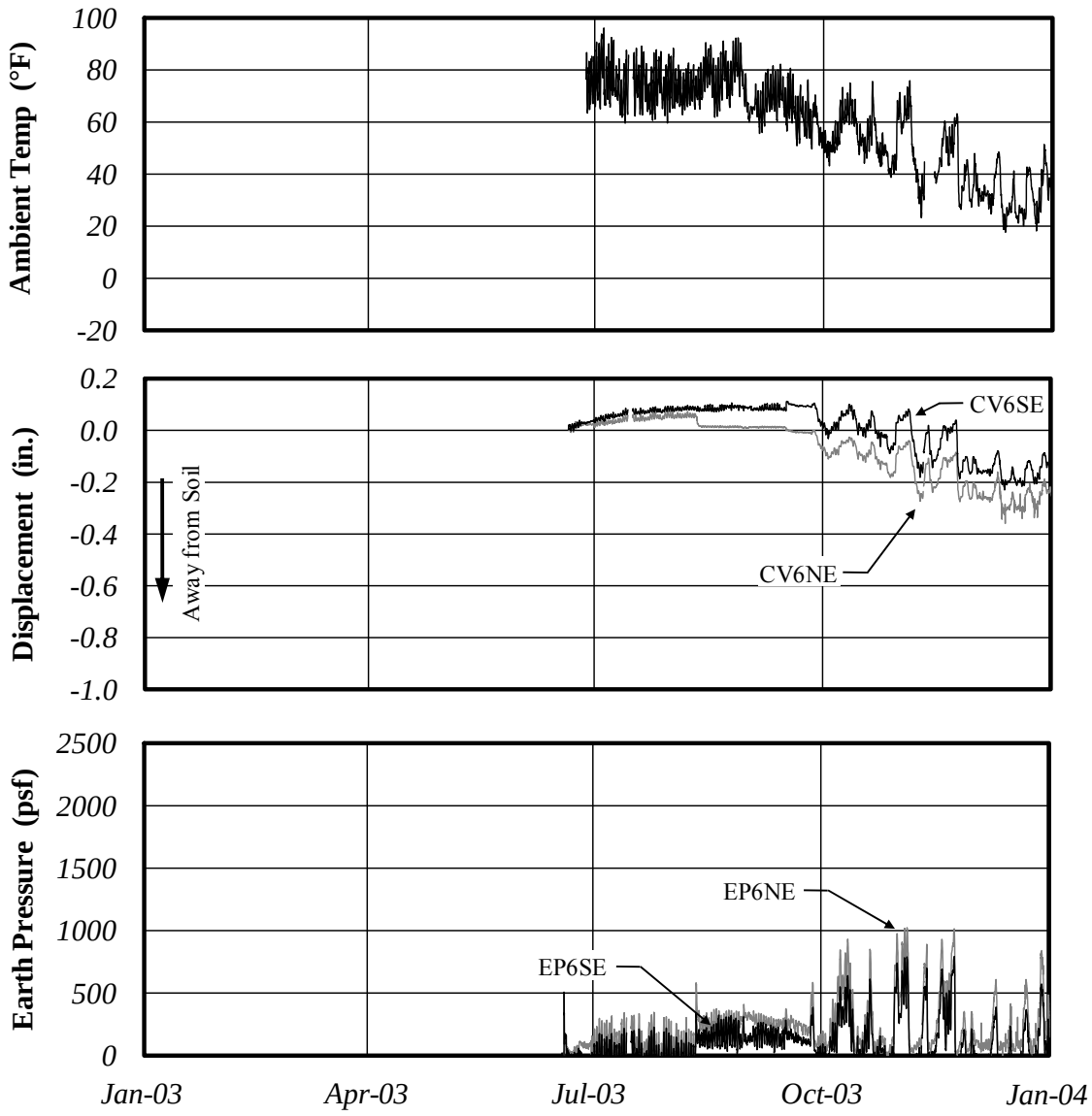

Figure 3.7: SR18 Results (2003)

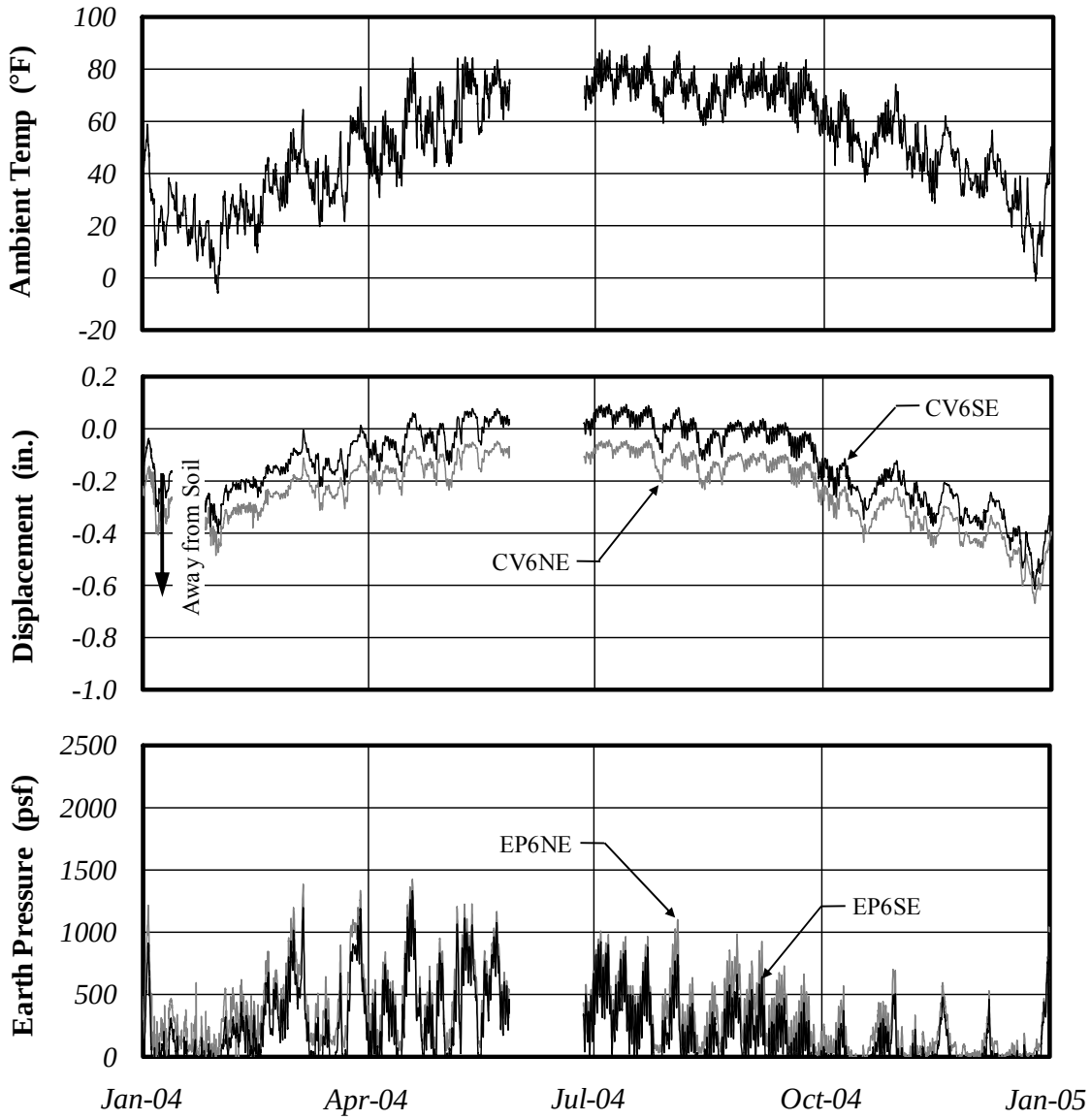

Figure 3.8: SR18 Results (2004)

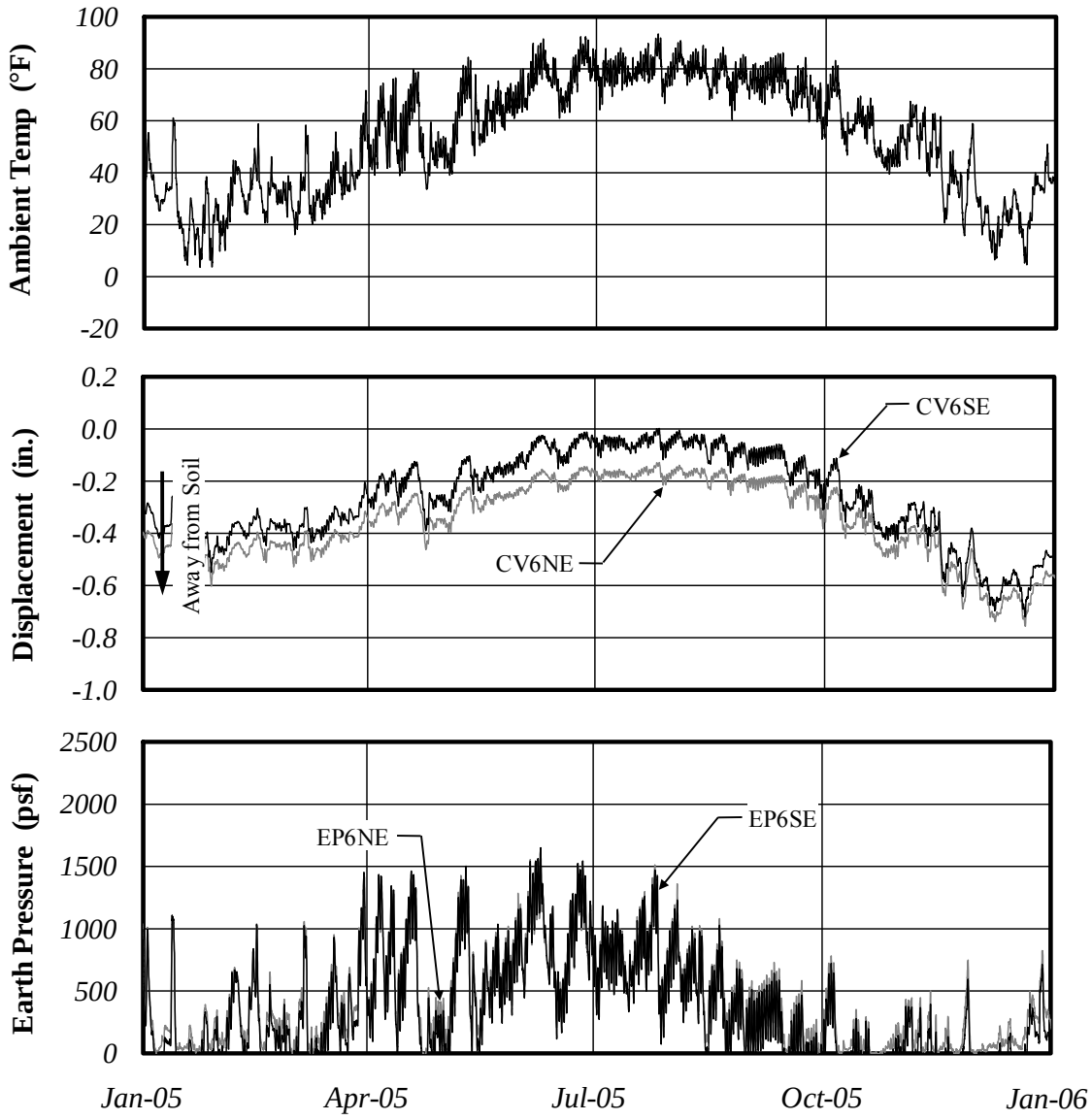

Figure 3.9: SR18 Results (2005)

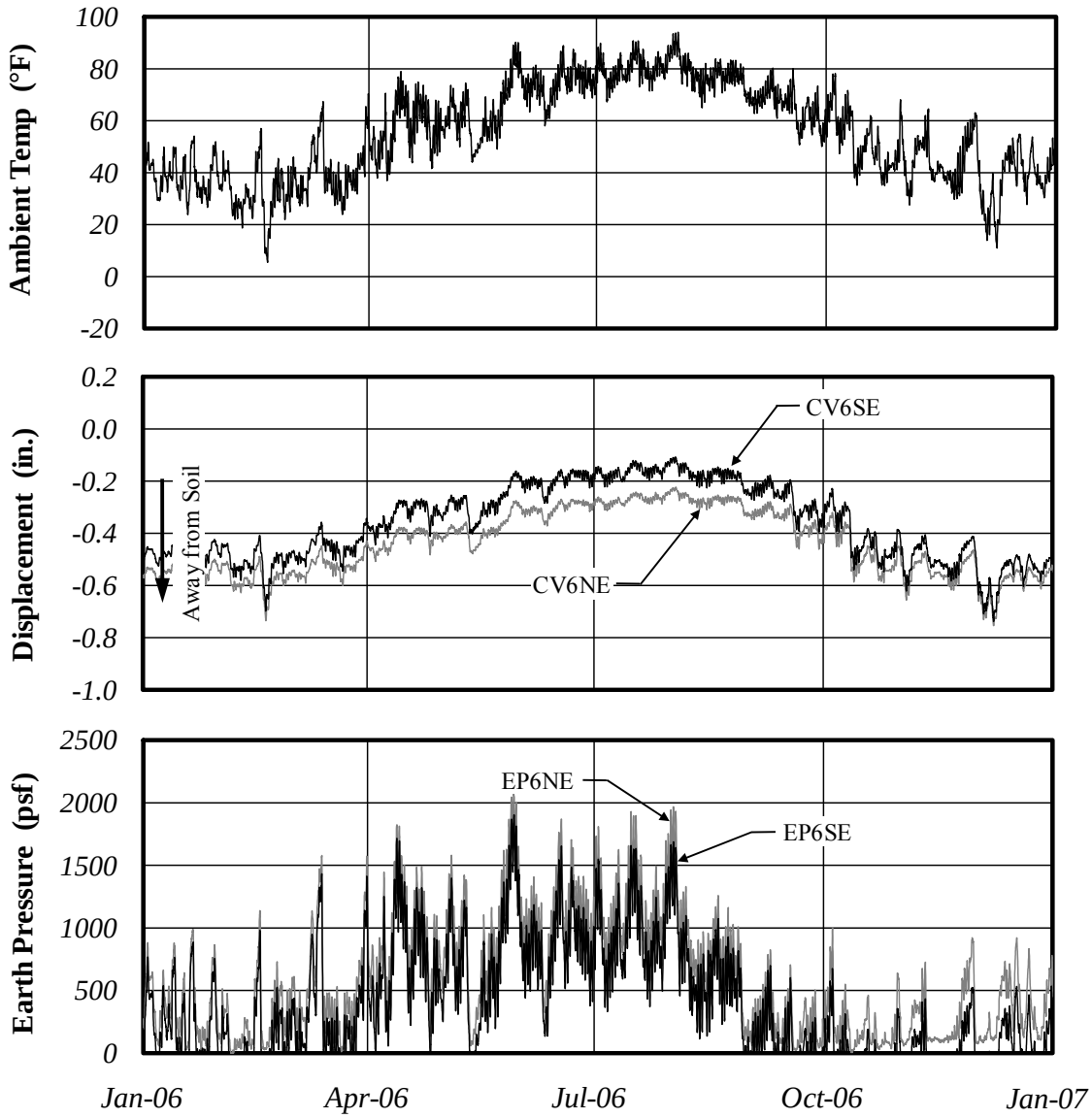

Figure 3.10: SR18 Results (2006)

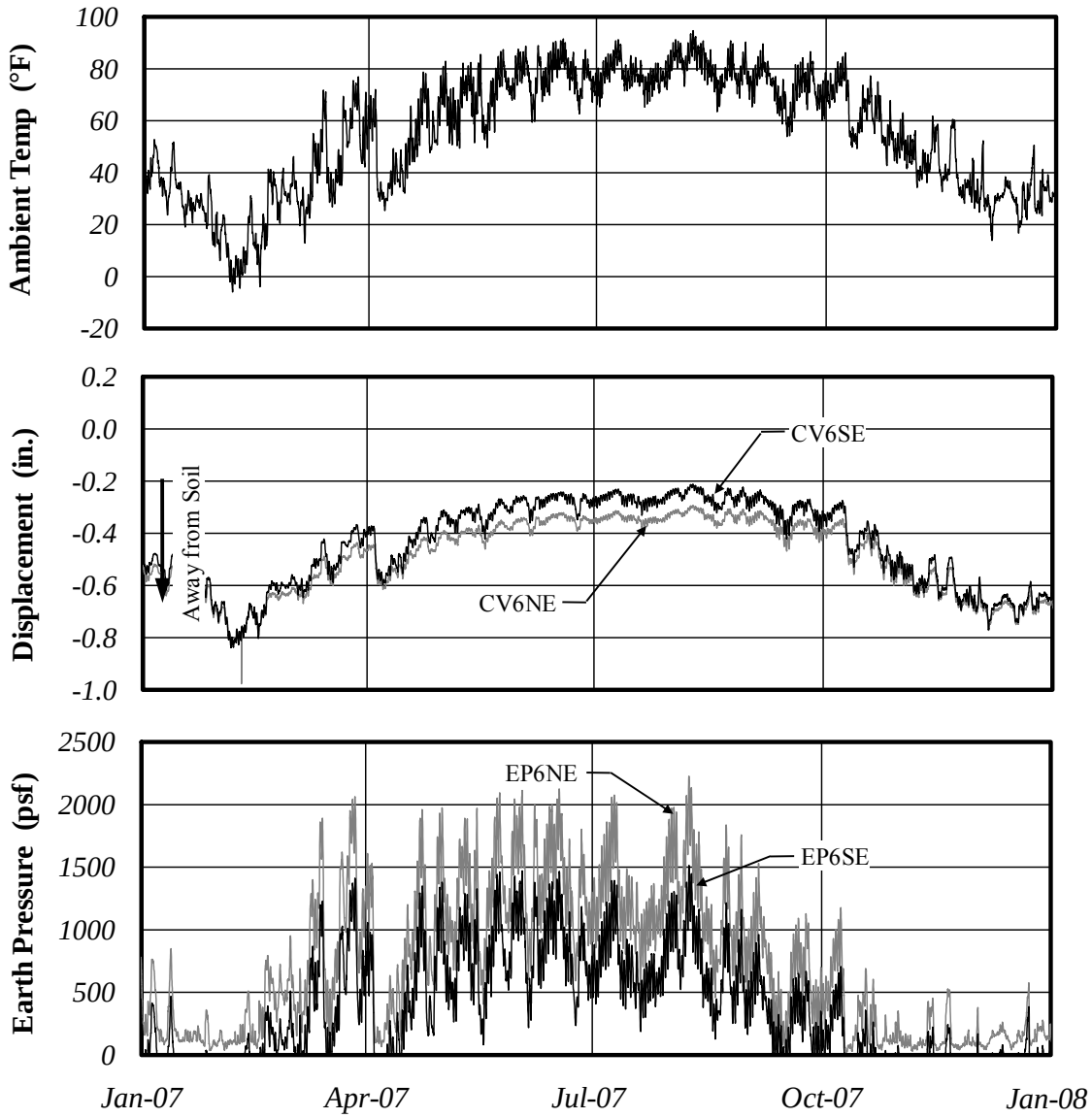

Figure 3.11: SR18 Results (2007)

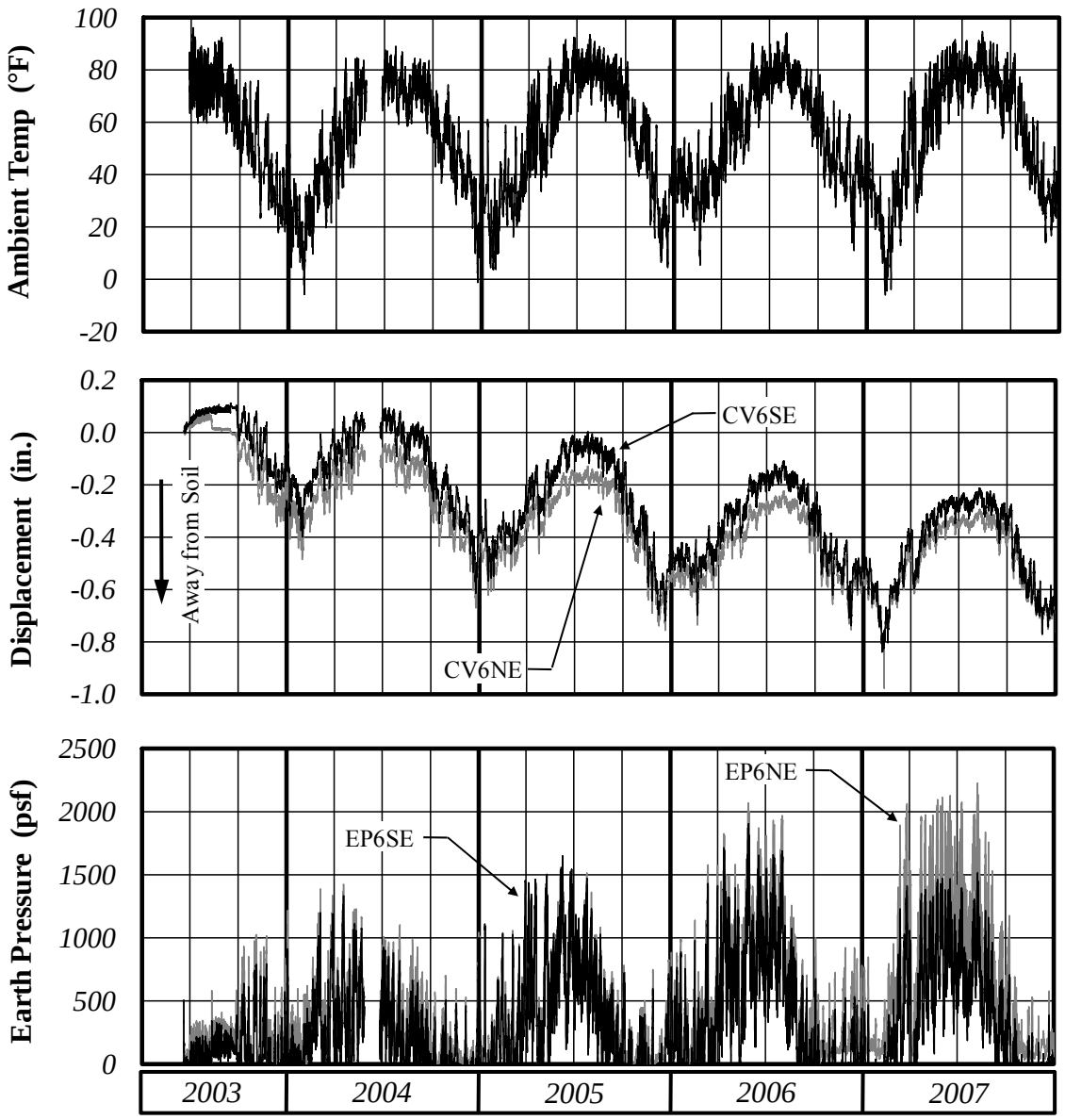

Figure 3.12: SR18 Results (2003-2007)

3.5 Evaluation of Results

It may be seen from Figure 3.12 that the abutment movements and corresponding earth pressures are in response to changes in ambient temperature. The ambient temperature ranges from approximately 0°F - 90°F. The measured abutment movements have a consistent annual variation of approximately 0.6 in. However, the abutment displacements steadily move in the negative direction (away from the backfill). Additionally, the measured earth pressures correspond to movements of the abutment. Increasing earth pressures occur as the abutment moves toward the backfill. Measured earth pressures reduce to near zero levels each winter as the abutment moves away from the backfill. Maximum earth pressures for each cell increase each year with the exception of 2007. In 2007, EP6NE, which is located at the abutment centerline, recorded an increase in annual maximum pressure while EP6SE did not.

The abutment undergoes a complex, cyclic loading/unloading history in response to changes in ambient temperature. The combination of long-term movement of the abutment away from the backfill material and increasing annual maximum earth pressures may be evidence of so-called "soil-ratcheting". A thorough analysis of the soil-ratcheting behavior would require a detailed two or three-dimensional finite element model of the abutment-soil-pile system incorporating a load-path dependent soil stress-strain model. However, such an analysis is beyond the scope of this investigation. For purposes of this study, an approximate relationship between earth pressure and wall displacement was developed based on a combination of field data and classical earth pressure theory. The first step in developing this relationship was to isolate the initial loading curves from the total record. For this analysis, a series of high-pressure events were identified for each earth pressure cell.

3.5.1 High-Pressure Events

A computer program was written to extract the initial loading curves of the pressure-displacement history based on high-pressure events identified in the two earth pressure records. High-pressure events are defined as a period of time during which the abutment experiences the highest pressure to date in its loading history. Twelve high-

pressure events were identified for the North pressure cell (EP6NE) and ten events were identified for the South pressure cell (EP6SE). These high-pressure events and corresponding displacement values are shown in Figure 3.13 and Figure 3.14 along with a pressure-displacement plot.

As shown in these figures, the high-pressure events occur as the bridge expands and the abutment moves toward the backfill. However, the high-pressure events occur at increasingly negative values of displacement, indicating an overall movement of the abutment from its initial position toward the center of the bridge. In summary, two observations are made:

1. There is a consistent, annual range of abutment movement equal to approximately 0.6 in.
2. There is a long-term trend of abutment movement away from the backfill accompanied by increasing earth pressure.

The purpose of isolating the initial loading portions of the record was to remove the effects of soil-ratcheting and create a pressure-displacement curve which approximates the initial, monotonic loading curve.

3.5.2 Construction of Loading Curves

To reconstruct a continuous initial loading curve without the effect of soil-ratcheting, each high-pressure event was translated along the displacement axis as shown in Figure 3.15. It was then observed that instead of one initial loading curve there appears to have been a different loading curve for each successive year. The annual loading curves are shown in Figure 3.16. As shown, all curves appear to have a consistent initial slope of 11,000 psf/in. However, the curves become non-linear at a pressure which increases each successive year. The slope of 11,000 psf/in also appears consistent with the linear portion of the unaltered loading curves of Figure 3.13 and Figure 3.14.

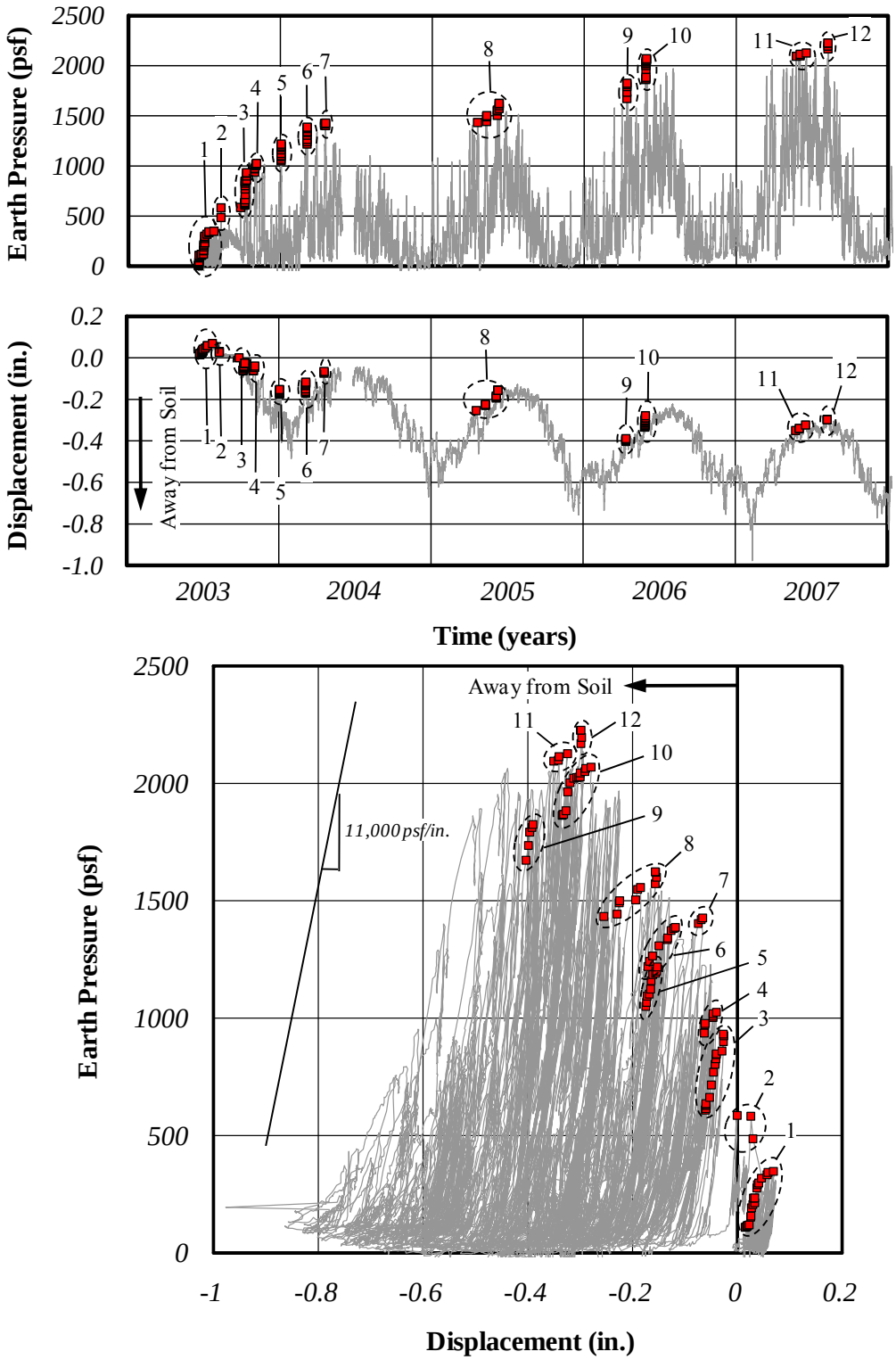

Figure 3.13: High Pressure Events (NE)

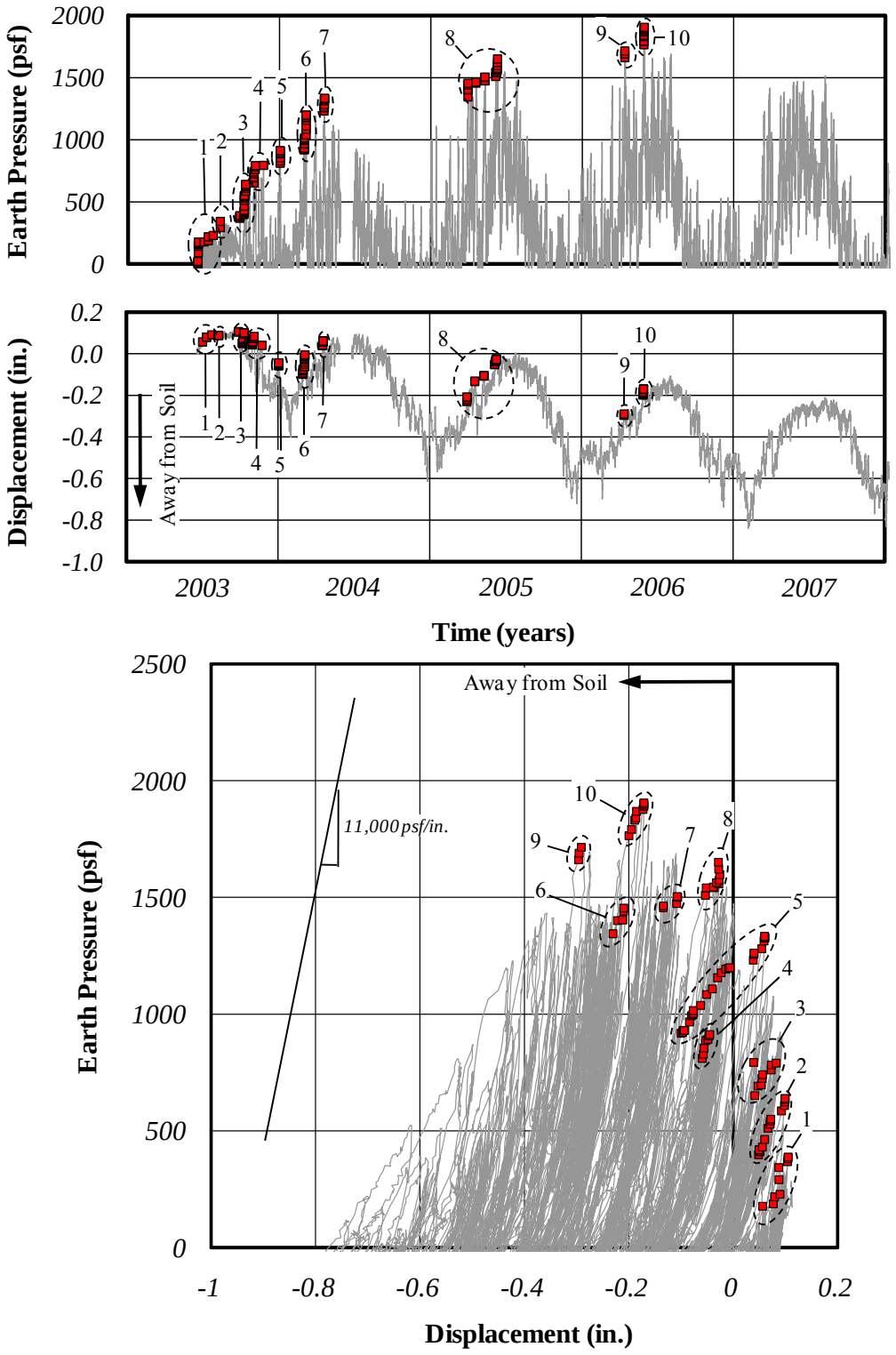

Figure 3.14: High Pressure Events (SE)

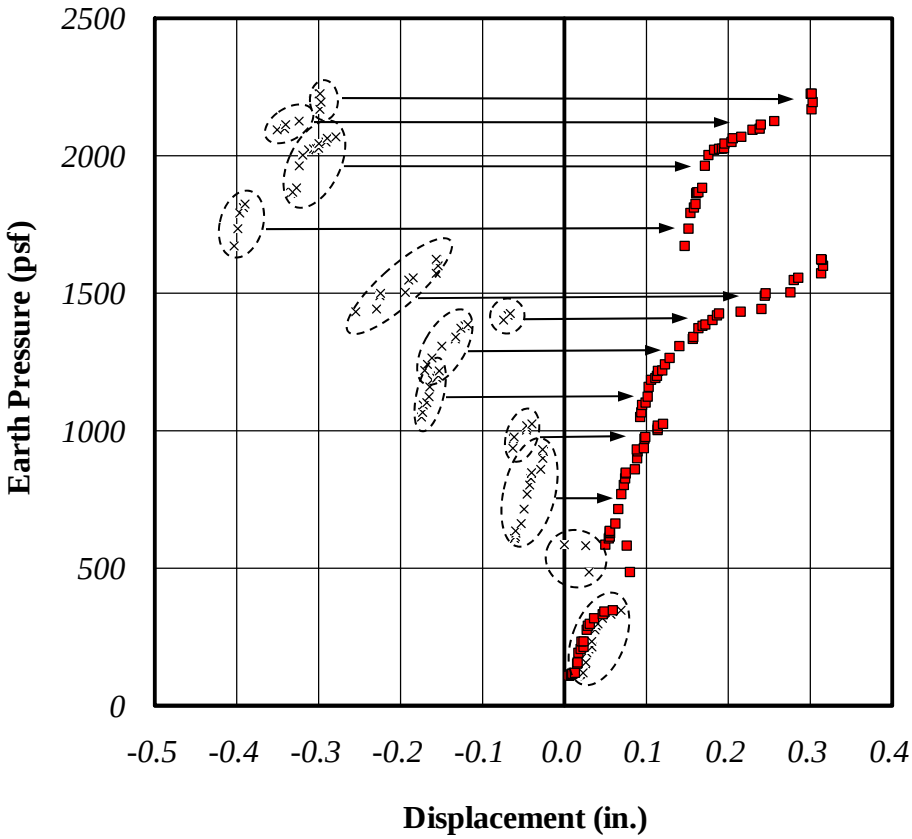

Figure 3.15: Loading Curve Construction (EP6NE)

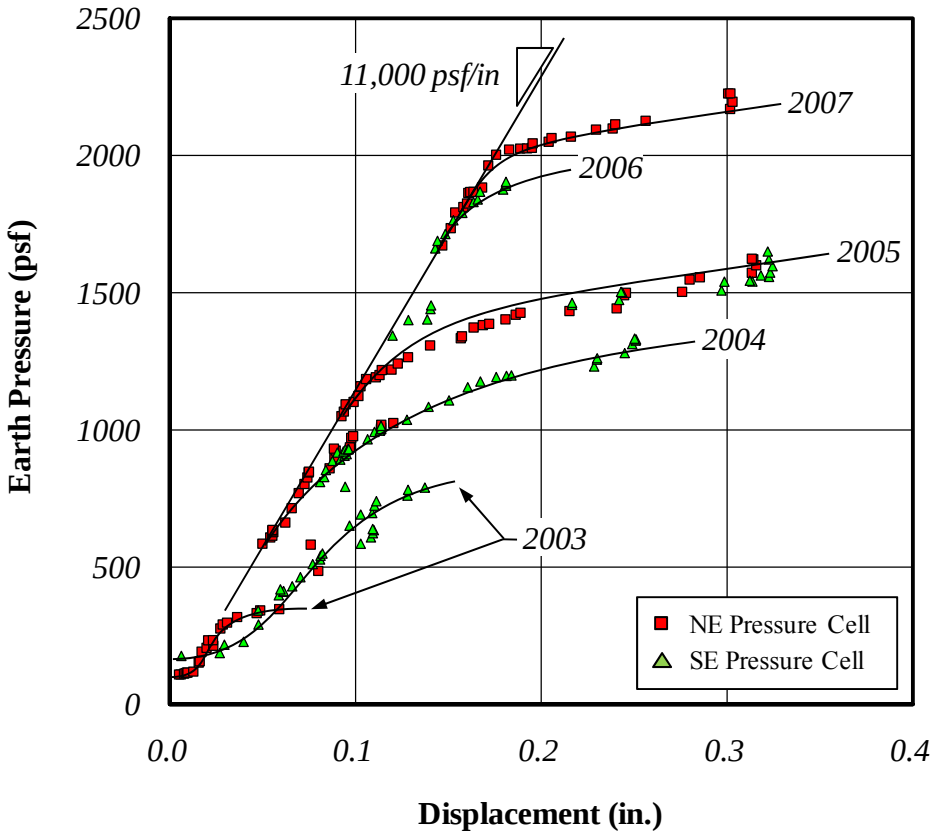

Figure 3.16: Annual Loading Curves

3.6 Comparison of Measured Earth Pressures with Theory

Lateral (horizontal) earth pressures, σ_h, are related to the vertical overburden pressure, σ_v, by the coefficient of lateral earth pressure, *K*.

$$\sigma_h = K\sigma_v = K\gamma z \tag{3.1}$$

where:

γ = unit weight of the soil (lb/ft^3)

z = depth below ground surface (ft)

The value of *K* depends on movement of the soil mass in question and ranges from a minimum value of K_a to a maximum value of K_p representing the active and passive states of stress, respectively. According to the Rankine theory of earth pressure, the lateral earth pressure coefficients K_a and K_p are computed as

$$K_a = \tan^2\left(45° - \frac{\phi}{2}\right) \tag{3.2}$$

$$K_p = \tan^2\left(45° + \frac{\phi}{2}\right) \tag{3.3}$$

where:

ϕ = angle of internal friction (degrees)

The earth pressure cells discussed in the previous section are located at a depth of 8.75 ft below the ground surface. Assuming the backfill material properties to be γ = 120 pcf and ϕ = 30°, the active and passive pressures developed at the level of the pressure cells are then:

$$\sigma_p = K_p\gamma z$$

$$\sigma_p = \tan^2\left(45° + \frac{30°}{2}\right)(120 \text{ pcf})(8.75 \text{ ft}) = 3150 \text{ psf}$$

$$\sigma_a = K_a \gamma z$$

$$\sigma_a = \tan^2\left(45° - \frac{30°}{2}\right)(120 \text{ pcf})(8.75 \text{ ft}) = 350 \text{ psf}$$

It may be seen in Figure 3.12 that the recorded earth pressures routinely fall below the theoretical active pressure value of 350 psf during the winter months. This implies that failure of the backfill material along an active plane is possible which may account for the ratcheting phenomenon. On the other extreme, the theoretical passive pressure value of 3150 psf is significantly higher than the highest recorded earth pressure. The annual loading curves of Figure 3.16 exhibit a strongly non-linear pressure-displacement relationship at pressures significantly below 3150 psf. Adjusting the value of ϕ to match the measured earth pressures results in unrealistically low values of ϕ.

The Rankine theory of earth pressure is based on the state of stress of a soil element located on a vertical plane in a mass of soil. The Coulomb and log-spiral earth pressure theories are so-called wedge theories which are based on the force equilibrium of a soil mass or wedge. These theories are commonly used to estimate the forces resisted by a retaining structure. However, none of the classical earth pressure theories provide any information regarding the magnitude of movements required to achieve either the active or passive states. It is generally recognized that much more movement is required to reach the passive state than the active state. The movement required to reach the passive or active state is most often expressed as a percent of the height of the retaining wall and typically ranges from two to four percent (Cole and Rollins 2006, Fang 1986). Assuming a required movement of two percent, the movement, Δ, required to fully develop the passive pressure behind the abutment considered in the field investigation is then:

$$\Delta = 0.02(8.75 \text{ ft})\left(12 \tfrac{\text{in.}}{\text{ft}}\right) = 2.1 \text{ in.}$$

Assuming an elastic-plastic behavior of the soil, the slope of the earth pressure-displacement curve would be:

$$k = \frac{\sigma_p}{\Delta} = \frac{3150 \text{ psf}}{2.1 \text{ in.}} = 1{,}500 \frac{\text{psf}}{\text{in.}}$$

The measured field value (11,000 psf/in.) is approximately seven times greater then the stiffness computed in this way. The slope parameter is essentially the modulus of subgrade reaction, *k*, typically measured at the surface by a plate load test. Typical values of *k* for medium sand are 5,000 – 42,000 psf/in. (60 – 500 kcf) (Bowles, 1988). The measured *k* falls within this range while the value computed using the assumed displacement limits is well below this range. Given the wide range of typical values for *k*, the large difference in the measured and computed *k*, and the inherent variability of soil properties, a wide range of values for *k* will be investigated in the analytical portion of this report.

3.7 Summary

Based on the data and analysis presented in this chapter, several observations were made. First, the measured earth pressures increased each year since construction except for 2007 when one cell showed an increased pressure and one did not. Secondly, the measured abutment displacements show a consistent annual cycle of displacements on the order of 0.6 in. coupled with a consistent movement away from the backfill material of 0.1 in. per year. This could be attributed to creep and shrinkage of the superstructure or may be evidence of "soil-ratcheting". For the purposes of this report, the most important observation from field data is the initial linear relationship between pressure and displacement of 11,000 psf/in.

CHAPTER 4: LABORATORY INVESTIGATION

4.1 Introduction

The continuous nature of integral abutment bridges results in a much higher displacement demand on the abutment, foundation piles, and surrounding soil than for conventional bridges. Consequently, the pile-abutment connection was identified as a critical detail for both thermal and seismic response. Previous tests of this connection (Chovichien 2004) focused on relatively small pile sections and on existing construction details. The current series of tests was designed to evaluate larger sections and evaluate methods of increasing the displacement capacity of the abutment-pile connection.

4.2 Test Variables

The displacement capacity of the abutment-pile connection was assumed to be limited by two factors: significant damage to the pile head or concrete surrounding the pile head, and the ability of the pile to sustain axial load. Three variations of the existing connection detail were identified for laboratory testing: (1) increasing the pile head embedment length, (2) adding confining reinforcement around the pile head to control cracking and damage of the abutment, and (3) creating a "pin" detail allowing the pile head to rotate in the abutment. These variations were selected for further study due to their potential for increasing displacement capacity of the connection. Accordingly, the laboratory test program was designed as presented in Table 4.1. Only weak-axis bending was considered in this study as this is the preferred orientation discussed by Chovichien (2004). Each variable is discussed in detail in the following sections.

Table 4.1: Laboratory Test Matrix

Series	Specimen	Section	Embedment Length (in.)		Confining Reinforcement[(1)]		Hinge Detail
			15	24	A	B	
1	1	HP12x53	X				
	2	HP12x53		X			
	3	HP12x53	X				X
2	4	HP14x89	X				
	5	HP14x89		X			
	6	HP14x89		X	X		
	7	HP14x89		X		X	

(1) Two levels of confining reinforcement were used and are referred to as A and B. Confining reinforcement details are given in Table 4.3

4.2.1 Embedment Length

Embedment length was identified as a parameter which may increase the displacement capacity of the connection by decreasing damage to the concrete surrounding the pile head. It was hypothesized that damage of the concrete surrounding the pile head comes from two sources: localized damage (cracking, crushing, etc.) due to high stress concentrations at the pile-concrete interface, and a mechanical prying action caused by the rotation of the pile head inside the damaged region of the concrete. Embedding the pile head further into the abutment, into a region unaffected by localized damage, should increase the displacement capacity of the connection by reducing damage caused by mechanical prying action. To test this hypothesis, two embedment lengths were selected for use in the laboratory investigation: 15 in. and 24 in. The current INDOT standard detail specifies an embedment of 15 in.

Additionally, a simple model was used to estimate the embedment of a pile required to achieve its plastic moment capacity. Considering pure bending of the pile and neglecting bond and frictional forces, moment at the abutment-pile interface must be resisted through bearing of the pile on the abutment. The resulting forces are shown in

Figure 4.1. If the pile is assumed to rotate rigidly about the center of its embedment and the ACI rectangular stress block is assumed to apply, the required embedment length L may be computed as:

$$L = \sqrt{\frac{2M_p}{0.85 f_c' b \beta_1 \left(1 - \frac{\beta_1}{2}\right)}} \tag{4.1}$$

where:

M_p = plastic moment of the pile section

$f_c^{'}$ = specified compressive strength of concrete

b = width of the bearing area

β_1 = Parameter defined in 10.2.7 of ACI 318-05

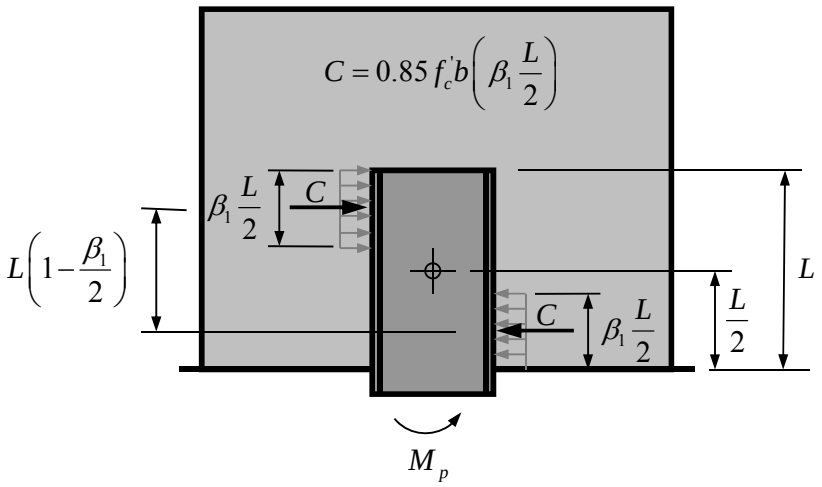

Figure 4.1: Embedment Length Model

The embedment length required by Equation 4.1 is summarized in Table 4.2 for all HP sections. The width of the bearing area is assumed to be the flange width for strong axis bending and the depth of the section for weak axis bending. Only weak-axis is considered here. Results from this simple model suggest that an embedment of 20 in.

is adequate to allow development of the full plastic moment of the largest H-pile section in weak-axis bending. As mentioned previously, INDOT currently uses an embedment of 15 in. This model suggests that 15 in. is only sufficient to develop the plastic moment of sections in weak axis bending up to and including HP12x74.

Table 4.2: Required Embedment Length (f_y = 50 ksi, f'_c = 4 ksi, β_1 = 0.85)

Weak-Axis Bending				
Section	**Z_y (in.^{3})**	**d (in.)**	**M_p (in.-kips)**	**L (in.)**
HP14x117	91.4	14.2	4570	19.7
HP14x102	78.8	14.0	3940	18.4
HP14x89	67.7	13.8	3385	17.2
HP14x73	54.6	13.6	2730	15.5
HP12x84	53.2	12.3	2660	16.1
HP12x74	46.6	12.1	2330	15.2
HP12x63	38.7	11.9	1935	14.0
HP12x53	32.2	11.8	1610	12.8
HP10x57	30.3	9.99	1515	13.5
HP10x42	21.8	9.70	1090	11.6
HP8x36	15.2	8.02	760	10.7

4.2.2 Confining Reinforcement

Previous tests by Chovichien (2004) illustrate the damage which may occur at the pile-abutment connection (Figure 4.2). Spalling and local crushing was observed at the pile-abutment interface. Cracks were observed to form at the tips of the pile flanges and extend at approximately 45º toward the free surface. It was suggested that confining reinforcement around the pile head may increase the displacement capacity of the connection by decreasing damage to the concrete surrounding the pile head. The confining reinforcement was intended to limit damage to the concrete by increasing

compressive strength within the confined zone, and limiting mechanical prying action by controlling crack width. Two levels of confining reinforcement were selected for use in the laboratory investigation. The details of the confining reinforcement are given in Table 4.3. The proposed arrangement of this reinforcement is shown in Figure 4.3.

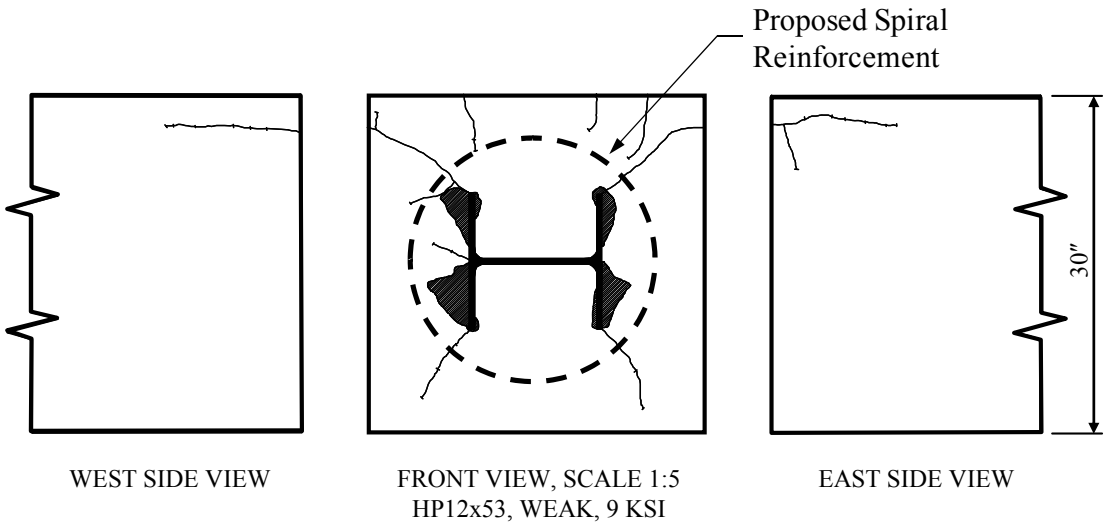

Figure 4.2: Observed Damage (Chovichien 2004)

Table 4.3: Confining Reinforcement Details

Identifier	Bar Size	Diameter (in.)	Height, h (in.)	Pitch, S (in.)
A	# 4	22.5	24	2.5
B	# 4	22.5	24	1.5

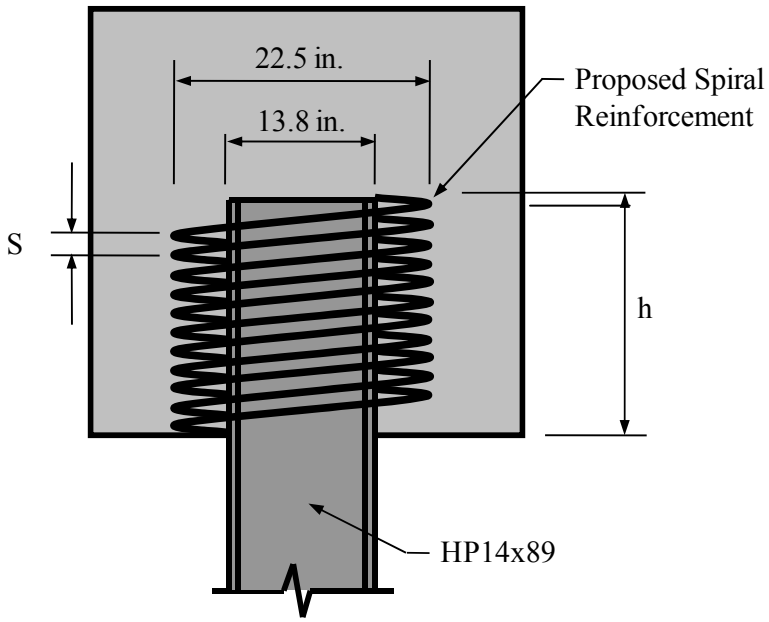

Figure 4.3: Confining Reinforcement Detail

4.2.3 Pin Detail

A "pin" detail has been used by INDOT on several integral abutment bridges. In this detail the pile head was surrounded on all sides by a 1" layer of polystyrene as shown in Figure 4.4. This detail was intended to provide enough rotational capacity to allow the pile to be designed as pin-headed. The detail was also thought to increase the displacement capacity of the connection by eliminating damage of the concrete surrounding the pile-head. However, this comes at the expense of stiffness of the connection, as the polystyrene is expected to add considerable flexibility to the connection. The ability of the polystyrene to perform under a large number of load reversals is uncertain. The possibility exists that the pile head may "walk", or move laterally, under cyclic loading. In addition, axial load capacity of the connection is also in question as the loads are resisted through bearing of the pile tip alone. Since the rationale behind the pin detail is to allow as much rotation as possible, only the 15 in. embedment length was tested in the laboratory investigation.

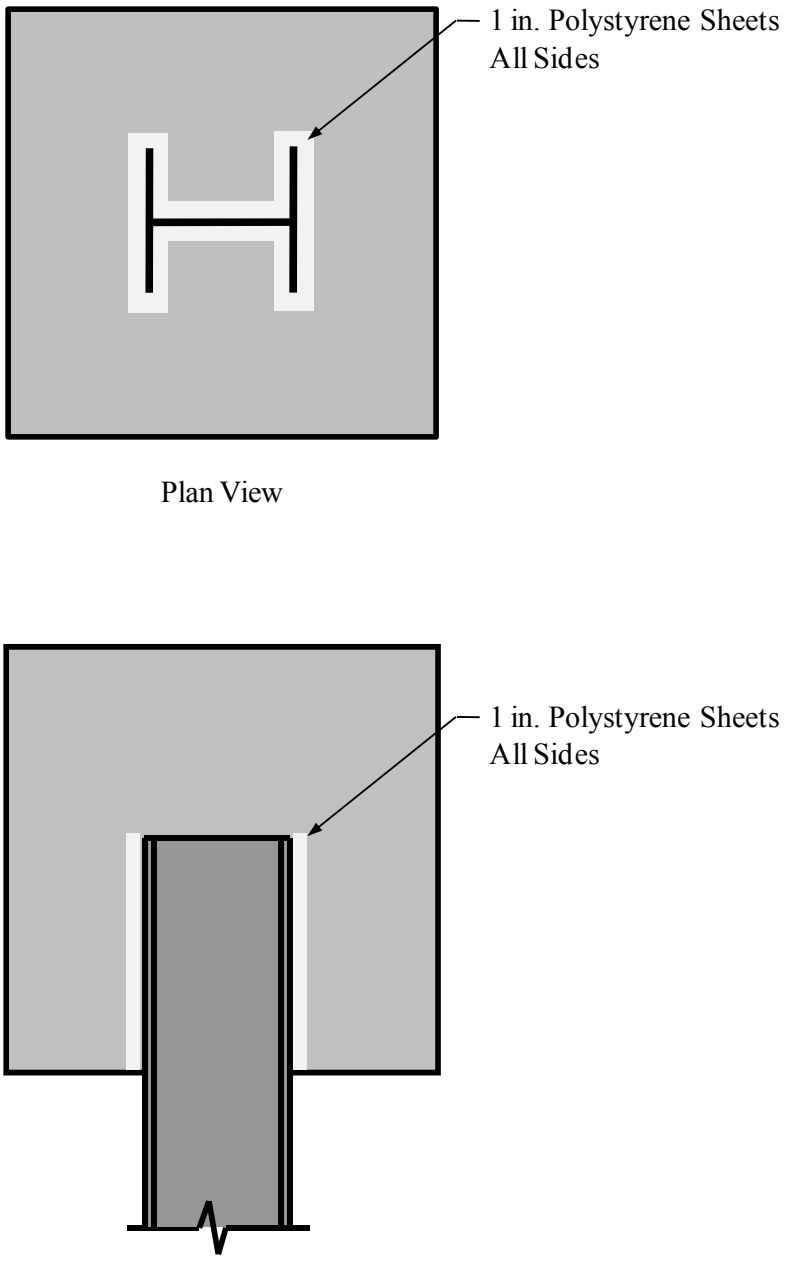

Figure 4.4: Pin Connection Detail

4.3 Specimen Design

The specimens used in the current series of tests were modified versions of those used by Chovichien (2004). The abutment-pile connection is represented as a cantilever section embedded in a concrete support block as shown in Figure 4.5. The cantilever section is subjected to an axial load, P, representing the weight of the supported structure and a cyclic lateral load, H, representing the effects of lateral bridge movement. The dimensions of the specimen and reinforcement are based on typical abutment details. In Chovichien's tests, the support block and post-tensioning system which held the specimen in place also provided confinement of the concrete surrounding the pile head which is not present in the field. To better simulate field conditions, the length of the specimen was extended creating a cantilever which is free of confining stresses on both faces (Figure 4.6). The length of the pile section, L, extending beyond the test specimen is based on the approximate location of the point of inflection of a pile under lateral loading. Analytical modeling and field data presented by Chovichien (2004) have shown that this length is dependent on soil properties and ranges from approximately 4 to 8 ft for weak-axis bending. For the current series of tests, a length, L, of 6 ft was chosen. Steel reinforcement used in the specimen is illustrated in Figure 4.7.

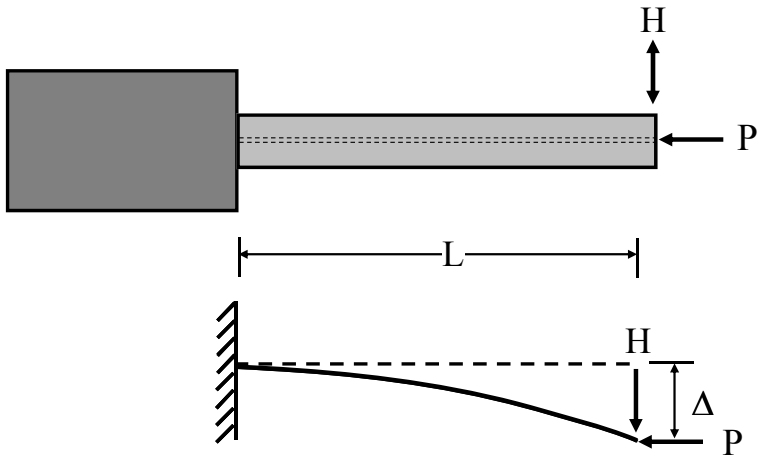

Figure 4.5: Specimen Design

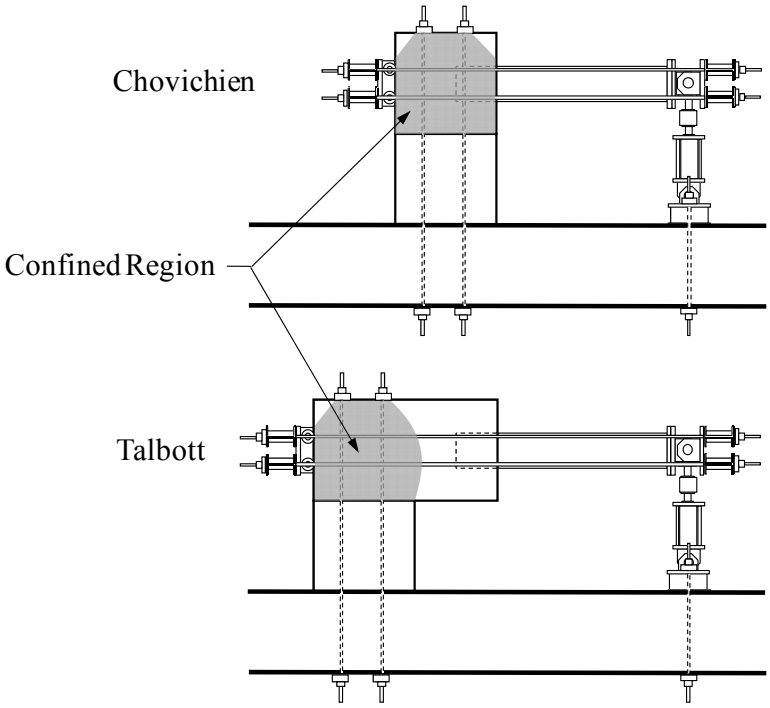

Figure 4.6: Modified Chovichien Specimen

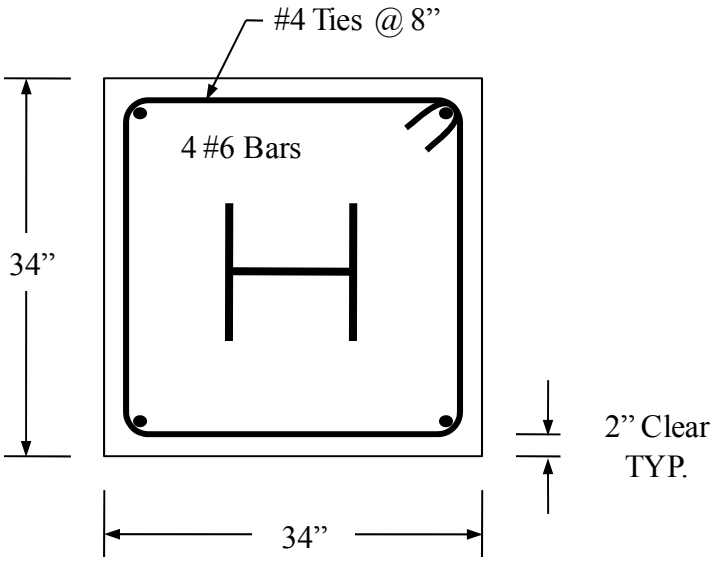

Figure 4.7: Test Specimen Reinforcement

4.4 Test Setup

The test setup used in this investigation consisted of three parts: the clamping system, the axial load system, and the lateral load system. The test setup is shown in Figure 4.8. The elements of each system are described in the following subsections.

4.4.1 Clamping System

The test specimen was secured to the strong floor using the clamping system. The test specimen rested on a reinforced concrete support block. The test specimen and support block were post-tensioned to the laboratory strong floor using four 1-1/4" diameter threaded rods. Each rod was post-tensioned to 70 kips resulting in a total post-tensioning force of 280 kips.

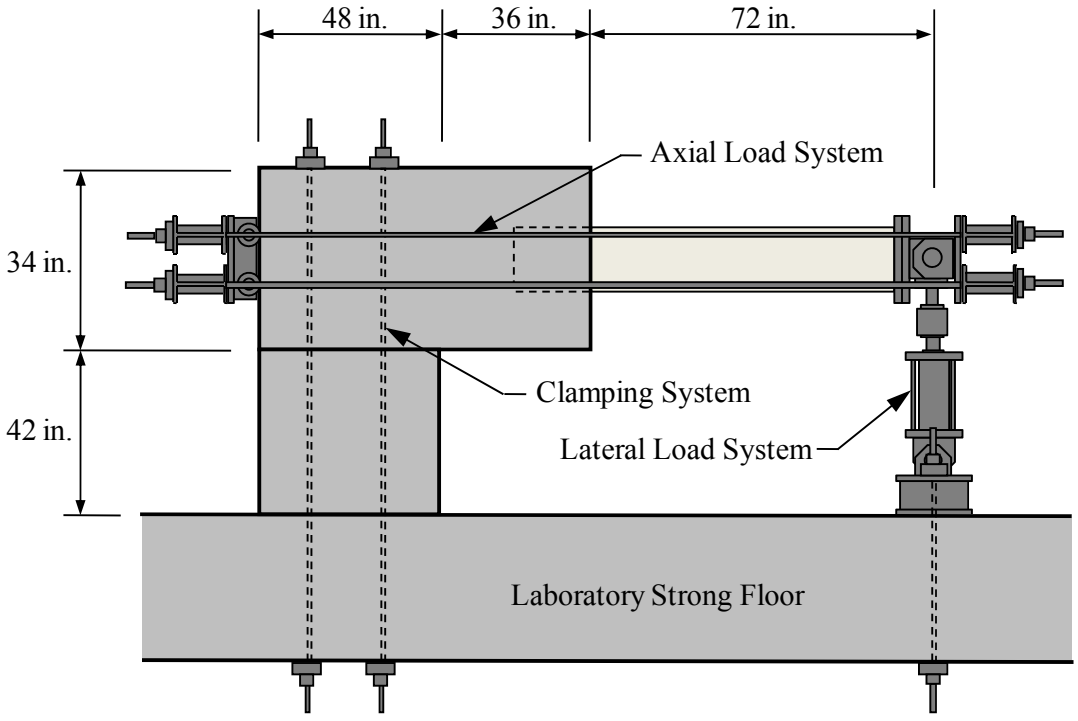

Figure 4.8: Test Setup

4.4.2 Axial Load System

The axial load system was designed to move vertically along with the pile tip, allowing the applied axial load to remain horizontal. Axial load was applied using four 1-3/8"-dia. Dywidag Bars. An axial load producing a uniform compressive stress of 12.5 ksi ($0.25f_y$) in the pile was applied to each specimen. This level of axial load is the maximum allowed under current INDOT and AASHTO design standards.

4.4.3 Lateral Load System

Lateral load was applied to the pile tip using a double-acting, hydraulic ram as shown in Figure 4.8. The hydraulic ram had a capacity of approximately 50 kips. The lateral and axial load systems were connected to the pile tip through a pin connection to eliminate moment at the pile tip. For small displacements (< 0.50 in.), a hand pump was used to apply hydraulic pressure to the ram. For large displacements (> 0.50 in.), a small electric pump was used. The hydraulic ram assembly was also post-tensioned to the laboratory strong floor using two 1-3/8"-dia. Dywidag bars to prevent uplift at full capacity of the lateral load system (approx. 50 kips).

4.5 Instrumentation

The locations of instruments used in these tests are presented in Figure 4.9. Displacements of the pile tip were measured relative to the strong floor using a linear variable differential transformer (LVDT) mounted to the pin assembly of the axial load system. Additionally, LVDTs were mounted to the test specimen at the front and rear face of the support block to monitor rotations of the test specimen relative to the strong floor. Lateral loads were measured using a 150-kip capacity load cell located between the hydraulic ram and the axial load system pin assembly. Axial load was monitored using strain gages applied to each of the four 1-3/8" Dywidag bars that were part of the axial load system. All data were collected at one second intervals for the duration of the test.

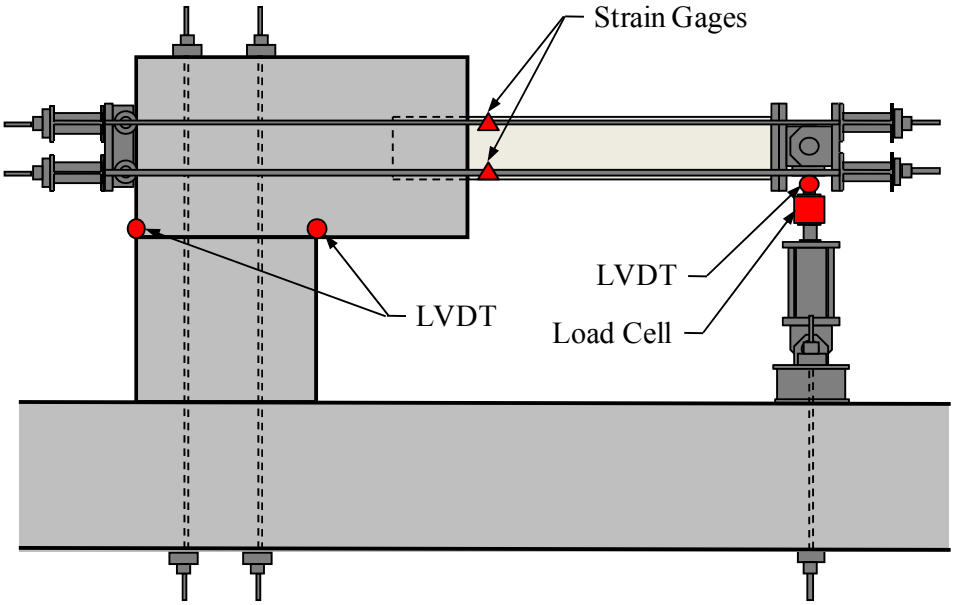

Figure 4.9: Instrumentation Location

4.6 Materials

Standard material testing was performed on all construction materials according to applicable ASTM standards. All testing was carried out in the Purdue University Bowen Laboratory and Kettelhut Laboratory. The results of the concrete compression tests and the steel tension tests are presented in the following sections.

4.6.1 Concrete

Concrete for all test specimens was provided by a local ready-mix concrete supplier. An INDOT Class C mix was specified for all test specimens, and actual mix proportions delivered are presented in Table 4.4. Compression tests were performed on 6”x12” cylinders for all specimens. The results of the compressive tests are presented in Figure 4.10 and Table 4.5.

Table 4.4: Concrete Mix Proportions

Material	Unit	Specimen						
		1	2	3	4	5	6	7
#8 Stone	pcy	1782	1787	1787	1787	1787	1787	1793
#23 Sand	pcy	1262	1273	1267	1260	1260	1260	1267
Cement (Type I)	pcy	658	657	658	655	657	657	657
Water Reducer	ozcy	13	20	20	20	20	20	20
Air Entrainment	ozcy	5	3	3	3	3	3	3
Water	pcy	198	155	185	208	198	187	172

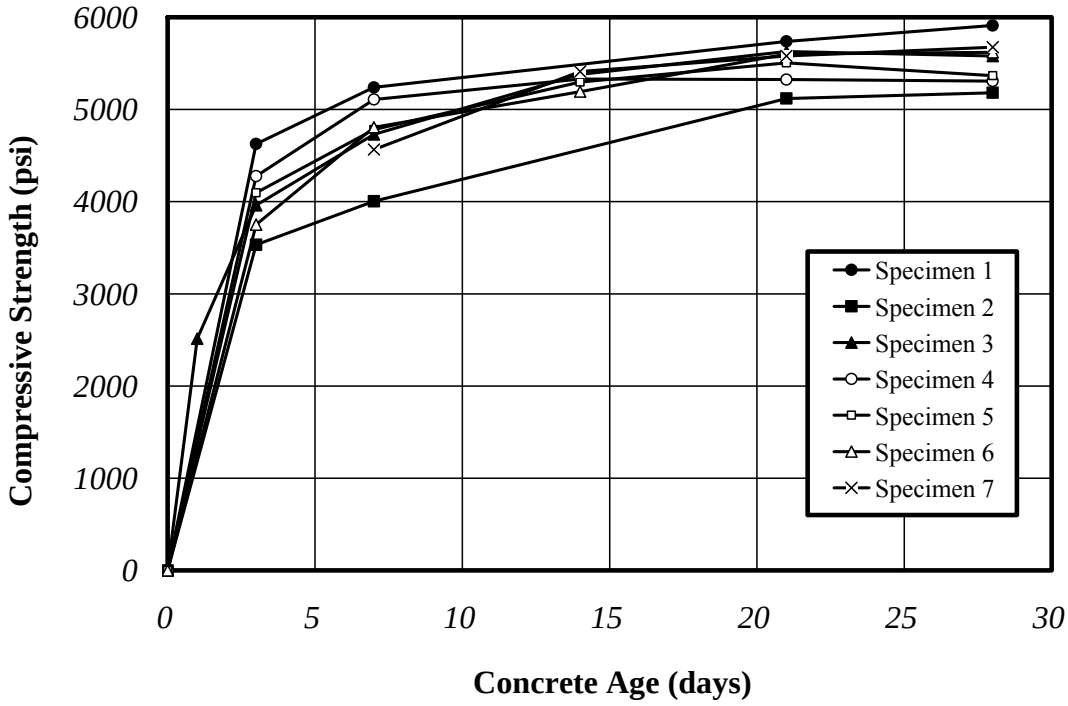

Figure 4.10: Concrete Compressive Strength Gain

Table 4.5: Concrete Compressive Strength at 28 Days

Specimen	f_c' (psi)
1	5,910
2	5,180
3	5,580
4	5,310
5	5,370
6	5,620
7	5,670

4.6.2 Reinforcing Steel

The concrete reinforcing steel used in this investigation was ASTM A 615 Grade 60. The concrete reinforcing steel was not tested during the laboratory investigation as the reinforcement was not a primary variable in the testing program. Further, for the spiral reinforcement, yielding is not expected.

4.6.3 Piles

Tension coupon tests were performed to determine the stress-strain relationship of the steel used in the pile sections. Two size piles were tested during the laboratory investigation: HP12x53 and HP14x89. The individual test specimens for each size were cut from a single length of pile. Therefore, individual tests of each specimen were not performed since they all came from the same heat of steel. Three coupons were cut from the flanges of each size pile. Coupon dimensions are shown in Figure 4.11, and each coupon was tested according to ASTM A370-02. A 120-kip capacity MTS Universal testing machine was used to perform the tests. Strains were measured directly using a bonded strain gage and indirectly using an extensometer. The results are summarized in Figure 4.12 and Table 4.6.

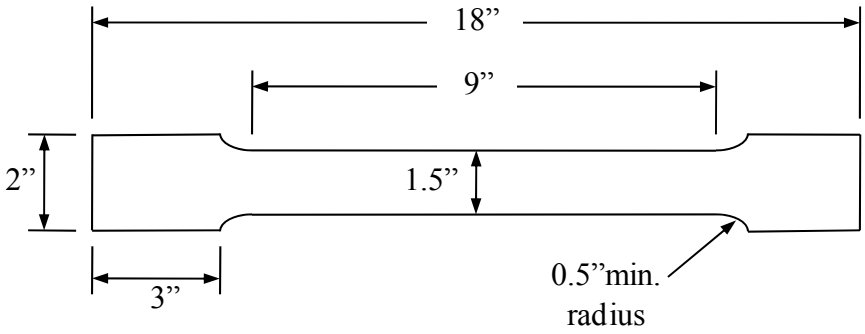

Figure 4.11: Tension Coupon Dimensions

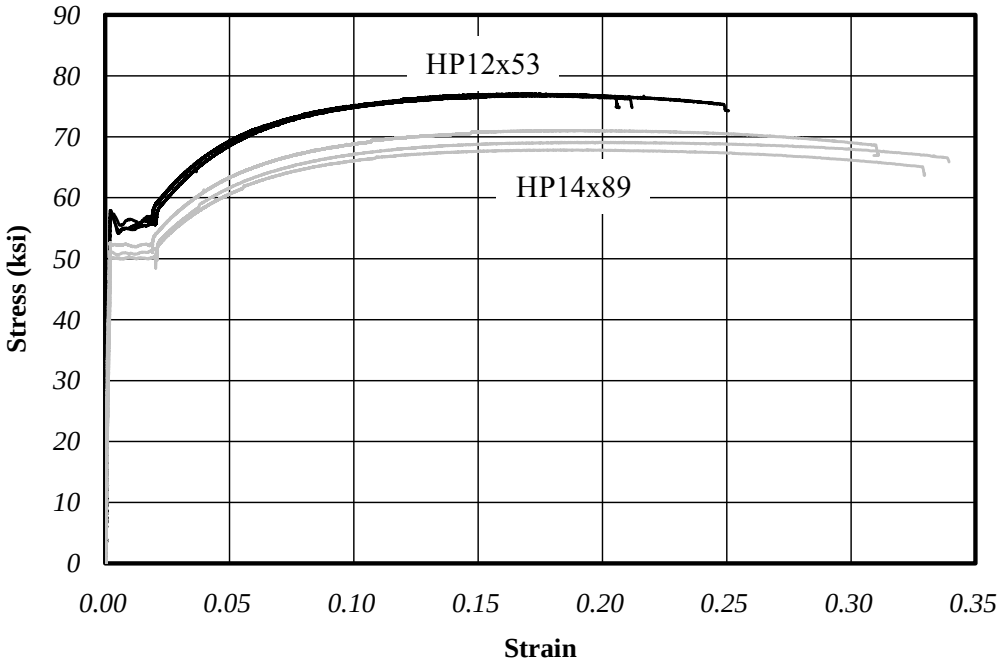

Figure 4.12: Coupon Stress-Strain Relationships

Table 4.6: Tension Coupon Test Results

Section	Coupon	Yield Stress (ksi)
HP12x53	1	54
	2	56
	3	55
	Average	55
HP14x89	1	52
	2	50
	3	51
	Average	51

4.7 Specimen Construction

All test specimens were constructed and tested at the Bowen Laboratory. The specimens were constructed in a vertical orientation (Figure 4.13). The pile section was lowered into the fresh concrete using an overhead crane. The pile was held in place for 24 hours before release. A wooden alignment frame was constructed to keep the pile centered and plumb with respect to the concrete block. After curing, each specimen was lowered into a horizontal position for testing. Concrete cylinders were cast at the same time and cured in the same manner as the test specimens.

The concrete support block was constructed at the same time as Specimen 1. The support block was cast and cured in a manner similar to the test specimens. The support block contained minimum temperature and shrinkage reinforcement required by ACI 318-05.

Figure 4.13: Specimen Construction

4.8 Test Protocol

The objective of the current series of tests is to evaluate performance under seismic loading. Previous tests of the same connection by Chovichien focused on cyclic thermal loading. Consequently, Chovichien applied a large number of cycles to the specimen representing the entire service life of the bridge. While a seismic event may not produce nearly as many cycles of significant displacement, the displacement history used by Chovichien was used in the current series of tests. This was done to allow direct comparison of the results from both series of tests. The target displacement history is presented in Table 4.7 along with the actual load cycles performed.

Table 4.7: Summary of Loading Histories

Displacement (in.)	Number of Cycles							
	Target	Specimen						
		1	2	3	4	5	6	7
0.25	5	5	5	5	5	5	5	5
0.50	10	10	10	10	10	10	10	10
0.75	25	25	25	25	25	25	25	25
1.00	50	50	50	50	50	50	50	50
1.25	50	50	50	50	50	50	50	50
1.50	50	50	50	50	50	50	50	50
1.75	50	50	50	50	50	50	50	50
2.00	50	10	50	50	50	50	50	5
2.25	50	10	50	50	10	50	50	--
2.50	50	10	50	50	--	50	--	--
2.75	50	10	--	--	--	--	--	--
3.00	50	--	--	--	--	--	--	--
Total	490	280	390	390	300	390	340	245

4.9 Test Results

The following sections present the results of the laboratory investigation. A summary of the results is provided for each specimen.

4.9.1 Specimen 1 (HP12x53, 15" Embedment, 12.5 ksi)

Test results for Specimen 1 are summarized in Table 4.8. Lateral load, pile tip displacement, and axial load histories are presented in Figure 4.14. Load-displacement curves at each displacement level are presented in Figure 4.15 while the complete set of load-displacement curves is presented in Figure 4.16. Specimen 1 exhibited linear-elastic behavior at the 0.25" and 0.50" displacement levels. The first observed yielding of the pile section occurred during the 0.75" displacement level. Stable hysteretic loops were observed from the 0.75" through the 1.25" displacement levels. The first significant cracking of the concrete surrounding the pile head of Specimen 1 occurred at the 1.25" displacement level. Significant deterioration of the concrete surrounding the pile head occurred at the 1.50" displacement level. At this level, cracks in the concrete surrounding the pile head extended through the sides and top of the specimen as shown in

Figure 4.17. At higher displacement levels, these cracks widened considerably under application of lateral load. Eventually, diagonal cracks formed on the sides of the specimen just behind the embedment of the pile. Additionally, crushing of the concrete located between the flanges was also observed. Deterioration of the connection is reflected in the pinching of the hysteresis loops of Figure 4.15. At large displacements, the system was unable to maintain axial load (Figure 4.14) due to an overall loss of integrity of the system. Testing was stopped due to loss of lateral stiffness and the inability of the system to maintain axial load.

Table 4.8: Specimen 1 – Test Summary

Displacement Range (in.)	Number of Cycles	Cumulative Cycles	Average Axial Load (kips)	Max Lateral Load (kips)	
				Up	Down
0.25	5	5	192.4	6.4	-6.1
0.50	10	15	189.2	11.2	-11.8
0.75	25	40	190.8	22.2	-16.7
1.00	50	90	194.1	21.7	-19.7
1.25	50	140	187.8	25.9	-21.1
1.50	50	190	189.5	27.5	-22.3
1.75	50	240	179.7	18.2	-15.4
2.00	10	250	169.4	13.4	-14.5
2.25	10	260	182.0	13.8	-16.0
2.50	10	270	166.2	13.4	-15.6

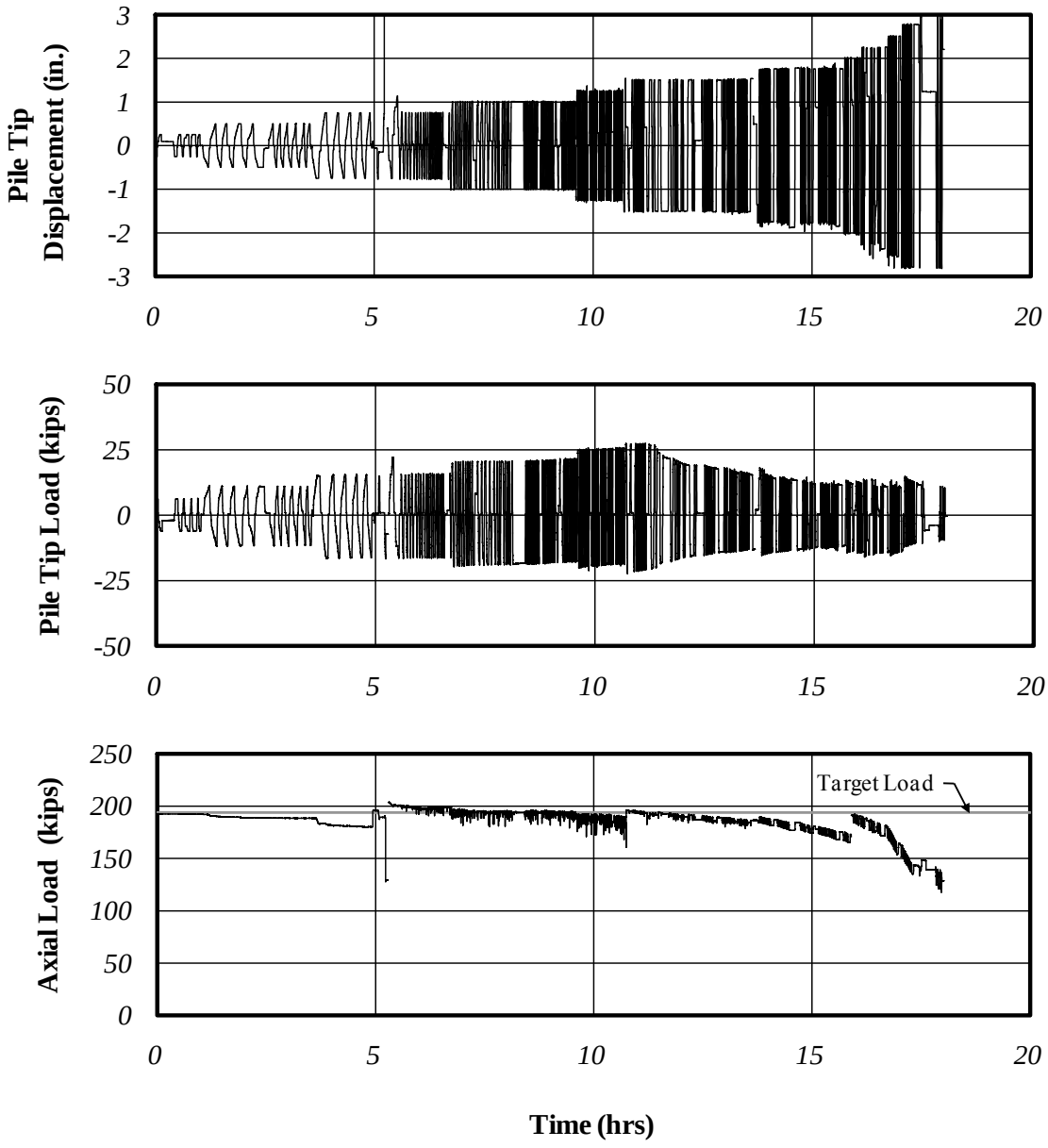

Figure 4.14: Specimen 1 – Load and Displacement Histories

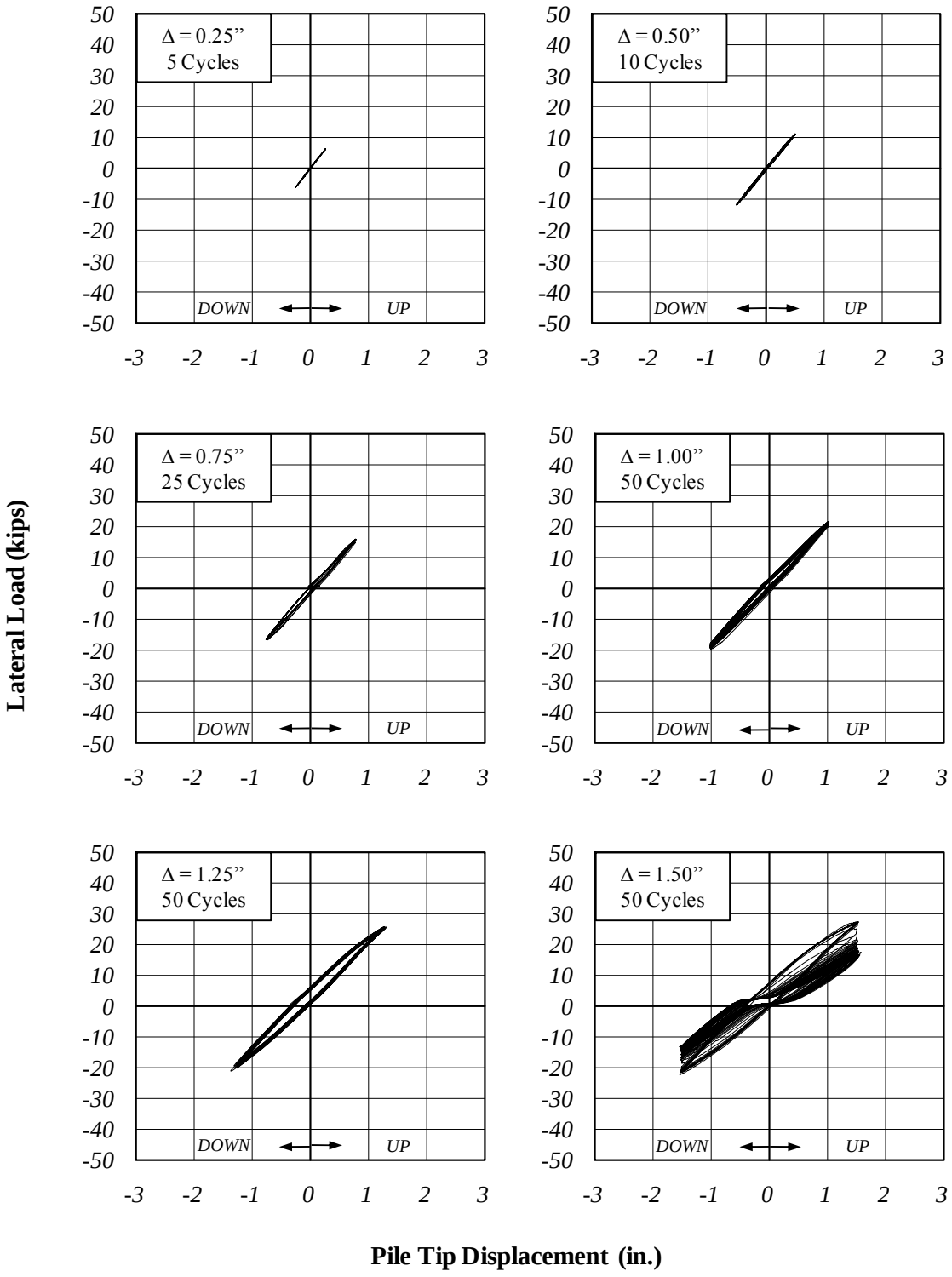

Figure 4.15: Specimen 1 – Load-Displacement Curves

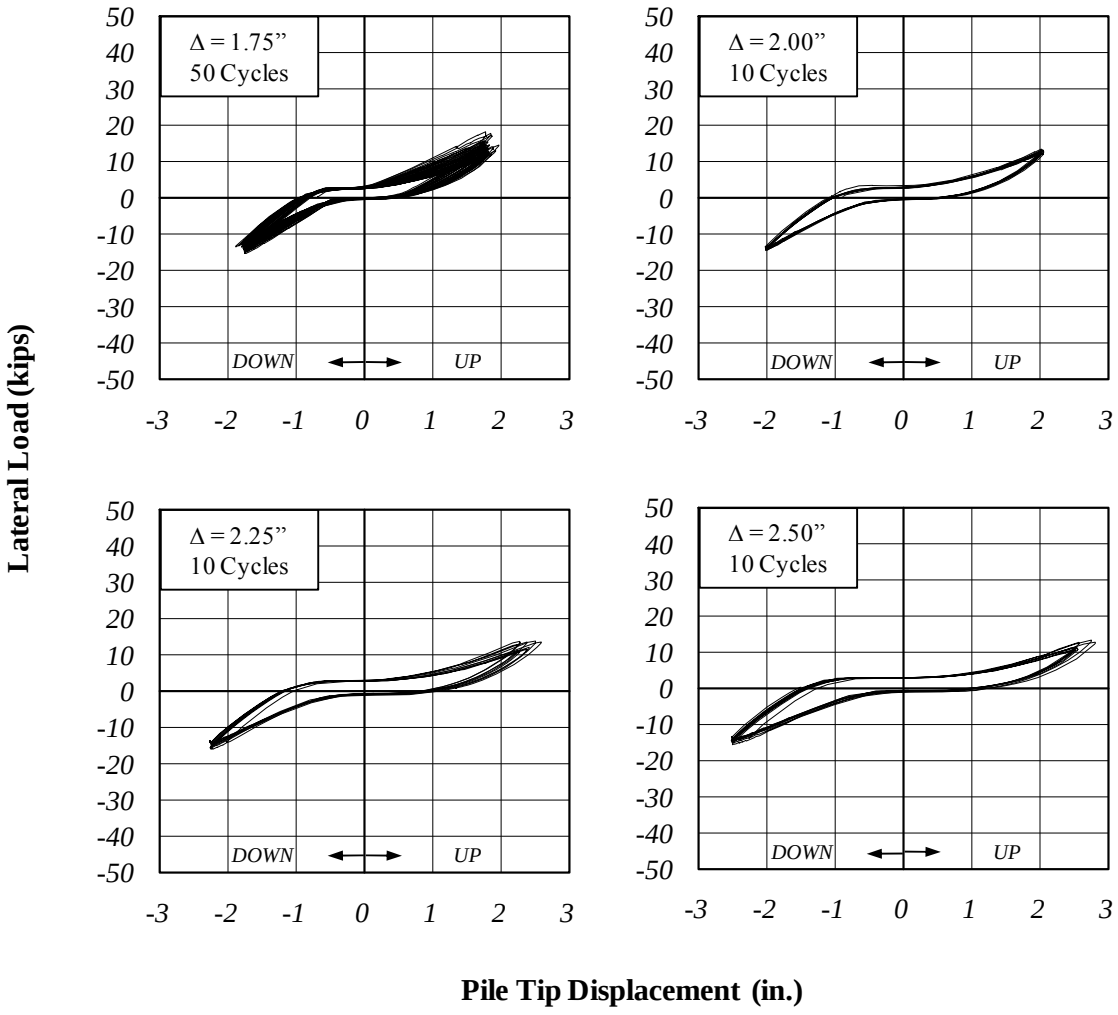

Figure 4.15 (continued): Specimen 1 – Load-Displacement Curves

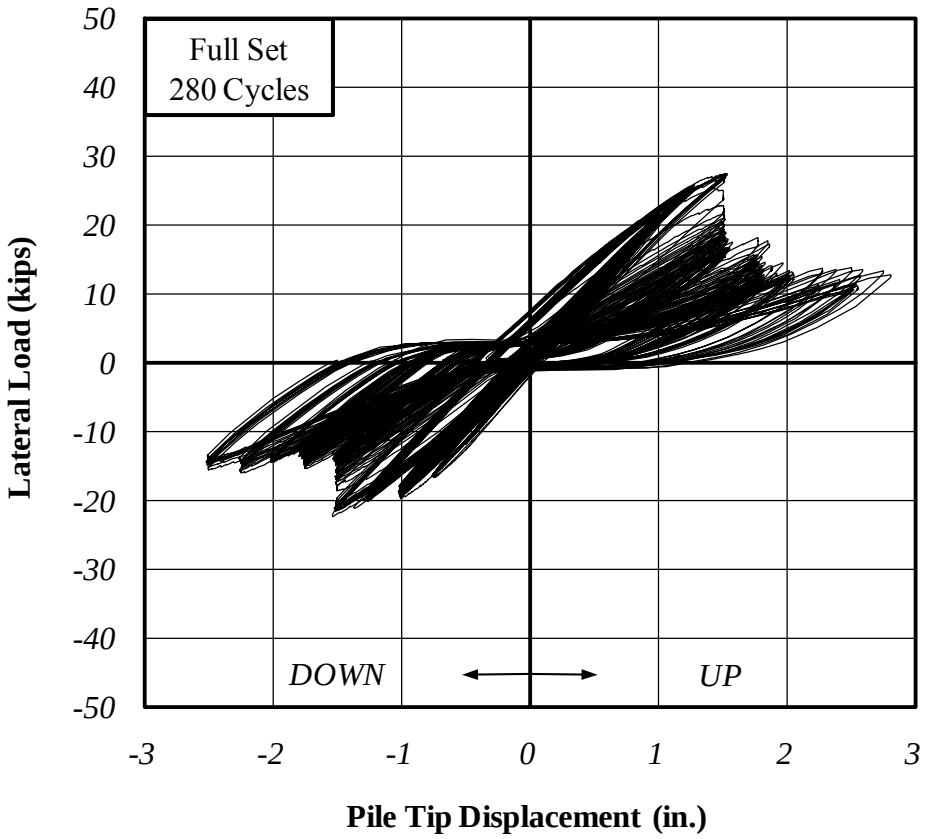

Figure 4.16: Specimen 1 – Complete Load-Displacement Curves

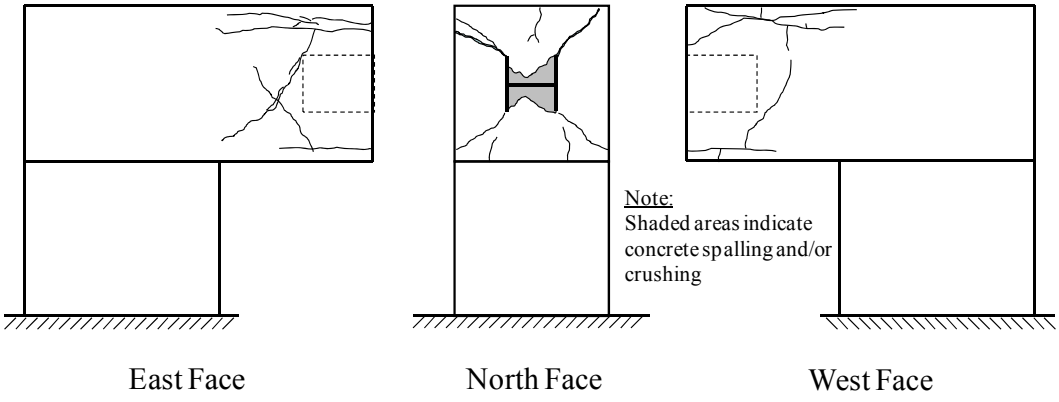

Figure 4.17: Specimen 1 – Crack Map

4.9.2 Specimen 2 (HP12x53, 24” Embedment, 12.5 ksi)

Test results for Specimen 2 are summarized in Table 4.9. Lateral load, pile tip displacement, and axial load histories are presented in Figure 4.18. Load-displacement curves for each displacement level are presented in Figure 4.19 while the complete set of load-displacement curves is presented in Figure 4.20. The behavior of Specimens 1 and 2 were nearly identical up to the 1.50” displacement level. While the majority of damage observed in Specimen 1 occurred at this level, the hysteresis loops of Specimen 2 remain relatively stable. Further, even though the crack patterns of Specimens 1 and 2 were nearly identical (Figure 4.17, Figure 4.21), the crack widths were noticeably smaller for Specimen 2. Peak lateral load remained relatively stable at displacement levels beyond 1.50 in. Peak lateral load decreased slightly at the 2.50 in. displacement level. Stable hysteresis loops formed at each displacement level. A slight buckling of the flanges was observed at the highest displacement levels. No fracturing of the flanges was observed. Testing was discontinued at the 2.50 in. displacement level due to displacement limits of the test setup.

Table 4.9: Specimen 2 – Test Summary

Displacement Range (in.)	Number of Cycles	Cumulative Cycles	Average Axial Load (kips)	Max Lateral Load (kips)	
				Up	Down
0.25	5	5	204.2	6.9	-6.4
0.50	10	15	202.6	11.9	-10.6
0.75	25	40	201.1	16.8	-15.2
1.00	50	90	199.1	20.8	-18.8
1.25	50	140	198.7	23.6	-21.3
1.50	50	190	198.2	24.8	-22.4
1.75	50	240	202.7	25.5	-23.0
2.00	50	290	199.3	25.5	-22.9
2.25	50	340	193.7	25.5	-23.1
2.50	50	390	202.0	24.7	-22.1

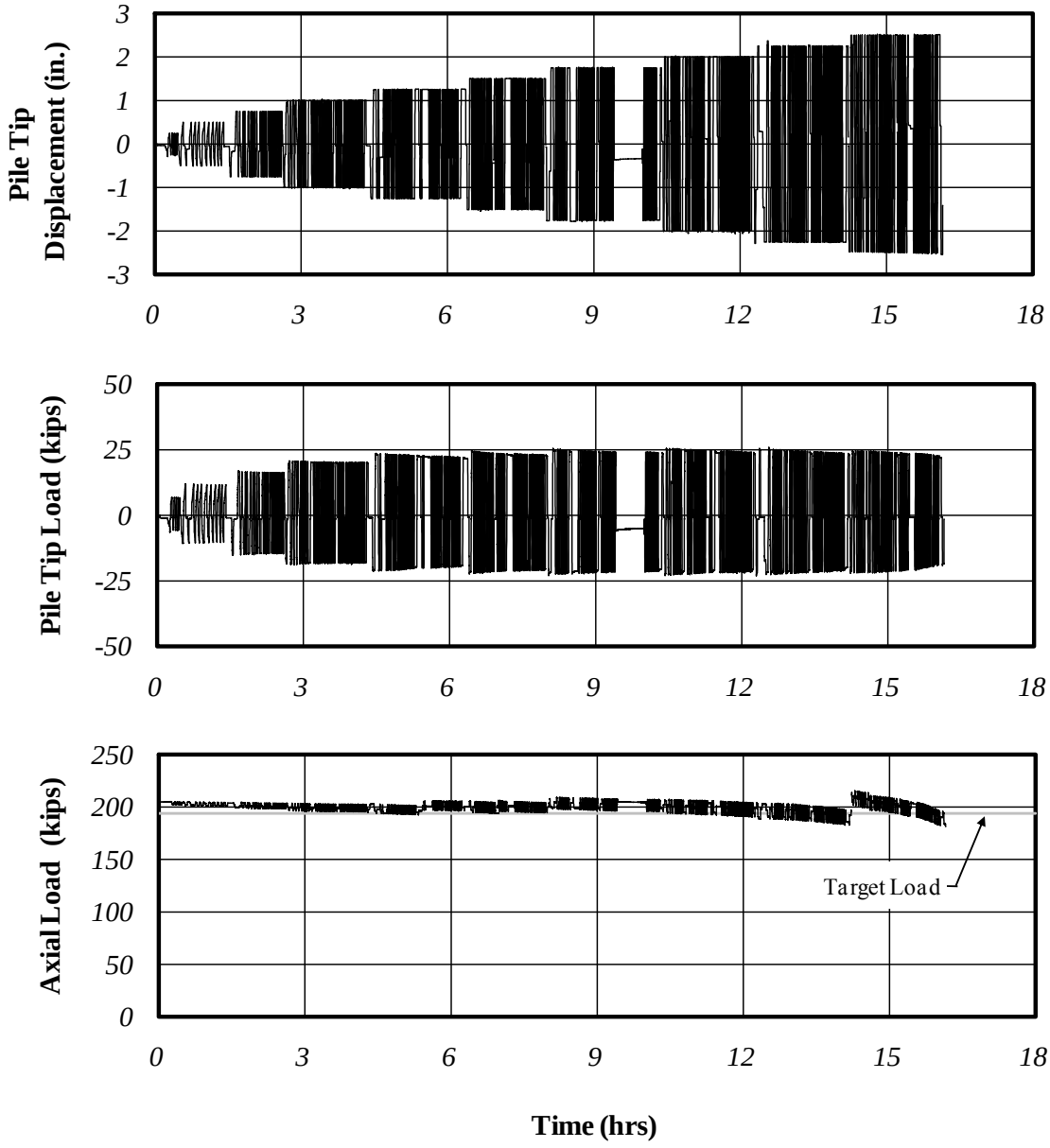

Figure 4.18: Specimen 2 – Load and Displacement Histories

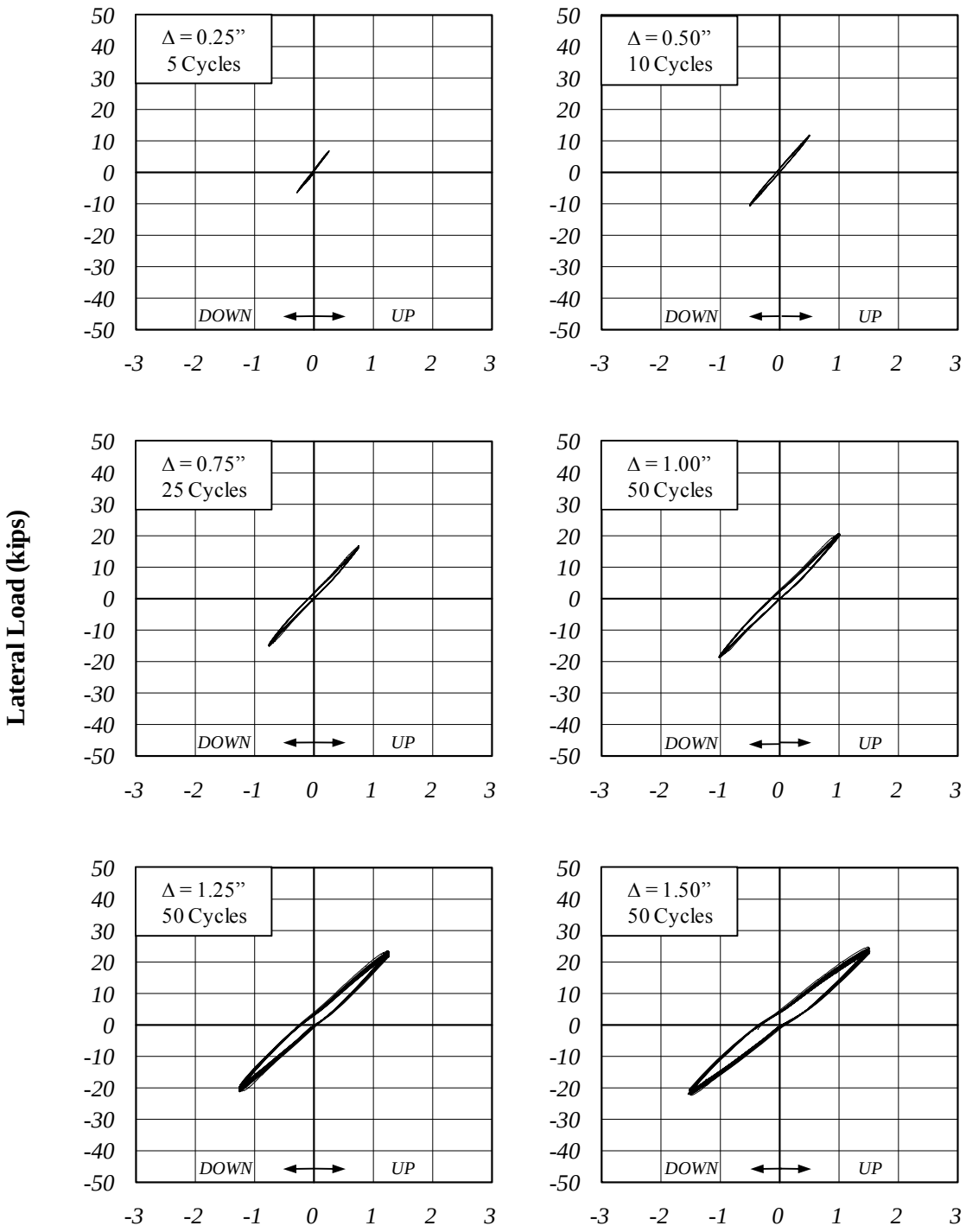

Figure 4.19: Specimen 2 – Load-Displacement Curves

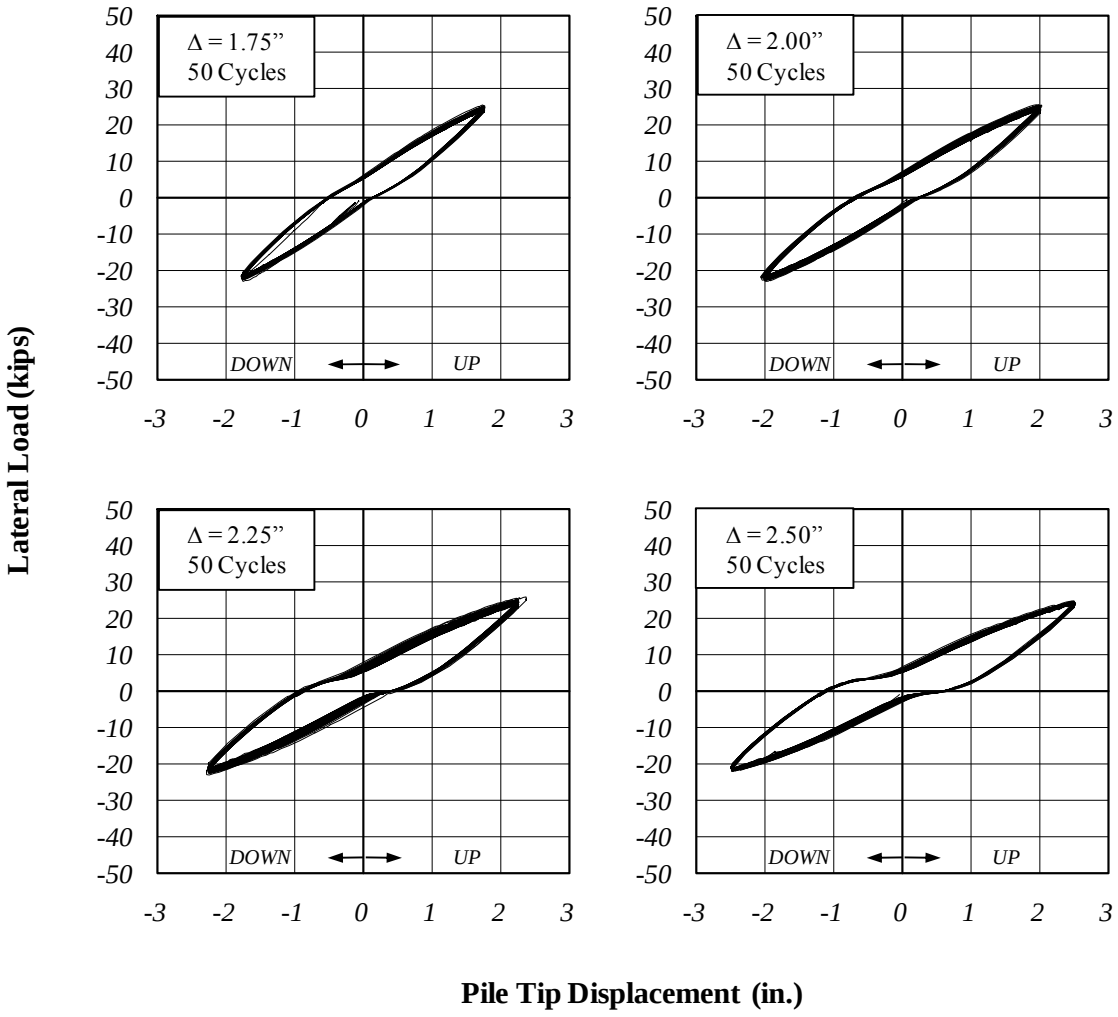

Figure 4.19 (continued): Specimen 2 – Load-Displacement Curves

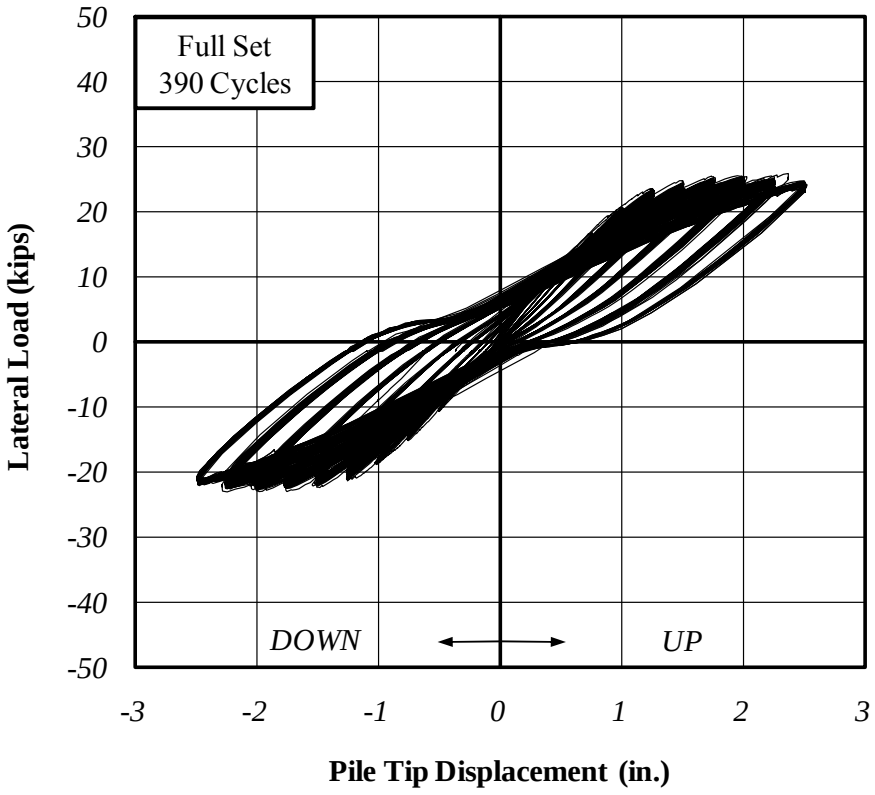

Figure 4.20: Specimen 2 – Complete Load-Displacement Curves

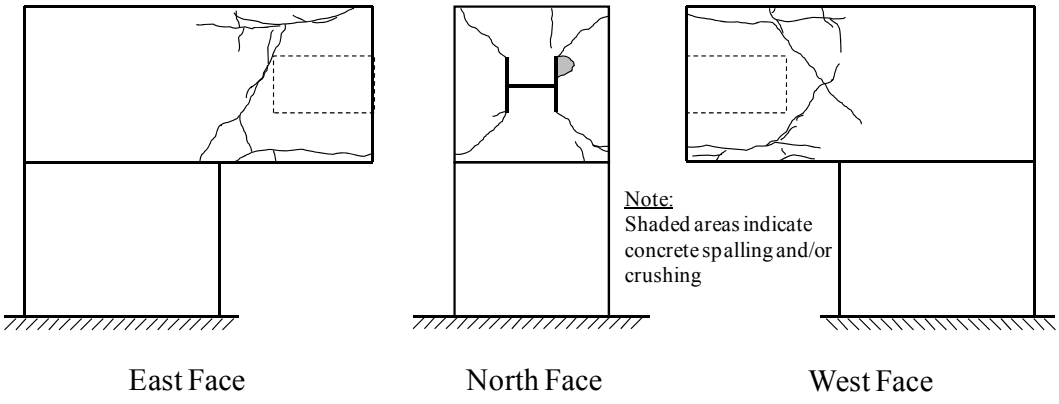

Figure 4.21: Specimen 2 – Crack Map

4.9.3 Specimen 3 (HP12x53, 15” Embedment, 12.5 ksi, 1” Polystyrene Wrap)

Specimen 3 contained the 1” polystyrene wrap. To prevent damage to the polystyrene wrap before testing, a bracing frame was constructed around the pile as shown in Figure 4.22. The bracing frame prevented rotation of the pile head prior to testing, and was left in place until Specimen 3 was secured in the test setup. The frame was removed prior to application of the axial load.

Test results for Specimen 3 are summarized in Table 4.10. Lateral load, pile tip displacement, and axial load histories are presented in Figure 4.23. Load-displacement curves for each displacement level are presented in Figure 4.24 while the complete set of load-displacement curves is presented in Figure 4.25. As expected, the polystyrene wrap resulted in a considerably more flexible connection compared to Specimens 1 and 2. At the conclusion of the test, there was no visible damage to either the pile or the concrete. There was no visible “walking”, or unintentional lateral movements, of the pile head. After testing, the pile and polystyrene wrap were removed from the concrete to examine the condition of the interior. No visible damage to the interior of the concrete was observed. Signs of minor localized yielding of the flange tips were observed at the bearing surface. Stable hysteresis curves were observed for each displacement level. The specimen was able to maintain a relatively constant axial load even at the largest displacement levels. Testing was stopped when the displacement capacity of the test setup was reached.

Table 4.10: Specimen 3 – Test Summary

Displacement Range (in.)	Number of Cycles	Cumulative Cycles	Average Axial Load (kips)	Max Lateral Load (kips)	
				Up	Down
0.25	5	5	200.9	3.9	-3.2
0.50	10	15	199.3	6.6	-4.5
0.75	25	40	196.1	8.2	-5.1
1.00	50	90	192.5	8.9	-5.3
1.25	50	140	198.5	9.9	-5.7
1.50	50	190	196.5	9.6	-5.9
1.75	50	240	196.5	9.5	-5.8
2.00	50	290	202.6	9.4	-5.4
2.25	50	340	193.5	9.1	-5.0
2.50	50	390	196.1	8.9	-4.5

Figure 4.22: Specimen 3 – Bracing Frame

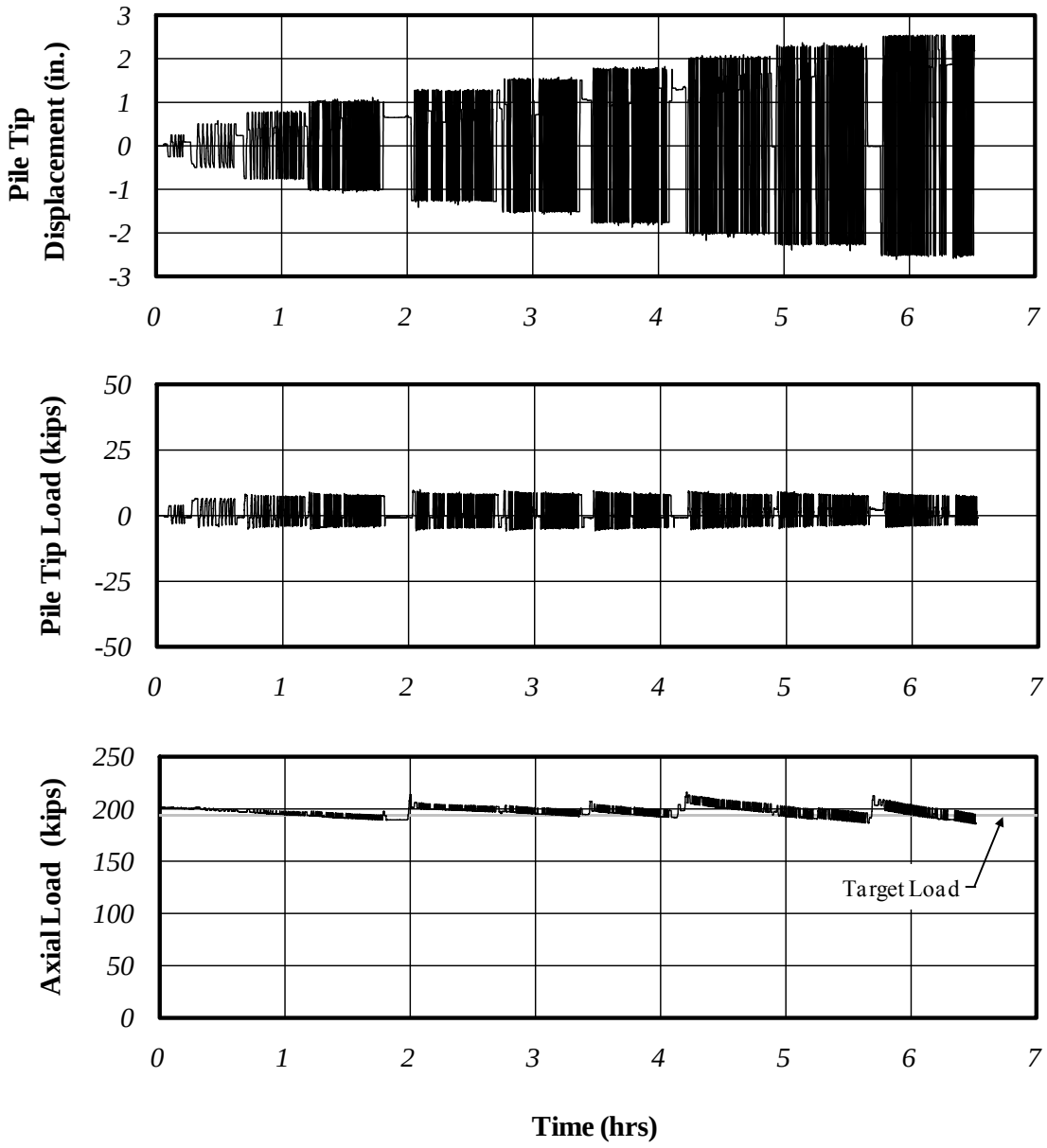

Figure 4.23: Specimen 3 – Load and Displacement Histories

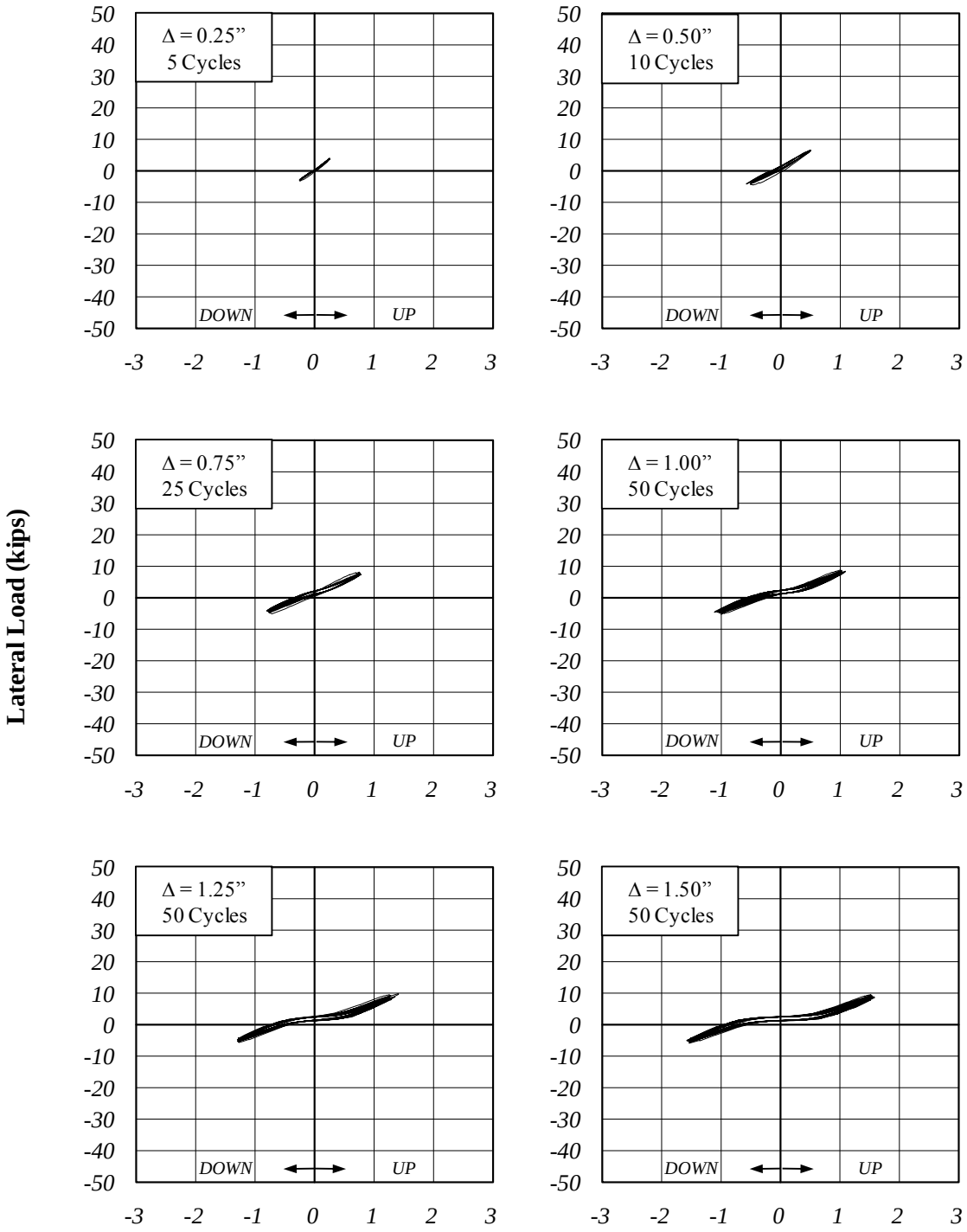

Figure 4.24: Specimen 3 – Load-Displacement Curves

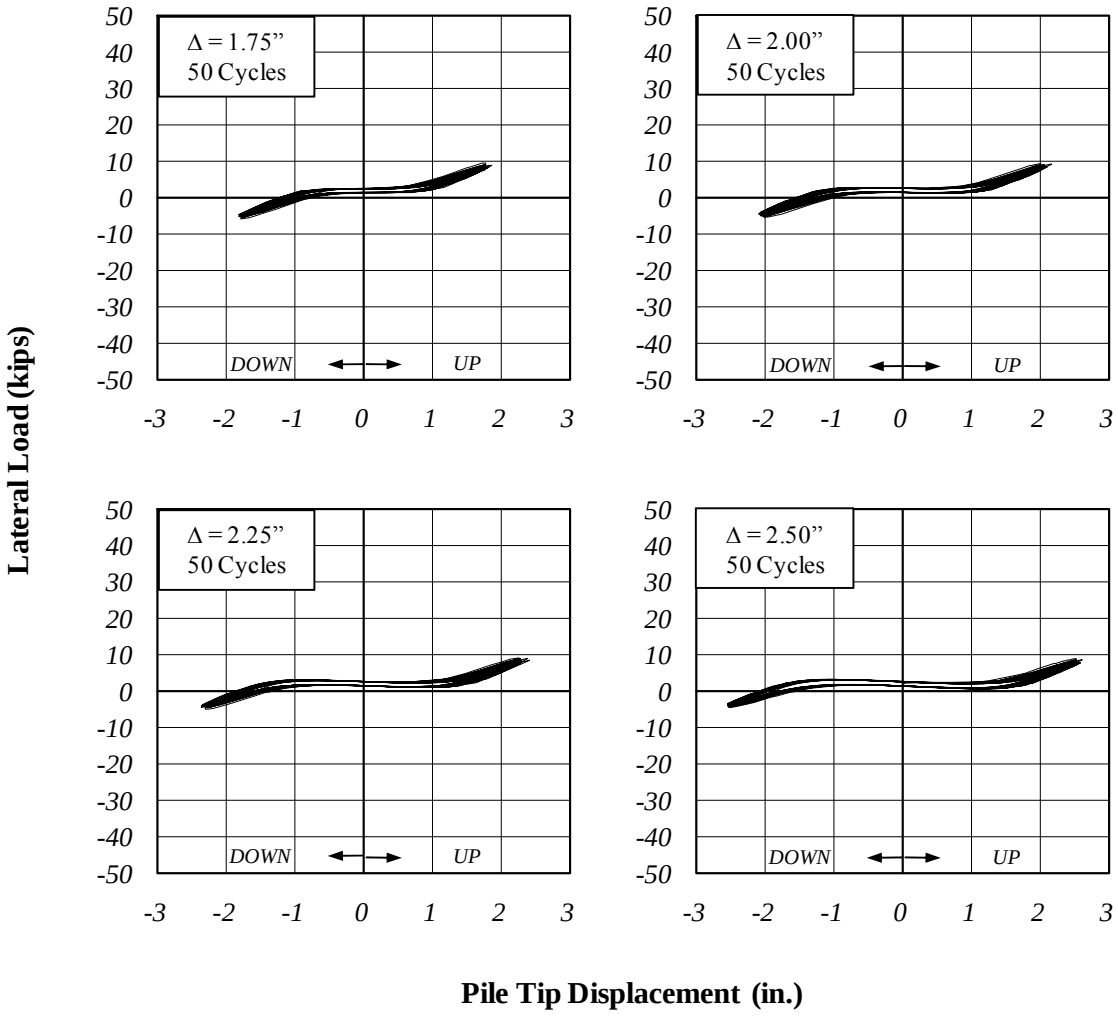

Figure 4.24 (continued): Specimen 3 – Load-Displacement Curves

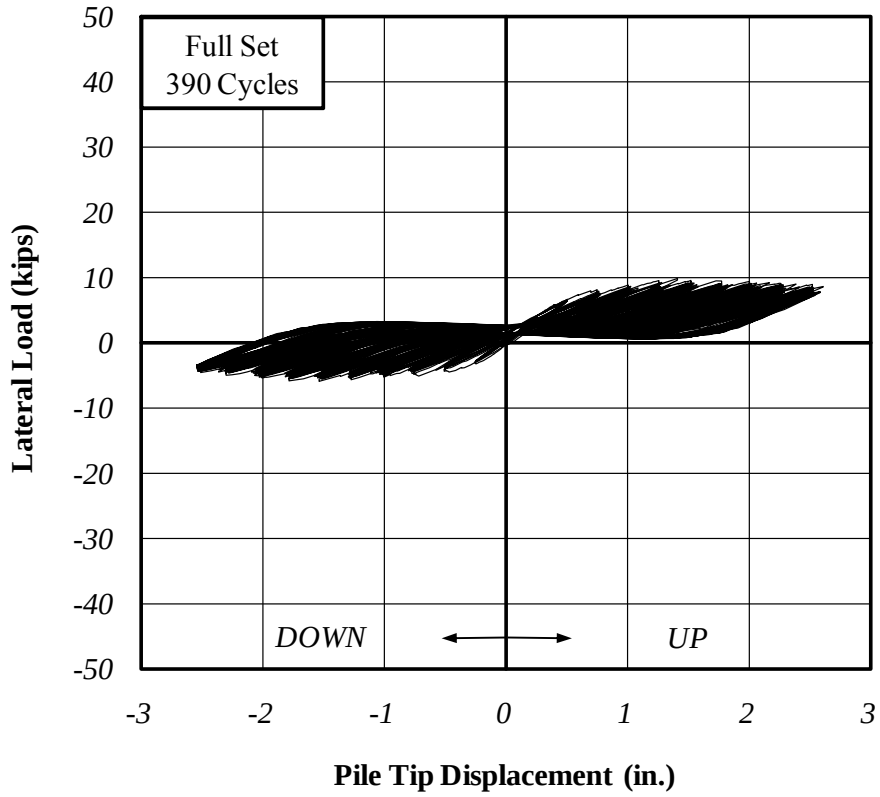

Figure 4.25: Specimen 3 – Complete Load-Displacement Curves

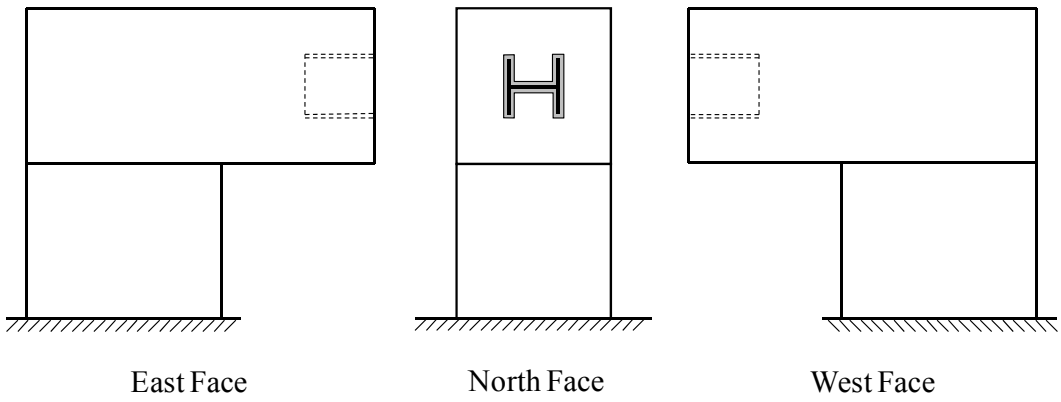

Note:
The shaded area represents the polystyrene wrap. No visible damage to the concrete was observed for Specimen 3

Figure 4.26: Specimen 3 – Crack Map

4.9.4 Specimen 4 (HP14x89, 15" Embedment, 12.5 ksi)

Test results for Specimen 4 are summarized in Table 4.11. Lateral load, pile tip displacement, and axial load histories are presented in Figure 4.27. Load-displacement curves for each displacement level are presented in Figure 4.28 while the complete set of load-displacement curves is presented in Figure 4.29. Cracking of the concrete surrounding the pile head was observed during the 0.75 in. displacement level. At displacement levels above 1.00 in., large crack widths and large rotations of the pile head were noted. The connection lost approximately one-half of its lateral load capacity during the 1.75 in. displacement cycles. Relatively stable hysteresis loops were achieved at the 2.00 in. displacement level. However, at this level, the specimen began demonstrating a tendency to lose axial load (Figure 4.27). Testing was stopped at the 2.25 in. displacement level due to the inability of the specimen to maintain axial load. Severe cracking of the concrete was observed on all faces of the specimen. The final pattern of cracking is presented in Figure 4.30.

Table 4.11: Specimen 4 – Test Summary

Displacement Range (in.)	Number of Cycles	Cumulative Cycles	Average Axial Load (kips)	Max Lateral Load (kips)	
				Up	Down
0.25	5	5	332.8	11.1	-12.5
0.50	10	15	330.5	20.6	-22.7
0.75	25	40	329.2	28.9	-26.9
1.00	50	90	324.4	29.4	-25.1
1.25	50	140	320.0	27.9	-22.8
1.50	50	190	311.7	27.8	-22.7
1.75	50	240	301.3	26.0	-19.1
2.00	50	290	301.4	17.3	-11.6
2.25	10	300	289.3	14.5	-9.1

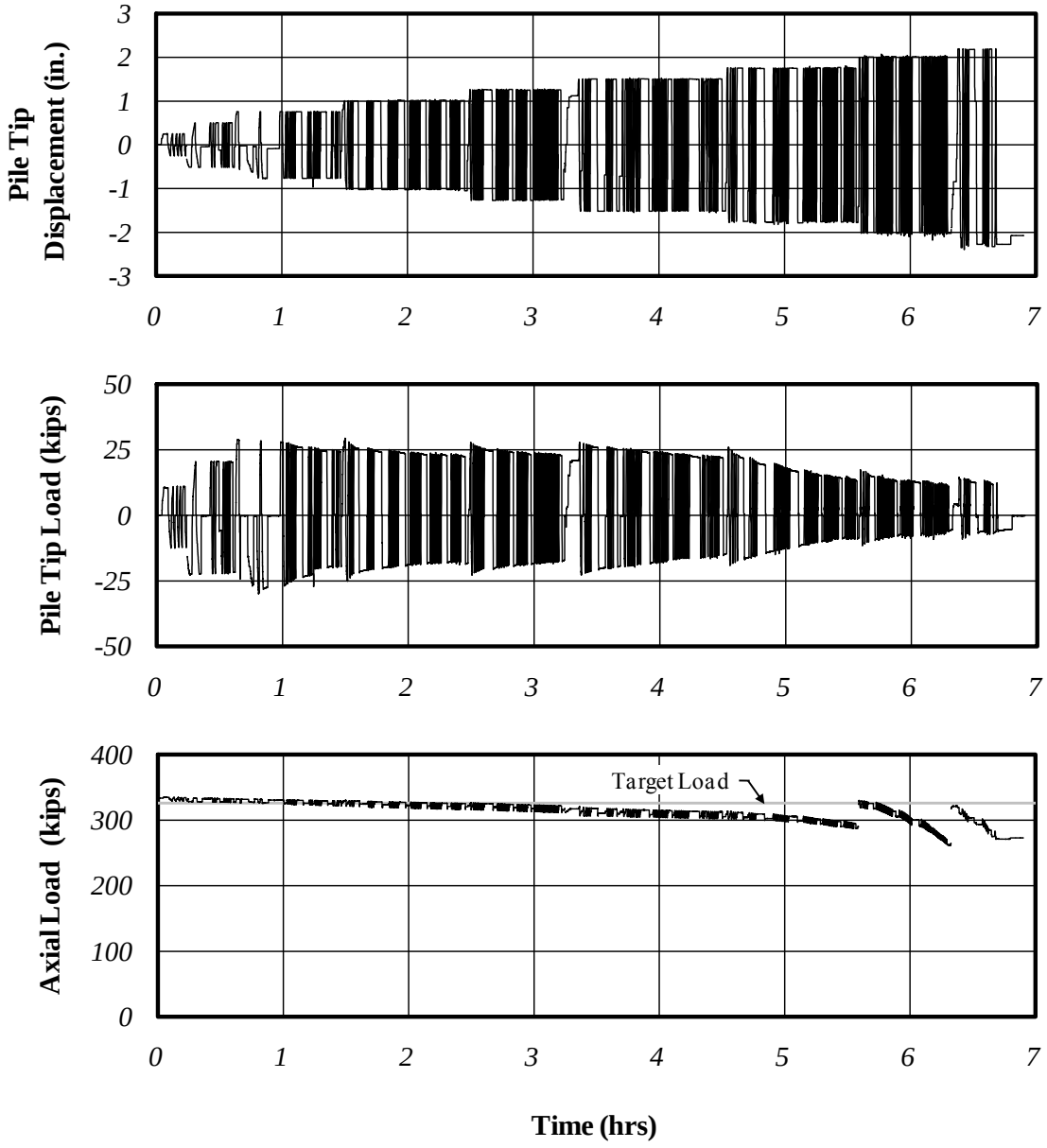

Figure 4.27: Specimen 4 – Load and Displacement Histories

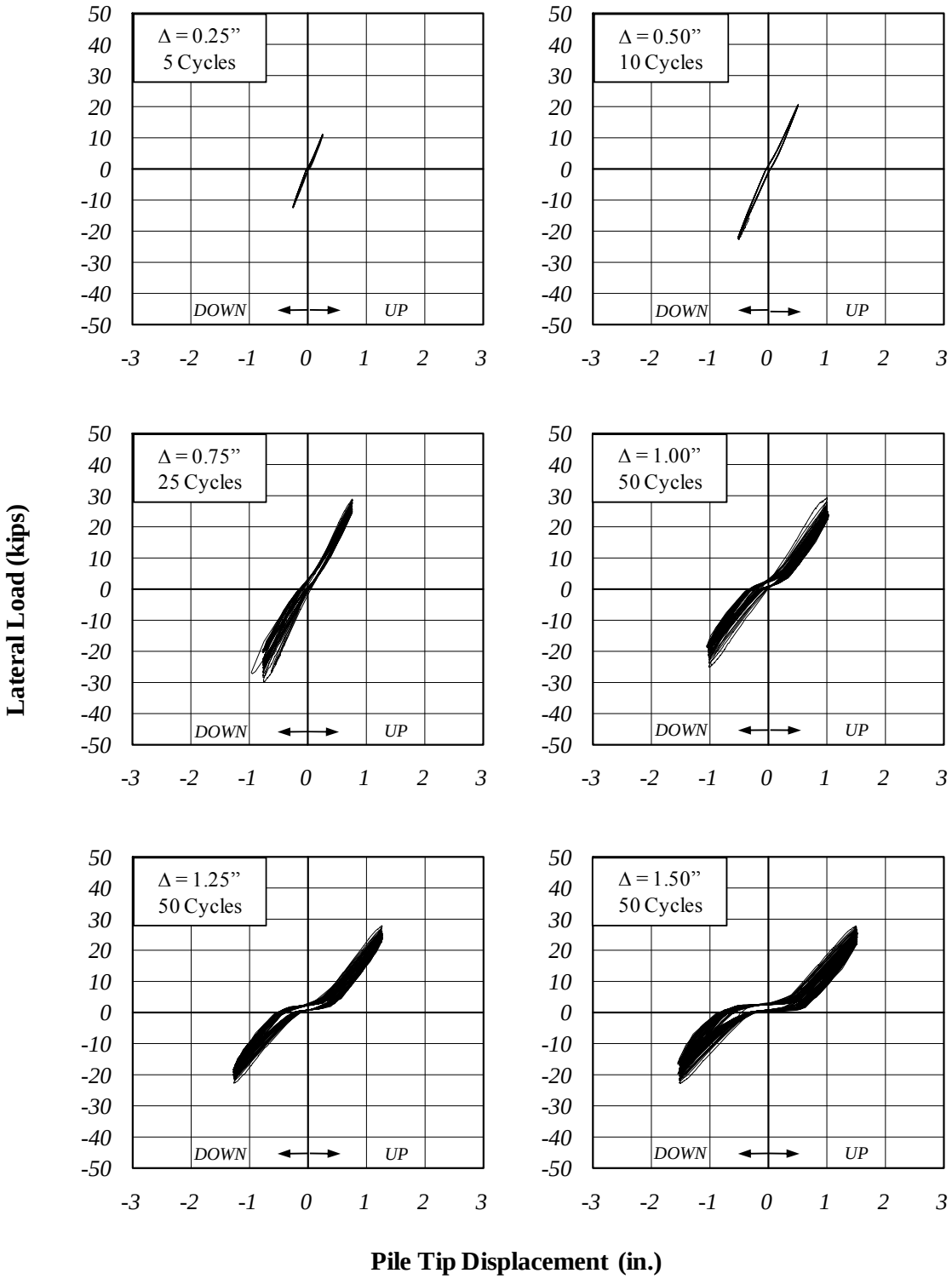

Figure 4.28: Specimen 4 – Load-Displacement Curves

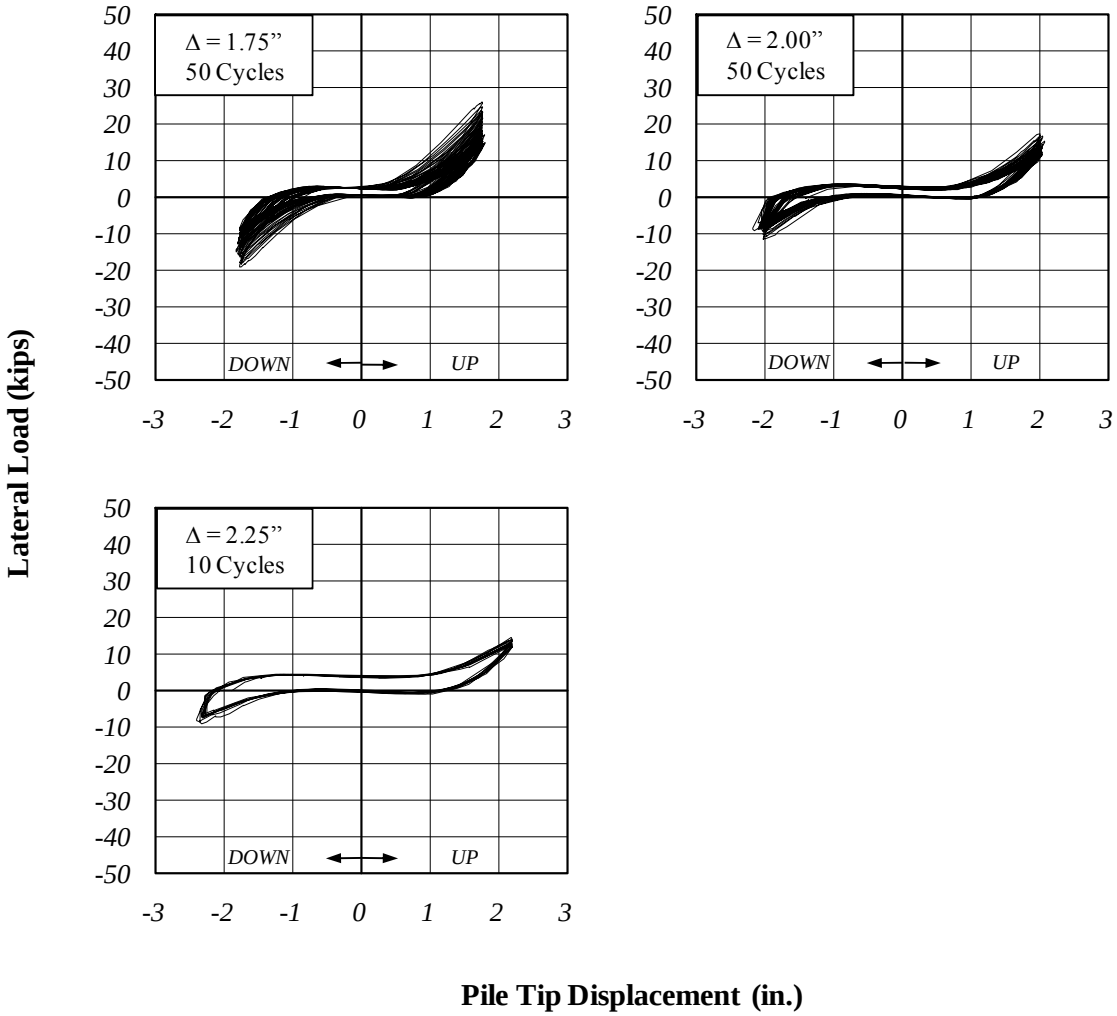

Figure 4.28 (continued): Specimen 4 – Load-Displacement Curves

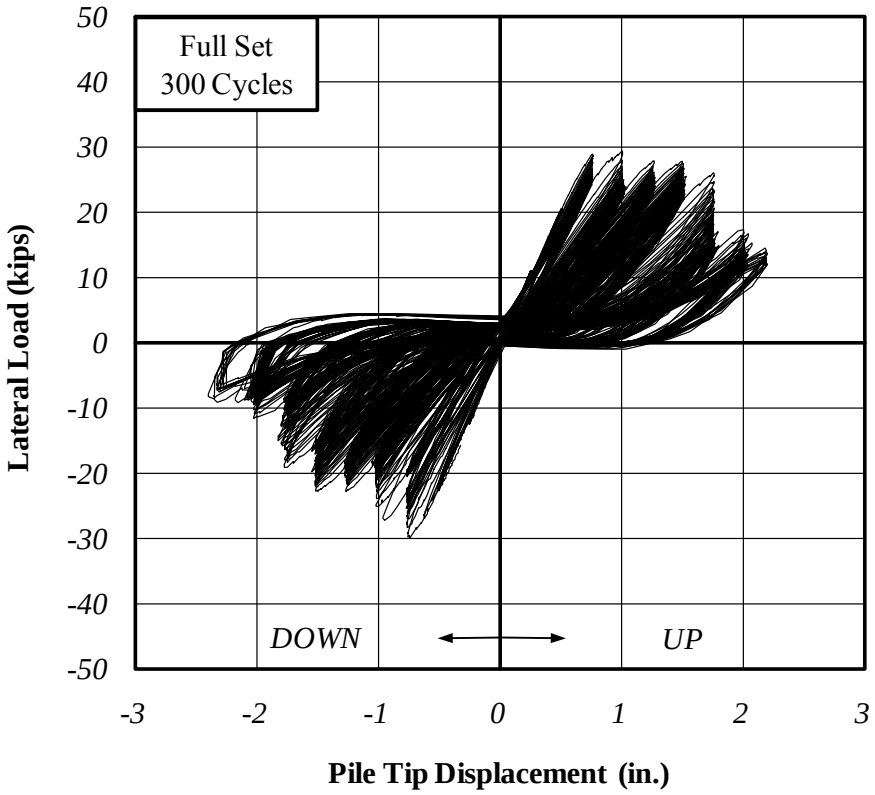

Figure 4.29: Specimen 4 – Complete Load-Displacement Curves

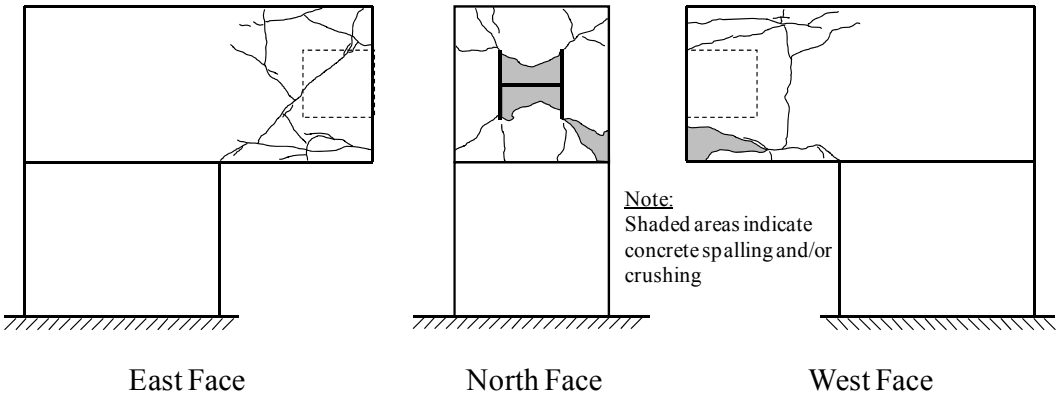

Figure 4.30: Specimen 4 – Crack Map

4.9.5 Specimen 5 (HP14x89, 24" Embedment, 12.5 ksi)

Test results for Specimen 5 are summarized in Table 4.12. Lateral load, pile tip displacement, and axial load histories are presented in Figure 4.31. Load-displacement curves for each displacement level are presented in Figure 4.32 while the complete set of load-displacement curves is presented in Figure 4.33. Similar to Specimen 4, first cracking of the concrete surrounding the pile head was observed during the 0.75 in. displacement level. At displacement levels greater than 1.00 in. large crack widths and rotations of the pile head were noted. However, the magnitude of the crack widths and rotations of the pile head were noticeably smaller than those observed in Specimen 4, particularly in the Up direction. The behavior of Specimen 5 at large displacement levels was qualitatively similar to Specimen 4. However, Specimen 5 achieved much larger lateral loads compared to Specimen 4. Severe cracking of the concrete was observed on all faces of the specimen. However, no local crushing or spalling of the concrete surrounding the pile head was observed. The final pattern of cracking is presented in Figure 4.34. The test was discontinued at the 2.50 in. displacement level due to the displacement capacity of the test setup.

Table 4.12: Specimen 5 – Test Summary

Displacement Range (in.)	Number of Cycles	Cumulative Cycles	Average Axial Load (kips)	Max Lateral Load (kips)	
				Up	Down
0.25	5	5	328.1	13.4	-11.2
0.50	10	15	323.5	23.1	-20.8
0.75	25	40	320.3	31.7	-28.3
1.00	50	90	317.5	35.2	-31.2
1.25	50	140	330.2	37.9	-31.2
1.50	50	190	324.9	38.1	-28.0
1.75	50	240	318.9	37.0	-26.5
2.00	50	290	312.2	34.6	-18.7
2.25	50	340	330.1	32.7	-16.7
2.50	50	390	313.2	28.4	-13.1

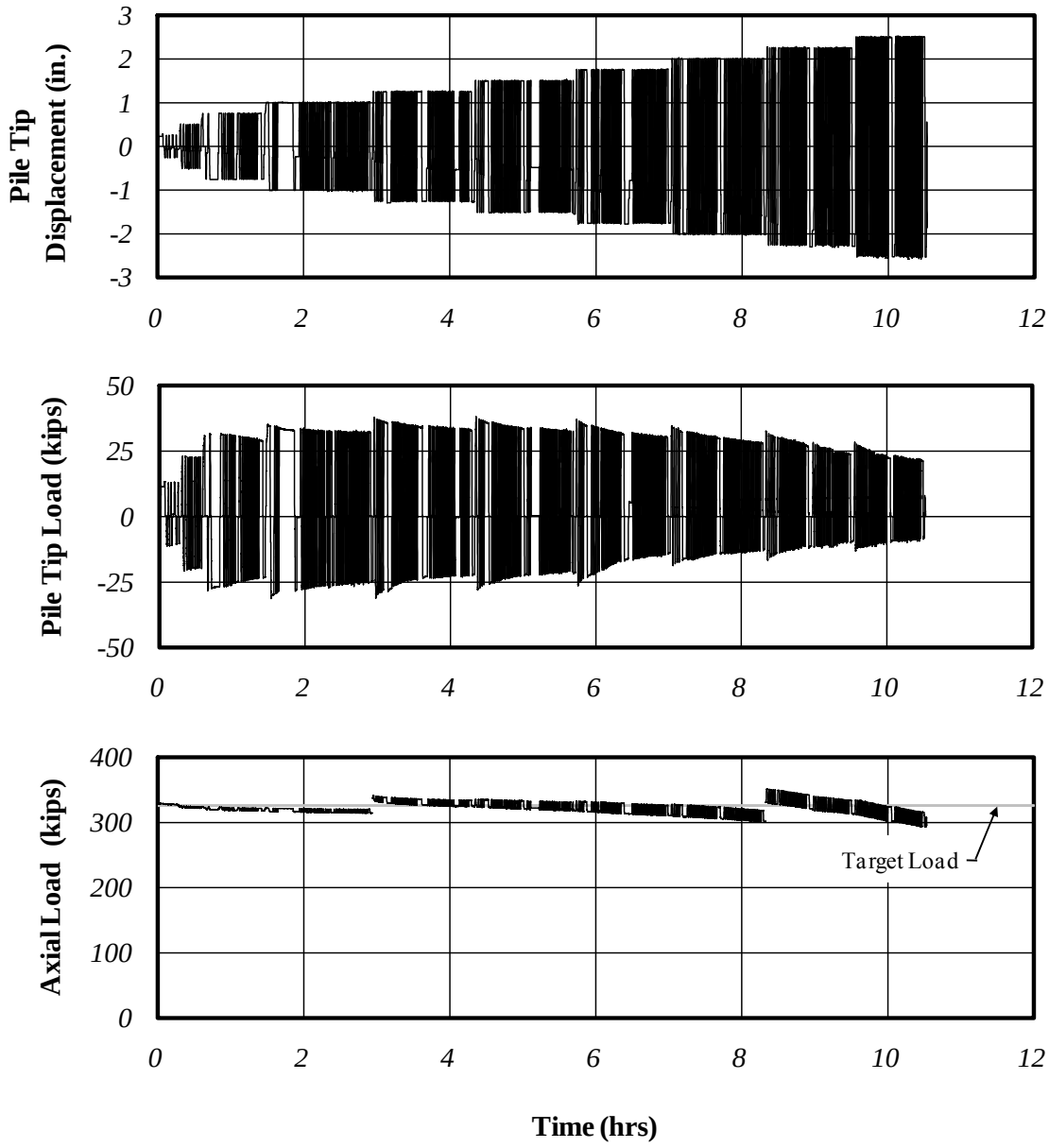

Figure 4.31: Specimen 5 – Load and Displacement Histories

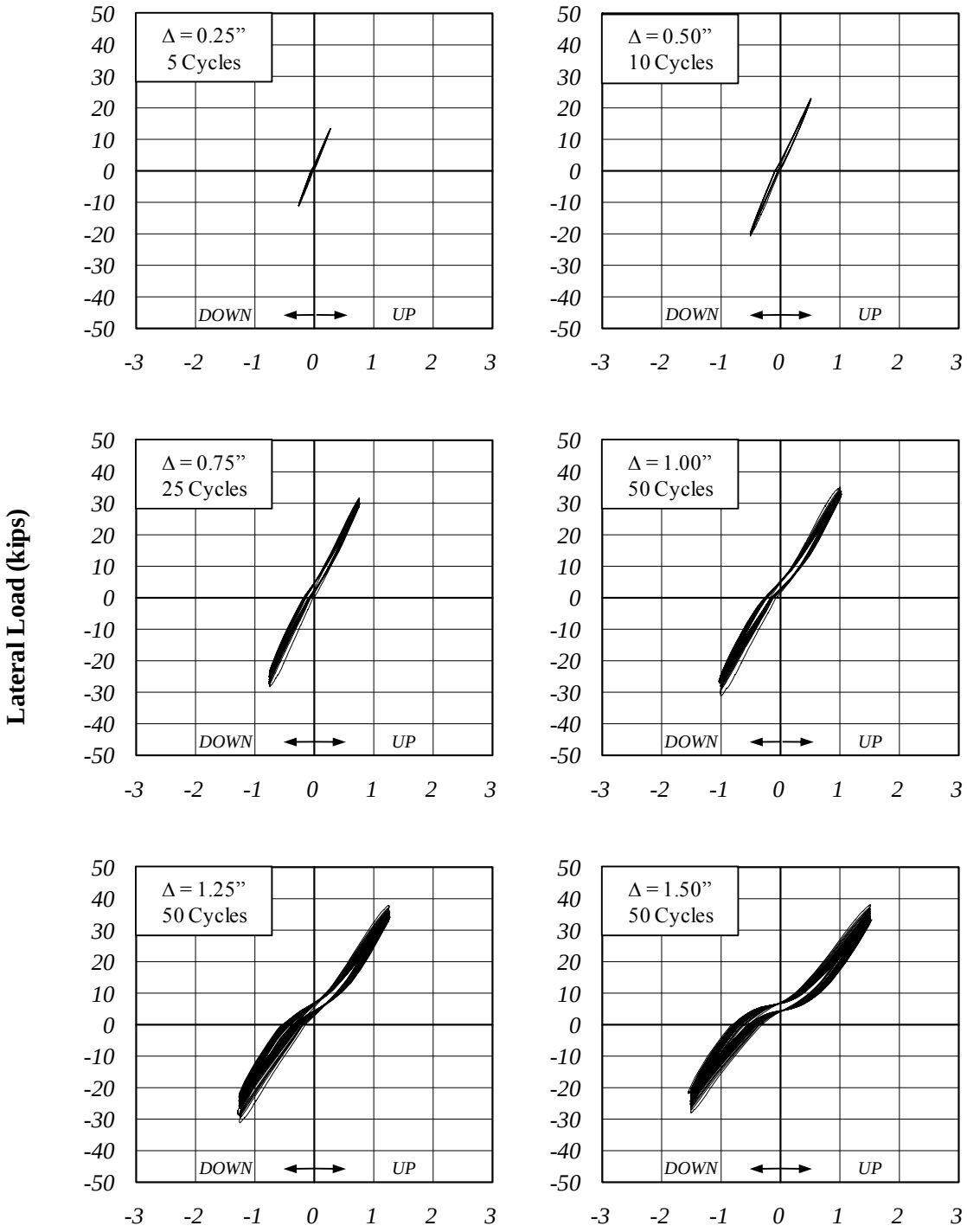

Figure 4.32: Specimen 5 – Load-Displacement Curves

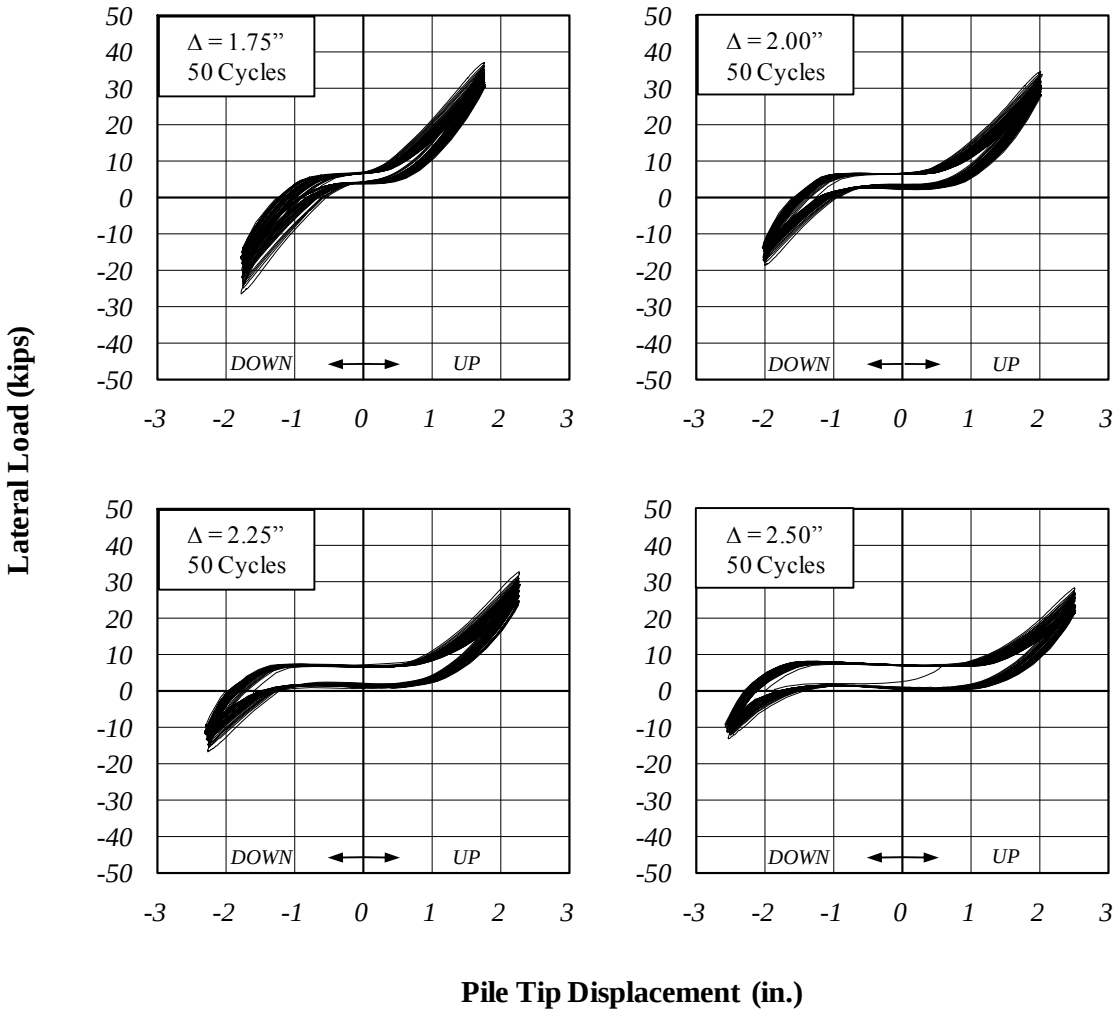

Figure 4.32 (continued): Specimen 5 – Load-Displacement Curves

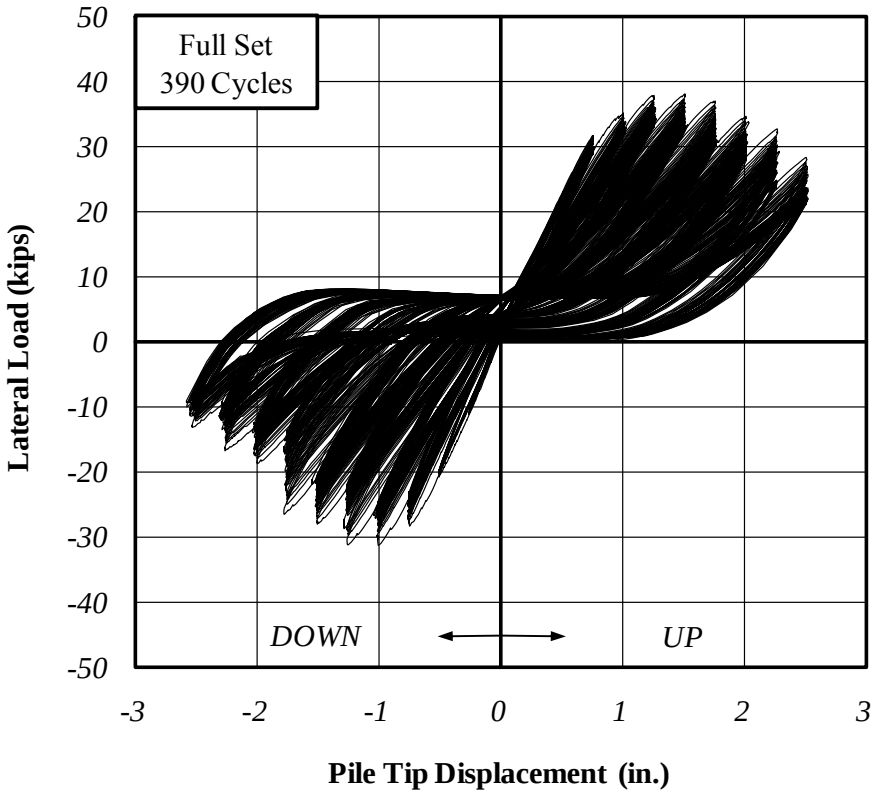

Figure 4.33: Specimen 5 – Complete Load-Displacement Curves

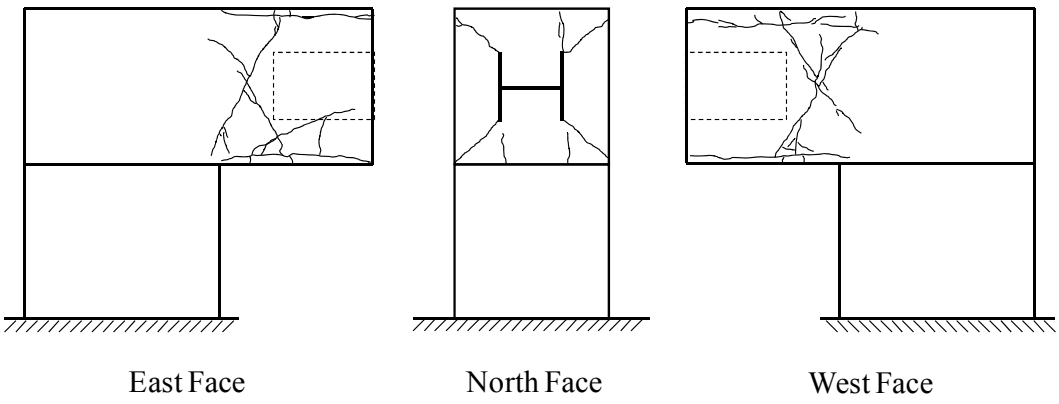

Figure 4.34: Specimen 5 – Crack Map

4.9.6 Specimen 6 (HP14x89, 24" Embedment, 12.5 ksi, Confinement A)

Test results for Specimen 6 are summarized in Table 4.13. Lateral load, pile tip displacement, and axial load histories are presented in Figure 4.35. Load-displacement curves for each displacement level are presented in Figure 4.36 while the complete set of load-displacement curves is presented in Figure 4.37. First cracking of the concrete surrounding the pile head was observed during the 0.75 in. displacement level. It should be noted that an accidental overload occurred as seen in Figure 4.36 (Δ=1.25 in.). This overload is important as it may have influenced the downward portion of subsequent load cycles. Regardless, the test specimen achieved stable hysteresis loops at all displacement levels. Unlike previous specimens, Specimen 6 did not experience a drop in lateral load capacity at large displacement levels. Overall, the extent of cracking and crack widths was significantly lower than those observed in Specimens 4 and 5. The final pattern of cracking is shown in Figure 4.38. Testing was discontinued at the 2.25 in. displacement level due to the lateral load capacity of the test setup. Previous specimens were able to be tested beyond the 2.25 in. displacement level due to a loss of lateral load resisting capacity. As mentioned previously, Specimen 6 did not experience a drop in lateral load resisting capacity. Consequently, the lateral load capacity of the test setup was the limiting factor in this case.

Strain gages were installed on the spiral reinforcement of Specimen 6 in an attempt to quantify the effectiveness of the spiral. The locations of these gages are shown in Figure 4.39. Strain gages S2 and S3 measured negligible strains throughout the entire test and are not presented here. Of more significance were strains measured by Gages S1 and B1 which are presented in Figure 4.40. The measured strains were very small for displacement cycles less than 1.00 in. Beginning with the 1.00 in displacement cycles, the measured strains began increasing and continued increasing for the duration of the test. By the end of testing, the measured strains had increased to approximately 400 $\mu\varepsilon$ or approximately 11.6 ksi (20% of the yield stress).

Table 4.13: Specimen 6 – Test Summary

Displacement Range (in.)	Number of Cycles	Cumulative Cycles	Average Axial Load (kips)	Max Lateral Load (kips)	
				Up	Down
0.25	5	5	324.5	11.1	-10.9
0.50	10	15	321.9	19.6	-19.5
0.75	25	40	331.4	26.8	-27.1
1.00	50	90	327.3	29.7	-32.4
1.25	50	140	322.1	32.8	-44.3
1.50	50	190	321.9	36.4	-33.5
1.75	50	240	323.4	38.9	-37.4
2.00	50	290	321.0	40.2	-40.6
2.25	50	340	318.0	41.4	-43.2

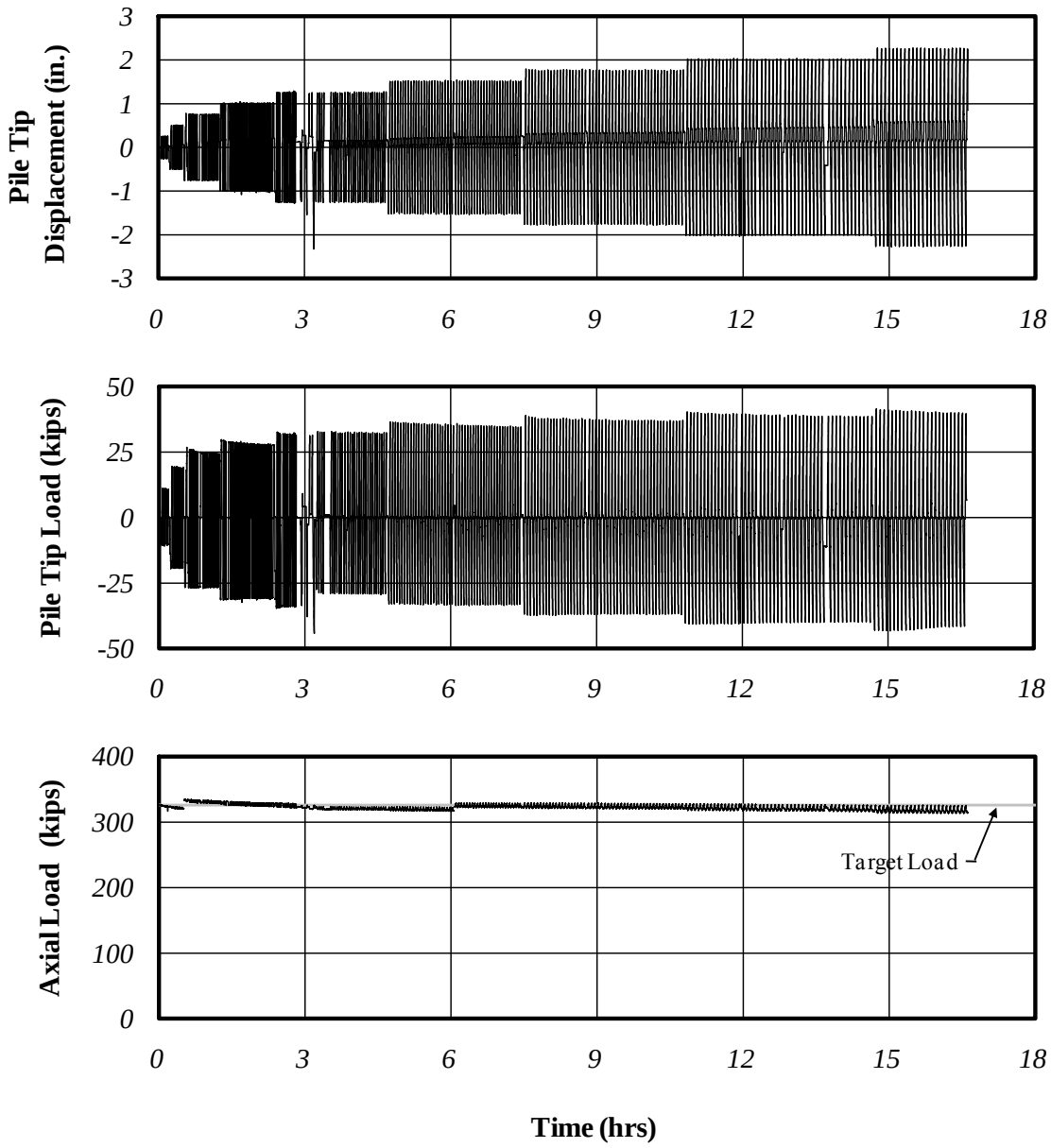

Figure 4.35: Specimen 6 – Load and Displacement Histories

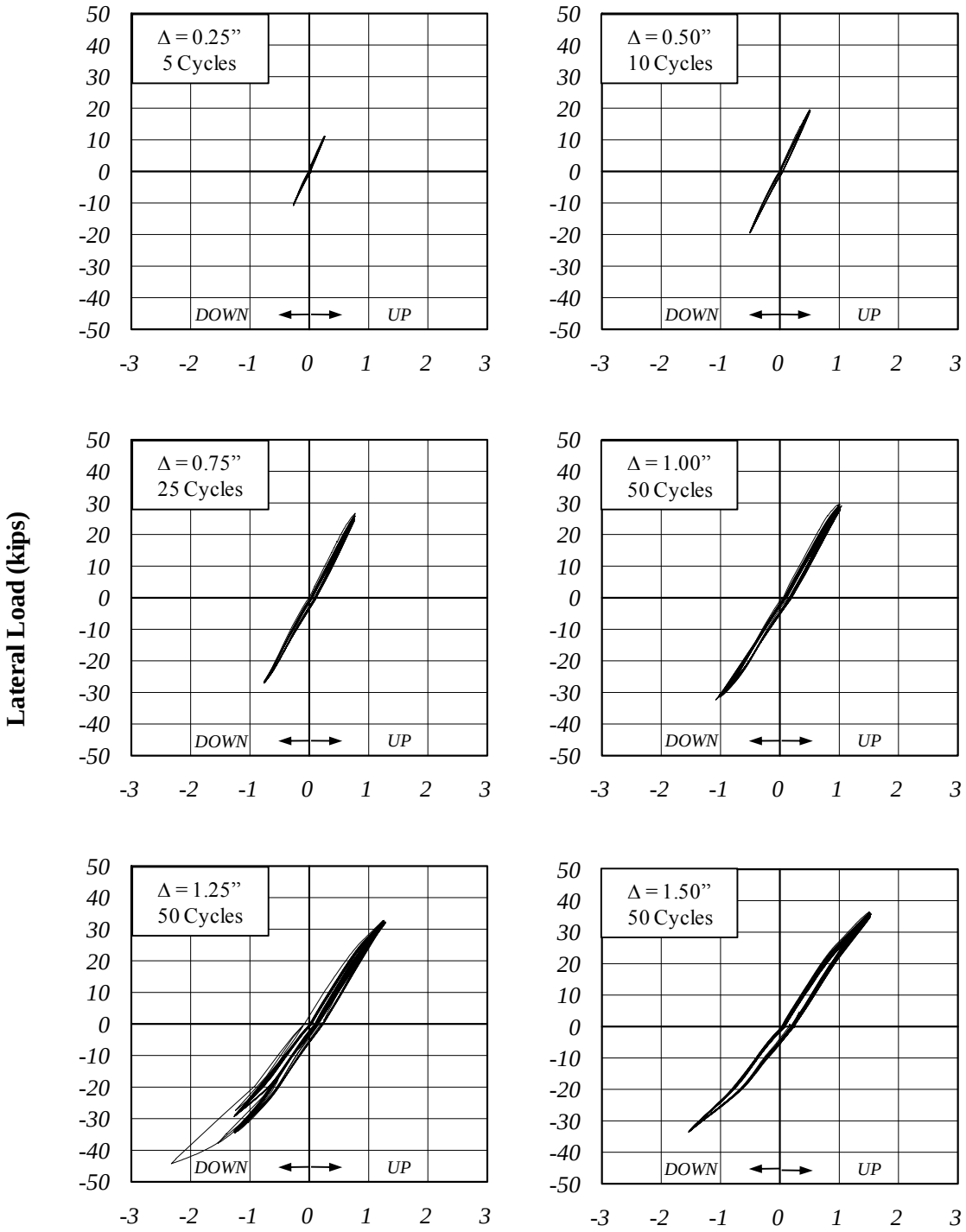

Figure 4.36: Specimen 6 – Load-Displacement Curves

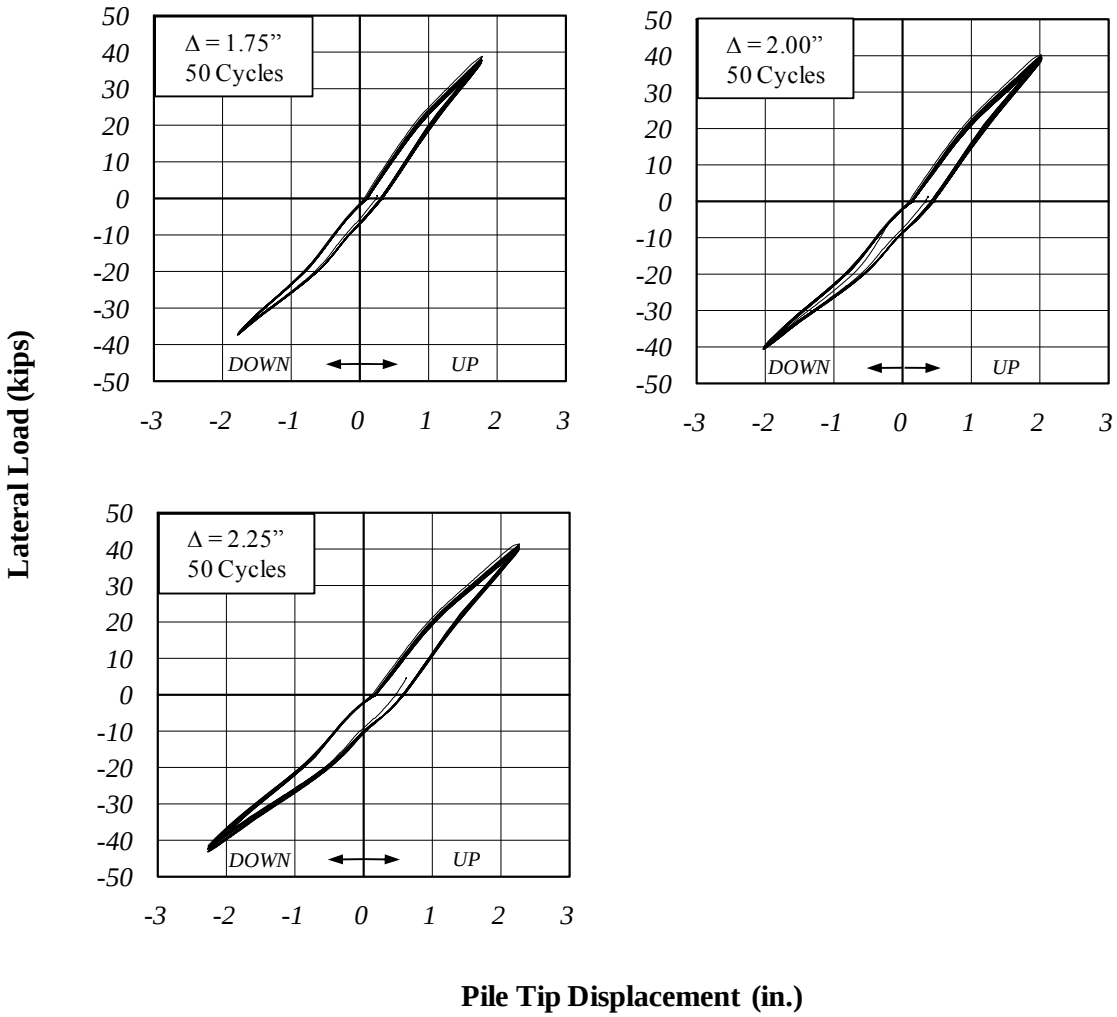

Figure 4.36 (continued): Specimen 6 – Load-Displacement Curves

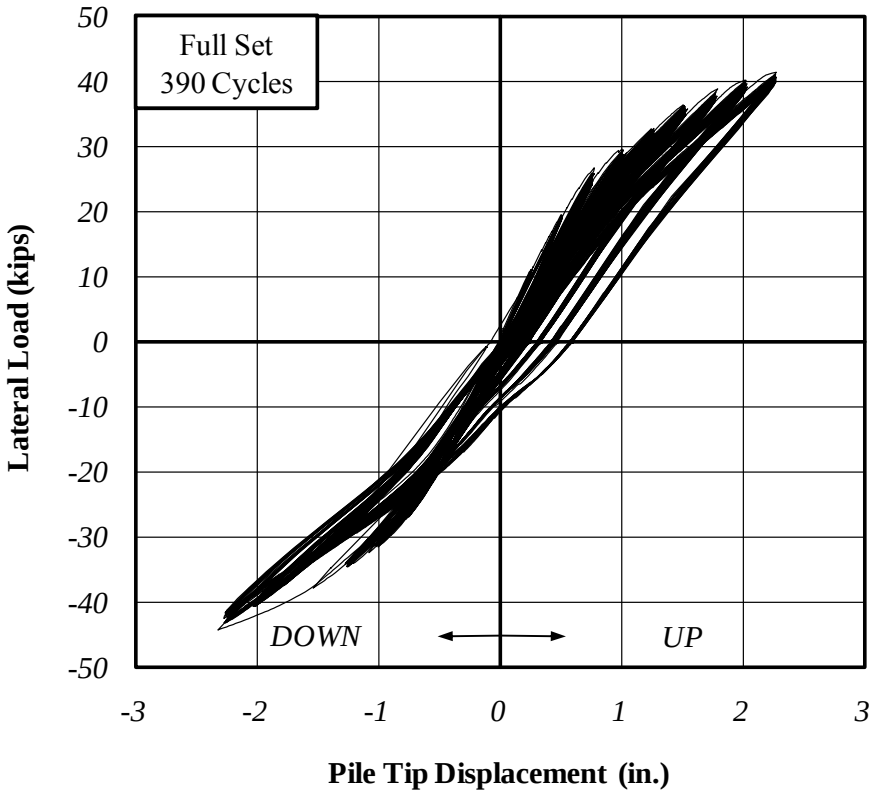

Figure 4.37: Specimen 6 – Complete Load-Displacement Curves

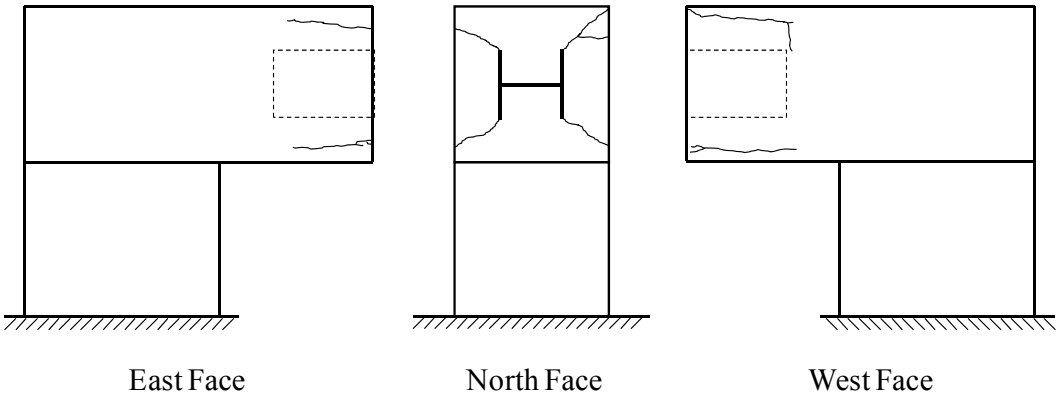

Figure 4.38: Specimen 6 – Crack Map

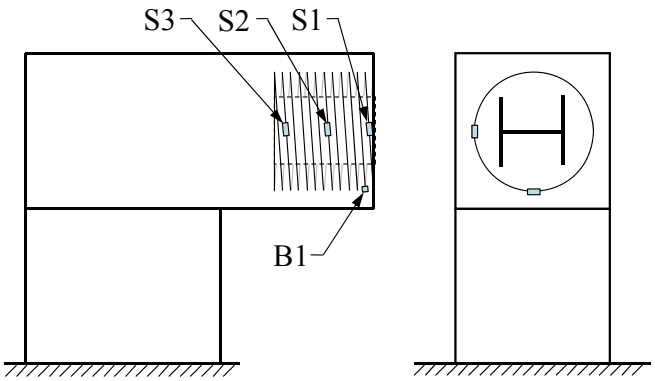

Figure 4.39: Specimen 6 – Strain Gage Locations

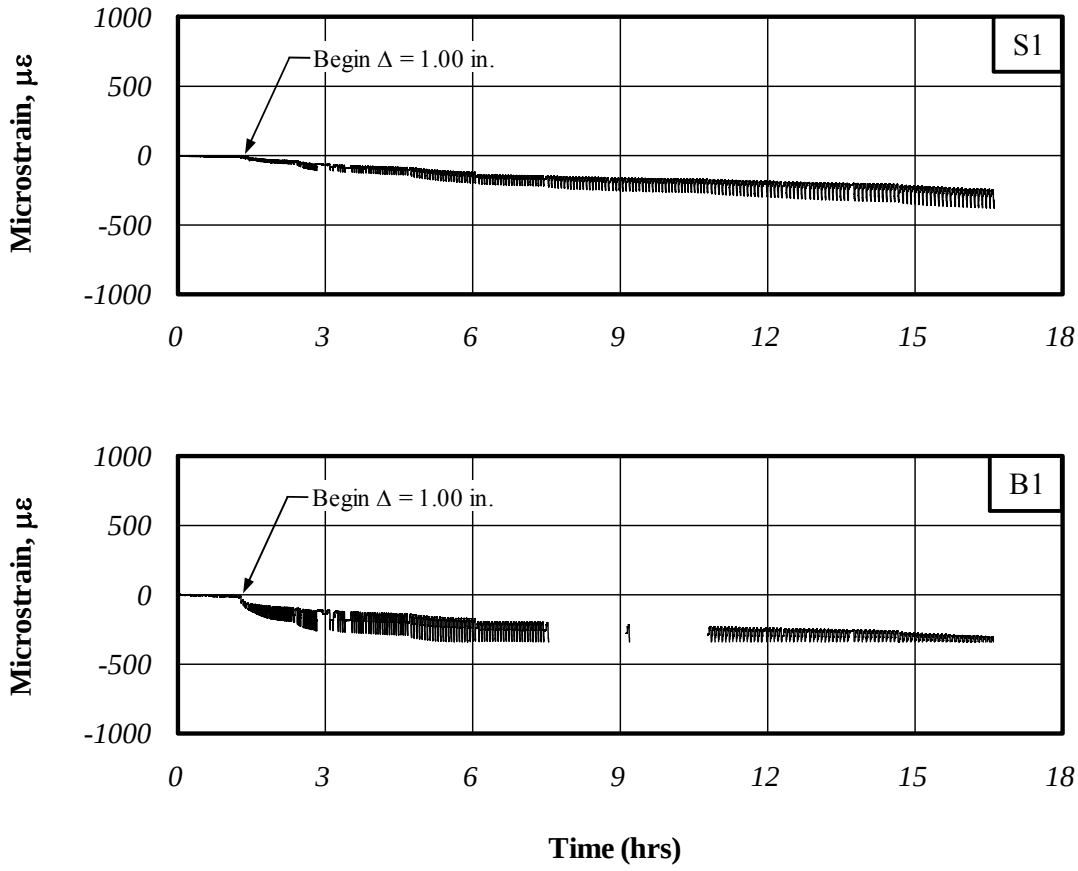

Figure 4.40: Specimen 6 – Spiral Reinforcement Strains

4.9.7 Specimen 7 (HP14x89, 24" Embedment, 12.5 ksi, Confinement B)

Test results for Specimen 7 are summarized in Table 4.14. Lateral load, pile tip displacement, and axial load histories for Specimen 7 are presented in Figure 4.41. Load-displacement curves for each displacement level are presented in Figure 4.42 while the complete set of load-displacement curves is presented in Figure 4.43. Specimen 7 performed similarly to Specimen 6 up to the 1.50 in. displacement level. At this displacement level, flexural cracks formed in the cantilevered section at the support block (Figure 4.44) corresponding to a lateral load of approximately 45 kips. The flexural cracking moment based on a section through the specimen at the support block (Section A-A in Figure 4.44) was computed to be approximately 5500 in.-kips. This calculation was based on a modulus of rupture, f_r, of $7.5\sqrt{f_c'}$ and assumed the axial load applied to the pile resulted in a uniform precompression at Section A-A. The computed cracking moment corresponds to a lateral load of approximately 50 kips, which is in general agreement with the formation of these cracks. In spite of the formation of flexural cracks, Specimen 7 continued to perform well at higher displacement levels. No decreases of lateral load capacity were observed at large displacements. Axial load was maintained throughout the test (Figure 4.41). Additionally, no spalling or crushing of the concrete surrounding the pile head was observed. Testing was discontinued at the 2.00 in. displacement level due to the lateral load capacity of the test setup. Similar to Specimen 6, Specimen 7 did not experience a decrease in lateral load capacity at large displacements and therefore reached the lateral load capacity of the test setup at a lower displacement than Specimens 1-5. The final pattern of cracking is shown in Figure 4.44.

Similar to Specimen 6, strain gages were installed on the spiral reinforcement of Specimen 7. The locations of these strain gages are shown in Figure 4.45. Because the strain gages located away from the face of Specimen 6 measured negligible strain, no gages were installed in these locations for Specimen 7. For Specimen 7, one strain gage was installed at mid height (SG 00). A second strain gage was installed at 45° from the primary axis of the specimen (SG 45). It was thought that SG 45 would be located near a crack and provide more insight into the role of the spiral reinforcement. The measured strains are presented in Figure 4.46. The maximum measured strain for Specimen 7 was

approximately 100 $\mu\varepsilon$, or 5% of the yield strain. SG-00 measured a consistent tensile strain which increased throughout testing, similar to the results of Specimen 6. SG-45 measured both tensile and compressive strains with a trend toward increasing tensile strain. This may be due to the proximity of SG-45 to the cracks on the front face of Specimen 7 emanating at the flange tips. The opening and closing of the crack in response to lateral loading would result in tensile and compressive stresses in the portion of the spiral crossing the crack. The lower stresses measured in Specimen 7 compared to Specimen 6 are consistent with the fact that Specimen 7 had more confining reinforcement.

Table 4.14: Specimen 7 – Test Summary

Displacement Range (in.)	Number of Cycles	Cumulative Cycles	Average Axial Load (kips)	Max Lateral Load (kips)	
				Up	Down
0.25	5	5	326.3	11.9	-14.7
0.50	10	15	323.7	21.9	-23.6
0.75	25	40	318.9	30.1	-30.7
1.00	50	90	319.2	36.8	-36.6
1.25	50	140	320.9	41.4	-39.3
1.50	50	190	315.3	44.1	-42.9
1.75	50	240	312.9	45.4	-44.9
2.00	5	245	307.3	46.5	-45.2

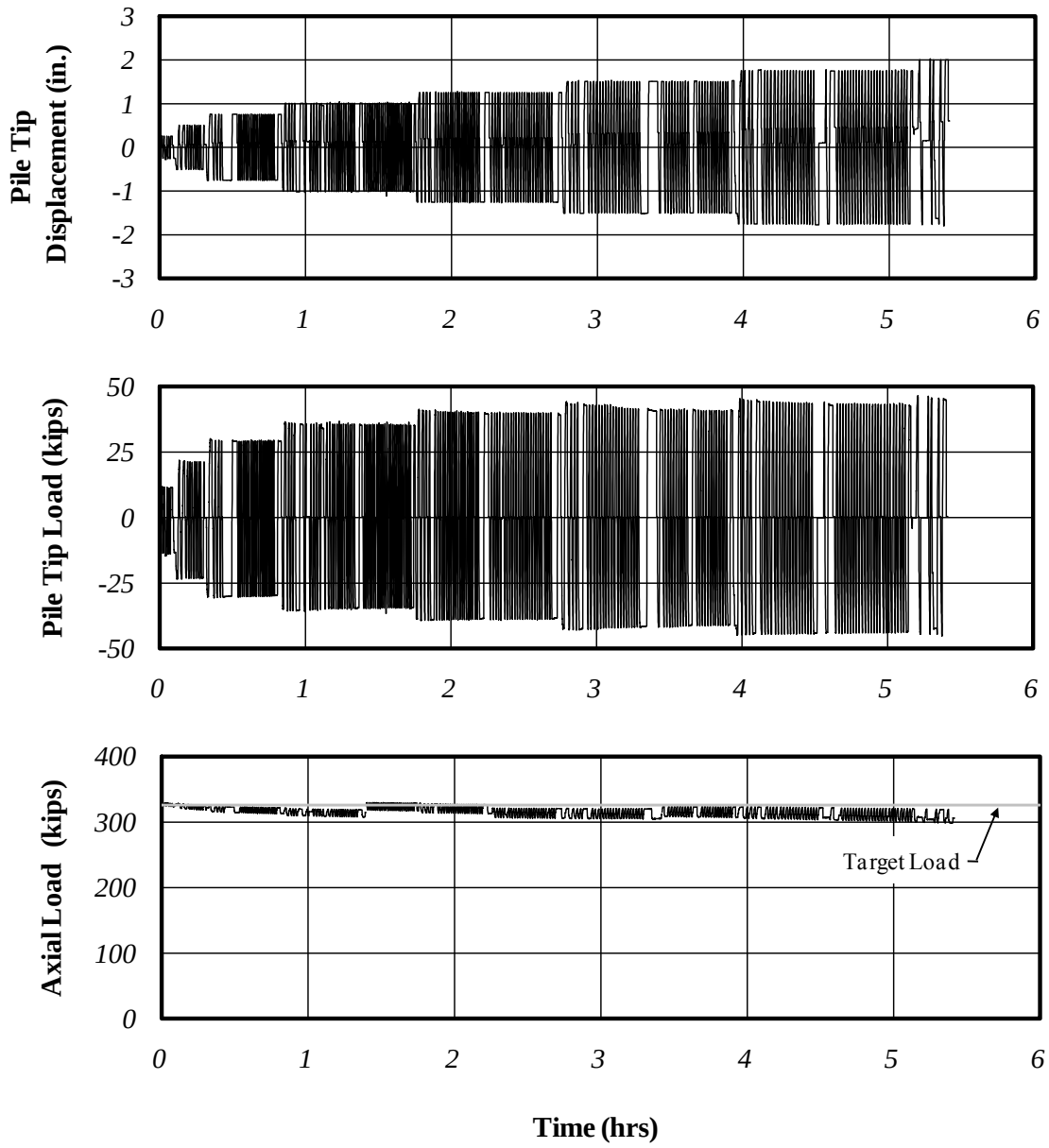

Figure 4.41: Specimen 7 – Load and Displacement Histories

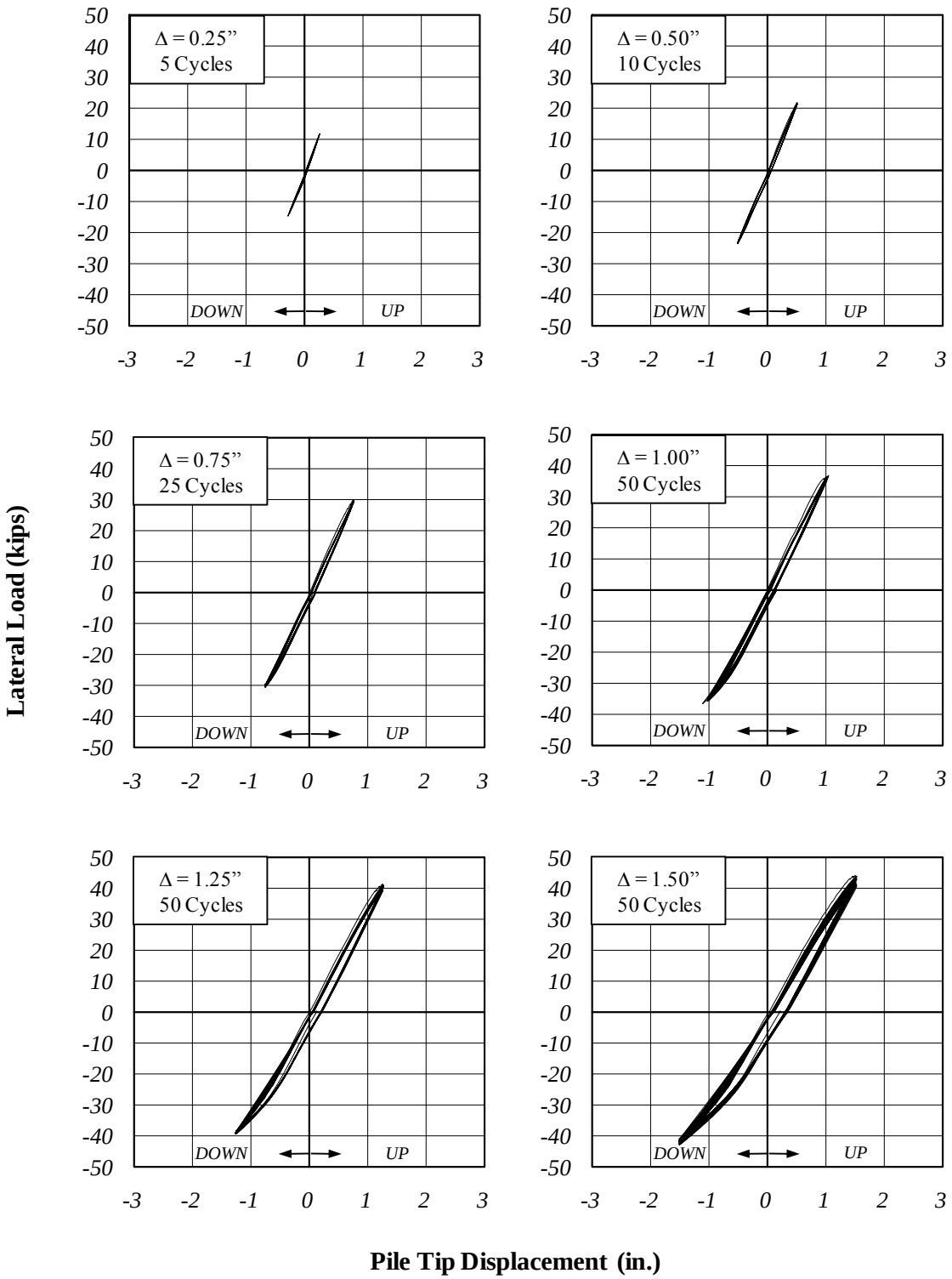

Figure 4.42: Specimen 7 – Load-Displacement Curves

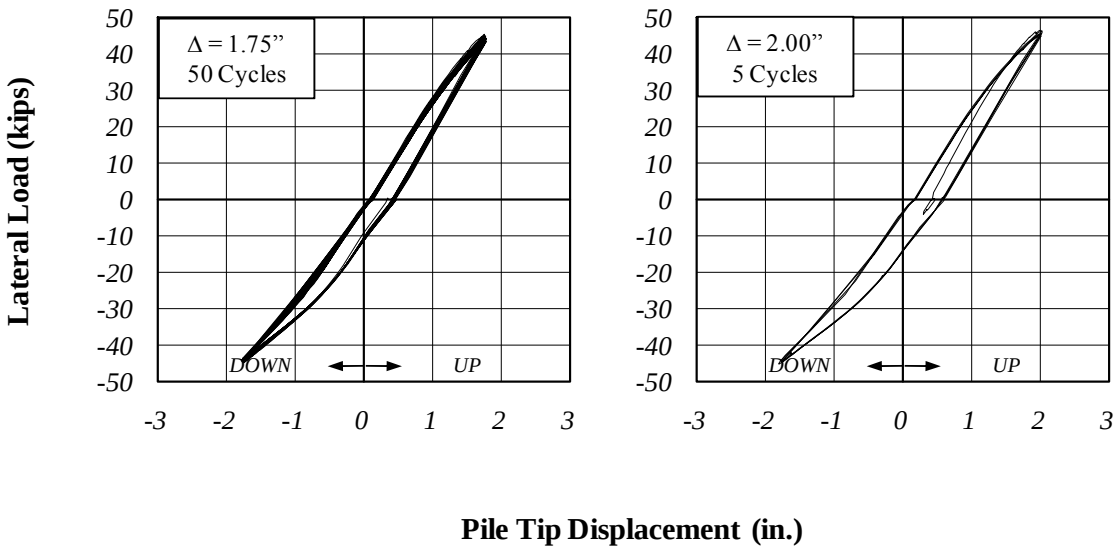

Figure 4.42 (continued): Specimen 7 – Load-Displacement Curves

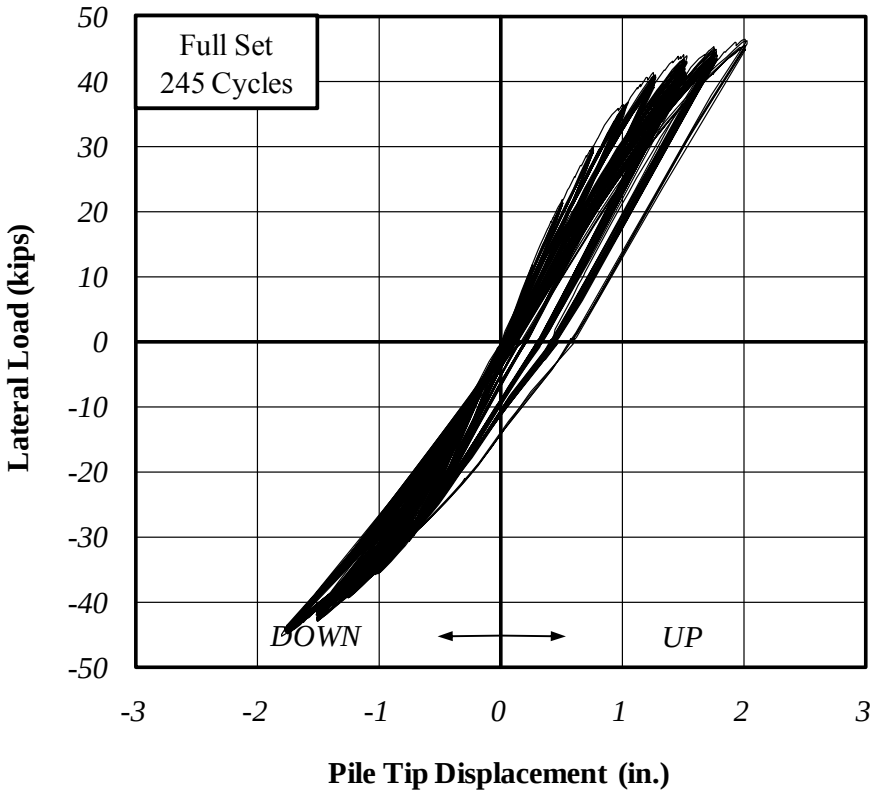

Figure 4.43: Specimen 7 – Complete Load-Displacement Curves

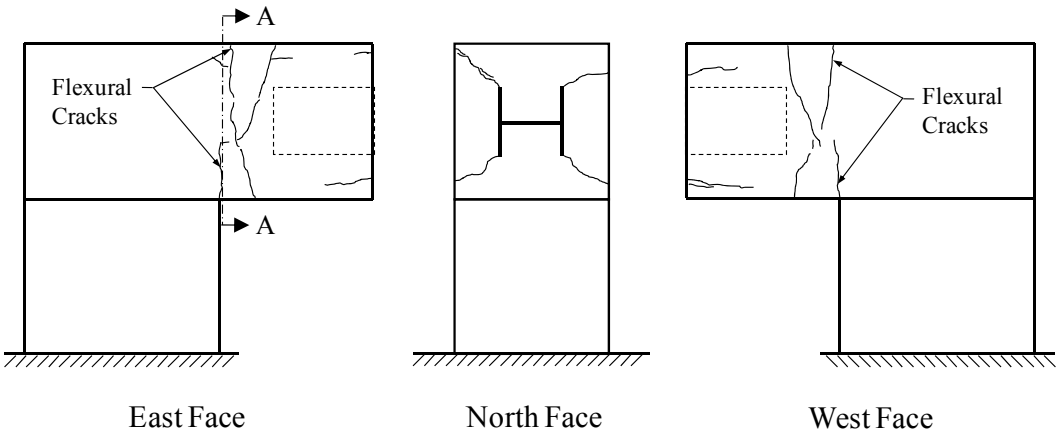

Figure 4.44: Specimen 7 – Crack Map

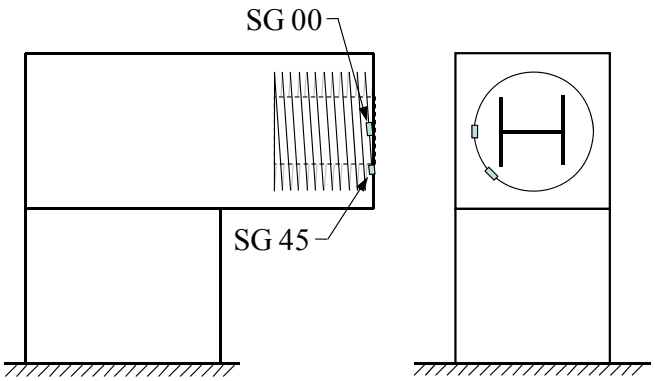

Figure 4.45: Specimen 7 – Strain Gage Locations

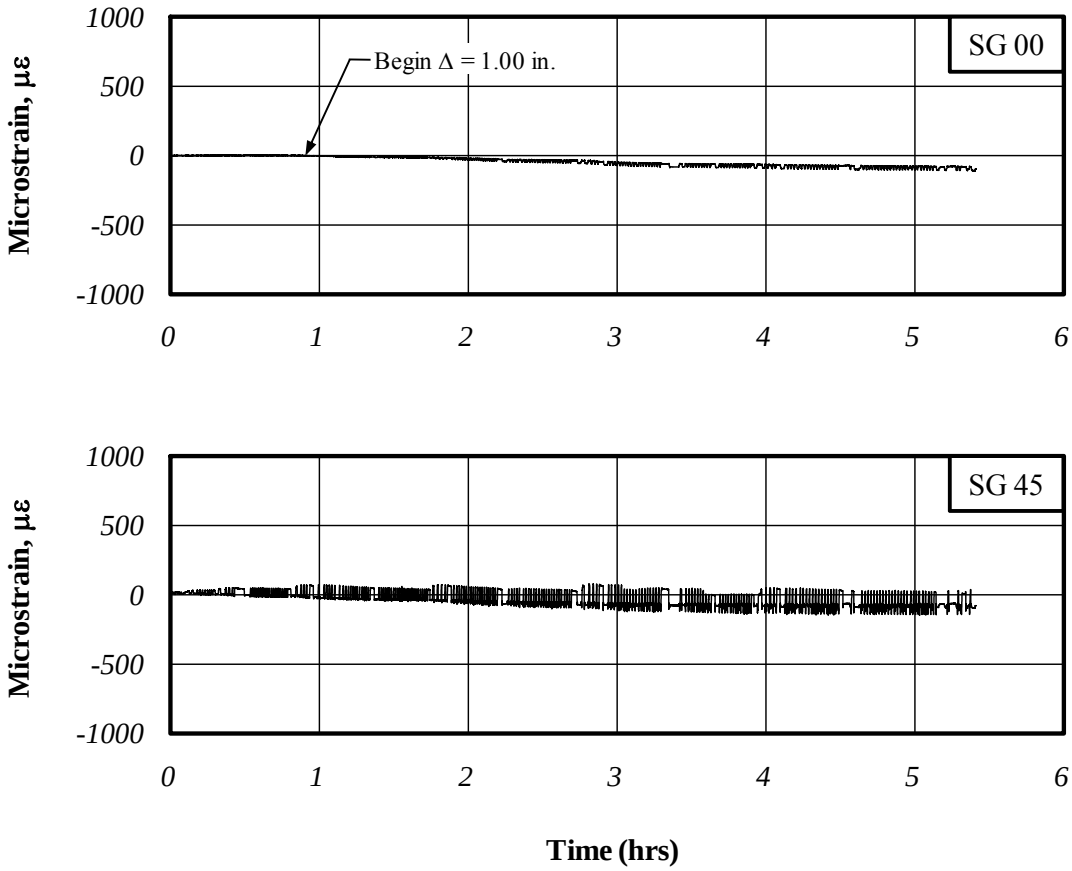

Figure 4.46: Specimen 7 – Spiral Reinforcement Strains

4.10 Summary of Chovichien's Test Results

The results of Chovichien's investigation (Chovichien 2004) will also be used in the following chapters along with the current series of tests to evaluate the displacement capacity of integral abutments. For convenience, relevant portions of those results are reproduced here. Only those specimens which were tested in bending about the weak axis were considered as outlined in Table 4.15. The specimen numbers are preceded with the letter "C", for Chovichien, to distinguish them from the current series of tests. One of the test variables examined by Chovichien was pile axial load. The 9 ksi axial stress represents the AASHTO requirement of $0.25f_y$ for A36 steel. Chovichien also tested a specimen with 18 ksi axial load, or $0.50f_y$ for A36 steel, to investigate the effects of higher axial load.

Table 4.15: Summary of Chovichien's Specimens

Specimen	Section	Axial Load (ksi)
C1	HP8x36	9
C4	HP8x36	18
C5	HP10x42	9
C6	HP12x53	9

4.10.1 Specimen C1 (HP8x36, 15" Embedment, 9 ksi)

An axial load of approximately 95 kips was applied to the tip of Specimen C1. All flanges of the section began buckling between the 1.00 in. and the 2.00 in. displacement ranges. All flanges had fully buckled by the 2.50 in. displacement range. Failure of Specimen C1 was due to reduced lateral load capacity resulting from the fracturing of all flanges. Very minor damage (minor spalling, etc.) was observed in the concrete surrounding the pile head. Figure 4.47 presents the load-deflection curves for each displacement level. The complete set of load-deflection curves is presented in Figure 4.48.

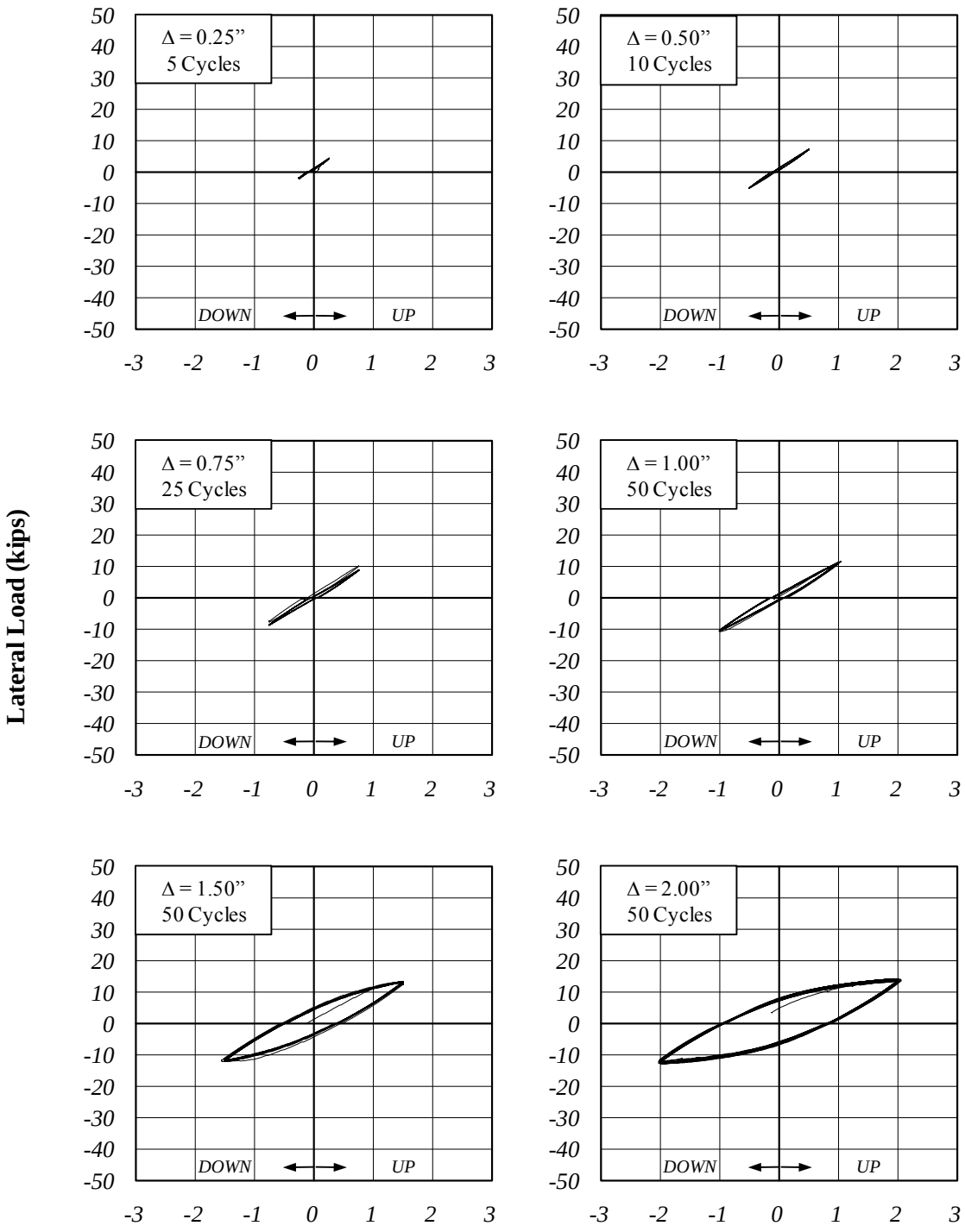

Figure 4.47: Specimen C1 – Load-Deflection Curves

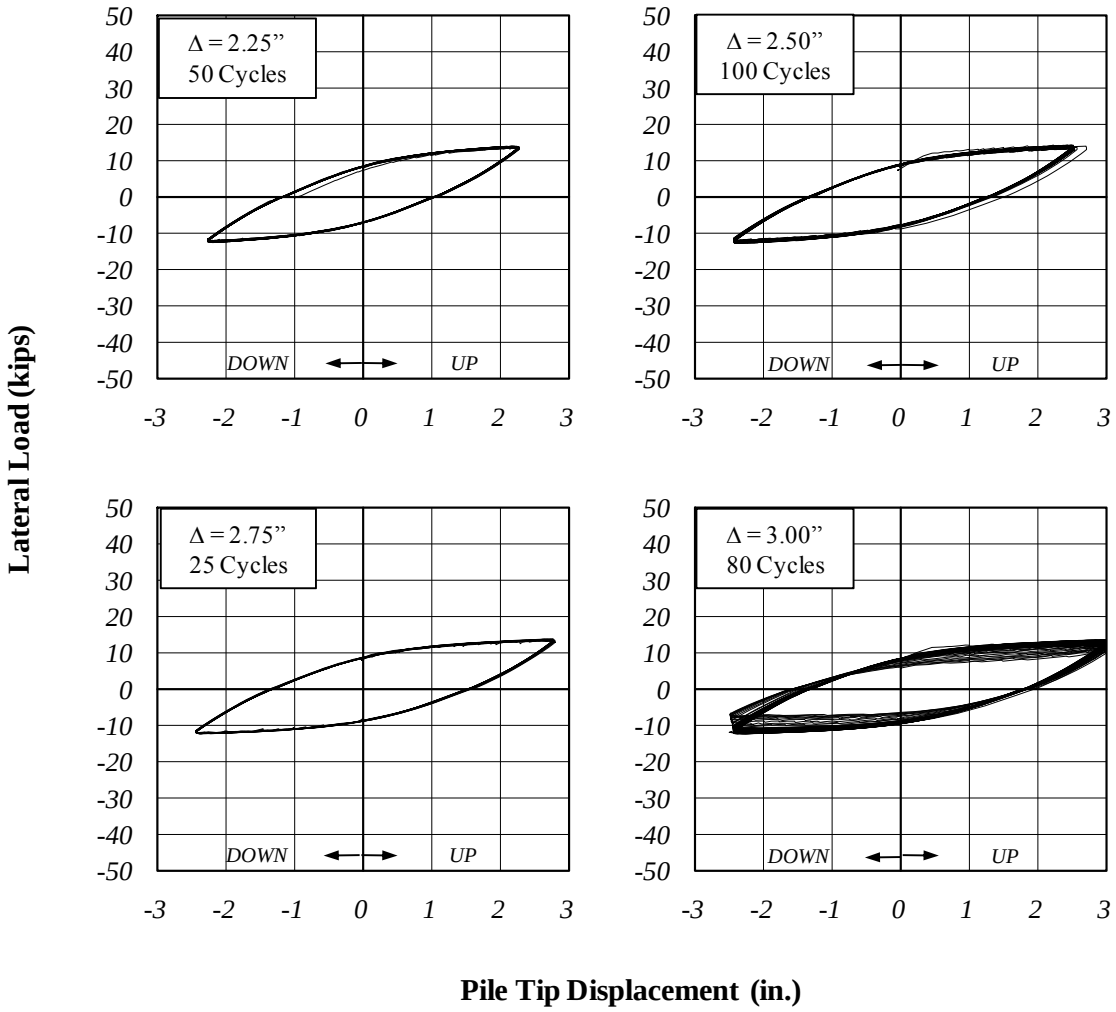

Figure 4.47 (continued): Specimen C1 – Load-Deflection Curves

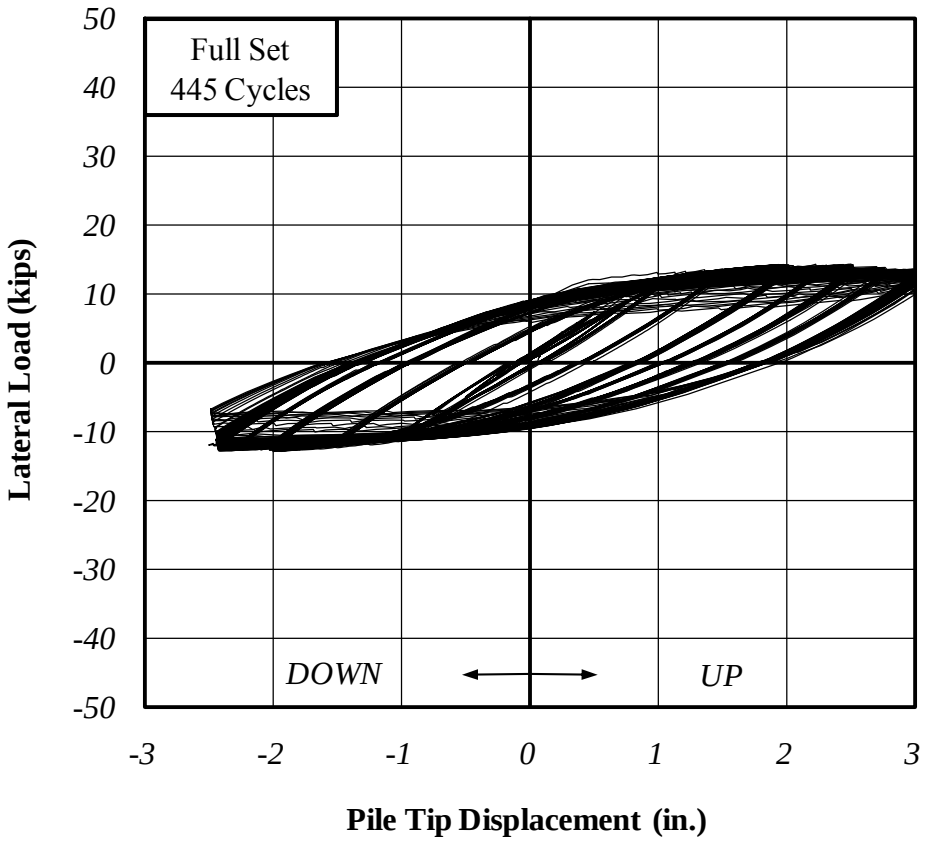

Figure 4.48: Specimen C1 – Complete Load-Deflection Curves

4.10.2 Specimen C4 (HP8x36, 15” Embedment, 18 ksi)

An axial load of approximately 190 kips was applied to Specimen C4. All flanges buckled by the 2.25 in. displacement range. Failure of Specimen C4 was due to loss of lateral load capacity due to severe buckling of all flanges and the web. Very minor damage (minor spalling, etc.) was observed in the concrete surrounding the pile head. Figure 4.49 presents the load-deflection curves for each displacement level. The complete set of load-deflection curves is presented in Figure 4.50.

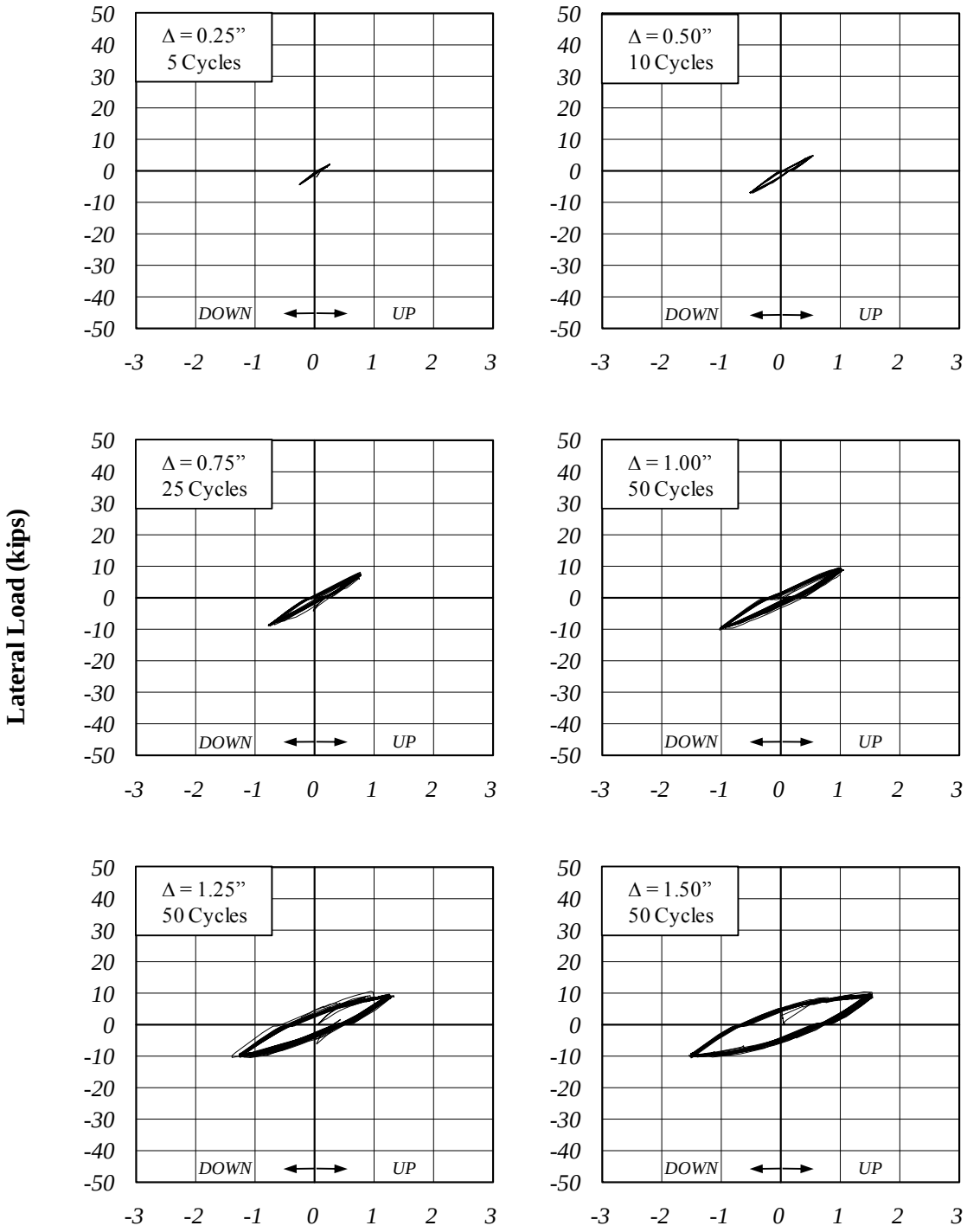

Figure 4.49: Specimen C4 – Load-Deflection Curves

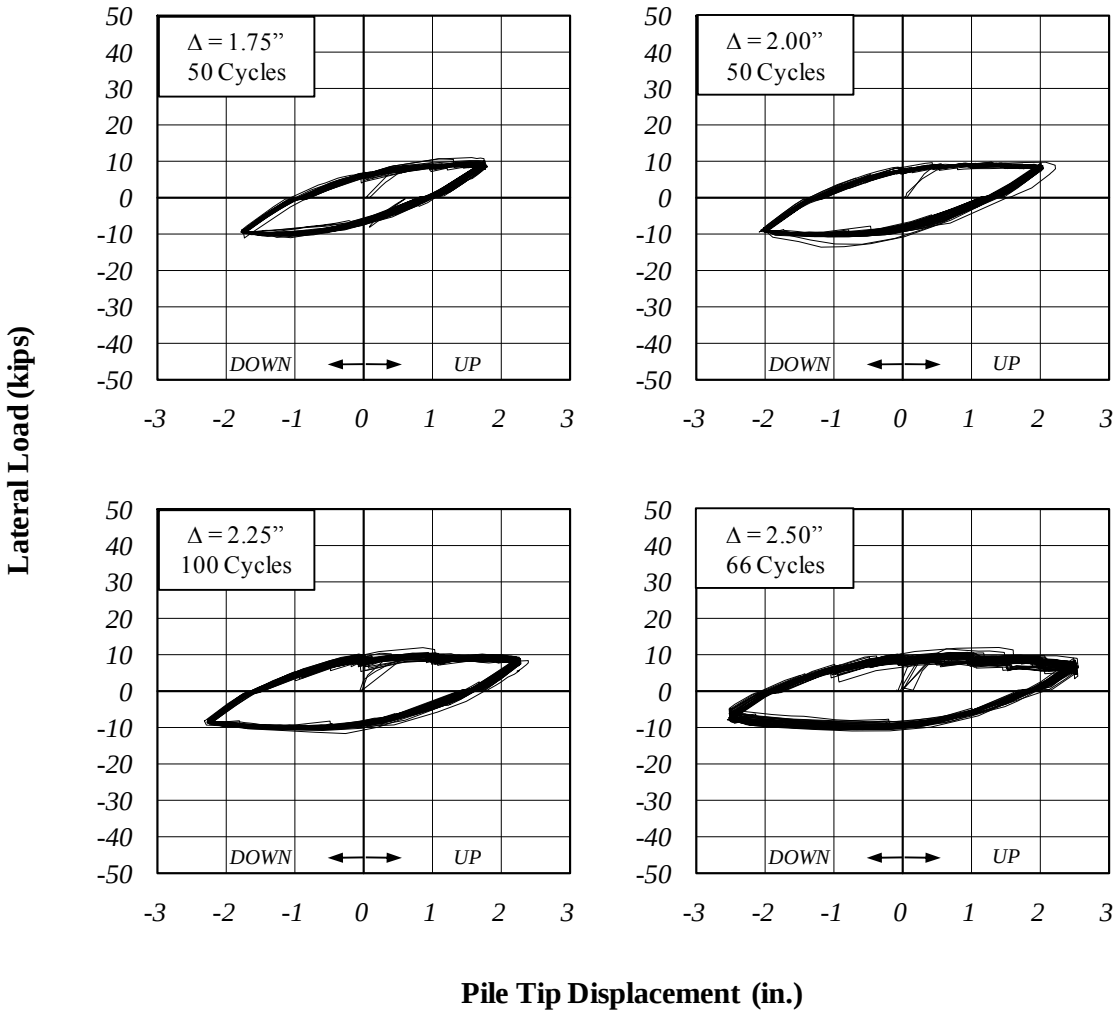

Figure 4.49 (continued): Specimen C4 – Load-Deflection Curves

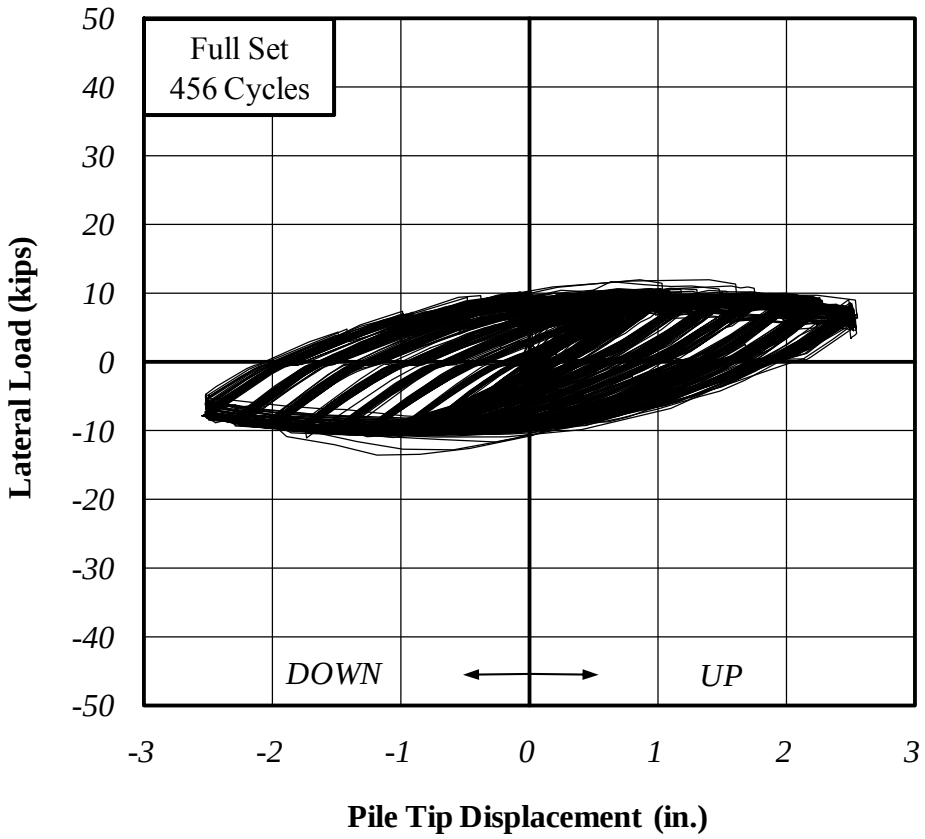

Figure 4.50: Specimen C4 – Complete Load-Deflection Curves

4.10.3 Specimen C5 (HP10x42, 15” Embedment, 9 ksi)

An axial load of approximately 112 kips was applied to Specimen C5. Failure of Specimen C5 was due to loss of lateral load capacity due to severe fracturing of all flanges. Minor damage (spalling, etc.) was observed in the concrete surrounding the pile head. Figure 4.51 presents the load-deflection curves for each displacement level. The complete set of load-deflection curves is presented in Figure 4.52.

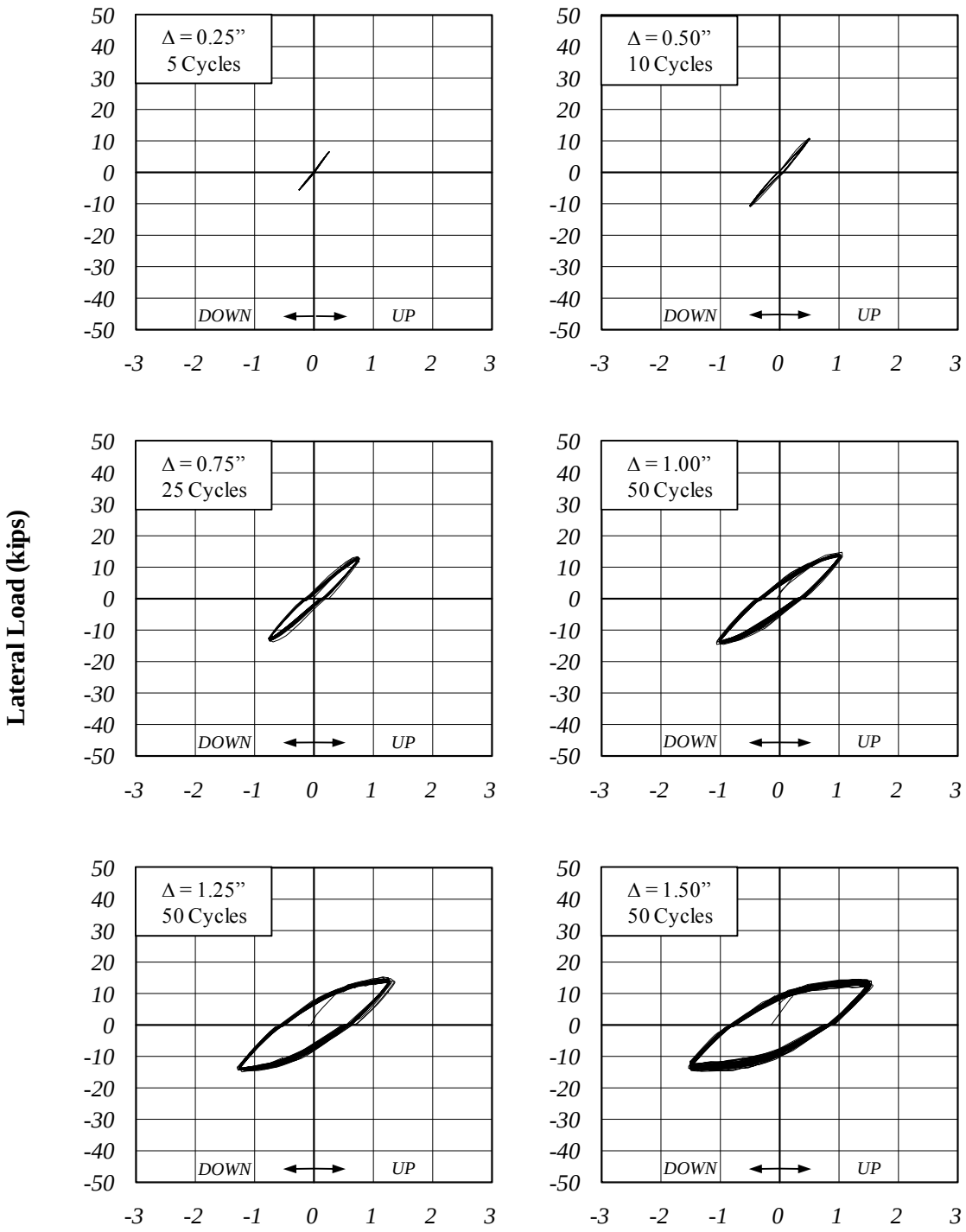

Figure 4.51: Specimen C5 – Load-Deflection Curves

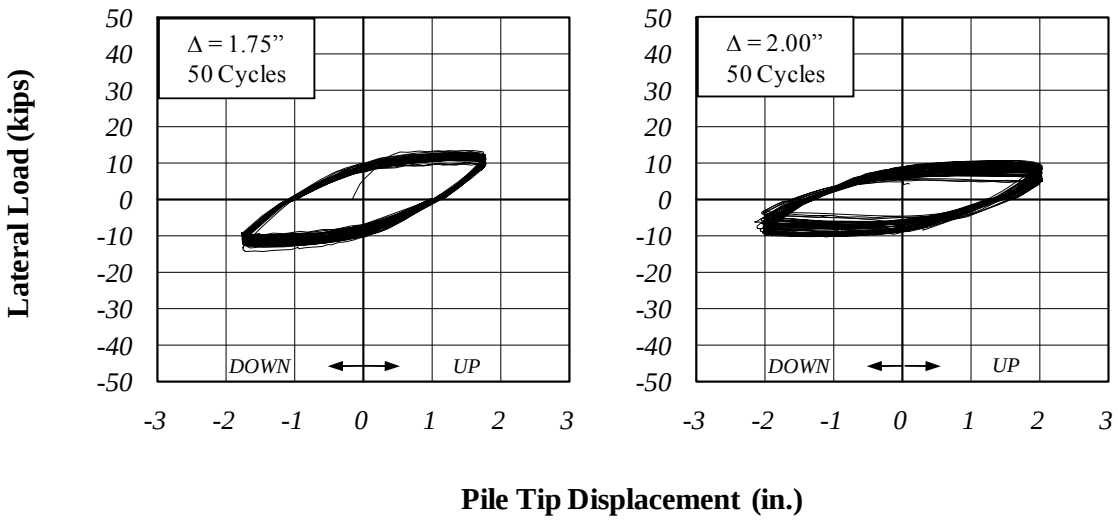

Figure 4.51 (continued): Specimen C5 – Load-Deflection Curves

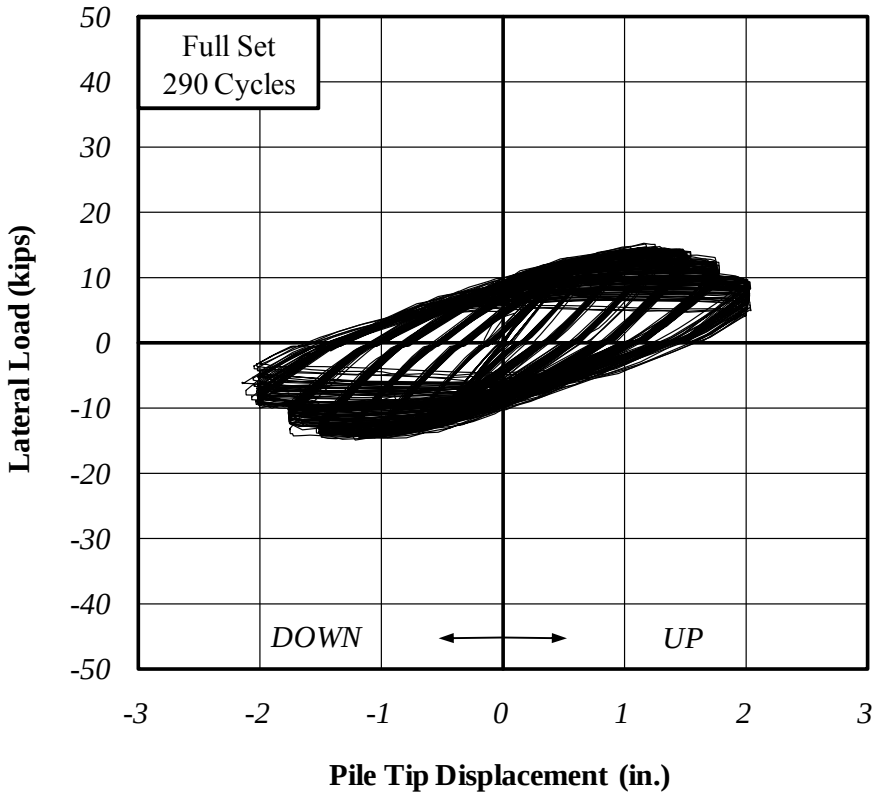

Figure 4.52: Specimen C5 – Complete Load-Deflection Curves

4.10.4 Specimen C6 (HP12x53, 15” Embedment, 9 ksi)

An axial load of approximately 140 kips was applied to Specimen C6. All flanges buckled during the 1.25 in. displacement range and all flanges had fractured by the end of the 1.75 in. displacement range. More severe damage was observed in the concrete surrounding the pile head for Specimen C6 than in C1, C4, and C5. Failure of Specimen C6 was due to a loss of lateral load capacity resulting from a combination of flange buckling, fracture of the flanges, and deterioration of the concrete surrounding the pile head. Figure 4.53 presents the load-deflection curves for each displacement level. The complete set of load-deflection curves is presented in Figure 4.54.

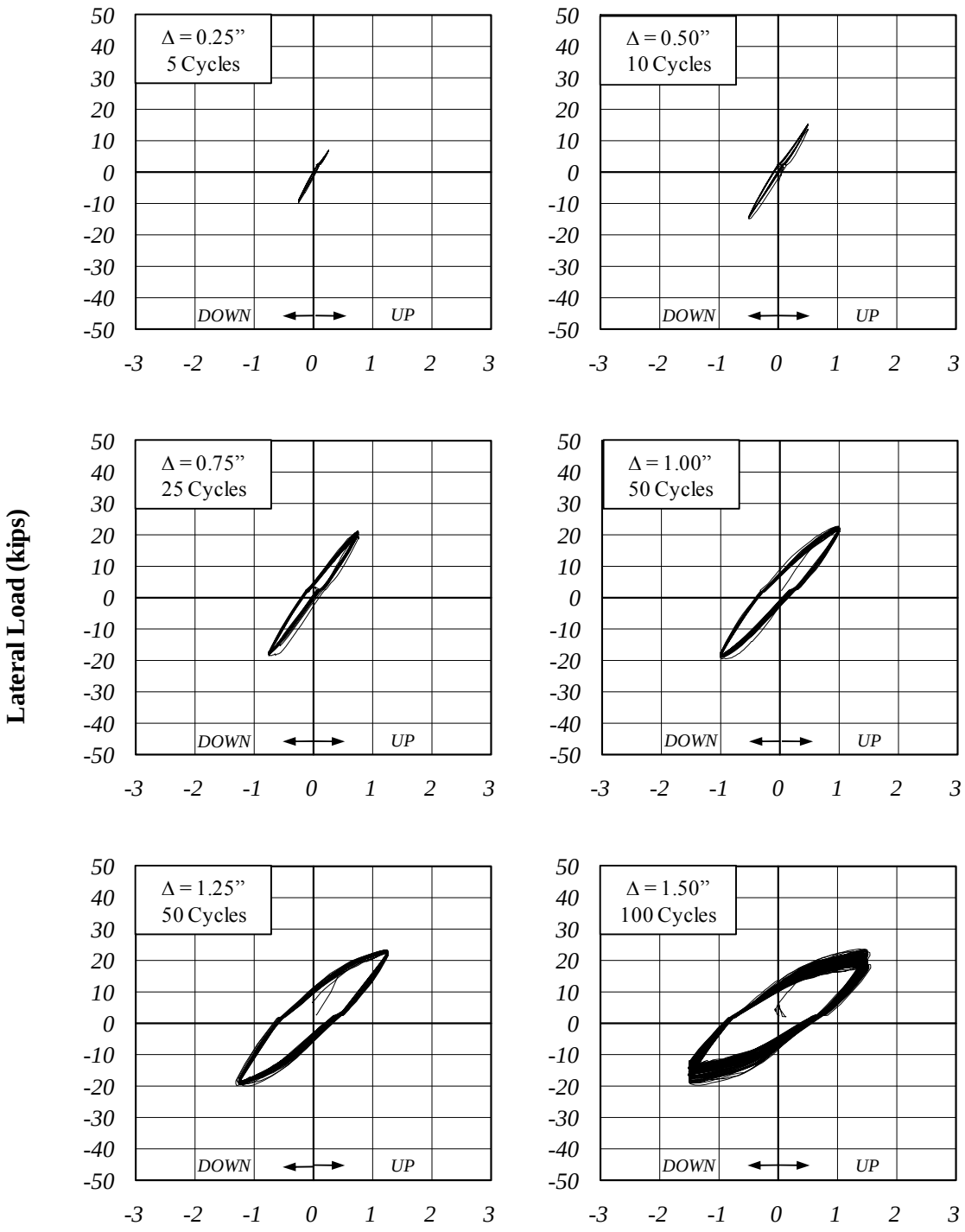

Figure 4.53: Specimen C6 – Load-Deflection Curves

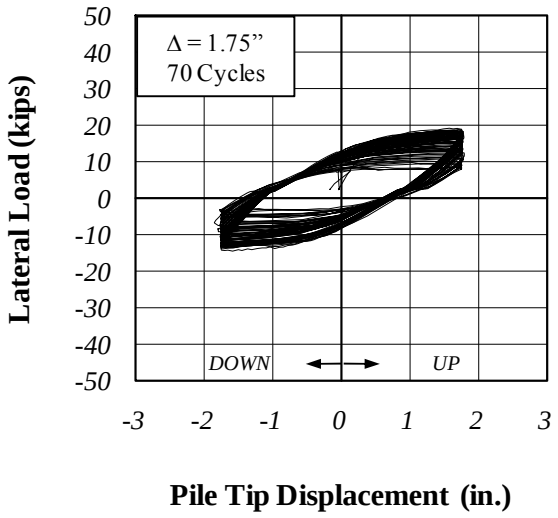

Figure 4.53 (continued): Specimen C6 – Load-Deflection Curves

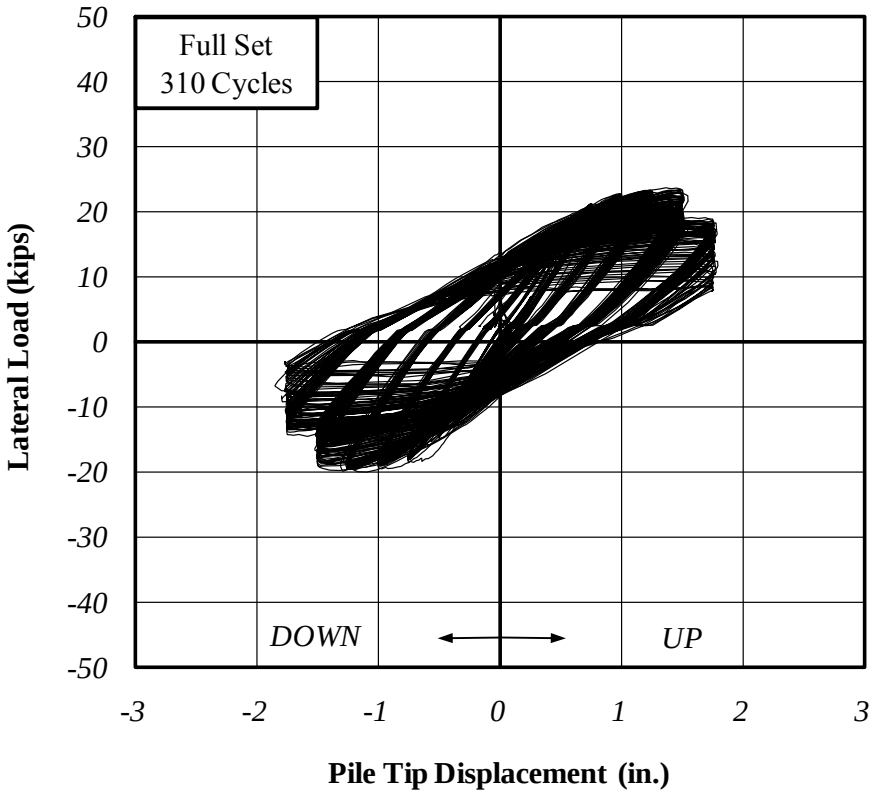

Figure 4.54: Specimen C6 – Complete Load-Deflection Curves

4.11 Evaluation of Results

Laboratory results were evaluated using two methods: construction of response envelopes and analytical modeling. Each method is described and the results are presented in the following sections.

4.11.1 Response Envelopes

A response envelope is constructed for each specimen by first isolating the endpoints of each load cycle (Figure 4.55). The envelope is then constructed by connecting the average lateral load at each displacement level (Figure 4.56). The envelope provides a clearer picture of the response than examining the entire history. It also allows for simpler comparison between specimens. The response curves for each specimen, including those of Chovichien, are presented as Figure 4.56 - Figure 4.66. The behavior of each group of specimens may then be examined using their response envelopes.

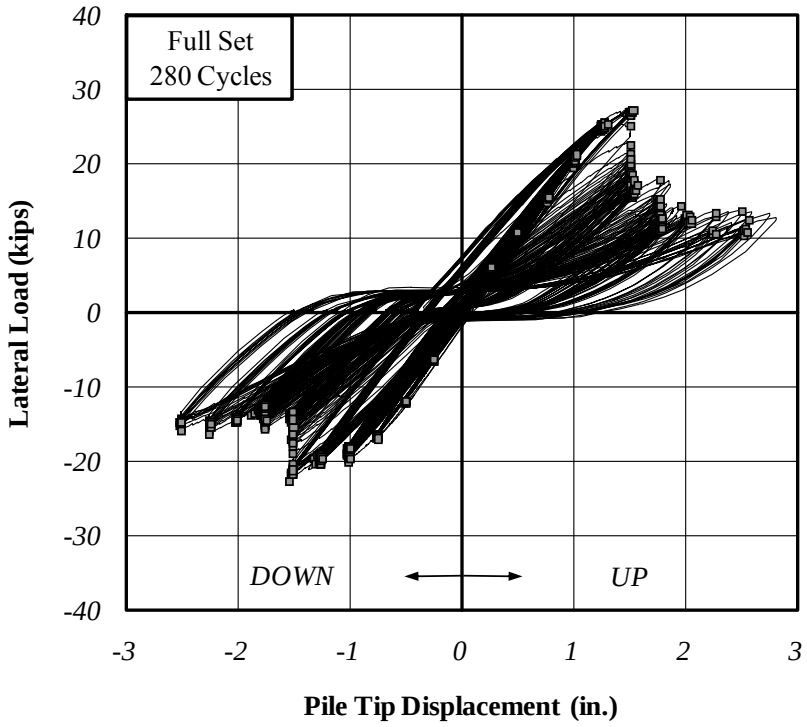

Figure 4.55: Development of Response Envelope (Specimen 1)

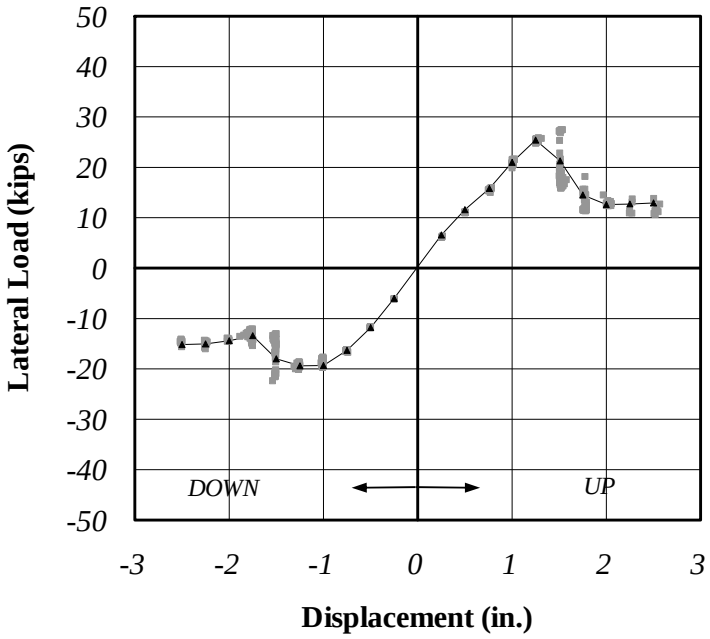

Figure 4.56: Response Envelope (Specimen 1)

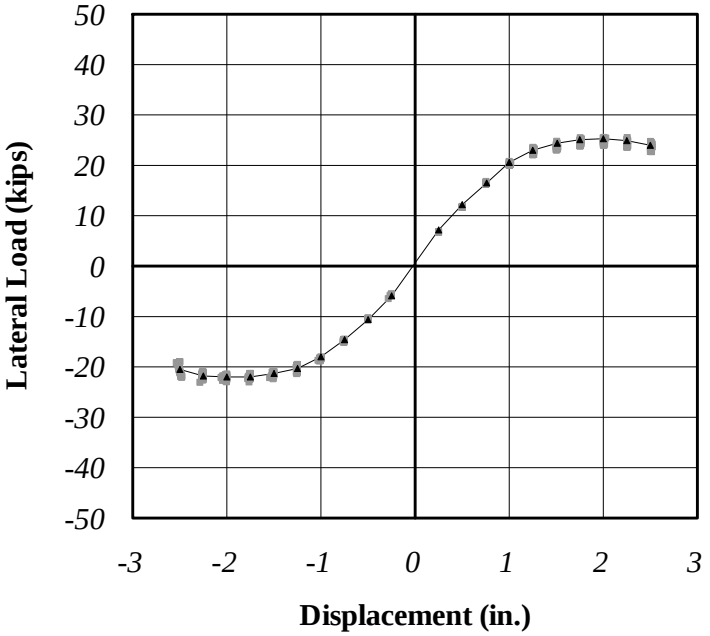

Figure 4.57: Response Envelope (Specimen 2)

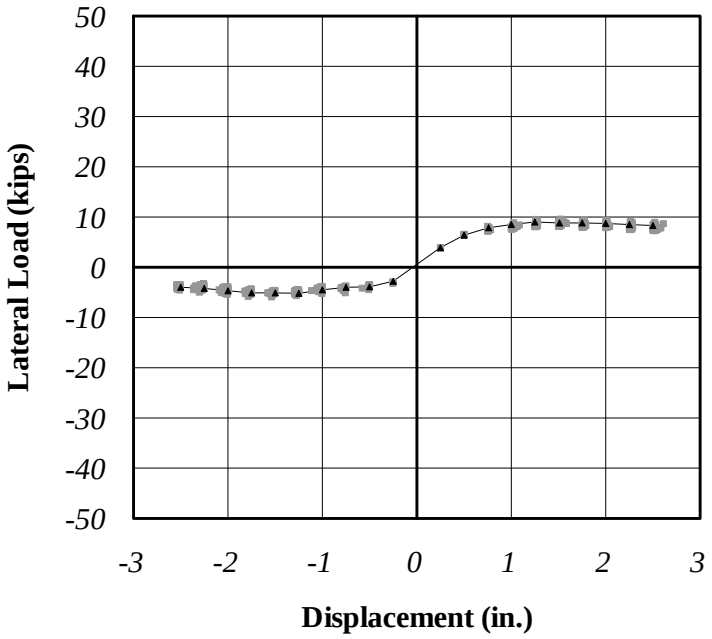

Figure 4.58: Response Envelope (Specimen 3)

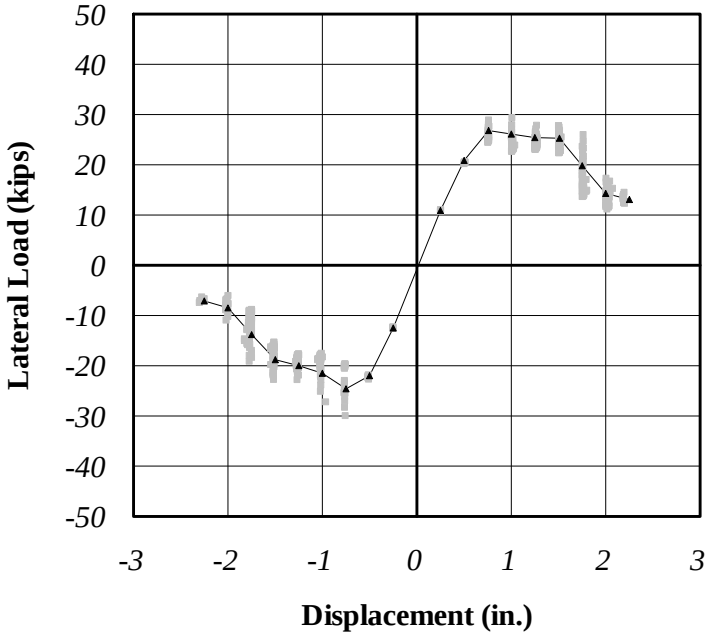

Figure 4.59: Response Envelope (Specimen 4)

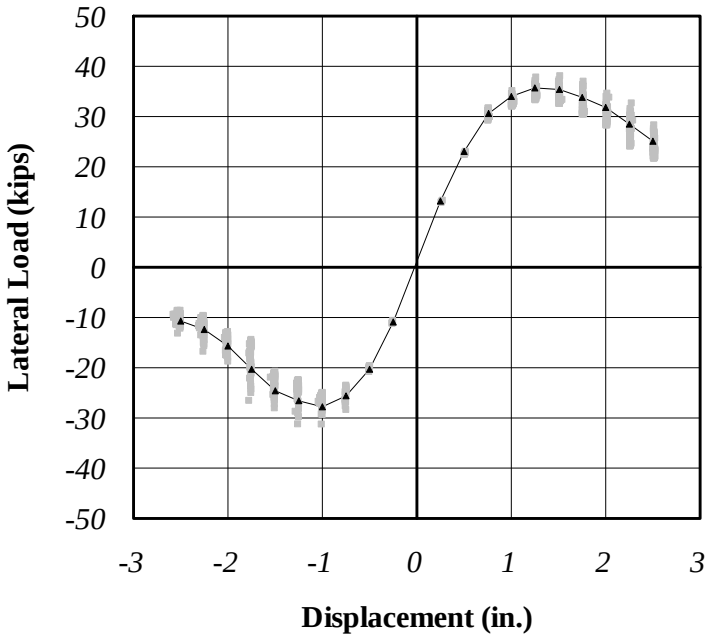

Figure 4.60: Response Envelope (Specimen 5)

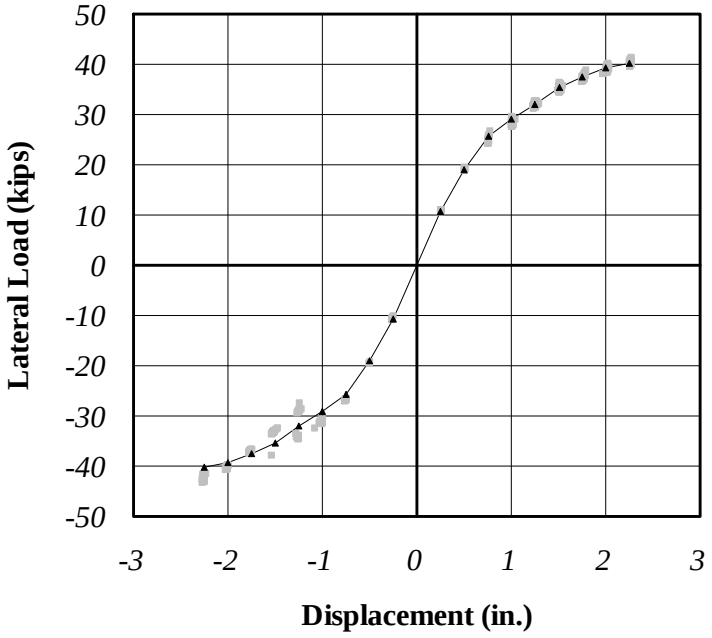

Figure 4.61: Response Envelope (Specimen 6)

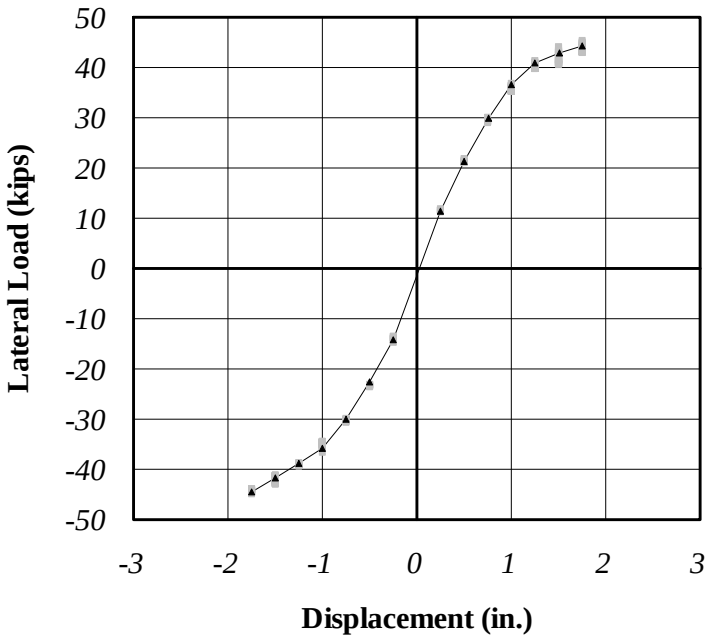

Figure 4.62: Response Envelope (Specimen 7)

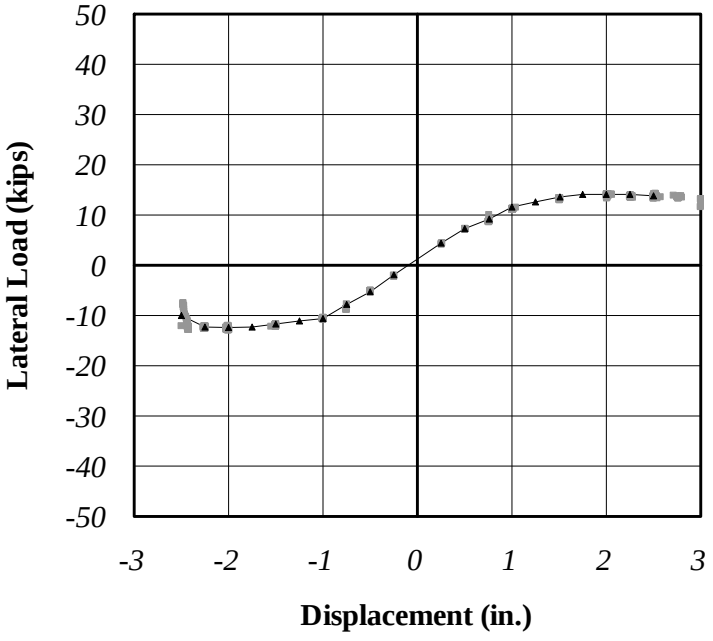

Figure 4.63: Response Envelope (Specimen C1)

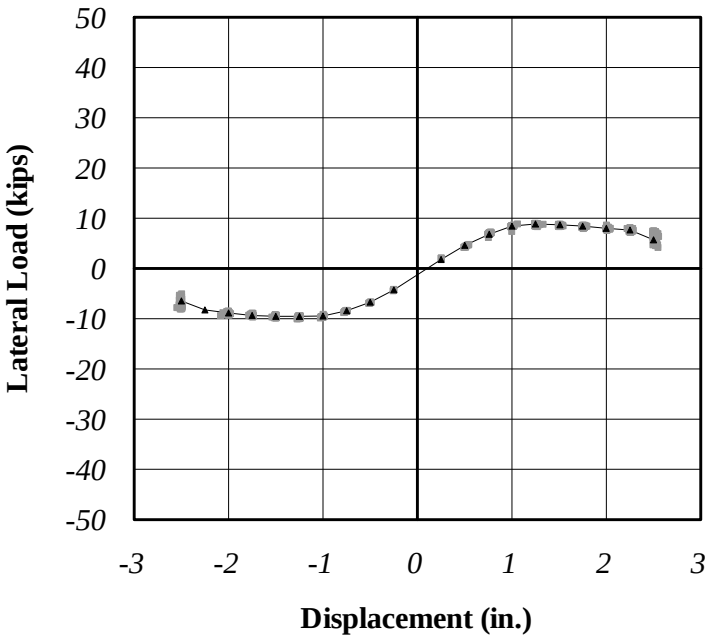

Figure 4.64: Response Envelope (Specimen C4)

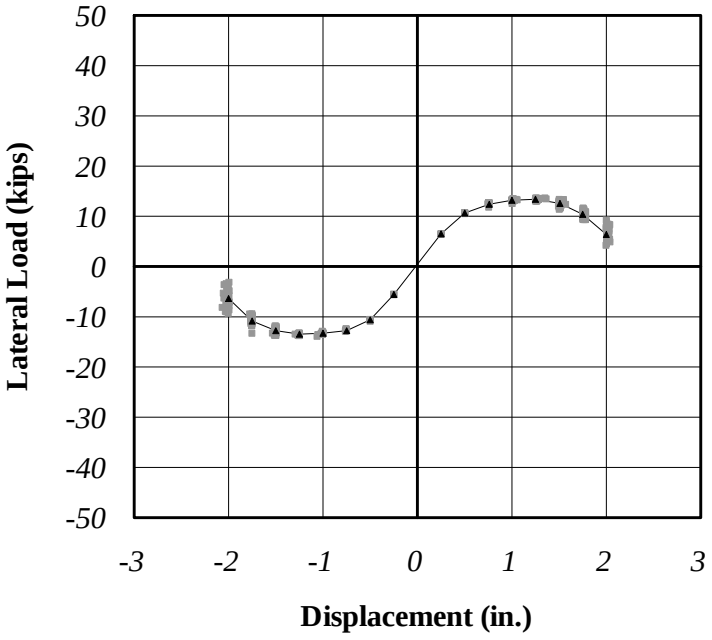

Figure 4.65: Response Envelope (Specimen C5)

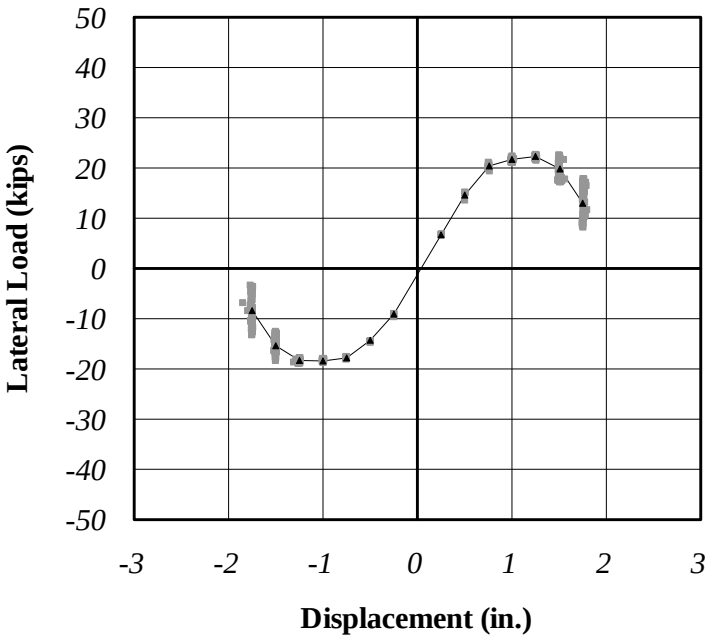

Figure 4.66: Response Envelope (Specimen C6)

4.11.1.1 Response Envelope: HP8x36

Two HP8x36 specimens were tested by Chovichien: C1 and C4. Both specimens had an embedment length of 15 in. These specimens were constructed to evaluate the effect of axial load. The axial load applied to C4 (18 ksi) was two times that applied to C1 (9 ksi). The response envelopes for these specimens are presented in Figure 4.67. The two specimens behaved similarly up to the 1.00 in. displacement level. Beyond this level, Specimen C4 began to diverge significantly from C1, especially in the positive (up) direction. Flange buckling was observed for both specimens at displacements beyond 1.00 in. The difference in behavior at these displacement levels is attributable to the extent of flange buckling in each specimen. Second-order effects due to axial load are more severe in Specimen C4, contributing to the different behavior. Specimens C1 and Specimen C4 demonstrated a decreased lateral load capacity at displacements above 2.25 in. and 1.50 in., respectively.

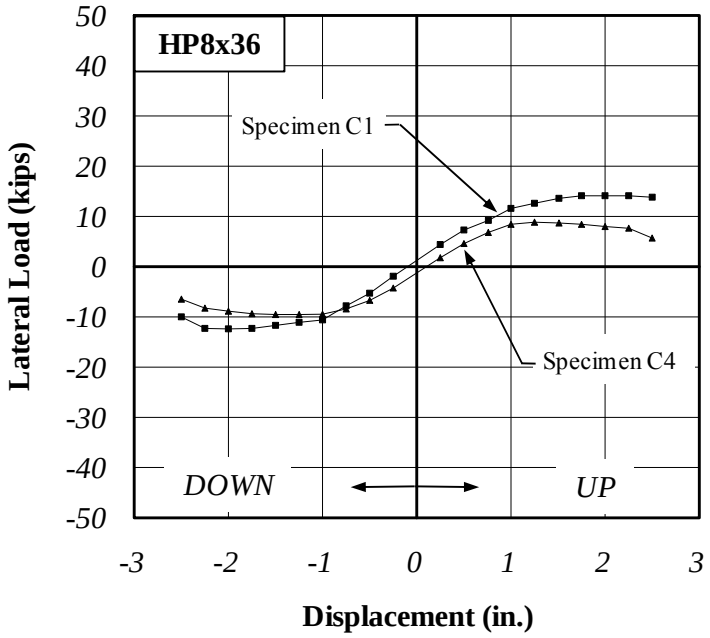

Figure 4.67: HP8x36 Response Envelopes

4.11.1.2 Response Envelope: HP10x42

A single HP10x42 section with an embedment length of 15 in. was tested by Chovichien. Its response envelope is presented in Figure 4.68. Specimen C5 demonstrated a decreased lateral load capacity at displacements above 1.25 in.

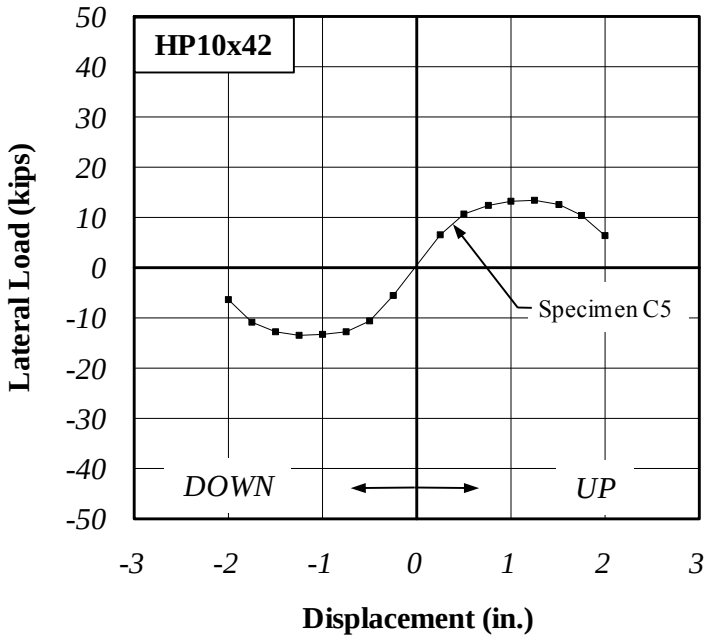

Figure 4.68: HP10x42 Response Envelope

4.11.1.3 Response Envelope: HP12x53

Three HP12x53 specimens were tested in the current series of tests. One HP12x53 specimen was tested by Chovichien. The response envelopes of all HP12x53 specimens are presented in Figure 4.69. Specimens 1 and C6 had embedment lengths of 15 in. and performed similarly. Specimens 1 (15 in. embedment) and 2 (24 in. embedment) performed nearly identically up to the 1.00 in. displacement level. Beyond the 1.00 in. displacement level Specimens 1 and C6 experienced a large decrease in lateral load capacity. Specimen 2, which had an embedment length of 24 in., achieved much higher lateral loads at displacement levels beyond 1.00 in. Specimen 3 featured the polystyrene "pin" connection. Specimen 3 exhibited a much lower stiffness than the other HP12x53 sections. It is noted that Specimens 1 and C6 approached the performance of the "pin" connection at large displacement levels, further illustrating the degradation in performance.

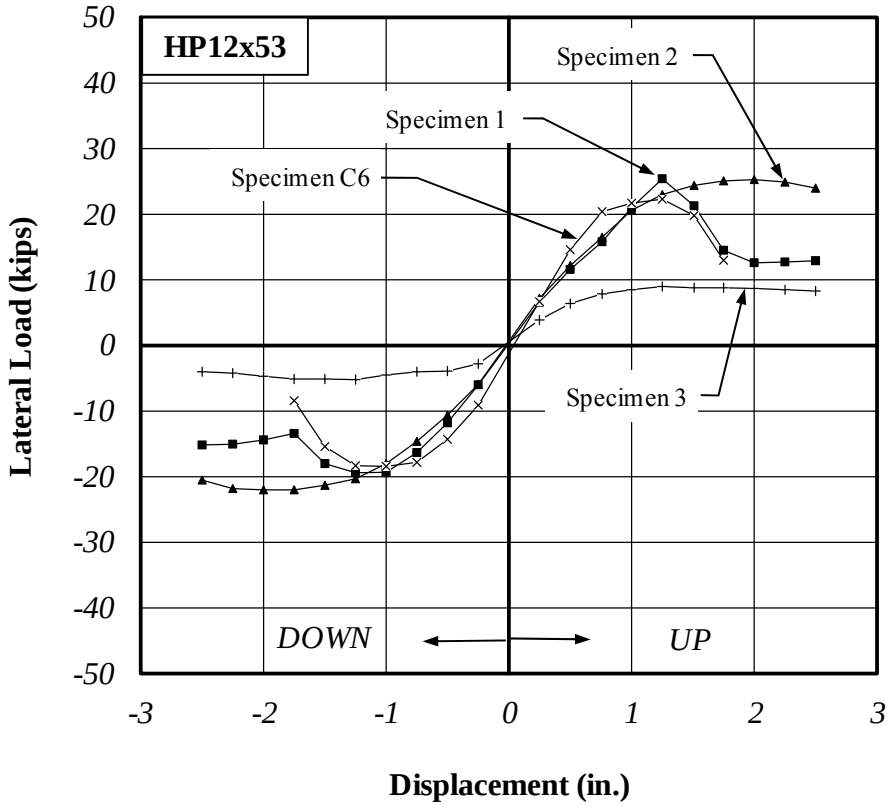

Figure 4.69: HP12x53 Response Envelopes

4.11.1.4 Response Envelope: HP14x89

Four HP14x89 specimens were tested in the current series of tests. The response envelopes are presented as Figure 4.70. All specimens behaved similarly at displacement levels below 0.75 in. Specimen 4 (15" embedment, no confinement) performed less favorably than Specimen 5 (24" embedment, no confinement). The effect is more pronounced in the positive (up) direction. Specimens 6 and 7 included confining reinforcement and generally performed better than Specimens 4 and 5 at displacement levels above 1.00 in. Specimen 7 included a larger amount of confining reinforcement than Specimen 6 and appears to have performed noticeably better. Specimens 4 and 5 experienced decreased lateral load resisting capacity at displacement levels above 1.25 in. Specimens 6 and 7 did not experience a decrease in lateral load capacity during testing.

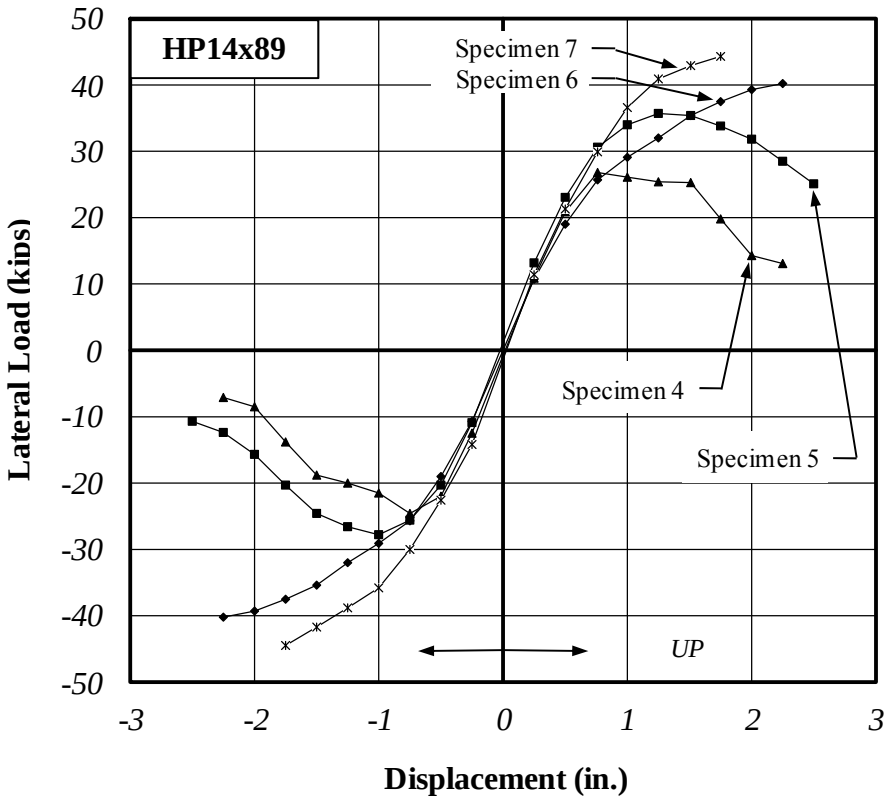

Figure 4.70: HP14x89 Response Envelopes

4.12 Conclusions

Several conclusions were drawn based on the results of the current series of tests along with those of Chovichien (2004). The effects of each test variable are discussed in the following sections followed by design recommendations.

4.12.1 Effect of Embedment Length

It was observed that increasing embedment length from 15 in. to 24 in. resulted in an increased lateral load capacity for both the HP12x53 and HP14x89 sections. With an embedment length of 15 in., the HP12x53 and HP14x89 sections experienced a decreased lateral load capacity at displacement levels of 1.00 in. and greater (Figure 4.69, Figure 4.70). When the embedment length was increased to 24 in., neither section experienced a decrease in lateral load capacity.

4.12.2 Pin Connection

The polystyrene "pin" connection (Specimen 3) performed well. After testing, the specimen showed no visible signs of damage. There was no observed "walking" or unintentional lateral movements of the pile head under cyclic loading. However, the lateral load resisting capability of the "pin" connection was substantially less than other specimens. This may or may not be significant depending on the design requirements of a particular project.

4.12.3 Effect of Confining Reinforcement

Confining reinforcement was used in Specimens 6 and 7. The specimens containing confining reinforcement reached significantly higher lateral loads than those without confining reinforcement. The specimens containing confining reinforcement had crack patterns similar to those observed in specimens with no confining reinforcement. However, the specimens which contained confining reinforcement had consistently smaller crack widths. In Specimen 7, the confining reinforcement increased the strength of the section enough to force a flexural crack to form at the base of the cantilever section. This failure mechanism should be considered in the design of the abutment. In

general, the addition of spiral reinforcement increased the lateral load strength and displacement capacity of the connection by controlling crack width.

4.13 Recommendations for Analysis and Design

Based on the results of the laboratory investigation, several recommendations for analysis and design are made. To develop these recommendations, however, it is important to relate displacements measured in the laboratory to the field displacements of the abutment.

4.13.1 Relationship of Laboratory and Field Displacements

In the laboratory, displacements of the pile tip were measured with respect to the fixed abutment. As discussed earlier, the length of pile selected for use in the laboratory represents the approximate location of the inflection point of the pile in the field. If the abutment was unable to rotate, ignoring the effect of the soil surrounding the pile, field displacements would correspond to exactly 2 times the laboratory displacements (Figure 4.71a). Because the abutment is able to rotate to some degree, the field displacements are expected to be greater than 2 times the laboratory displacements (Figure 4.71b). It is therefore considered conservative to estimate the field displacements as 2 times the laboratory displacements. Using this relationship, two limiting displacements were established: the zero-damage displacement limit and the acceptable damage displacement limit. For purposes of this report, "damage" is defined as a loss of load carrying capacity. Both damage limits are discussed in the following sections.

4.13.2 Zero-damage Displacement Limit

The zero-damage displacement limit was defined as the displacement below which the test specimen was able to maintain lateral and axial load carrying capacity. Based on the test results, a laboratory displacement level of approximately 1 in. was selected as the zero-damage displacement limit. No test specimen experienced a decreased lateral or axial load capacity at laboratory displacements below 1 in. Some test specimens were able to go beyond the 1 in. displacement level with no decrease in capacity; particularly those with increased embedment length and confining

reinforcement. However, the 1 in. displacement level was selected because it is conservative and also represents current INDOT construction (with 15 in. embedment). Based on the previous discussion, a laboratory deflection of 1 in. corresponds to a field displacement of approximately 2 in. Therefore, on the basis of laboratory testing, it is estimated that integral abutments constructed using current INDOT details can experience a longitudinal displacement of approximately 2 in. without experiencing a decreased lateral or axial load carrying capacity of the abutment-pile connection.

4.13.3 Acceptable-Damage Displacement Limit

The acceptable-damage limit was defined as the displacement above which the abutment-pile connection experienced a decrease in both axial and lateral load carrying capacity. Based on the test results, a laboratory displacement level of approximately 2 in. was selected as the acceptable-damage displacement limit. As discussed previously, a laboratory deflection of 2 in. corresponds to a field displacement of approximately 4 in. Therefore, on the basis of laboratory testing, it is estimated that integral abutments constructed using current INDOT details (with 15 in. embedment) can experience a longitudinal displacement of approximately 4 in. without experiencing a decrease in axial load carrying capacity (< 5% decrease) of the abutment-pile connection. For displacements between the zero-damage and acceptable-damage limits, the abutment-pile connection may experience decreased lateral load carrying capacity but will be able to maintain axial load (< 5% decrease).

4.13.4 Recommendations for Analytical Investigation

The zero and acceptable damage limits discussed in the previous sections were developed with current INDOT design details in mind. They are based on the lower-bound performance of the test specimens, which corresponds to the current details. These limits could be increased, if necessary, by incorporating the alternate details tested in the laboratory investigation (increased embedment length, “pin” detail, or confining reinforcement). An analytical investigation was then performed to estimate the seismic displacements of the abutment to evaluate the adequacy of the current details based on

the established displacement limits. The details of the analytical investigation are provided in Chapter 5.

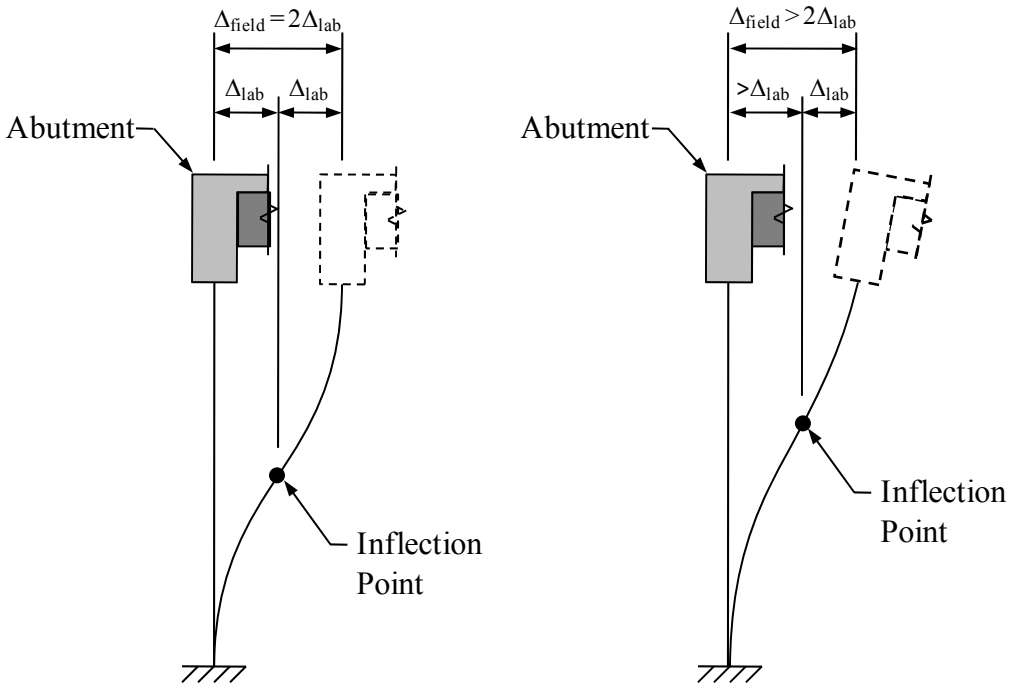

(a) Fixed Abutment *(b) Abutment with Rotation*

Figure 4.71: Laboratory versus Field Displacements

CHAPTER 5: ANALYTICAL INVESTIGATION

5.1 Introduction

An analytical investigation was conducted to estimate the longitudinal displacements of an integral abutment during a seismic event. Displacements were computed based on the design ground motions developed in Chapter 2. Portions of the analytical model were calibrated to the field results discussed in Chapter 3. The computed seismic displacements are compared to the allowable displacements developed based on laboratory experiments discussed in Chapter 4.

5.2 Modeling Approach

A series of detailed two-dimensional models were constructed using SAP2000 v9. The two-dimensional models represent the bridge, including the foundation piles, as a portal frame. The model is fixed at the base of the piles. The soil surrounding the piles and behind the abutments is modeled as a series of non-linear spring elements. Intermediate bridge piers are modeled as roller supports. This assumption is conservative for the estimation of abutment displacements and represents typical construction with the use of elastomeric bearings. A typical two-dimensional bridge model is shown in Figure 5.1. The model geometry and properties of each element of the two-dimensional model are discussed in the following sections.

5.2.1 Geometry

Five bridge lengths were used in this investigation: 200 ft, 400 ft, 600 ft, 800 ft, and 1000 ft. The span lengths for each case were 60-70 ft. An abutment height of 10 ft and pile length of 40 ft was used for all cases. The selected span lengths, abutment heights,

and pile lengths represent typical construction. The geometry and support conditions of these models are summarized in Figure 5.2. These layouts are considered the control geometry. The effect of varying span length will also be considered. The superstructure was discretized into 10 ft elements to ensure a reasonable distribution of mass. To allow the incorporation of soil springs, the abutments were discretized into 1 ft elements. Similarly, the piles were discretized into 1 ft elements for the top 10 ft of pile and 2 ft elements for the remaining 30 ft.

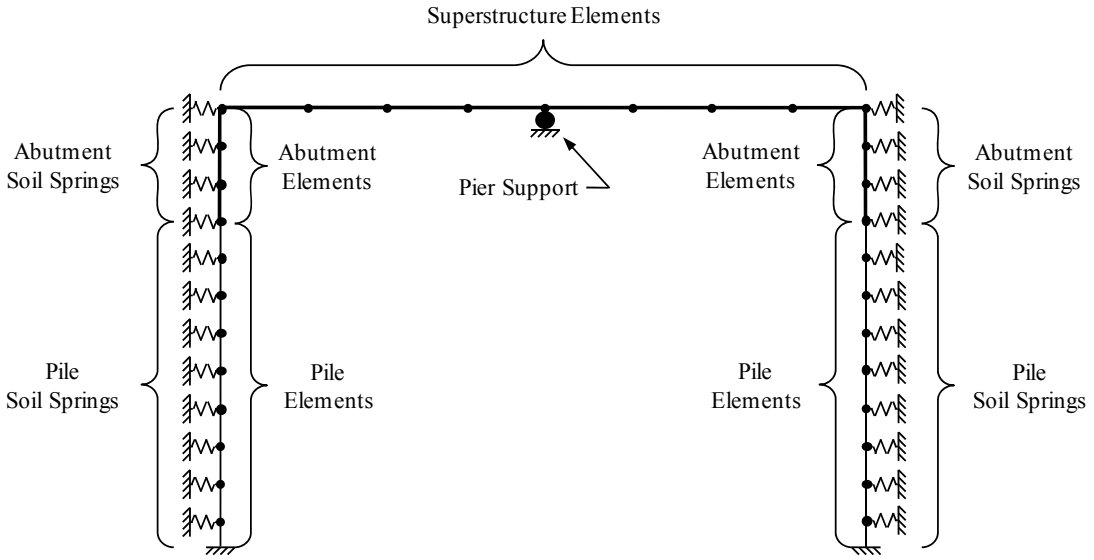

Figure 5.1: General Two-Dimensional Bridge Model

5.2.2 Superstructure Element Properties

The superstructure elements were modeled after the SR18 Bridge discussed in the field investigation which represents a fairly typical integral abutment bridge. The idealized cross-section used in the analysis is shown in Figure 5.3. Accordingly, the superstructure elements have a moment of inertia of 4.56×10^6 in.^{4} and a cross-sectional area of 9,100 in.^{2} The modulus of elasticity for the superstructure elements was taken as 3,600 ksi which corresponds to a concrete strength of 4000 psi. As mentioned previously, the superstructure elements have a length of 10 ft.

5.2.3 Abutment Element Properties

The abutment was assumed to be 10 ft high, 50 ft wide, and 3 ft deep corresponding to a moment of inertia of 2.33 x 10^6 in^4 and a cross-sectional area of 21,600 $in.^2$ The modulus of elasticity of the abutment elements was taken as 3,600 ksi. The abutment was modeled with 1 ft elements to allow the incorporation of the abutment-soil springs.

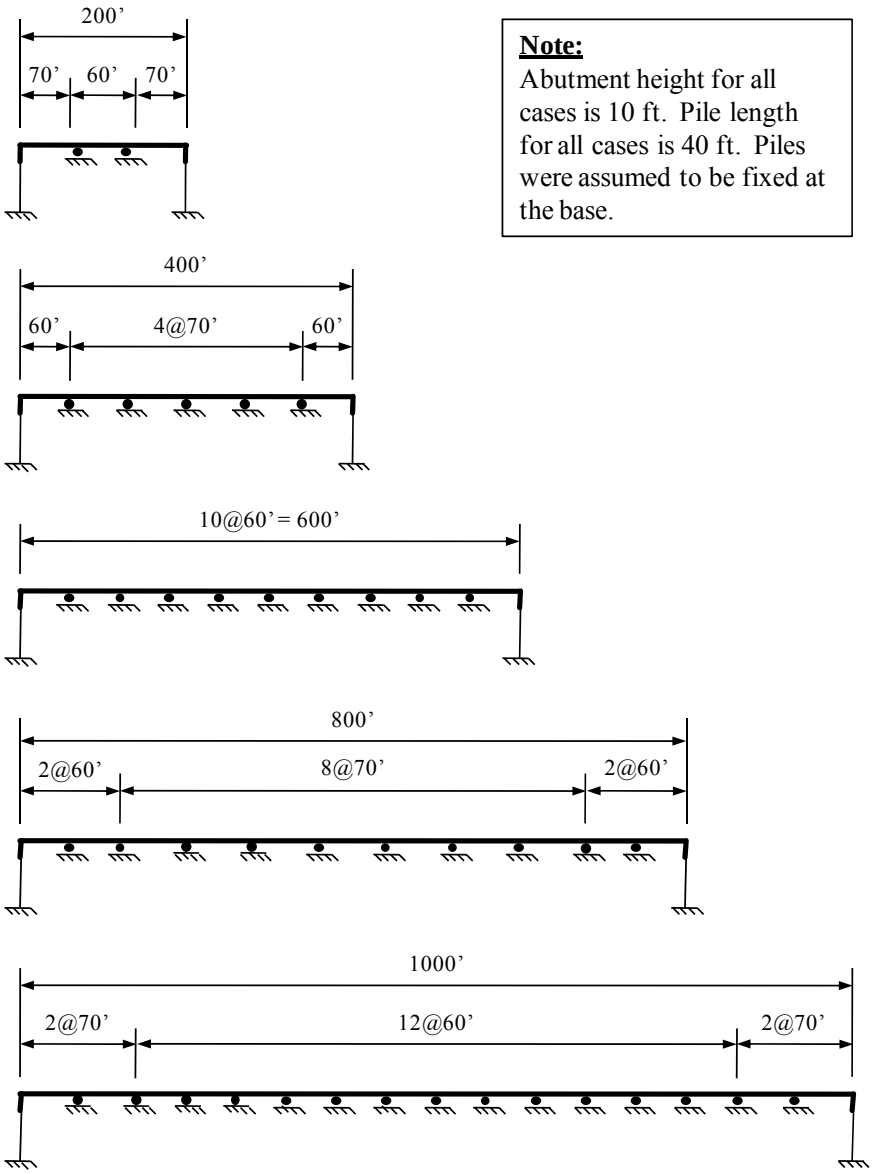

Note:
Abutment height for all cases is 10 ft. Pile length for all cases is 40 ft. Piles were assumed to be fixed at the base.

Figure 5.2: Analysis Geometry

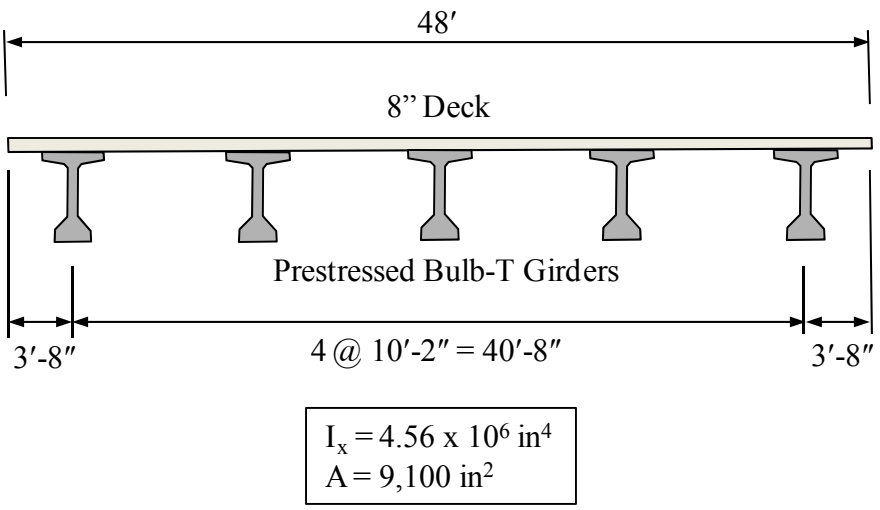

Figure 5.3: Superstructure Element Properties

5.2.4 Pile Element Properties

For the pile elements, it was assumed that the abutment was supported on a single row of 10 – HP12X53 piles oriented in weak-axis bending. The HP12X53 section is the smallest typically used in integral abutment construction in Indiana and represents a lower bound in terms of lateral pile stiffness. The moment of inertia and cross-section area for a single HP12X53 pile are 127 in.^{4} and 15.5 in.^{2}, respectively. The row of ten piles is then lumped together in the two-dimensional model resulting in a pile element with a moment of inertia and cross-sectional area of 1,270 in.^{4} and 155 in.^{2}, respectively. The piles are modeled using 1 ft elements for the first 10 ft of pile and 2 ft elements for the remaining 30 ft.

5.2.5 Pile-Soil Spring Properties

The pile-soil springs were modeled using non-linear link elements with elastic-plastic force-displacement characteristics as shown in Figure 5.4. The values for k and P_u were computed using the following expressions which are based on the recommendations of Greimann (1984):

$$k = \left(\frac{J\gamma}{1.35}\right) \cdot z \cdot s \tag{5.1}$$

$$P_u = \left(3\gamma B k_p\right) \cdot z \cdot s \tag{5.2}$$

$$\Delta_u = \frac{P_u}{k} = \frac{4.05 B k_p}{J} \tag{5.3}$$

where:

k = spring stiffness (lb/ft)

P_u = maximum spring force (lb)

Δ_u = displacement associated with P_u (ft)

J = 200 for loose sand ($\phi = 30°$)

= 600 for medium sand ($\phi = 35°$)

= 1500 for dense sand ($\phi = 40°$)

γ = unit weight of soil (lb/ft^3)

z = depth below ground surface (ft)

s = spring spacing (ft)

B = pile width (ft)

k_p = coefficient of passive earth pressure

= $\tan^2\left(45° + \frac{\phi}{2}\right)$

It may be seen from Eq (5.1) and Eq (5.2) that the spring stiffness and maximum spring force increase linearly with depth. However, Δ_u depends on the angle of internal friction, ϕ, and pile width, B, and does not vary with depth. The pile-soil spring parameters computed according to these relationships are given in Table 5.1. The values presented in this table are for a single HP12X53 pile. Because ten piles are considered in the analysis, the table values are multiplied by 10 for use in the two-dimensional models.

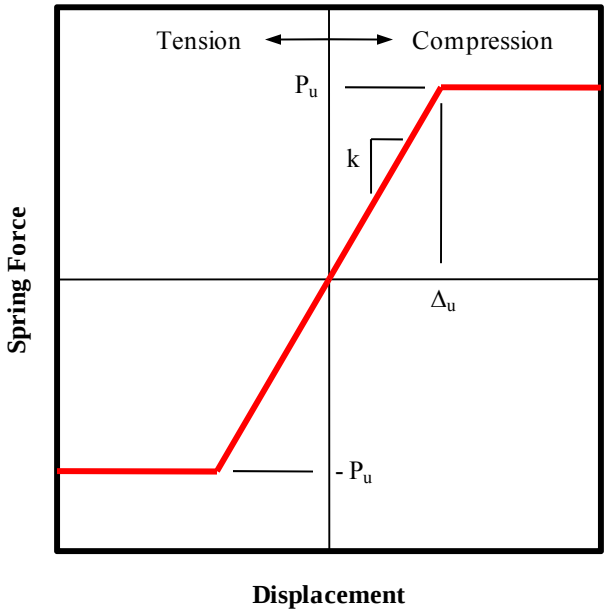

Figure 5.4: Typical Pile-Soil Spring

Table 5.1: Pile-Soil Spring Parameters

		Loose Δ_u = 0.717 in.		Medium Δ_u = 0.294 in.		Dense Δ_u = 0.147 in.	
z (ft)	s (ft)	k (kips/in)	P_u (kips)	k (kips/in)	P_u (kips)	k (kips/in)	P_u (kips)
1	1.5	2.2	1.6	6.7	2.0	16.7	2.4
2	1.0	3.0	2.1	8.9	2.6	22.2	3.3
3	1.0	4.4	3.2	13.3	3.9	33.3	4.9
4	1.0	5.9	4.2	17.8	5.2	44.4	6.5
5	1.0	7.4	5.3	22.2	6.5	55.6	8.1
6	1.0	8.9	6.4	26.7	7.8	66.7	9.8
7	1.0	10.4	7.4	31.1	9.1	77.8	11.4
8	1.0	11.9	8.5	35.6	10.5	88.9	13.0
9	1.0	13.3	9.6	40.0	11.8	100.0	14.7
10	1.5	22.2	15.9	66.7	19.6	166.7	24.4
12	2.0	35.6	25.5	106.7	31.4	266.7	39.1
14	2.0	41.5	29.7	124.4	36.6	311.1	45.6
16	2.0	47.4	34.0	142.2	41.8	355.6	52.1
18	2.0	53.3	38.2	160.0	47.0	400.0	58.6
20	2.0	59.3	42.5	177.8	52.3	444.4	65.1
22	2.0	65.2	46.7	195.6	57.5	488.9	71.6
24	2.0	71.1	51.0	213.3	62.7	533.3	78.1
26	2.0	77.0	55.2	231.1	67.9	577.8	84.7
28	2.0	83.0	59.5	248.9	73.2	622.2	91.2
30	2.0	88.9	63.7	266.7	78.4	666.7	97.7
32	2.0	94.8	68.0	284.4	83.6	711.1	104.2
34	2.0	100.7	72.2	302.2	88.8	755.6	110.7
36	2.0	106.7	76.5	320.0	94.1	800.0	117.2
38	2.0	112.6	80.7	337.8	99.3	844.4	123.7
40	2.0	118.5	85.0	355.6	104.5	888.9	130.2

Note : Table values are for a single HP12X53 section oriented in weak-axis bending

5.2.6 Abutment-Soil Spring Properties

The abutment-soil springs were modeled using non-linear link elements. These elements have an elastic-plastic, force-displacement relationship in compression and zero force in tension. A typical force-displacement relationship is shown in Figure 5.5. This force-displacement relationship is used because the backfill material provides resistance as the abutment moves toward the soil but not as the abutment moves away from the backfill material. The ultimate capacity of the abutment-soil springs was based on the Rankine passive earth pressure and the geometry of the model. Accordingly, the ultimate capacity for each spring was computed as:

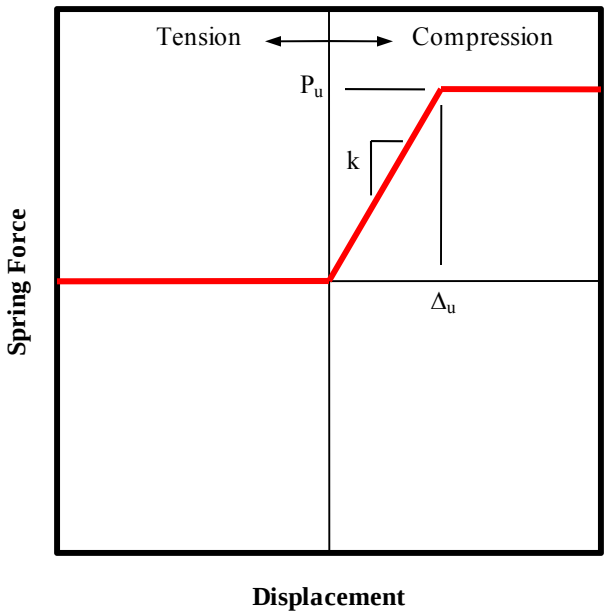

Figure 5.5: Typical Abutment-Soil Spring

$$P_u = (k_p \gamma z) \cdot w \cdot s$$
$$P_u = \left(\tan^2\left(45° + \frac{\phi}{2}\right)\gamma z\right) \cdot w \cdot s \quad (5.4)$$

where:

w = abutment width (ft)

s = spring spacing (ft)

Two approaches were taken for the calculation of k and Δ_u: estimating Δ_u based on common design assumptions and then computing k (displacement approach), and estimating k based on the field investigation and computing Δ_u (stiffness approach). The details of each approach are discussed in the following subsections and the values used in the two-dimensional model are shown in Table 5.2.

5.2.6.1 Displacement Approach

It is commonly accepted that it takes much more movement for a mass of soil to achieve a passive state than an active state. However, the magnitude of movement required to reach the passive state is not well understood. It is commonly assumed in design that the required movement is 2% of the wall height. This value also appears in the AASHTO Specifications (AASHTO 2002, 2004). For the models used in this investigation, it was assumed that the maximum spring force was reached at a displacement, Δ_u = 0.02(10 ft) = 0.2 ft or 2.4 in.

5.2.6.2 Stiffness Approach

The abutment-soil spring stiffnesses were also estimated based on the measured subgrade modulus, n_h, discussed in Chapter 3. It was shown in Chapter 3 that the measured subgrade modulus was approximately 11 ksf/in. at the level of the earth pressure cells located 8.75 ft below the ground surface. For the stiffness approach it was assumed that the subgrade modulus varied linearly from a value of zero at the ground surface (z = 0) to a value of 11 ksf/in. at the location of the earth pressure cells (Figure 5.6). The subgrade modulus at any depth may then be expressed as:

$$n_h = \left(11\frac{ksf}{in}\right)\left(\frac{z}{8.75}\right) \tag{5.5}$$

where:

z = depth below ground surface (ft)

s = spring spacing (ft)

The spring stiffness may then be computed as:

$$k = n_h \cdot w \cdot s \tag{5.6}$$

As can be seen in Table 5.2, the spring stiffnesses computed by this approach are approximately 7 times stiffer than those computed from the displacement approach. Both

approaches will be used to the analyses to determine the influence on overall abutment response. Also shown in the table are spring stiffness values for a subgrade modulus of 5.5 ksf/in. and 22 ksf/in. representing one-half and twice the measured value respectively. These values will be used to determine the sensitivity of the model to the value of subgrade modulus.

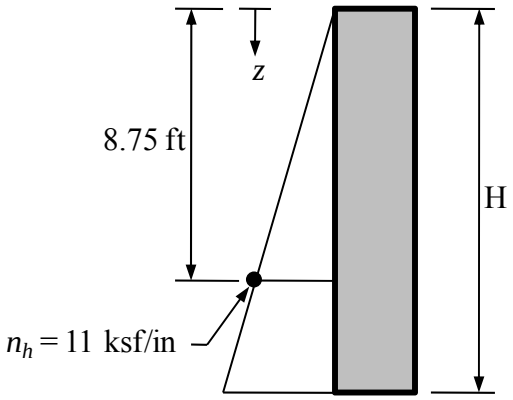

Figure 5.6: Variation of Subgrade Modulus

5.3 Analysis Cases

Five series of analyses were conducted to evaluate the effects of: (1) no backfill resistance, (2) backfill stiffness, (3) backfill strength, (4) span length, and (5) the "pin" detail which was tested in the experimental investigation. The details of each series are discussed in the following sections and summarized in Table 5.3. For each series, displacements of the abutment were computed using the 26 ground motions described in Chapter 2: 8 unscaled motions, 6 AASHTO-scaled motions, 6 EE-scaled motions, and 6 MCE-scaled ground motions. Non-linear time-history analysis was performed for all cases. While a spectral analysis could be performed with the design spectra, this procedure cannot account for the non-linearity of response. Therefore the scaled ground motions developed in Chapter 2 were used. Is should be noted that the unscaled records represent actual ground motions and are useful in that regard. However, they do not necessarily represent design requirements for Indiana.

Table 5.2: Abutment-Soil Spring Parameters

Depth z (ft)	Spacing s (ft)	Passive Pressure p_p (ksf)	Passive Force P_p (kips)	k (kips/in.)			
				Disp. Approach	Stiffness Approach		
				Δ_u = 2.40 in.	n_h = 5.5 ksf/in Δ_u = 0.704 in.	n_h = 11 ksf/in Δ_u = 0.352 in.	n_h = 22ksf/in Δ_u = 0.176 in.
1	1.5	0.443	33	14	47	94	189
2	1	0.886	44	18	63	126	251
3	1	1.328	66	28	94	189	377
4	1	1.771	89	37	126	251	503
5	1	2.214	111	46	157	314	629
6	1	2.657	133	55	189	377	754
7	1	3.100	155	65	220	440	880
8	1	3.543	177	74	251	503	1006
9	1	3.985	199	83	283	566	1131
10	1	4.428	221	92	314	629	1257

5.3.1 Series 1 – Pile Springs (No Backfill)

Models constructed for Series 1 had no abutment-soil springs. Lateral load resistance was provided by the foundation piles and pile-soil springs only. To determine the influence of soil stiffness, three soil stiffnesses were included in Series 1: loose (ϕ = 30°), medium (ϕ = 35°), and dense (ϕ = 40°). The pile-soil spring values corresponding to these three cases were shown previously in Table 5.1.

5.3.2 Series 2 – Backfill Stiffness

Models constructed for Series 2 included abutment-soil springs. Lateral load resistance was provided by the abutment-soil springs, foundation piles, and pile-soil springs. For Series 2 the pile-soil spring values corresponding to a medium soil stiffness (ϕ = 35°) were used. The abutment-soil spring properties were derived using two approaches: (1) the displacement approach and (2) the stiffness approach. These approaches were discussed previously, and the abutment-soil spring parameters were shown in Table 5.2. For the displacement approach a single value of Δ_u/H = 0.02 was used. For the stiffness approach, three values of subgrade modulus were used: the measured value of 11,000 psf/in., one-half the measure value (5,500 psf/in.), and two times the measured value (22,000 psf/in.). The three values of subgrade modulus were intended to evaluate the sensitivity of the response to this parameter.

5.3.3 Series 3 – Backfill Strength

Models constructed for Series 3 were intended to examine the effects of the ultimate strength, P_{max}, of the backfill on abutment response. For Series 3, the soil-pile spring values corresponding to a medium soil stiffness (ϕ = 35°) were used. The soil-abutment spring stiffnesses used in Series 3 correspond to the case where n_h = 11,000 psf/in. Two cases of ultimate backfill strength were used: one-half of the ultimate value computed by the Rankine earth pressure theory and two times the value computed by the Rankine earth pressure theory (Table 5.2).

5.3.4 Series 4 – Span Length

Models constructed for Series 4 were intended to examine the effects of span length on the abutment response. The span lengths used in the other analysis series are shown in Figure 5.2. For Series 4, all models have 100 ft span lengths. Pile-soil spring parameters correspond to the medium soil stiffness case ($\phi = 35°$). Abutment-soil springs correspond to the stiffness approach where n_h = 11,000 psf/in, and P_{max} is computed using the Rankine earth pressure theory.

5.3.5 Series 5 – Pin Detail

Models constructed for Series 5 were intended to evaluate the effects of the "pin" detail, discussed in Chapter 4, on abutment response. The pin was modeled as a moment release in the pile-element which connects to the abutment resulting in zero-moment at the joint where the abutment and pile elements meet. Pile-soil spring parameters correspond to the medium soil stiffness case ($\phi = 35°$). Abutment-soil springs correspond to the stiffness approach where n_h = 11,000 psf/in, and P_{max} is computed using the Rankine earth pressure theory.

Table 5.3: Analysis Cases

	Model	L (ft)	ϕ (deg)	k (psf/in.)	P_{max} (psf)	Span Length (ft)	Pin Detail
Series 1 - Pile Springs (No Backfill)	1	200	30	No Abutment-Soil Springs		60-70	no
	2	400	30			60-70	no
	3	600	30			60-70	no
	4	800	30			60-70	no
	5	1000	30			60-70	no
	6	200	35			60-70	no
	7	400	35			60-70	no
	8	600	35			60-70	no
	9	800	35			60-70	no
	10	1000	35			60-70	no
	11	200	40			60-70	no
	12	400	40			60-70	no
	13	600	40			60-70	no
	14	800	40			60-70	no
	15	1000	40			60-70	no
Series 2 - Backfill Stiffness	16	200	35	5,500	P_p	60-70	no
	17	400	35	5,500	P_p	60-70	no
	18	600	35	5,500	P_p	60-70	no
	19	800	35	5,500	P_p	60-70	no
	20	1000	35	5,500	P_p	60-70	no
	21	200	35	11,000	P_p	60-70	no
	22	400	35	11,000	P_p	60-70	no
	23	600	35	11,000	P_p	60-70	no
	24	800	35	11,000	P_p	60-70	no
	25	1000	35	11,000	P_p	60-70	no
	26	200	35	22,000	P_p	60-70	no
	27	400	35	22,000	P_p	60-70	no
	28	600	35	22,000	P_p	60-70	no
	29	800	35	22,000	P_p	60-70	no
	30	1000	35	22,000	P_p	60-70	no

Table 5.3 (continued): Analysis Cases

	Model	L (ft)	ϕ (deg)	k (psf/in.)	P_{max} (psf)	Span Length (ft)	Pin Detail
Series 2 (continued)	31	200	35	P_p/0.02H	P_p	60-70	no
	32	400	35	P_p/0.02H	P_p	60-70	no
	33	600	35	P_p/0.02H	P_p	60-70	no
	34	800	35	P_p/0.02H	P_p	60-70	no
	35	1000	35	P_p/0.02H	P_p	60-70	no
Series 3 - Backfill Strength	36	200	35	11,000	0.5 P_p	60-70	no
	37	400	35	11,000	0.5 P_p	60-70	no
	38	600	35	11,000	0.5 P_p	60-70	no
	39	800	35	11,000	0.5 P_p	60-70	no
	40	1000	35	11,000	0.5 P_p	60-70	no
	41	200	35	11,000	2 P_p	60-70	no
	42	400	35	11,000	2 P_p	60-70	no
	43	600	35	11,000	2 P_p	60-70	no
	44	800	35	11,000	2 P_p	60-70	no
	45	1000	35	11,000	2 P_p	60-70	no
Series 4 Span Length	46	200	35	11,000	P_p	100	no
	47	400	35	11,000	P_p	100	no
	48	600	35	11,000	P_p	100	no
	49	800	35	11,000	P_p	100	no
	50	1000	35	11,000	P_p	100	no
Series 5 Pin Detail	51	200	35	11,000	P_p	60-70	yes
	52	400	35	11,000	P_p	60-70	yes
	53	600	35	11,000	P_p	60-70	yes
	54	800	35	11,000	P_p	60-70	yes
	55	1000	35	11,000	P_p	60-70	yes

5.4 Results

The fundamental period of vibration of the analytical models was computed. Figure 5.7 shows the variation of fundamental period with bridge length and backfill stiffness. The values of fundamental period shown in Figure 5.7 are based on a linear elastic analysis and do not reflect the effects of the nonlinearity of the soil springs. The design displacement spectra were computed for Evansville, IN and are presented in Figure 5.8. Figure 5.7 and Figure 5.8 may be used to roughly estimate the displacement of the abutment. It can be seen that, in the absence of backfill resistance, the fundamental period ranges from approximately 0.4 – 1.4 sec corresponding to an MCE displacement of approximately 2-6 in. It may also be seen that, incorporating backfill resistance, the fundamental period ranges from approximately 0.2 – 0.8 sec corresponding to an MCE displacement of approximately 0.5 – 3.5 in. Further, using the observed value of backfill stiffness (11,000 psf/in.), the fundamental period ranges from approximately 0.2 – 0.5 sec corresponding to an MCE displacement of approximately 0.2 – 2 in. These displacement values are rough estimates assuming an elastic response. Inelasticity would be expected to lengthen the period. The computed displacements considering inelastic response are presented in the following subsections.

Only maximum displacements of the abutments are presented in this study (Figure 5.9). The displacement values reported refer to the lateral displacements of the abutment at the location of abutment-pile connection. These displacements may be directly compared to the results of the laboratory investigation. Numerical results are given in Table 5.4 - Table 5.8. The event numbers shown in the tables correspond to those listed in Table 2.2. The values of average maximum displacements were tabulated separately for Eastern and Western U.S. ground motions. It should be noted that for the Eastern records, only the Saguenay event was scaled as discussed previously in Chapter 2. The average maximum displacement values are presented graphically in Figure 5.10 - Figure 5.14.

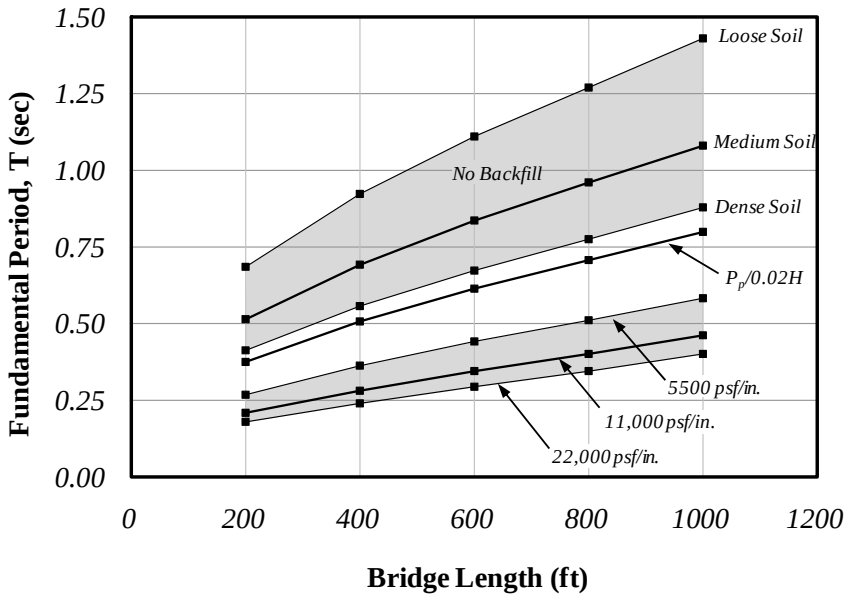

Figure 5.7: Fundamental Period of Vibration for various Bridge Lengths

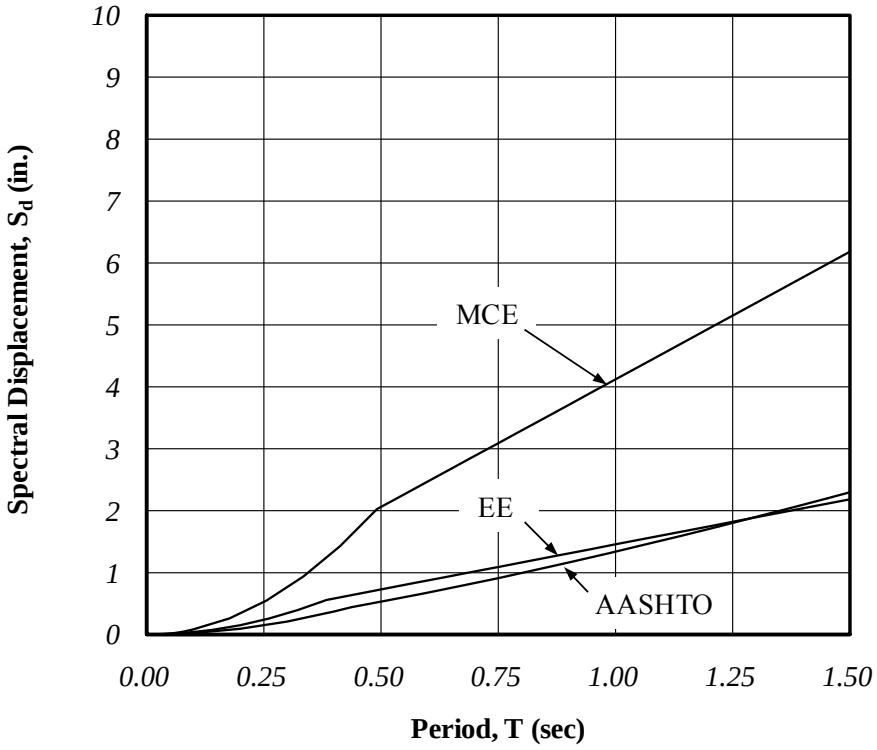

Figure 5.8: Evansville Design Displacement Spectra

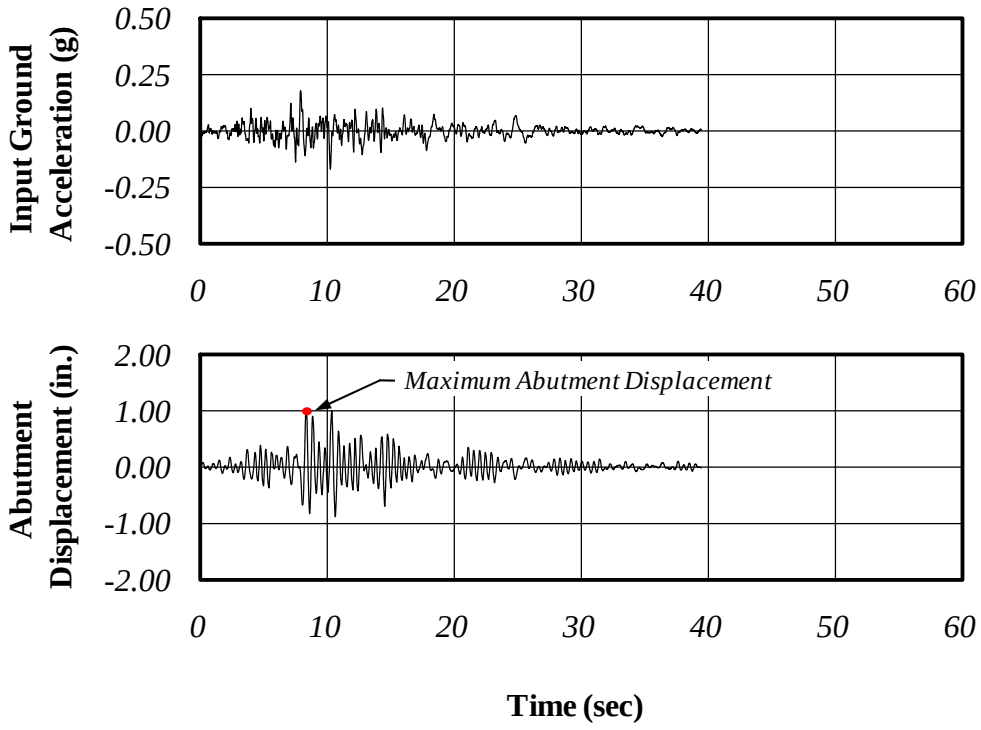

Figure 5.9: Maximum Abutment Displacement

5.4.1 Series 1 – No Backfill Resistance

The numerical results of the Series 1 models are presented in Table 5.4. The average maximum displacement values are presented in graphical form in Figure 5.10. The shaded areas of the figure represent the range of displacement results for different soil conditions. The bold line represents the medium condition ($\phi = 35°$). The upper and lower bound of the shaded regions are the loose ($\phi = 30°$) and dense ($\phi = 40°$) conditions, respectively. The zero-damage and acceptable-damage displacement limits determined in Chapter 4 are also shown in Figure 5.10.

For the AASHTO ground motions, none of the models exceeded the zero-damage displacement limit. For the EE ground motions, the zero-damage displacement limit was exceeded for Western U.S. ground motions with bridge lengths greater than 600 ft and a loose soil condition. For the MCE ground motions, the computed displacements exceeded the zero-damage limit for all bridge lengths using Western U.S. ground

motions. The MCE ground motions exceeded the acceptable-damage limit for lengths longer than 400 ft on loose soil and lengths longer than 800 ft for medium soil. The zero-damage limit was not exceeded in any case for the Eastern U.S. ground motion.

Table 5.4: Maximum Abutment Displacement (in.) – Series 1

		L	Eastern U.S. Ground Motions					Western U.S. Ground Motions						
		(ft)	(1)	(2)	(3)	Avg	Std Dev	(4)	(5)	(6)	(7)	(8)	Avg	Std Dev
UNSCALED	Loose	200	0.11	0.33	0.04	0.16	0.15	3.31	4.09	2.77	2.06	3.03	3.05	0.74
		400	0.13	0.40	0.02	0.18	0.19	4.11	5.33	3.69	2.27	4.12	3.91	1.10
		600	0.13	0.35	0.02	0.16	0.17	3.70	5.41	5.93	2.27	6.44	4.75	1.73
		800	0.12	0.43	0.02	0.19	0.21	2.90	6.92	7.39	4.22	9.07	6.10	2.50
		1000	0.11	0.44	0.02	0.19	0.22	3.89	8.19	6.23	4.67	7.52	6.10	1.83
	Medium	200	0.08	0.33	0.07	0.16	0.15	2.80	2.12	3.11	0.92	1.75	2.14	0.87
		400	0.10	0.29	0.04	0.14	0.13	3.29	4.76	3.29	2.13	3.01	3.30	0.95
		600	0.11	0.34	0.02	0.16	0.16	3.83	4.76	3.42	2.15	3.72	3.58	0.94
		800	0.12	0.29	0.02	0.14	0.14	3.54	4.95	4.02	1.36	5.76	3.93	1.67
		1000	0.11	0.30	0.02	0.14	0.15	3.10	4.84	5.79	2.97	7.12	4.76	1.78
	Dense	200	0.05	0.35	0.02	0.14	0.18	1.49	1.27	2.61	0.58	1.73	1.53	0.74
		400	0.07	0.26	0.08	0.14	0.11	2.59	2.62	2.31	1.53	1.98	2.21	0.46
		600	0.09	0.28	0.04	0.14	0.13	2.87	4.08	2.99	1.97	2.72	2.92	0.76
		800	0.10	0.34	0.02	0.15	0.17	3.50	3.90	3.19	1.88	3.39	3.17	0.76
		1000	0.10	0.34	0.02	0.15	0.17	3.15	4.21	2.95	1.38	4.46	3.23	1.22
AASHTO	Loose	200	--	0.20	--	--	--	0.82	0.70	0.65	1.18	0.50	0.77	0.25
		400	--	0.24	--	--	--	1.27	1.38	0.72	1.37	0.82	1.11	0.32
		600	--	0.21	--	--	--	1.21	1.28	0.75	1.24	1.20	1.14	0.22
		800	--	0.26	--	--	--	1.11	1.37	0.97	2.16	1.20	1.36	0.47
		1000	--	0.26	--	--	--	0.96	1.40	1.36	2.38	1.80	1.58	0.54
	Medium	200	--	0.20	--	--	--	0.60	0.39	0.54	0.54	0.35	0.49	0.11
		400	--	0.18	--	--	--	0.84	0.70	0.57	1.16	0.51	0.76	0.26
		600	--	0.20	--	--	--	1.13	1.27	0.68	1.26	0.59	0.99	0.33
		800	--	0.18	--	--	--	1.24	1.14	0.68	1.03	0.79	0.98	0.23
		1000	--	0.18	--	--	--	1.10	1.22	0.70	1.21	1.18	1.08	0.22
	Dense	200	--	0.19	--	--	--	0.23	0.26	0.40	0.28	0.35	0.30	0.07
		400	--	0.12	--	--	--	0.75	0.47	0.59	0.65	0.35	0.56	0.16
		600	--	0.17	--	--	--	0.81	0.65	0.47	1.08	0.45	0.69	0.26
		800	--	0.20	--	--	--	0.95	1.11	0.59	1.14	0.51	0.86	0.29
		1000	--	0.19	--	--	--	1.10	0.97	0.61	1.06	0.71	0.89	0.22

Table 5.4 (continued): Maximum Abutment Displacement (in.) – Series 1

		L	Eastern U.S. Ground Motions					Western U.S. Ground Motions						
		(ft)	(1)	(2)	(3)	Avg	Std Dev	(4)	(5)	(6)	(7)	(8)	Avg	Std Dev
EE	Loose	200	--	0.33	--	--	--	1.40	1.14	0.99	2.06	0.75	1.27	0.50
		400	--	0.40	--	--	--	2.26	2.05	1.09	2.27	1.27	1.79	0.57
		600	--	0.35	--	--	--	2.04	2.14	1.16	2.27	1.96	1.91	0.44
		800	--	0.43	--	--	--	1.67	2.19	1.59	4.22	1.89	2.31	1.09
		1000	--	0.44	--	--	--	1.68	2.74	2.18	3.50	2.85	2.59	0.69
	Medium	200	--	0.33	--	--	--	1.17	0.62	0.86	0.92	0.54	0.82	0.25
		400	--	0.29	--	--	--	1.57	1.42	0.79	2.13	0.81	1.35	0.56
		600	--	0.34	--	--	--	2.04	1.83	1.05	2.15	0.93	1.60	0.57
		800	--	0.29	--	--	--	1.85	1.95	1.02	1.36	1.22	1.48	0.40
		1000	--	0.30	--	--	--	1.71	1.99	1.19	2.97	1.83	1.94	0.65
	Dense	200	--	0.35	--	--	--	0.50	0.44	0.65	0.58	0.52	0.54	0.08
		400	--	0.26	--	--	--	1.32	0.84	0.88	1.53	0.52	1.02	0.40
		600	--	0.28	--	--	--	1.42	1.41	0.69	1.97	0.75	1.25	0.53
		800	--	0.34	--	--	--	1.65	1.75	0.95	1.88	0.81	1.41	0.49
		1000	--	0.34	--	--	--	1.72	1.64	0.92	1.38	1.00	1.33	0.36
MCE	Loose	200	--	0.72	--	--	--	3.31	4.09	1.82	5.01	2.16	3.28	1.33
		400	--	0.88	--	--	--	4.11	5.33	2.44	3.81	3.26	3.79	1.07
		600	--	0.77	--	--	--	3.70	5.41	3.04	9.09	4.40	5.13	2.38
		800	--	0.94	--	--	--	2.90	6.92	4.81	7.66	7.06	5.87	1.98
		1000	--	0.97	--	--	--	3.89	8.19	4.61	8.14	6.05	6.18	1.98
	Medium	200	--	0.70	--	--	--	2.80	2.12	2.09	3.32	1.45	2.36	0.72
		400	--	0.78	--	--	--	3.29	4.76	1.83	4.79	2.13	3.36	1.40
		600	--	0.78	--	--	--	3.83	4.76	2.33	3.31	2.83	3.41	0.94
		800	--	0.66	--	--	--	3.54	4.95	2.41	5.03	4.54	4.09	1.11
		1000	--	0.72	--	--	--	3.10	4.84	3.30	7.75	4.79	4.76	1.86
	Dense	200	--	0.82	--	--	--	1.49	1.27	1.67	1.84	1.30	1.51	0.24
		400	--	0.65	--	--	--	2.59	2.62	1.68	4.11	1.32	2.46	1.08
		600	--	0.75	--	--	--	2.87	4.08	1.74	4.20	1.96	2.97	1.15
		800	--	0.68	--	--	--	3.50	3.90	2.13	3.80	2.59	3.18	0.78
		1000	--	0.56	--	--	--	3.15	4.21	1.87	3.22	3.02	3.10	0.83

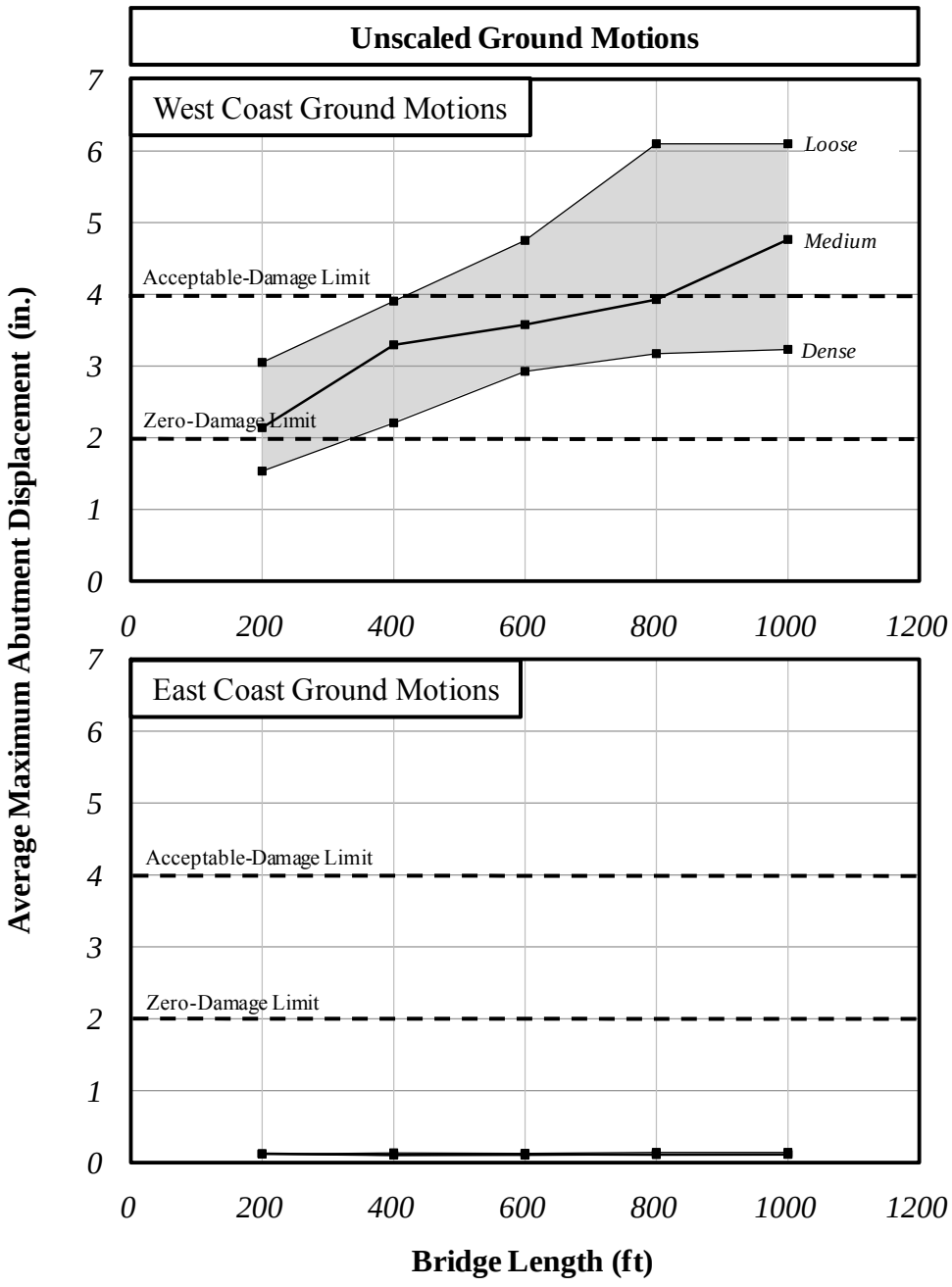

Figure 5.10: Average Maximum Abutment Displacements – Series 1

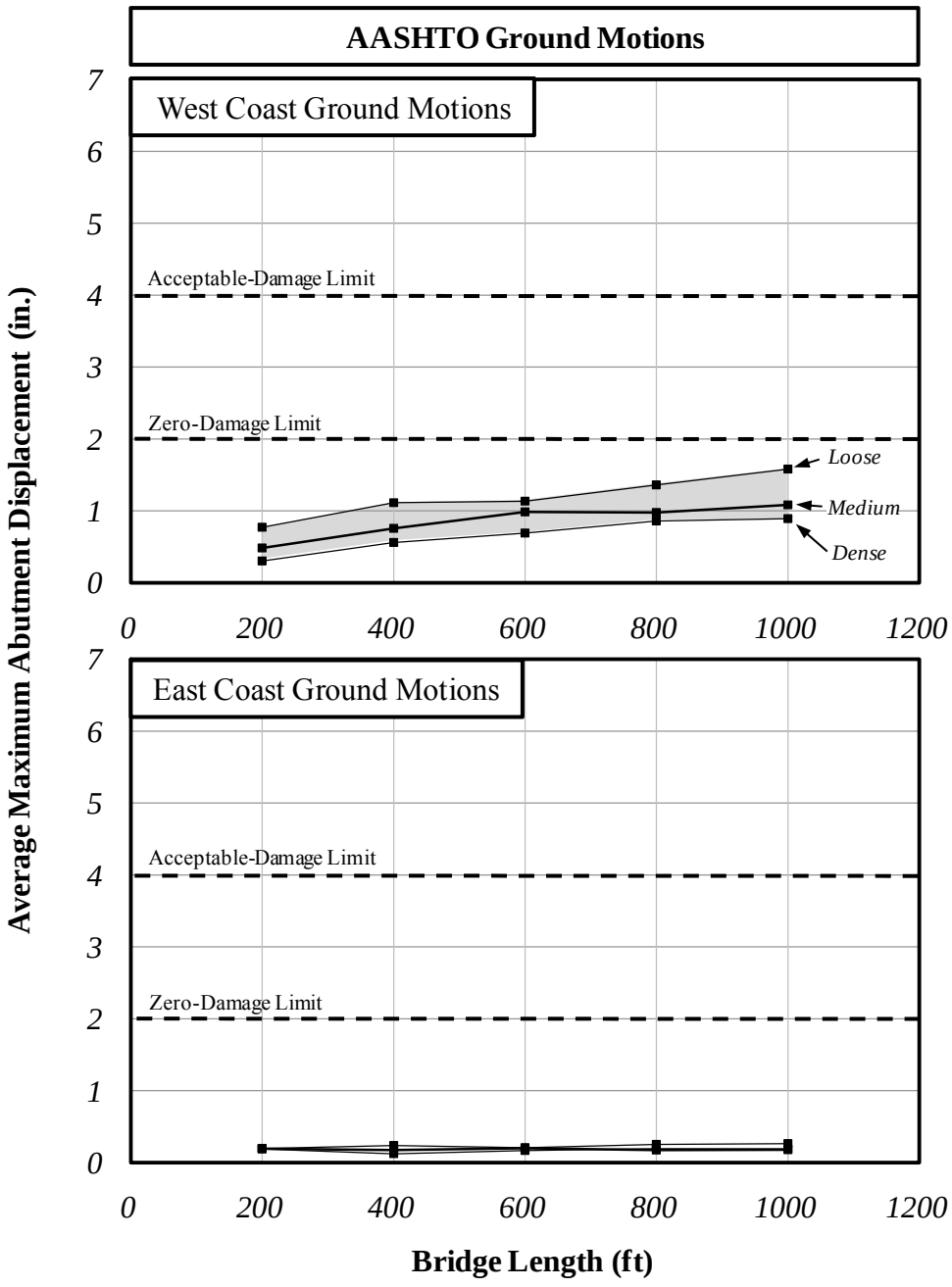

Figure 5.10 (continued): Average Maximum Abutment Displacements – Series 1

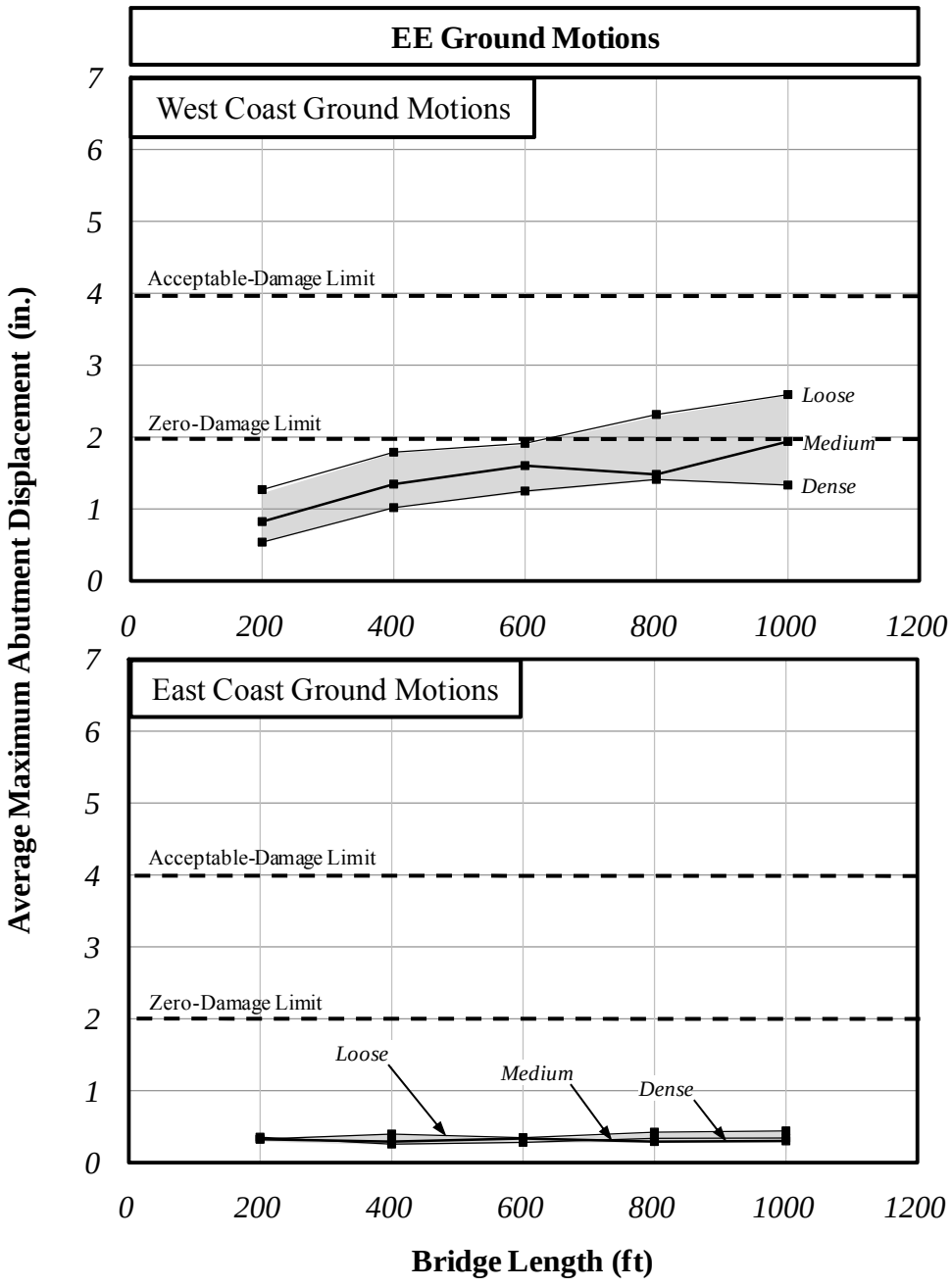

Figure 5.10 (continued): Average Maximum Abutment Displacements – Series 1

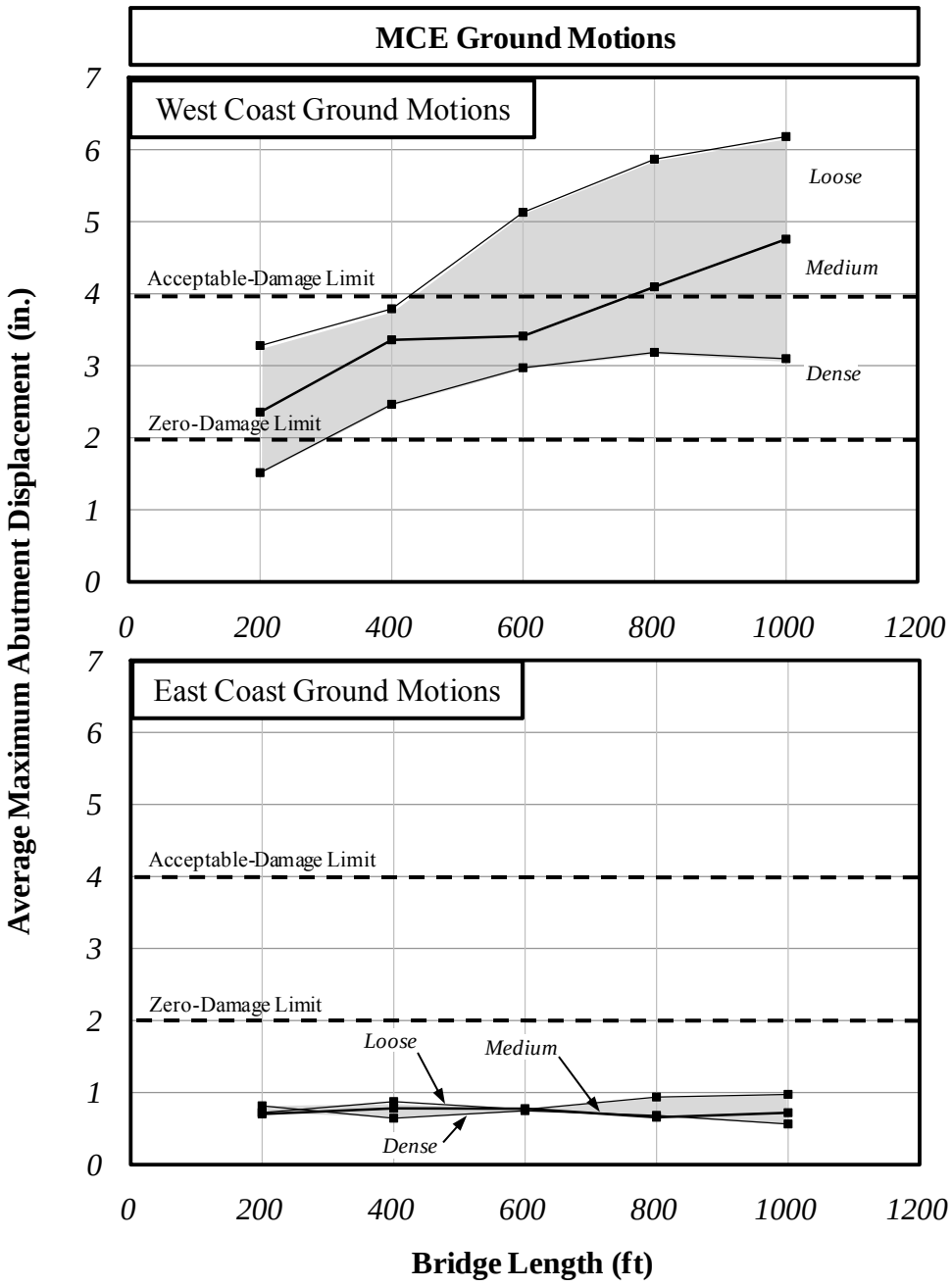

Figure 5.10 (continued): Average Maximum Abutment Displacements – Series 1

5.4.2 Series 2 – Backfill Stiffness

The numerical results of the Series 2 models evaluating backfill stiffness are presented in Table 5.5. The average maximum displacement values are presented in graphical form in Figure 5.11. The shaded areas of the figure represent displacement values based on a range of values of n_h used in the stiffness approach. The zero-damage and acceptable-damage displacement limits are also shown in Figure 5.11.

The displacements computed for Series 2 are generally smaller than those in Series 1 as expected due to the presence of the backfill. The displacements of the abutment computed using abutment-soil spring parameters based on the $\Delta_u/H = 0.02$ criteria correspond roughly to the case of no backfill resistance and dense soil considered in Series 1. The displacements of the abutment computed using the abutment-soil spring parameters based on the stiffness approach are significantly less than the displacements computed in Series 1 for all cases. For the AASHTO and EE ground motions, the computed responses did not exceed the zero-damage limit for any case. For the MCE ground motions, the computed displacements exceeded the zero-damage limit for bridge lengths greater than approximately 300 ft for abutment-soil springs based on the displacement approach and approximately 700 ft for abutment-soil springs based on the stiffness approach. In no case did the computed displacements exceed the acceptable-damage limit. In addition, the zero-damage limit was not exceeded for any case using Eastern U.S. ground motions.

Table 5.5: Maximum Abutment Displacement (in.) – Series 2

	k	L	Eastern U.S. Ground Motions					Western U.S. Ground Motions						
	(psf/in.)	(ft)	(1)	(2)	(3)	Avg	Std Dev	(4)	(5)	(6)	(7)	(8)	Avg	Std Dev
UNSCALED	P_p/0.02H	200	0.06	0.37	0.02	0.15	0.19	1.32	1.22	2.38	0.50	1.56	1.40	0.68
		400	0.08	0.25	0.07	0.13	0.10	2.50	2.17	2.76	1.11	1.66	2.04	0.66
		600	0.10	0.28	0.03	0.14	0.13	2.77	3.51	2.58	1.83	2.48	2.64	0.60
		800	0.10	0.30	0.02	0.14	0.15	3.23	4.21	3.30	1.83	2.94	3.10	0.85
		1000	0.10	0.31	0.02	0.14	0.15	3.46	4.19	3.13	1.71	3.41	3.18	0.91
	5,500	200	0.05	0.35	0.01	0.14	0.19	0.58	0.95	1.02	0.24	1.03	0.76	0.34
		400	0.05	0.32	0.02	0.13	0.16	1.31	1.08	2.36	0.52	1.46	1.34	0.67
		600	0.06	0.21	0.07	0.11	0.08	2.15	1.63	2.37	0.56	1.38	1.62	0.71
		800	0.07	0.21	0.04	0.11	0.09	2.27	2.11	1.72	1.33	1.72	1.83	0.37
		1000	0.08	0.25	0.03	0.12	0.12	2.38	3.14	2.25	1.46	2.14	2.28	0.60
	11,000	200	0.03	0.19	0.01	0.08	0.10	0.41	0.48	0.91	0.17	0.68	0.53	0.28
		400	0.04	0.26	0.01	0.10	0.14	0.55	0.87	1.46	0.23	1.05	0.83	0.47
		600	0.04	0.25	0.02	0.10	0.13	0.88	0.72	1.58	0.33	1.09	0.92	0.46
		800	0.04	0.20	0.04	0.09	0.09	1.39	0.99	1.67	0.50	1.07	1.12	0.44
		1000	0.05	0.14	0.04	0.08	0.05	1.48	1.34	1.50	0.63	1.00	1.19	0.37
	22,00	200	0.03	0.17	0.00	0.07	0.09	0.27	0.28	0.52	0.16	0.48	0.34	0.15
		400	0.03	0.16	0.00	0.06	0.08	0.28	0.45	0.56	0.12	0.66	0.41	0.22
		600	0.02	0.18	0.01	0.07	0.10	0.34	0.55	0.76	0.14	0.62	0.48	0.25
		800	0.02	0.14	0.01	0.06	0.07	0.41	0.44	0.83	0.18	0.61	0.49	0.24
		1000	0.03	0.13	0.02	0.06	0.07	0.78	0.56	1.00	0.31	0.64	0.66	0.26

Table 5.5 (continued) : Maximum Abutment Displacements (in.) – Series 2

	k (psf/in.)	L (ft)	Eastern U.S. Ground Motions (1)	(2)	(3)	Avg	Std Dev	Western U.S. Ground Motions (4)	(5)	(6)	(7)	(8)	Avg	Std Dev
AASHTO	P_p/0.02H	200	--	0.22	--	--	--	0.28	0.29	0.41	0.29	0.29	0.31	0.05
		400	--	0.13	--	--	--	0.68	0.46	0.54	0.54	0.36	0.52	0.12
		600	--	0.16	--	--	--	0.74	0.61	0.50	1.05	0.45	0.67	0.24
		800	--	0.17	--	--	--	0.84	0.99	0.60	1.16	0.52	0.82	0.27
		1000	--	0.18	--	--	--	1.02	1.03	0.62	1.07	0.61	0.87	0.23
	5,500	200	--	0.21	--	--	--	0.17	0.21	0.20	0.15	0.23	0.19	0.03
		400	--	0.19	--	--	--	0.35	0.27	0.38	0.31	0.24	0.31	0.06
		600	--	0.12	--	--	--	0.47	0.33	0.45	0.34	0.28	0.37	0.08
		800	--	0.13	--	--	--	0.53	0.40	0.43	0.72	0.29	0.47	0.16
		1000	--	0.15	--	--	--	0.59	0.45	0.36	0.88	0.36	0.53	0.22
	11,000	200	--	0.12	--	--	--	0.12	0.12	0.14	0.10	0.12	0.12	0.02
		400	--	0.16	--	--	--	0.16	0.19	0.18	0.14	0.16	0.17	0.02
		600	--	0.15	--	--	--	0.21	0.20	0.27	0.20	0.18	0.21	0.04
		800	--	0.12	--	--	--	0.33	0.22	0.31	0.30	0.17	0.27	0.07
		1000	--	0.08	--	--	--	0.36	0.28	0.34	0.32	0.22	0.30	0.05
	22,000	200	--	0.10	--	--	--	0.08	0.06	0.09	0.09	0.08	0.08	0.01
		400	--	0.10	--	--	--	0.09	0.08	0.11	0.07	0.09	0.09	0.01
		600	--	0.11	--	--	--	0.09	0.12	0.10	0.08	0.11	0.10	0.02
		800	--	0.08	--	--	--	0.10	0.12	0.15	0.11	0.12	0.12	0.02
		1000	--	0.08	--	--	--	0.19	0.14	0.19	0.16	0.12	0.16	0.03

Table 5.5 (continued) : Maximum Abutment Displacements (in.) – Series 2

	k	L	Eastern U.S. Ground Motions					Western U.S. Ground Motions						
	(psf/in.)	(ft)	(1)	(2)	(3)	Avg	Std Dev	(4)	(5)	(6)	(7)	(8)	Avg	Std Dev
EE	P_p/0.02H	200	--	0.37	--	--	--	0.48	0.47	0.64	0.50	0.44	0.50	0.08
		400	--	0.25	--	--	--	1.19	0.76	0.84	1.11	0.55	0.89	0.26
		600	--	0.28	--	--	--	1.31	1.02	0.71	1.83	0.69	1.11	0.48
		800	--	0.30	--	--	--	1.46	1.62	0.92	1.83	0.80	1.32	0.45
		1000	--	0.31	--	--	--	1.66	1.54	0.95	1.71	1.03	1.38	0.36
	5,500	200	--	0.35	--	--	--	0.29	0.33	0.30	0.24	0.34	0.30	0.04
		400	--	0.32	--	--	--	0.59	0.44	0.58	0.52	0.36	0.50	0.10
		600	--	0.21	--	--	--	0.86	0.53	0.68	0.56	0.43	0.61	0.17
		800	--	0.21	--	--	--	0.97	0.65	0.64	1.33	0.43	0.80	0.35
		1000	--	0.25	--	--	--	1.03	0.76	0.55	1.46	0.54	0.87	0.39
	11,000	200	--	0.19	--	--	--	0.20	0.19	0.22	0.17	0.18	0.19	0.02
		400	--	0.26	--	--	--	0.26	0.31	0.27	0.23	0.24	0.26	0.03
		600	--	0.25	--	--	--	0.35	0.32	0.41	0.33	0.26	0.33	0.05
		800	--	0.20	--	--	--	0.54	0.35	0.47	0.50	0.26	0.42	0.12
		1000	--	0.14	--	--	--	0.67	0.44	0.49	0.63	0.34	0.51	0.14
	22,000	200	--	0.17	--	--	--	0.13	0.10	0.13	0.16	0.12	0.13	0.02
		400	--	0.16	--	--	--	0.15	0.13	0.16	0.12	0.14	0.14	0.02
		600	--	0.18	--	--	--	0.14	0.20	0.16	0.14	0.17	0.16	0.02
		800	--	0.14	--	--	--	0.17	0.19	0.23	0.18	0.18	0.19	0.02
		1000	--	0.13	--	--	--	0.32	0.22	0.30	0.31	0.18	0.27	0.06

Table 5.5 (continued) : Maximum Abutment Displacements (in.) – Series 2

	k	L	Eastern U.S. Ground Motions					Western U.S. Ground Motions						
	(psf/in.)	(ft)	(1)	(2)	(3)	Avg	Std Dev	(4)	(5)	(6)	(7)	(8)	Avg	Std Dev
MCE	P_p/0.02H	200	--	0.84	--	--	--	1.32	1.22	1.52	1.38	1.16	1.32	0.14
		400	--	0.57	--	--	--	2.50	2.17	1.82	3.70	1.22	2.28	0.93
		600	--	0.66	--	--	--	2.77	3.51	1.55	4.52	1.82	2.84	1.22
		800	--	0.65	--	--	--	3.23	4.21	2.12	4.30	2.16	3.20	1.06
		1000	--	0.66	--	--	--	3.46	4.19	2.06	3.36	2.54	3.12	0.83
	5,500	200	--	0.79	--	--	--	0.58	0.95	0.67	0.57	0.86	0.73	0.17
		400	--	0.69	--	--	--	1.31	1.08	1.34	1.44	1.03	1.24	0.18
		600	--	0.46	--	--	--	2.15	1.63	1.57	2.68	1.11	1.83	0.60
		800	--	0.46	--	--	--	2.27	2.11	1.39	3.56	1.17	2.10	0.94
		1000	--	0.56	--	--	--	2.38	3.14	1.25	3.69	1.49	2.39	1.04
	11,000	200	--	0.44	--	--	--	0.41	0.48	0.48	0.40	0.45	0.44	0.04
		400	--	0.55	--	--	--	0.55	0.87	0.74	0.71	0.74	0.72	0.12
		600	--	0.53	--	--	--	0.88	0.72	0.95	1.01	0.78	0.87	0.12
		800	--	0.44	--	--	--	1.39	0.99	1.05	1.17	0.75	1.07	0.23
		1000	--	0.30	--	--	--	1.48	1.34	1.04	2.27	0.72	1.37	0.58
	22,000	200	--	0.43	--	--	--	0.27	0.28	0.28	0.36	0.33	0.30	0.04
		400	--	0.41	--	--	--	0.28	0.45	0.40	0.39	0.48	0.40	0.07
		600	--	0.35	--	--	--	0.34	0.55	0.41	0.40	0.47	0.43	0.08
		800	--	0.32	--	--	--	0.41	0.44	0.53	0.44	0.46	0.46	0.04
		1000	--	0.29	--	--	--	0.78	0.56	0.66	0.65	0.44	0.62	0.12

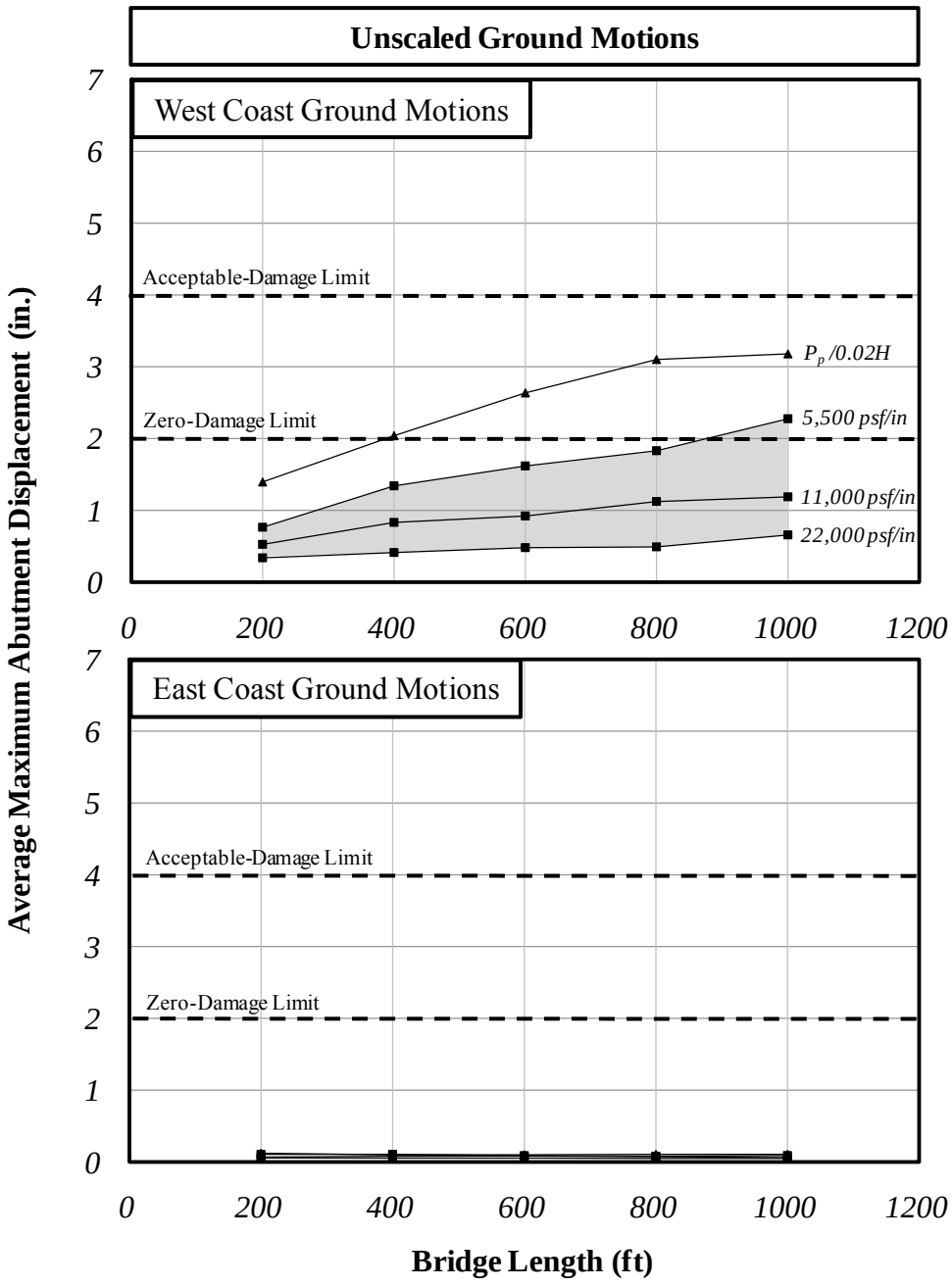

Figure 5.11: Average Maximum Abutment Displacements – Series 2

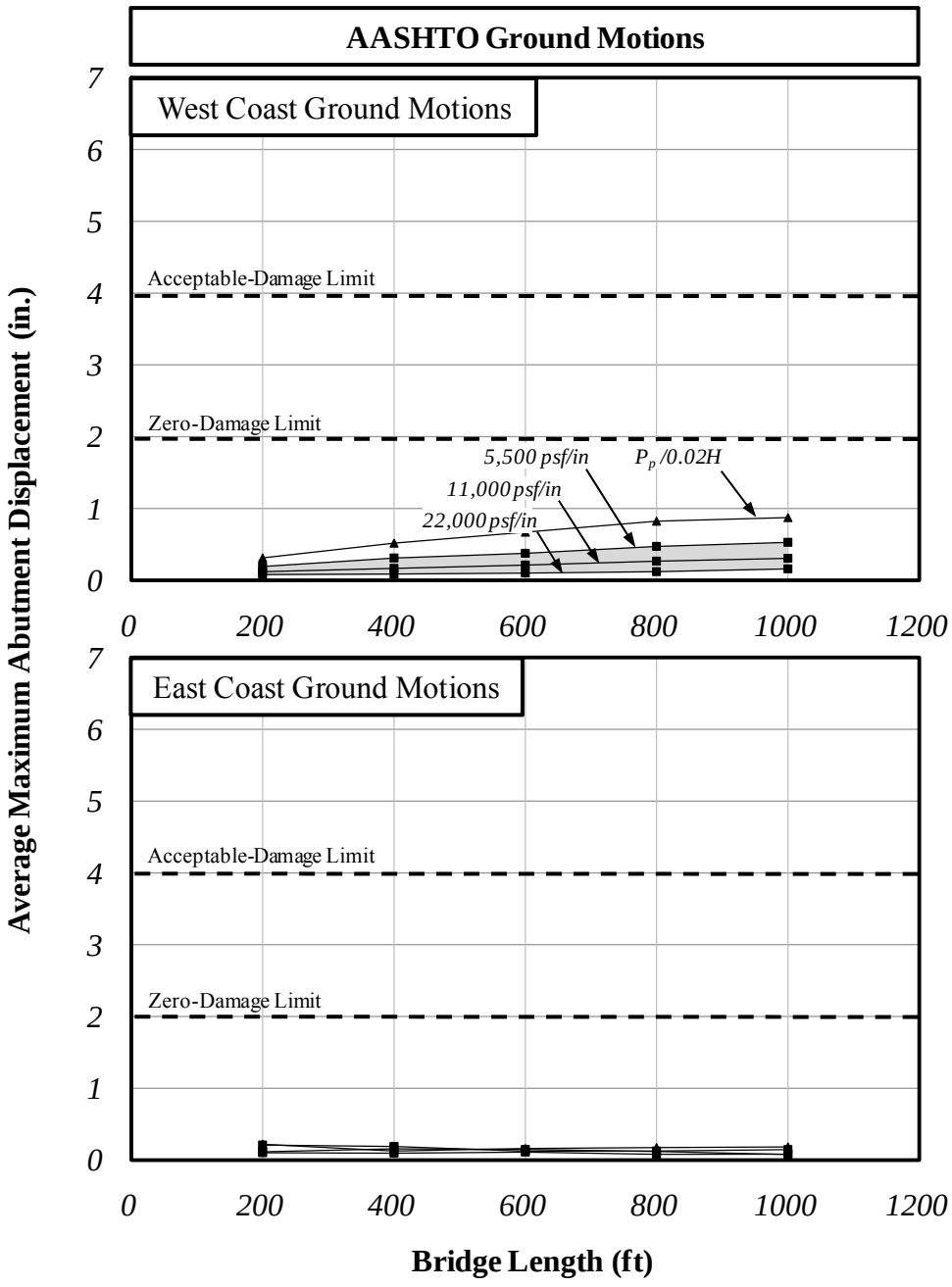

Figure 5.11 (continued): Average Maximum Abutment Displacements – Series 2

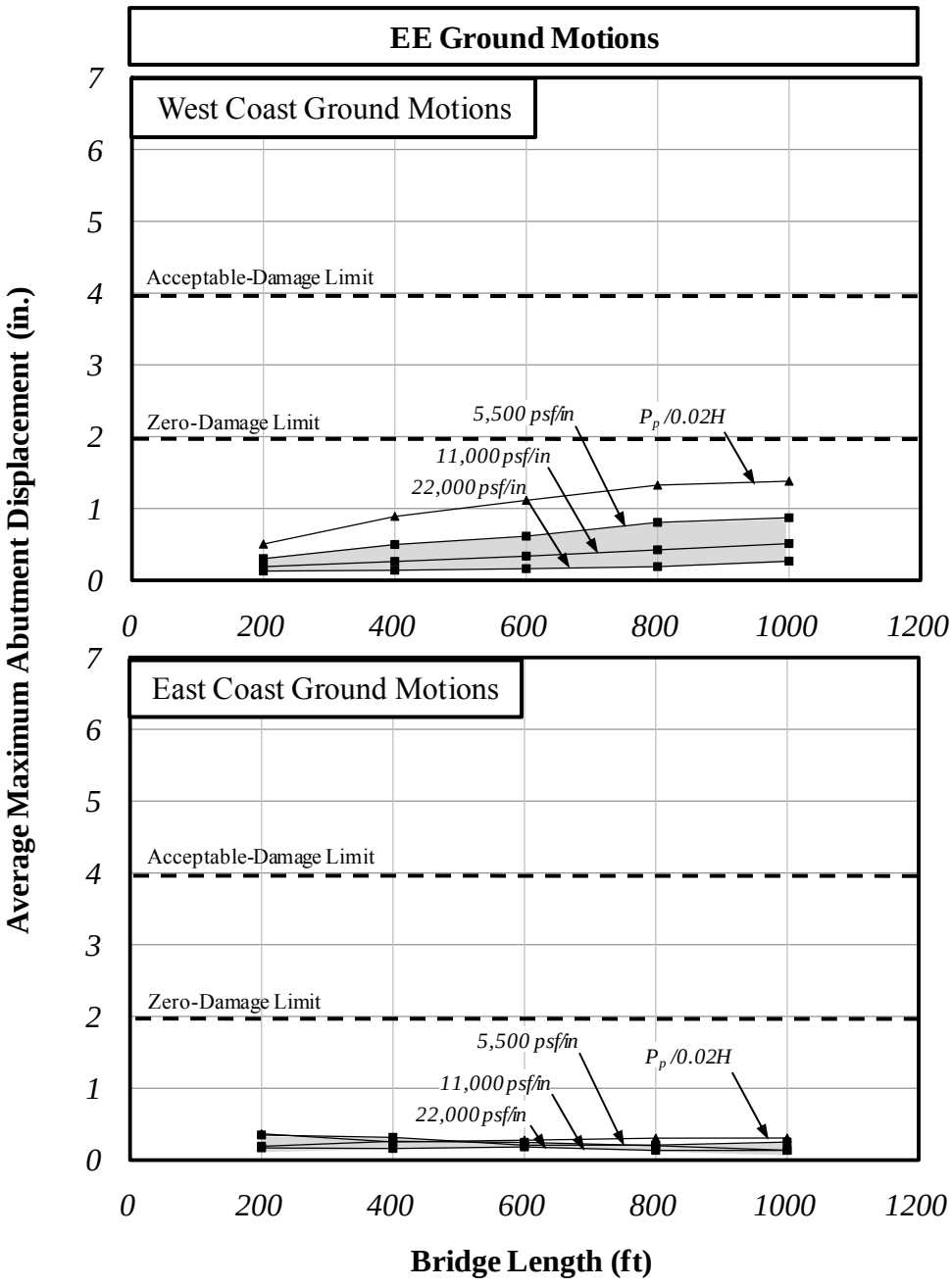

Figure 5.11 (continued): Average Maximum Abutment Displacements – Series 2

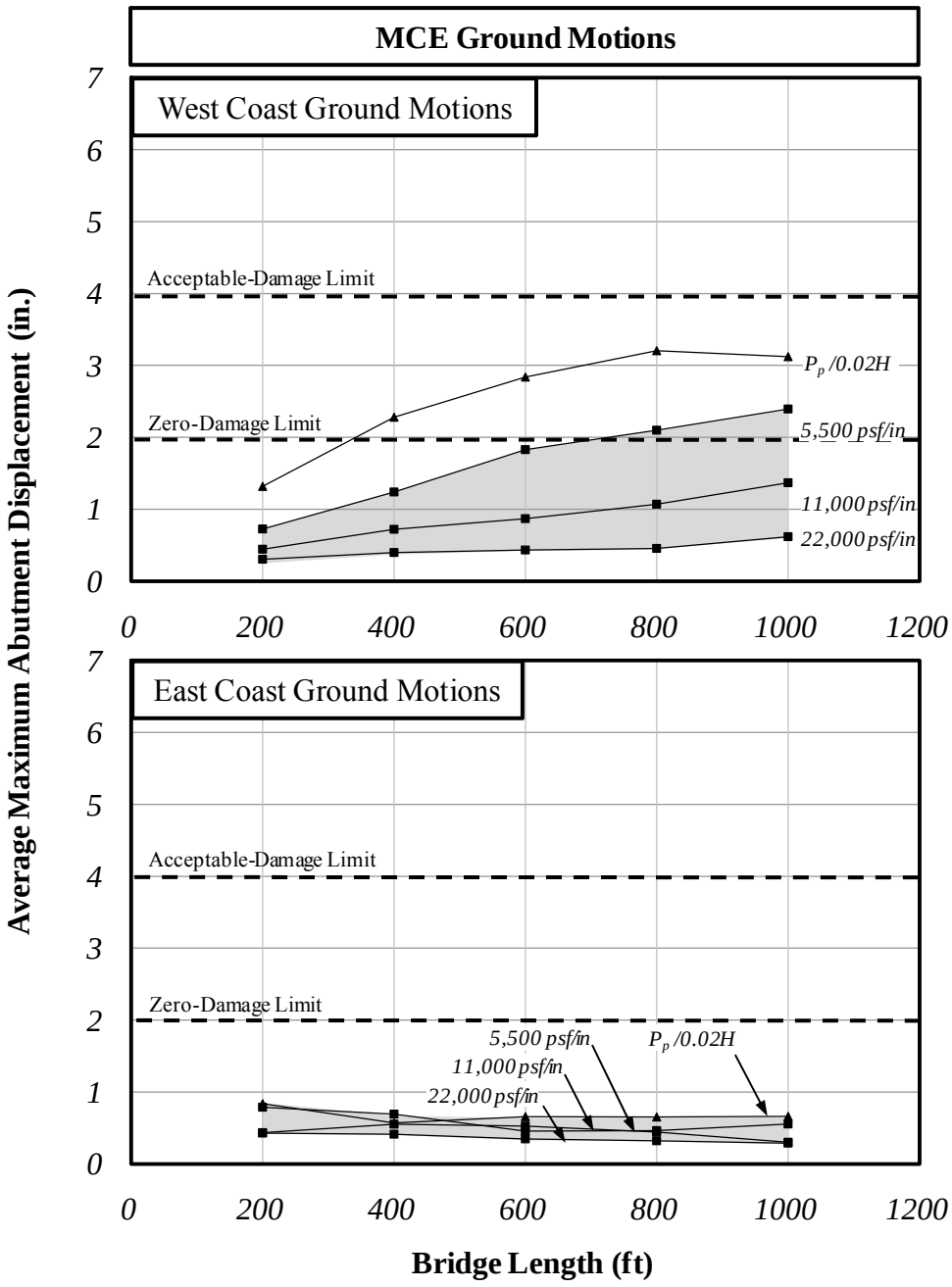

Figure 5.11 (continued): Average Maximum Abutment Displacements – Series 2

5.4.3 Series 3 – Backfill Strength

The numerical results of the Series 3 models evaluating the influence of backfill strength are presented in Table 5.6. The average maximum displacement values are presented in graphical form in Figure 5.12. For comparison, the results of Series 2 for n_h = 11,000 psf/in and $P_{max} = P_p$ have been reproduced in the figure. The zero-damage and acceptable-damage displacement limits determined in Chapter 4 are also shown.

As shown, varying the ultimate strength of the backfill material had relatively little effect on the displacements of the abutment. In no case did the computed displacements exceed the zero-damage limit.

Table 5.6: Maximum Abutment Displacements (in.) – Series 3

	P_{max}	L	Eastern U.S. Ground Motions					Western U.S. Ground Motions						
		(ft)	(1)	(2)	(3)	Avg	Std Dev	(4)	(5)	(6)	(7)	(8)	Avg	Std Dev
UNSCALED	$P_p/2$	200	0.03	0.20	0.01	0.08	0.10	0.47	0.93	1.29	0.17	1.18	0.81	0.48
		400	0.04	0.26	0.01	0.10	0.14	0.85	0.75	1.80	0.31	1.30	1.00	0.57
		600	0.04	0.25	0.02	0.10	0.13	1.44	1.11	1.80	0.49	1.12	1.19	0.48
		800	0.05	0.21	0.04	0.10	0.10	1.69	1.50	1.69	0.59	1.13	1.32	0.47
		1000	0.05	0.15	0.05	0.08	0.06	1.63	1.73	1.33	1.13	1.53	1.47	0.24
	$2P_p$	200	0.04	0.30	0.01	0.12	0.16	0.52	0.73	0.89	0.23	0.93	0.66	0.29
		400	0.04	0.26	0.02	0.11	0.13	0.75	0.88	1.70	0.36	1.20	0.98	0.50
		600	0.05	0.20	0.04	0.09	0.09	1.25	0.93	1.71	0.51	1.04	1.09	0.44
		800	0.05	0.15	0.05	0.08	0.06	1.59	1.31	1.82	0.57	1.09	1.28	0.48
		1000	0.06	0.17	0.03	0.09	0.08	1.50	1.56	1.48	1.05	1.26	1.37	0.21
AASHTO	$P_p/2$	200	--	0.12	--	--	--	0.12	0.12	0.15	0.10	0.12	0.12	0.02
		400	--	0.16	--	--	--	0.17	0.21	0.20	0.15	0.17	0.18	0.03
		600	--	0.16	--	--	--	0.25	0.22	0.30	0.23	0.19	0.24	0.04
		800	--	0.13	--	--	--	0.39	0.24	0.35	0.30	0.20	0.30	0.08
		1000	--	0.08	--	--	--	0.44	0.30	0.34	0.52	0.24	0.37	0.11
	$2P_p$	200	--	0.18	--	--	--	0.15	0.17	0.18	0.14	0.20	0.17	0.02
		400	--	0.15	--	--	--	0.21	0.22	0.30	0.21	0.21	0.23	0.04
		600	--	0.12	--	--	--	0.33	0.22	0.31	0.31	0.18	0.27	0.06
		800	--	0.09	--	--	--	0.41	0.28	0.35	0.34	0.23	0.32	0.07
		1000	--	0.10	--	--	--	0.41	0.32	0.31	0.61	0.24	0.38	0.15

Table 5.6 (continued) : Maximum Abutment Displacements (in.) – Series 3

	P_{max}	L	Eastern U.S. Ground Motions					Western U.S. Ground Motions						
		(ft)	(1)	(2)	(3)	Avg	Std Dev	(4)	(5)	(6)	(7)	(8)	Avg	Std Dev
EE	$P_p/2$	200	--	0.20	--	--	--	0.21	0.19	0.22	0.17	0.18	0.20	0.02
		400	--	0.26	--	--	--	0.31	0.36	0.36	0.31	0.29	0.32	0.03
		600	--	0.25	--	--	--	0.48	0.32	0.48	0.49	0.32	0.42	0.09
		800	--	0.21	--	--	--	0.77	0.41	0.52	0.59	0.32	0.52	0.17
		1000	--	0.15	--	--	--	0.79	0.56	0.50	1.13	0.31	0.66	0.31
	$2P_p$	200	--	0.30	--	--	--	0.26	0.27	0.28	0.23	0.29	0.27	0.02
		400	--	0.26	--	--	--	0.36	0.35	0.45	0.36	0.32	0.37	0.05
		600	--	0.20	--	--	--	0.55	0.35	0.46	0.51	0.28	0.43	0.11
		800	--	0.15	--	--	--	0.70	0.46	0.52	0.57	0.35	0.52	0.13
		1000	--	0.17	--	--	--	0.69	0.52	0.47	1.05	0.36	0.62	0.27
MCE	$P_p/2$	200	--	0.65	--	--	--	0.47	0.93	0.63	0.72	0.61	0.67	0.17
		400	--	0.58	--	--	--	0.85	0.75	1.08	1.16	0.96	0.96	0.17
		600	--	0.48	--	--	--	1.44	1.11	1.16	1.27	0.80	1.16	0.24
		800	--	0.40	--	--	--	1.69	1.50	1.14	2.31	0.72	1.47	0.60
		1000	--	0.36	--	--	--	1.63	1.73	0.91	2.56	0.97	1.56	0.67
	$2P_p$	200	--	0.68	--	--	--	0.52	0.73	0.60	0.53	0.73	0.62	0.10
		400	--	0.57	--	--	--	0.75	0.88	1.04	0.87	0.85	0.88	0.10
		600	--	0.44	--	--	--	1.25	0.93	1.07	1.17	0.73	1.03	0.21
		800	--	0.33	--	--	--	1.59	1.31	1.17	1.81	0.87	1.35	0.37
		1000	--	0.38	--	--	--	1.50	1.56	1.06	2.56	0.91	1.52	0.64

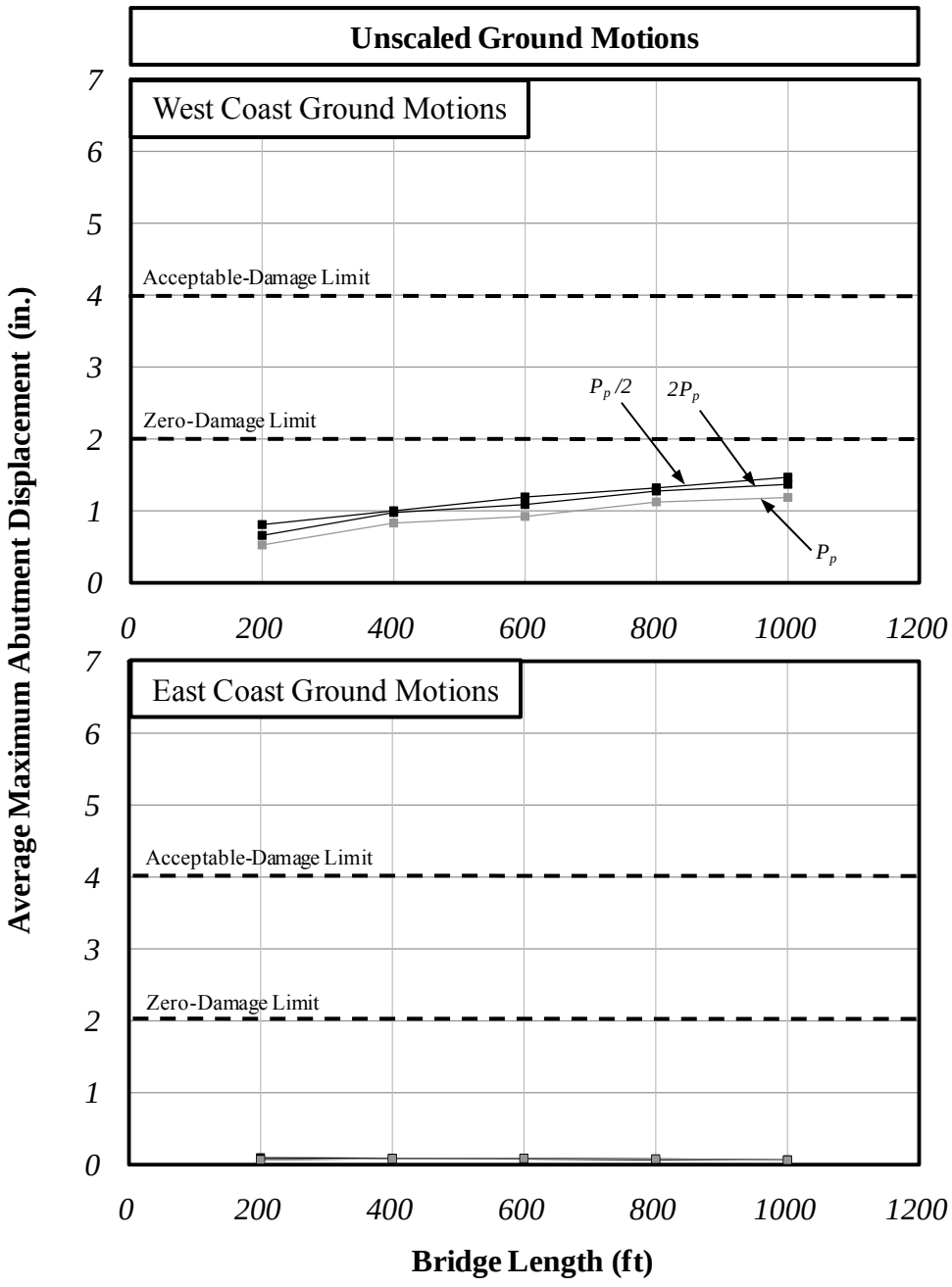

Figure 5.12: Average Maximum Abutment Displacements – Series 3

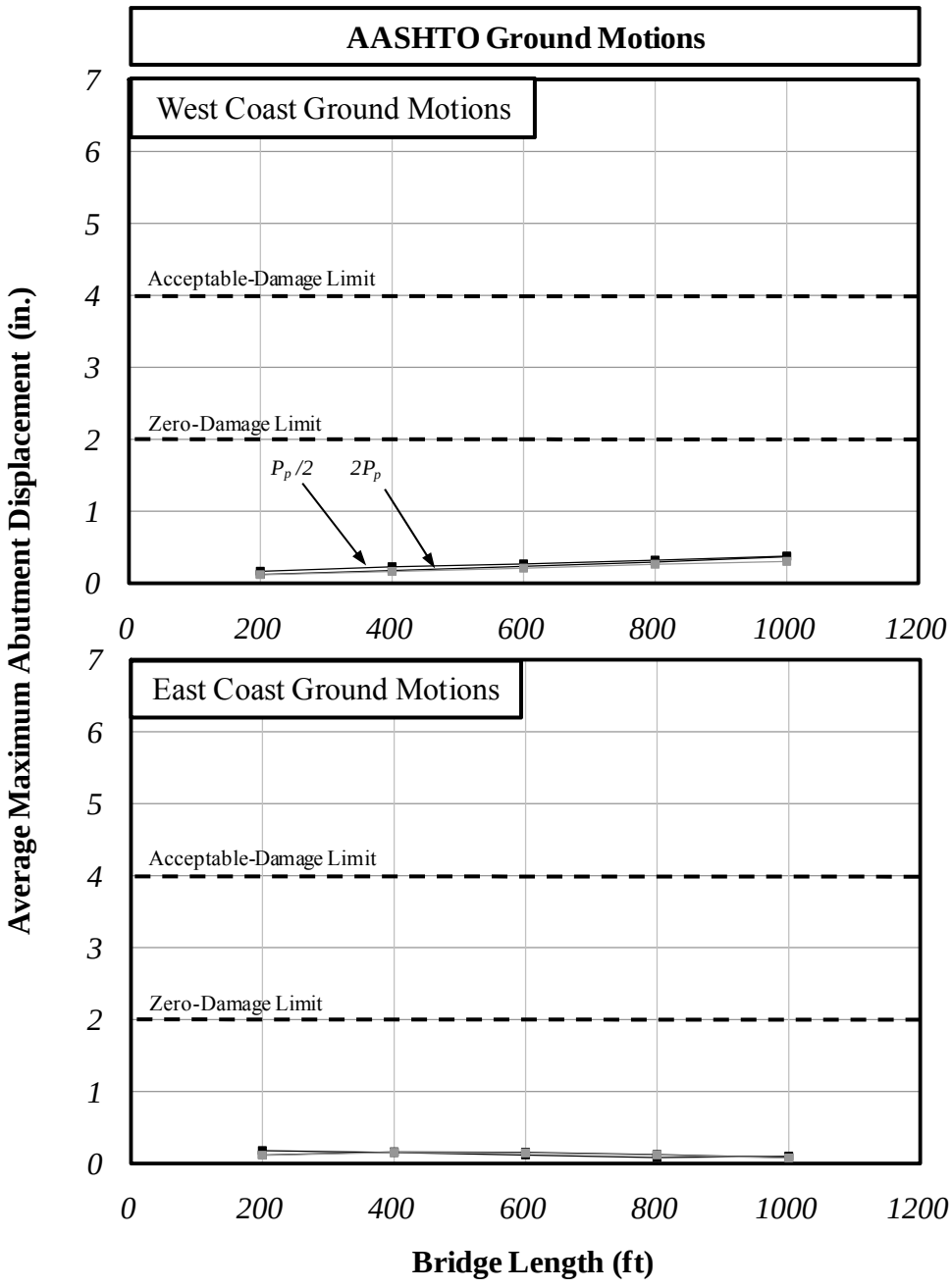

Figure 5.12 (continued): Average Maximum Abutment Displacements – Series 3

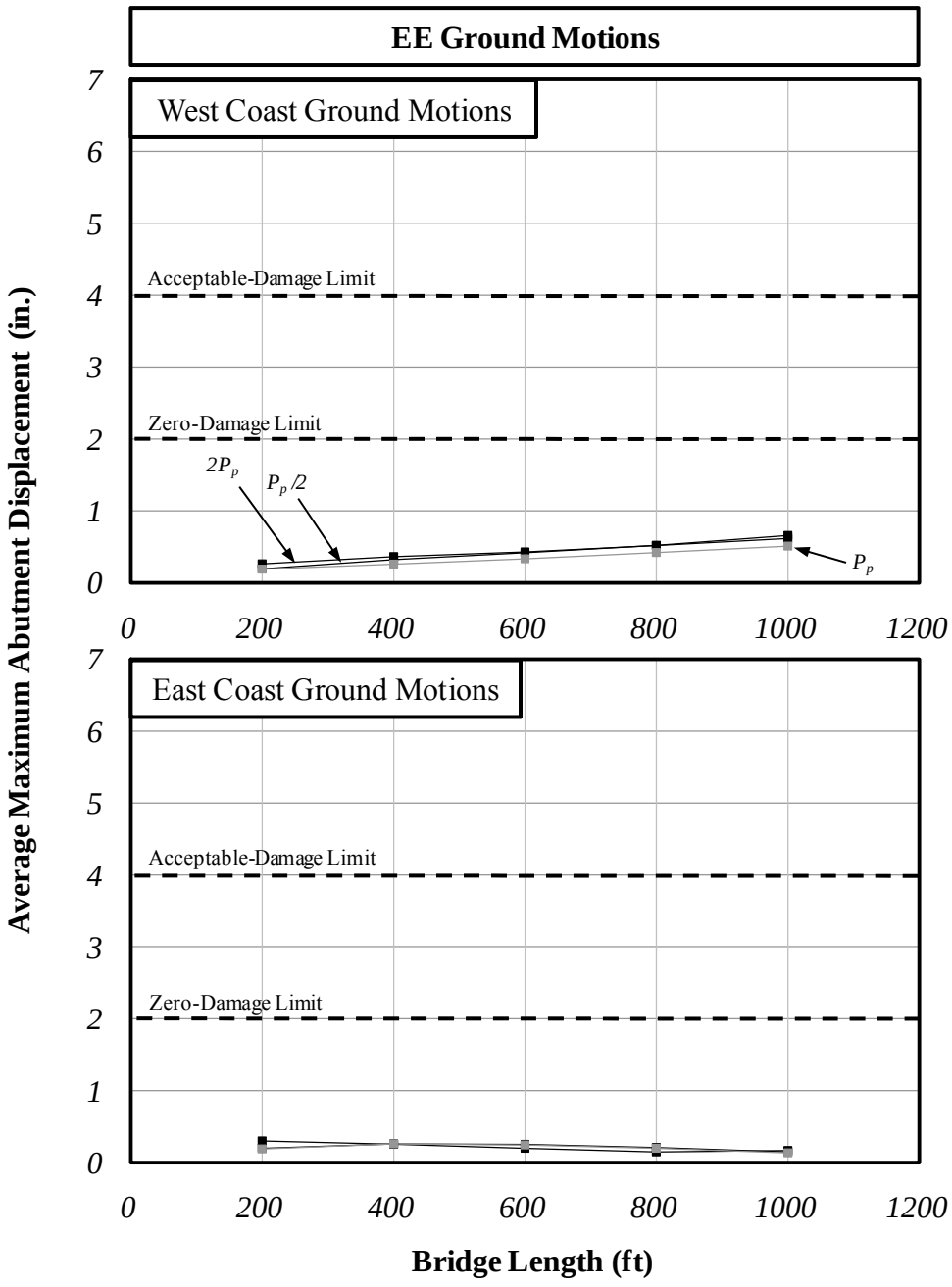

Figure 5.12 (continued): Average Maximum Abutment Displacements – Series 3

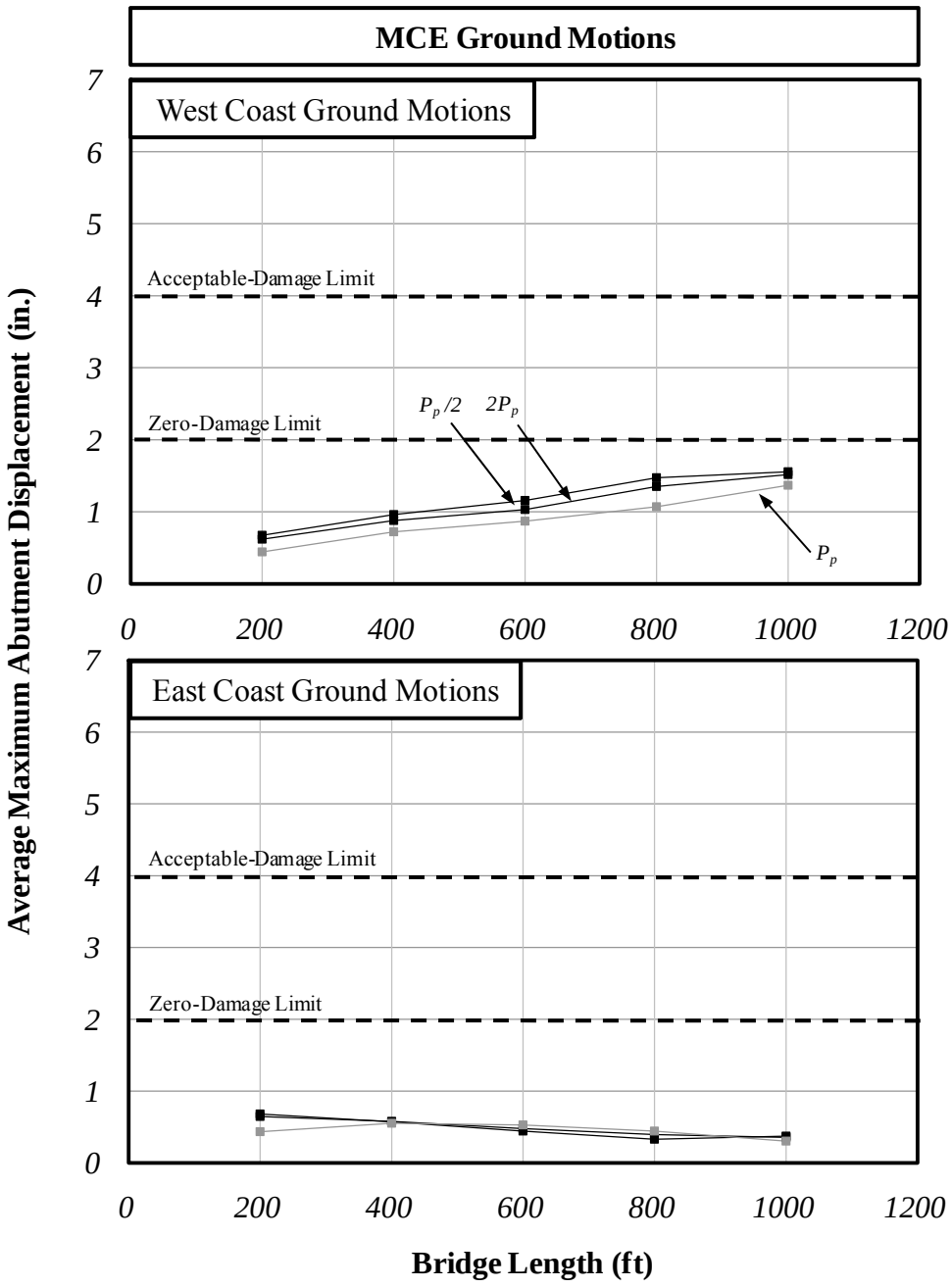

Figure 5.12 (continued): Average Maximum Abutment Displacements – Series 3

5.4.4 Series 4 – Span Length

The numerical results of the Series 4 models are presented in Table 5.7 to evaluate the influence of bridge span length. The average maximum displacement values are presented in graphical form in Figure 5.13. For reference, the results of Series 2 for n_h = 11,000 psf/in. have been reproduced in the figure. The only difference between this case and Series 4 is span length. The zero-damage and acceptable-damage displacement limits determined in Chapter 4 are also shown.

As shown, varying the span length of the models had relatively little effect on the displacements of the abutment. This was expected since the use of roller supports at the intermediate piers eliminates the influence of pier stiffness. In no case did the computed displacements exceed the zero-damage limit.

Table 5.7: Maximum Abutment Displacements (in.) – Series 4

	L	Eastern U.S. Ground Motions					Western U.S. Ground Motions						
	(ft)	(1)	(2)	(3)	Avg	Std Dev	(4)	(5)	(6)	(7)	(8)	Avg	Std Dev
UNSCALED	200	0.03	0.21	0.01	0.08	0.11	0.31	0.43	0.37	0.20	0.65	0.39	0.17
	400	0.03	0.14	0.01	0.06	0.07	0.41	0.50	1.07	0.21	0.70	0.58	0.33
	600	0.03	0.15	0.02	0.07	0.07	0.84	0.68	1.34	0.35	0.70	0.78	0.36
	800	0.04	0.13	0.04	0.07	0.05	1.20	0.94	1.37	0.36	0.85	0.94	0.39
	1000	0.05	0.13	0.03	0.07	0.05	1.20	1.14	1.13	0.70	0.91	1.02	0.21
AASHTO	200	--	0.13	--	--	--	0.09	0.10	0.07	0.12	0.12	0.10	0.02
	400	--	0.09	--	--	--	0.12	0.12	0.16	0.13	0.14	0.13	0.01
	600	--	0.09	--	--	--	0.21	0.15	0.21	0.21	0.14	0.18	0.04
	800	--	0.08	--	--	--	0.28	0.20	0.27	0.21	0.17	0.23	0.05
	1000	--	0.07	--	--	--	0.35	0.25	0.28	0.38	0.17	0.28	0.08
EE	200	--	0.21	--	--	--	0.15	0.16	0.11	0.20	0.18	0.16	0.03
	400	--	0.14	--	--	--	0.20	0.20	0.23	0.21	0.21	0.21	0.01
	600	--	0.15	--	--	--	0.34	0.24	0.31	0.35	0.20	0.29	0.06
	800	--	0.13	--	--	--	0.50	0.33	0.40	0.36	0.26	0.37	0.09
	1000	--	0.13	--	--	--	0.58	0.39	0.41	0.70	0.26	0.47	0.17
MCE	200	--	0.47	--	--	--	0.31	0.43	0.23	0.45	0.46	0.38	0.10
	400	--	0.32	--	--	--	0.41	0.50	0.59	0.50	0.52	0.51	0.07
	600	--	0.33	--	--	--	0.84	0.68	0.77	0.89	0.49	0.73	0.16
	800	--	0.28	--	--	--	1.20	0.94	0.88	1.35	0.67	1.01	0.27
	1000	--	0.28	--	--	--	1.20	1.14	0.81	2.04	0.64	1.16	0.54

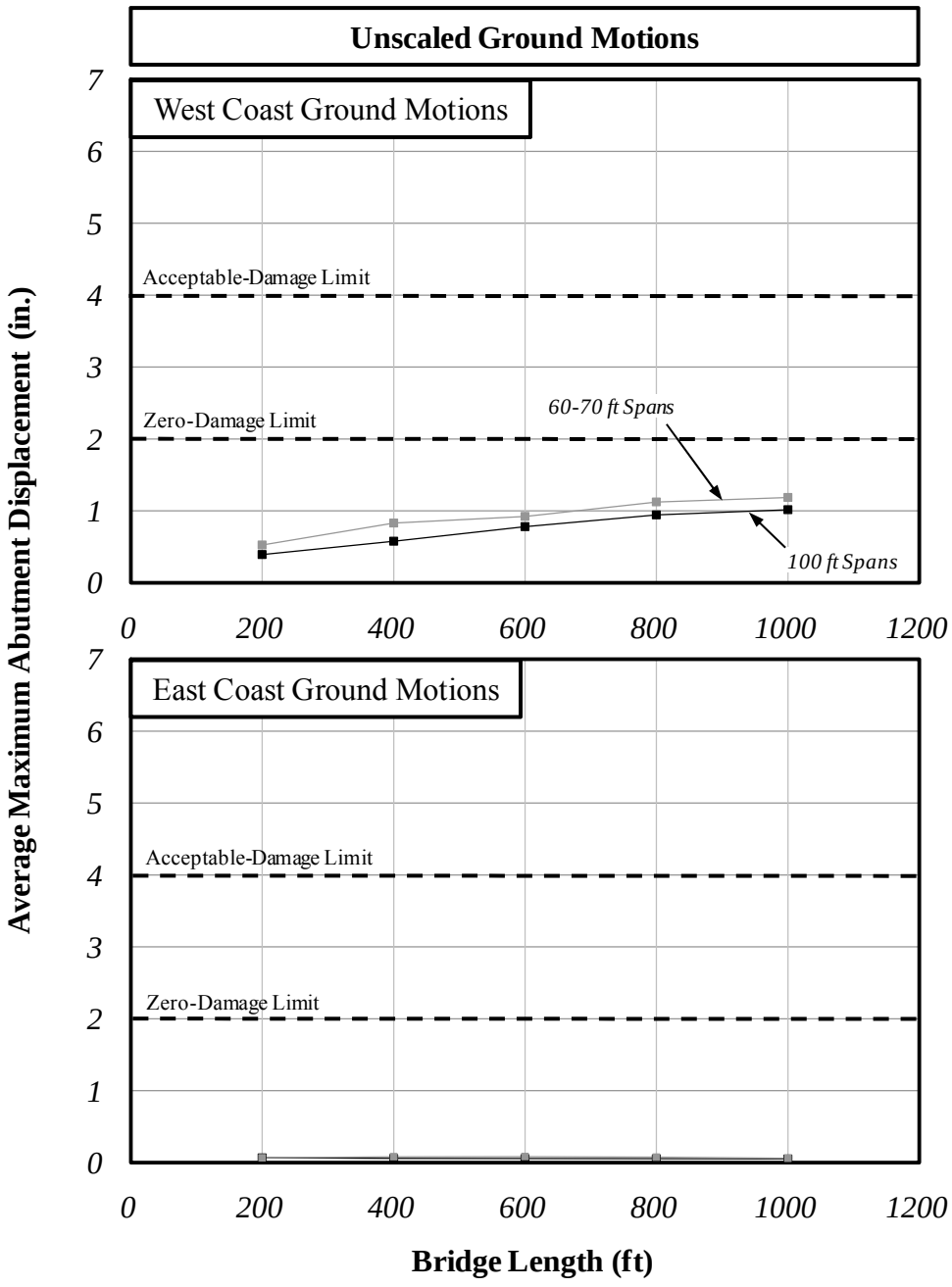

Figure 5.13: Average Maximum Abutment Displacements – Series 4

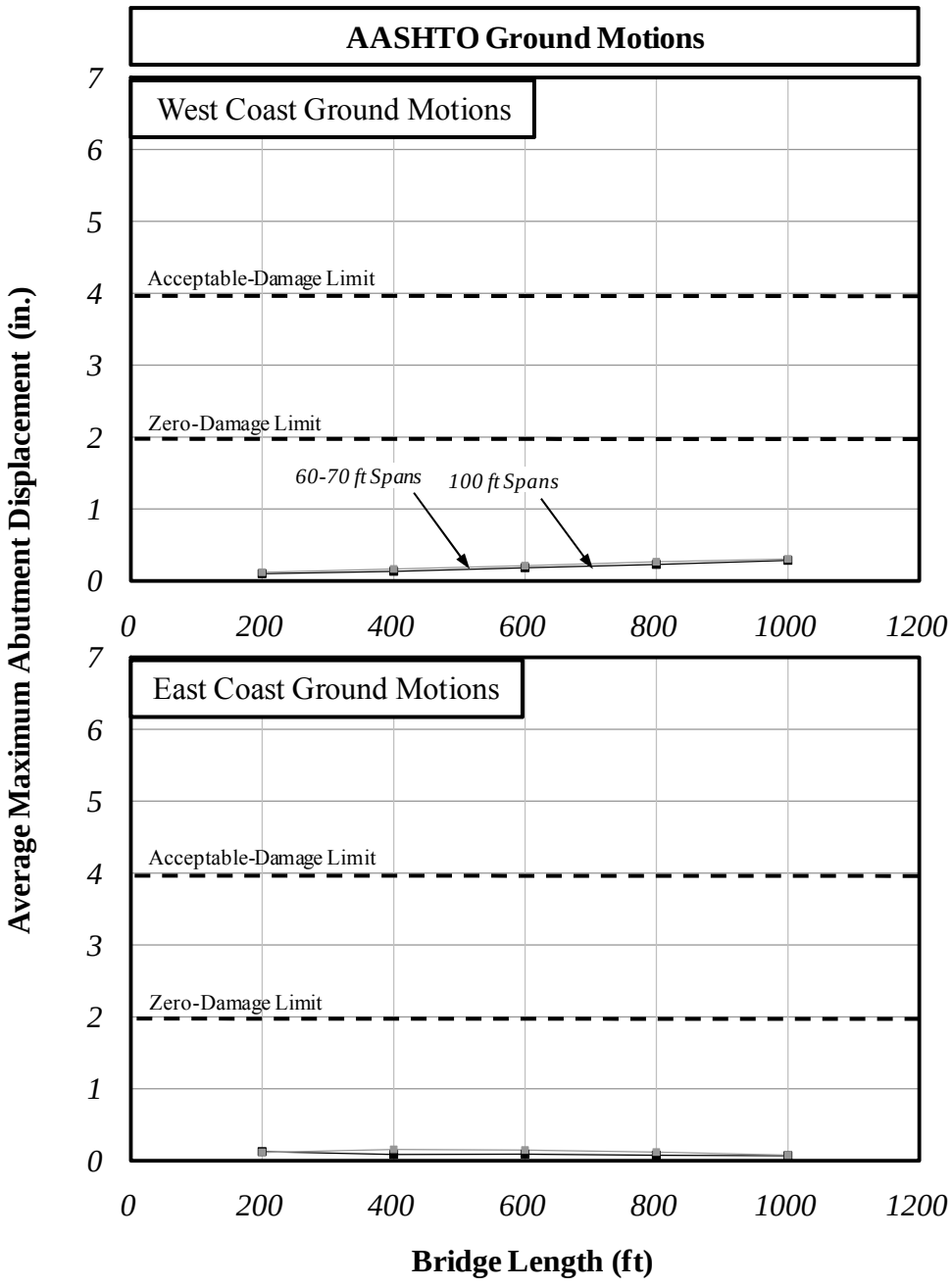

Figure 5.13 (continued): Average Maximum Abutment Displacements – Series 4

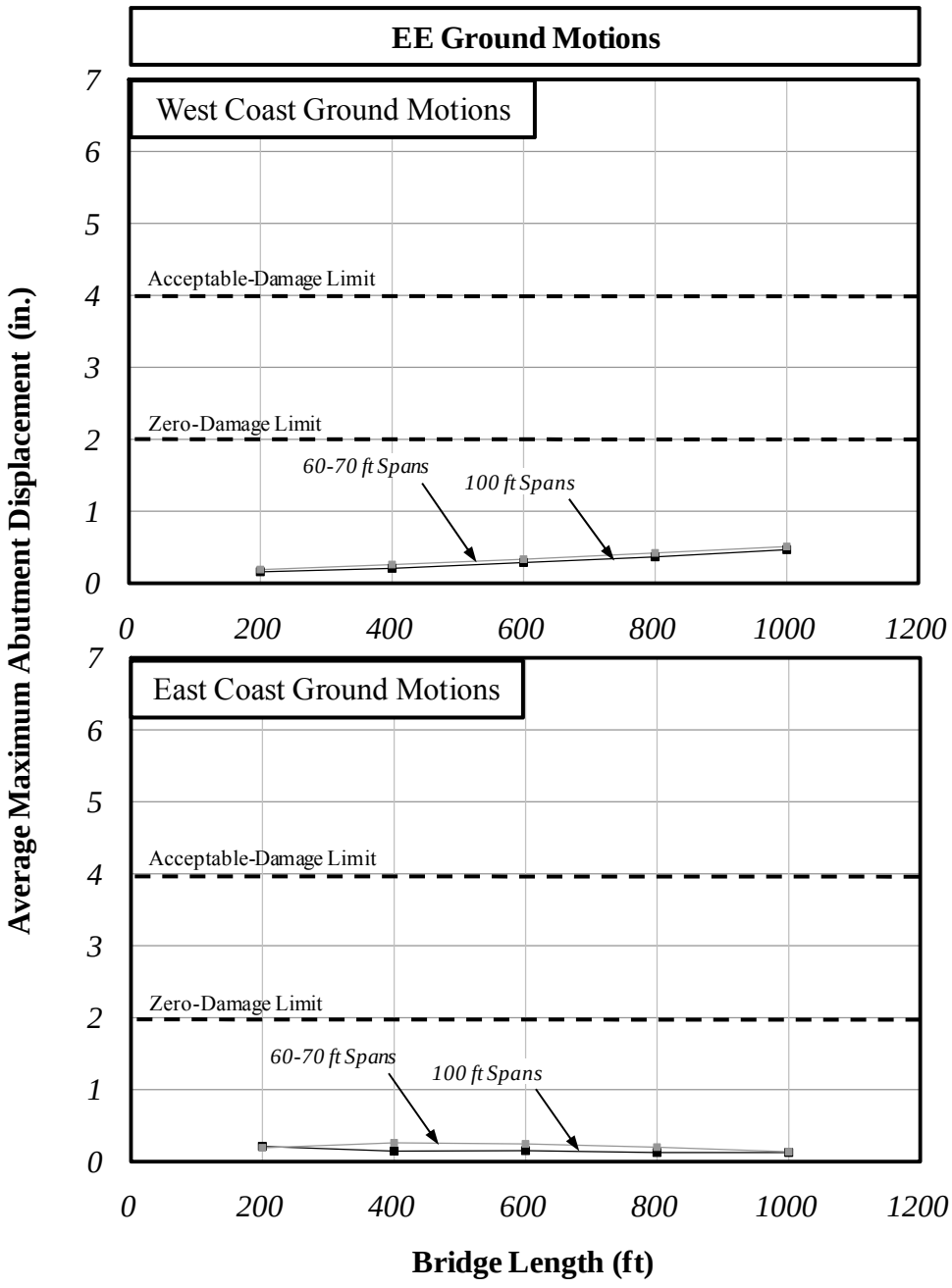

Figure 5.13 (continued): Average Maximum Abutment Displacements – Series 4

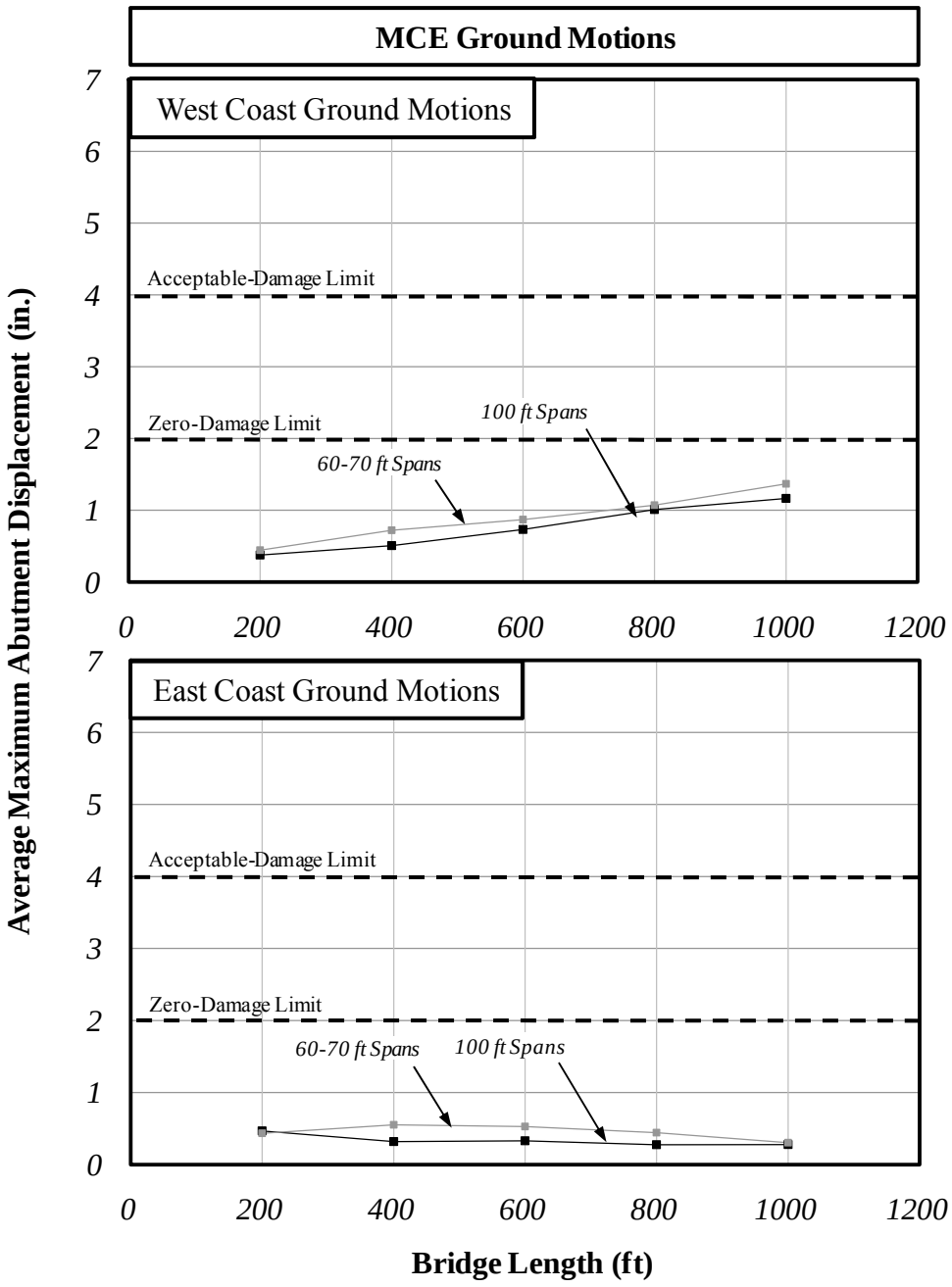

Figure 5.13 (continued): Average Maximum Abutment Displacements – Series 4

5.4.5 Series 5 – Pin Detail

The numerical results of the Series 5 models evaluating the influence of the pin detail are presented in Table 5.8. The average maximum displacement values are presented in graphical form in Figure 5.14. For reference, the results of Series 2 for n_h = 11,000 psf/in. have been reproduced in the figure. The only difference between this series and Series 5 is the inclusion of the pin detail. The zero-damage and acceptable-damage displacement limits determined in Chapter 4 are also shown.

As shown in the figures, the addition of the "pin" detail had relatively little effect on the displacements of the abutment. In no case did the computed displacements exceed the zero-damage limit. It should be noted that, although the computed displacements were compared to the zero-damage limit, the zero-damage limit does not have any real meaning for the pin detail. As discussed in Chapter 4, the pin detail had very little resistance to lateral loads throughout the range of displacements tested.

Table 5.8: Maximum Abutment Displacements (in.) – Series 5

	L	Eastern U.S. Ground Motions					Western U.S. Ground Motions						
	(ft)	(1)	(2)	(3)	Avg	Std Dev	(4)	(5)	(6)	(7)	(8)	Avg	Std Dev
UNSCALED	200	0.04	0.27	0.01	0.11	0.14	0.48	0.70	0.96	0.19	0.95	0.65	0.33
	400	0.04	0.26	0.01	0.10	0.14	0.81	0.92	1.88	0.31	1.40	1.06	0.60
	600	0.05	0.27	0.02	0.12	0.14	1.38	0.92	1.99	0.45	1.19	1.18	0.57
	800	0.05	0.21	0.05	0.10	0.09	1.78	1.41	1.82	0.52	1.03	1.31	0.55
	1000	0.06	0.16	0.04	0.09	0.06	1.78	1.75	1.38	1.04	1.38	1.46	0.31
AASHTO	200	--	0.16	--	--	--	0.14	0.15	0.19	0.11	0.17	0.15	0.03
	400	--	0.16	--	--	--	0.18	0.23	0.25	0.19	0.22	0.21	0.03
	600	--	0.16	--	--	--	0.30	0.24	0.33	0.26	0.22	0.27	0.05
	800	--	0.13	--	--	--	0.41	0.28	0.39	0.32	0.23	0.33	0.07
	1000	--	0.09	--	--	--	0.44	0.34	0.38	0.49	0.26	0.38	0.09
EE	200	--	0.27	--	--	--	0.24	0.24	0.28	0.19	0.25	0.24	0.03
	400	--	0.26	--	--	--	0.30	0.37	0.38	0.31	0.32	0.34	0.04
	600	--	0.27	--	--	--	0.50	0.39	0.50	0.45	0.32	0.43	0.08
	800	--	0.21	--	--	--	0.73	0.45	0.58	0.52	0.35	0.53	0.14
	1000	--	0.16	--	--	--	0.79	0.53	0.55	1.04	0.39	0.66	0.26
MCE	200	--	0.63	--	--	--	0.48	0.70	0.65	0.47	0.69	0.60	0.11
	400	--	0.53	--	--	--	0.81	0.92	1.14	1.18	0.95	1.00	0.16
	600	--	0.54	--	--	--	1.38	0.92	1.19	1.33	0.92	1.15	0.22
	800	--	0.46	--	--	--	1.78	1.41	1.26	2.35	0.93	1.55	0.55
	1000	--	0.36	--	--	--	1.78	1.75	1.07	2.87	0.93	1.68	0.77

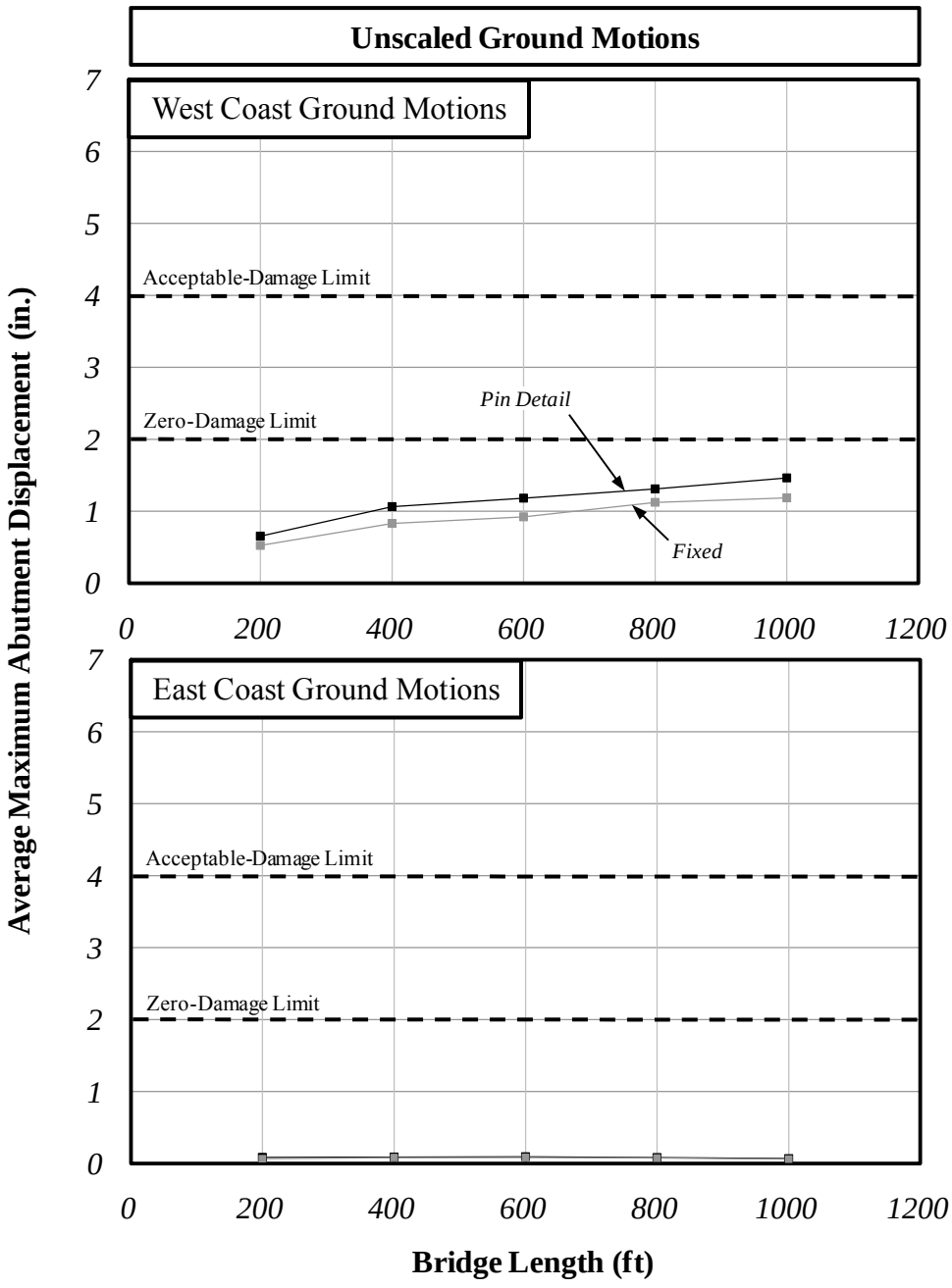

Figure 5.14: Average Maximum Abutment Displacement – Series 5

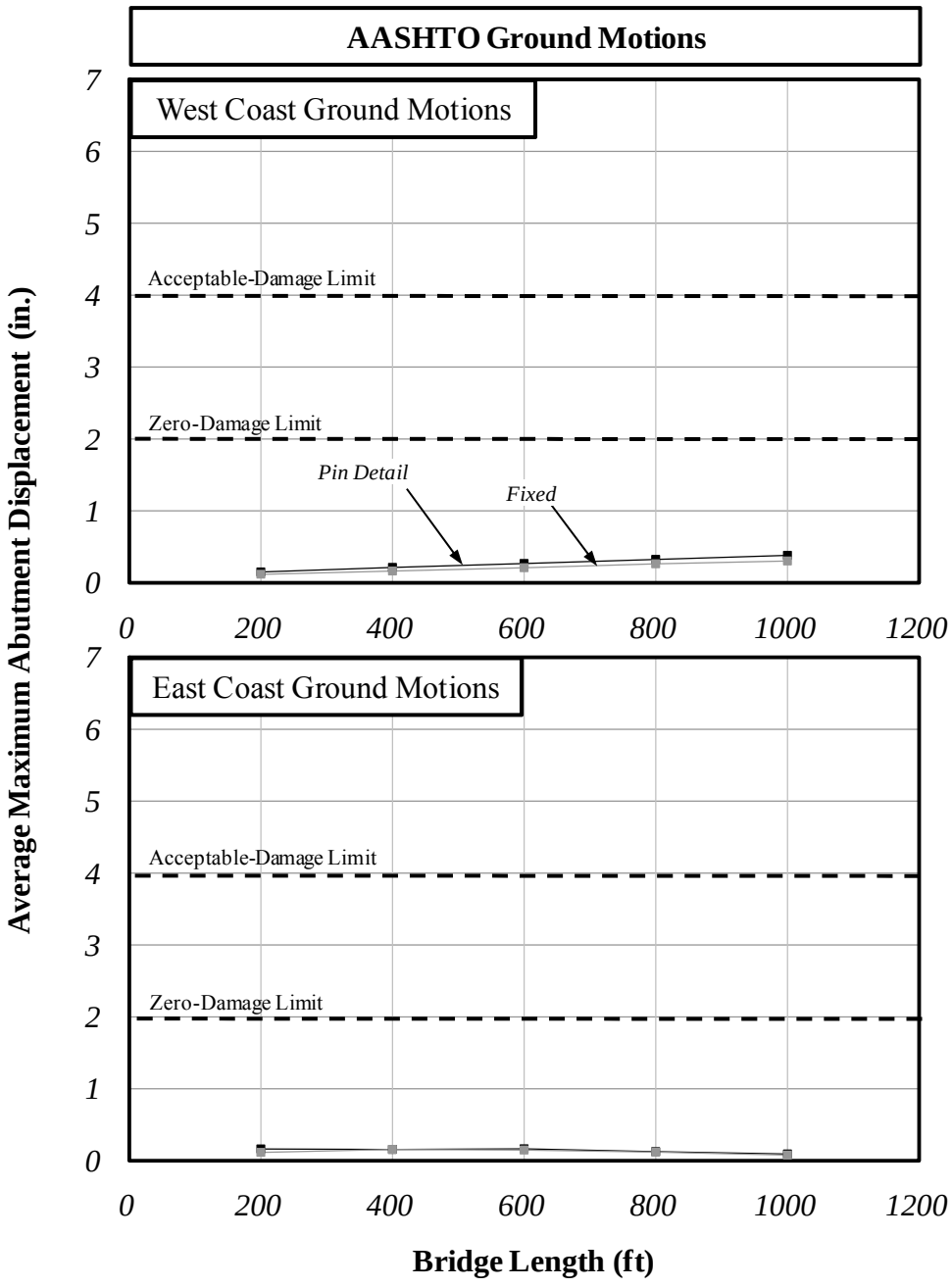

Figure 5.14 (continued): Average Maximum Abutment Displacement – Series 5

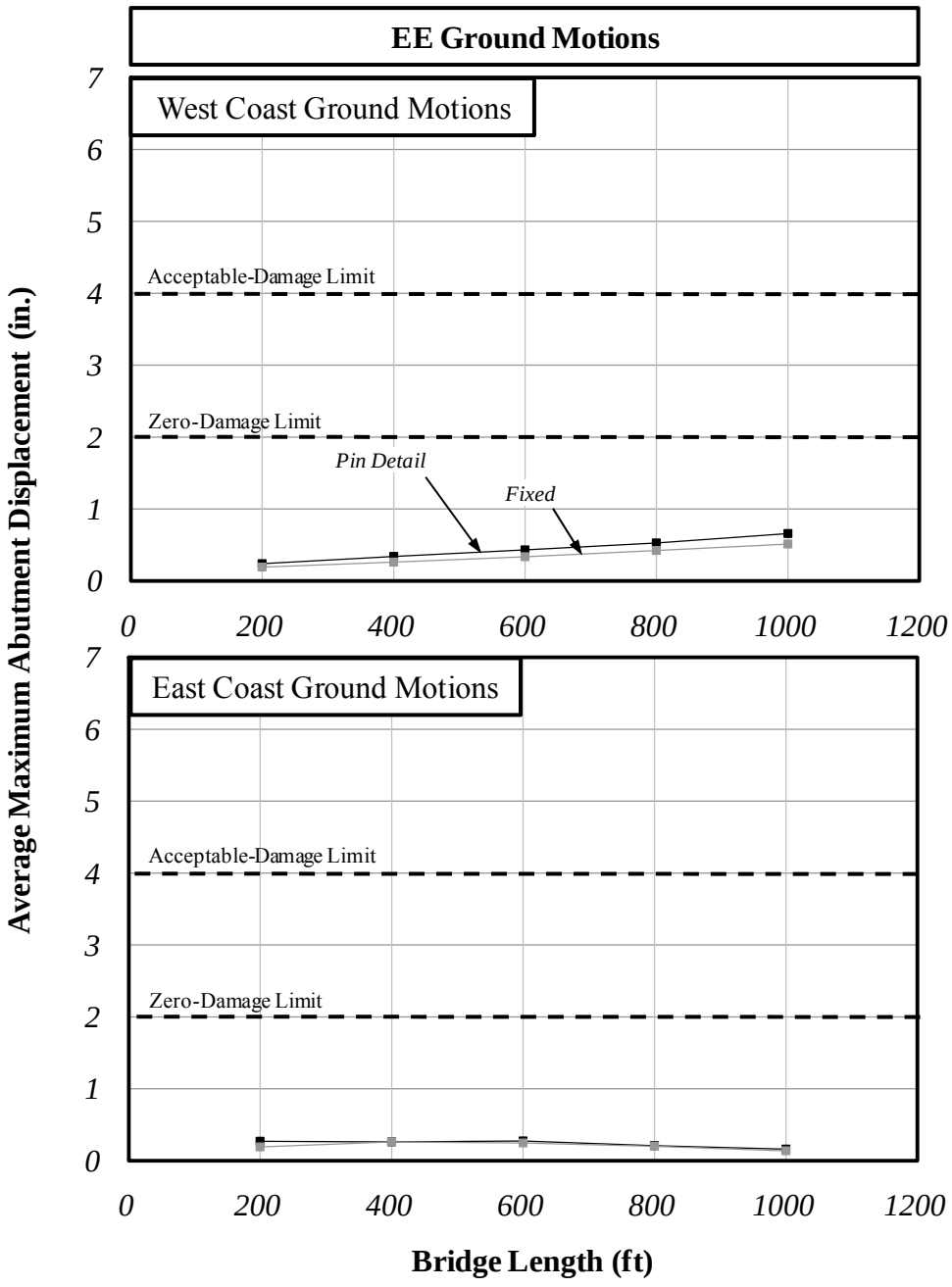

Figure 5.14 (continued): Average Maximum Abutment Displacement – Series 5

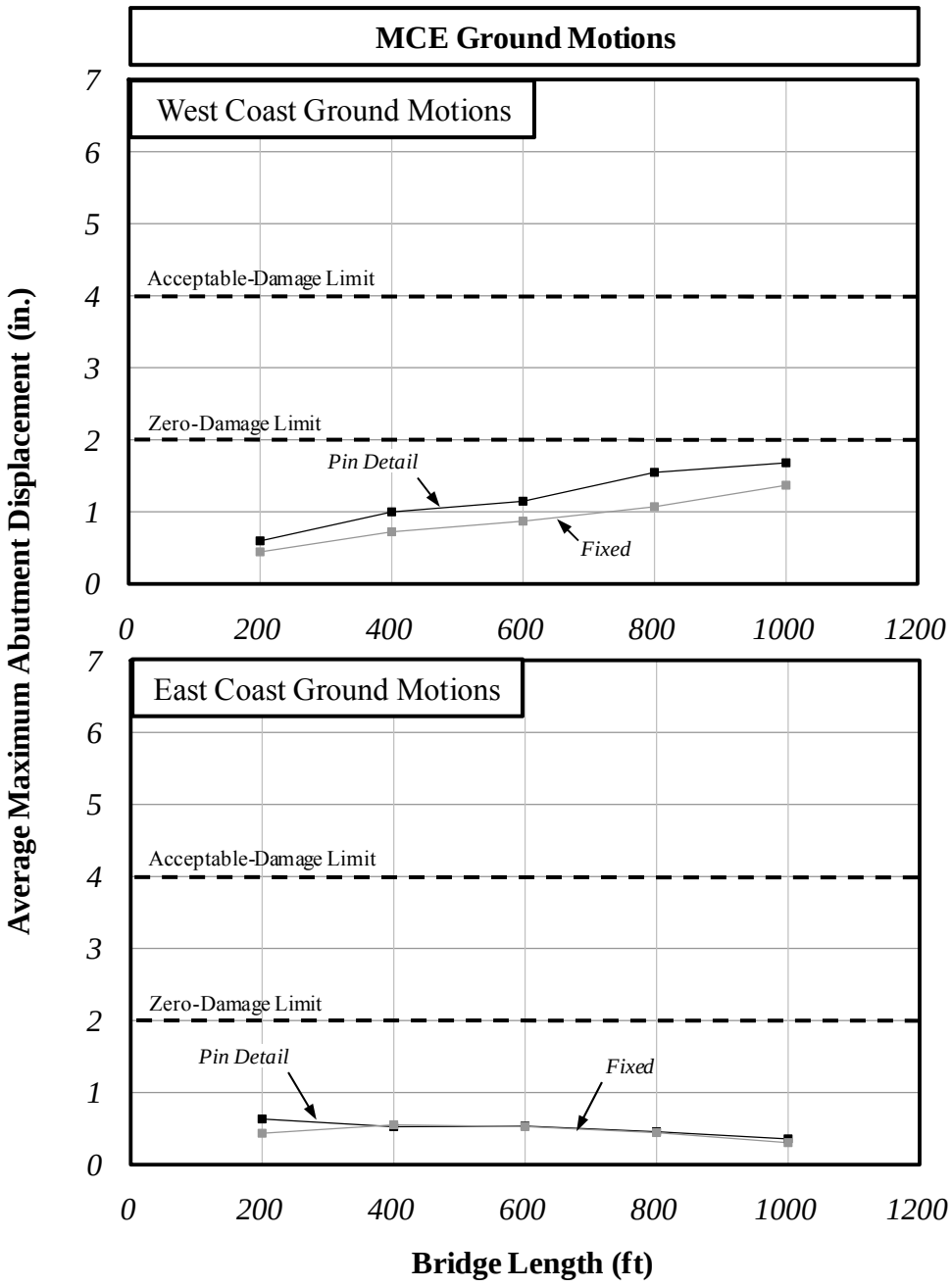

Figure 5.14 (continued): Average Maximum Abutment Displacement – Series 5

5.5 Conclusions

Based on the results of the analytical investigation, soil stiffness and backfill stiffness were identified as the primary variables influencing displacements of the abutment. Backfill strength, the "pin" detail, and span length were determined to be secondary variables. In the previous sections, the average maximum abutment displacements were used to compare the relative effects of the variables under consideration. The computed average maximum abutment displacements for Series 2 using the stiffness approach are reproduced in Figure 5.15 along with an additional curve showing the maximum computed displacements for the case of n_h = 5500 psf/in (one-half of the measured field value). As shown in the figure, the maximum computed abutment displacement does not vary much from the average for bridge lengths less than approximately 500 ft. For bridge lengths longer than approximately 500 ft the maximum computed abutment displacement is significantly larger than the average value. However, in no case did the maximum computed abutment displacement exceed the acceptable-damage limit for bridge lengths less than or equal to 1000 ft. Therefore, it was estimated that bridges less than approximately 1000 ft in length would experience an acceptable level of damage while bridges less than approximately 500 ft would experience no significant damage during the MCE.

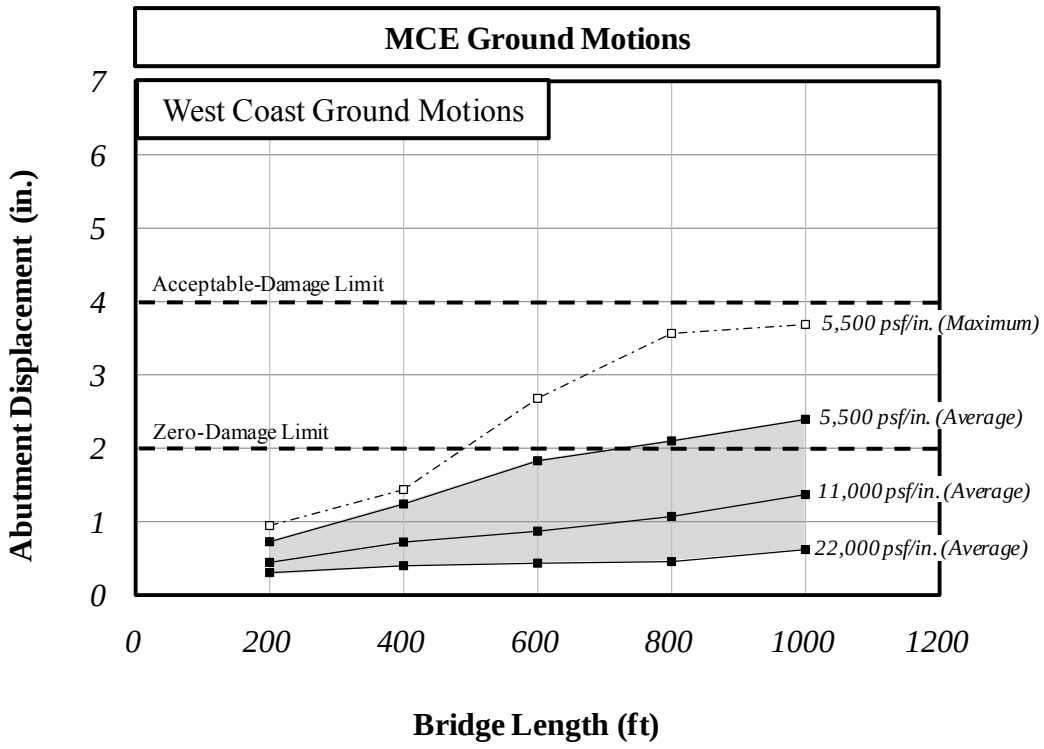

Figure 5.15: Comparison of Computed Average and Maximum Abutment Displacements (Series 2)

CHAPTER 6: SUMMARY AND CONCLUSIONS

6.1 Introduction

Integral abutment bridge construction is an increasingly popular alternative to conventional bridge construction because it eliminates expansion joints and bearings and their associated maintenance problems. However, in the absence of expansion joints and bearings, the abutments and foundation piles must be able to accommodate lateral movements of the bridge due to thermal expansion and contraction and seismic movements. Thermal movements have been investigated previously by Chovichien (2004), Bonzcar and Brena (2005), and Burdette (2005). The objective of this study was to evaluate the seismic resistance of integral abutment bridges based on the performance of the abutment-pile connection which is considered to be a critical detail. Accordingly, four major tasks were performed: (1) development of a series of design ground motions representing current estimates of the seismic hazard in Indiana, (2) evaluation of field data collected during an existing long-term integral abutment bridge monitoring project to estimate the relationship between abutment movements and earth pressures, (3) laboratory testing of current and proposed details of the abutment-pile connection to estimate displacement capacity, and (4) construction of analytical models to estimate seismic displacements of the abutment. Each task is briefly summarized in the following sections.

6.2 Design Ground Motions

The objective of this phase of the study was to develop a set of design ground motions based on current estimates of the seismic hazard in Indiana. To accomplish this objective a total of eight recorded ground motions were selected from publicly available

strong motion catalogs: three records from the Eastern United States and five from the Western United States. The recorded ground motions (excluding the Evansville and Miramichi events) were scaled to match design response spectra for Evansville, Indiana considering the default soil conditions as defined in each design specification. Several design specifications were considered and include the 17th Edition of the AASHTO Standard Specifications (AASHTO 2002), the 4th Edition of the AASHTO LRFD Specifications (AASHTO 2006) including 2008 interims, the Recommended LRFD Guidelines (ATC 2002), and the 1st Edition of the Guide Specifications for LRFD Seismic Bridge Design (AASHTO 2009).

The Standard Specifications and the AASHTO LRFD Specifications exclusive of the 2008 interims provide the same design spectra and are called in this report the "AASHTO design spectrum." This spectrum, which is based on a 10% probability of exceedance in 50 years, provides the lowest level of seismic demand and hence provides a lower bound of seismic response. The 2008 LRFD interims and the Guide Specification are based upon the Recommended LRFD Guidelines and provide a much higher level of seismic demand as defined by a 7% probability of exceedance in 75 years. While these requirements are based on the Recommended Guidelines, the Recommended Guidelines proposed a higher seismic demand based on a 3% probability of exceedance in 75 years. Therefore, the Recommended Guidelines provide an upperbound of seismic response.

Considering the various levels of response provided by the various design specifications and guidelines, three design spectra were used in analyses to bracket the response: the AASHTO design spectrum and the two design spectra defined in the Recommended LRFD Design Guidelines (ATC 2002) which represent the Expected Event (EE) and Maximum Considered Event (MCE). It should be noted that the Western United States ground motions fit the design spectra more closely across the range of periods. This is to be expected because the design spectra were developed from consideration of predominately west coast motions.

6.3 Field Investigation

The SR18 Bridge over the Mississinewa River was instrumented in 2003 to measure abutment movements and resulting lateral earth pressures. Using abutment movement and earth pressure data recorded from this bridge from May 2003 to December 2007 several observations were made:

1. There is a consistent, annual range of abutment movement equal to approximately 0.6 in.
2. There is a long-term trend of abutment movement away from the backfill accompanied by increasing earth pressure.

Additionally, an approximate linear relationship between displacement and earth pressure of 11,000 psf/in. was developed. This relationship was developed by isolating the initial loading portions of the field record. The pressure-displacement relationship developed from this analysis was used to construct an abutment-soil spring model used in the analytical investigation.

6.4 Experimental Investigation

A series of seven laboratory experiments were conducted to evaluate the displacement capacity of the abutment-pile connection. Current INDOT details were tested along with an increased embedment length, "pin" detail, and the addition of confining reinforcement around the pile head. Based on the results of the experimental investigation a zero-damage limit of 2 in. and an acceptable-damage limit of 4 in. were established. Seismic displacements of the abutment below the zero-damage limit would result in no loss of lateral or axial load capacity. Seismic displacements between the zero-damage and acceptable damage limits would result in a loss of lateral load capacity but no loss of axial load capacity. Seismic displacements of the abutment above the acceptable damage limit would result in a reduced lateral load and axial load capacity of the connection and significant damage to the abutment. The numerical values of the zero-damage and acceptable-damage limit were selected as lower bounds to the experimental results representing current INDOT details. These limits could be increased, if necessary, by the incorporation of the alternate details tested as part of the

experimental program (increased embedment length, confining reinforcement, and “pin” detail).

It was found that, in general, increased embedment length and the addition of confining reinforcement to the abutment-pile connection improved performance of the connection. Specimens with confining reinforcement did not experience a decreased lateral load capacity within the limits of the laboratory testing program. Additionally, the “pin” detail performed well in laboratory testing. The “pin” specimen maintained axial load throughout the testing program without damage to the concrete abutment. However, the “pin” connection had immense flexibility compared to the other specimens.

6.5 Analytical Investigation

A series of analytical models was constructed to estimate the seismic displacements of the abutment-pile connection. The approximate earth pressure-displacement relationship developed in the field investigation was incorporated in the analytical models. A parametric study was performed to examine the effect of the soil stiffness surrounding the pile, backfill stiffness, backfill strength, span length, and “pin” detail. Models were constructed with total bridge lengths ranging from 200 to 1000 ft. Based on the results of the analytical modeling the following observations were made:

1. In the absence of backfill resistance, bridges up to 1000 ft in length would experience no damage using the current AASHTO design spectrum. For the Expected Event (EE) design spectrum, bridges less than 600 ft in length would experience no damage, and bridges between 600 and 1000 ft in length would experience an acceptable level of damage. For the Maximum Considered Event (MCE), bridges less than 400 ft in length would experience an acceptable level of damage, and bridges greater than 400 ft in length would experience an unacceptable level of damage. The 400 ft length is based on a loose soil condition. Stiffer soils result in an increased length.
2. Considering resistance of the backfill, bridges up to 1000 ft in length would experience no damage using both the current AASHTO and Expected Event

(EE) design spectra. For the Maximum Considered Event (MCE) design spectrum, bridges less than 700 ft in length would experience no damage, and bridges between 700 and 1000 ft in length would experience an acceptable level of damage. The 700 ft length is based on a backfill stiffness which was conservatively estimated as one-half of the field measured value. This length decreases to 500 ft considering the maximum computed displacement (Figure 5.15) predicted by the Loma Prieta record.

3. The remaining parameters (backfill strength, individual span length, and "pin" connection) had little effect on the computed displacements.
4. As discussed previously in Chapter 2, the Western U.S. ground motion acceleration response spectra were a better match of the design spectra across the entire period range under consideration. The Eastern U.S. spectra did not match the design spectra as well across a wide range of periods. For the Eastern U.S. motions, the computed displacements depend on the range of periods used to scale the ground motions. However, regardless of the specific scaling method used for the Eastern U.S. motions, the Western U.S. motions govern the response.

6.6 Design Recommendations

Based on the results of this study, it is recommended that current INDOT integral abutment bridge details are sufficient to provide seismic resistance for bridges up to 500 ft in length. This length is selected considering actual seismic records as well as design based on the MCE for Indiana. Because the upper bound response as provided by the MCE (3% probability of exceedance in 75 years) was used in this evaluation, this recommendation is valid considering all current design specifications and guidelines including the 2008 interims to the LRFD Specifications and 1st Edition of the Guide Specifications for LRFD Seismic Bridge Design. Furthermore, this recommendation applies for an extremely wide range of soil conditions (including Site Class E as provided in the 2008 Interims and the Guide Specifications). The following additional recommendations are provided:

1. A pile embedment length of 24 in. in the abutment should be used. While the current embedment length of 15 in. was determined to be adequate based on laboratory tests, the specimen with a 24 in. embedment length had significantly improved performance at larger displacement levels (Figure 4.69). This length was also demonstrated analytically to be sufficient for the range of H-pile sections used in construction. This embedment length is recommended for all bridge construction as it provides enhanced behavior for both thermal and seismic considerations.
2. Integral abutment bridges can be used for lengths up to 1000 ft. For bridge lengths greater than 500 ft, confining reinforcement must be provided around the pile head. As a minimum, it is recommended that a #4 spiral with a 2.5 in. pitch be specified.
3. The use of a “pin” detail is not recommended for seismic applications. Although this detail performed adequately in laboratory tests, its performance under dynamic loading is uncertain. There is considerable benefit of continuity of the abutment and pile from both a vertical load path point of view and the lateral resistance provided by this connection.

LIST OF REFERENCES

1. AASHTO. (2002). *Standard Specifications for Highway Bridges* (17th ed.). Washington, D.C.: American Association of State Highway and Transportation Officials.

2. AASHTO. (2006). *AASHTO LRFD Bridge Design Specifications* (4th ed.). Washington, D.C.: American Association of State Highway and Transportation Officials.

3. AASHTO. (2009). Guide Specifications for LRFD Seismic Bridge Design (1st ed.). Washington, D.C.: American Association of State Highway and Transportation Officials.

4. ATC/MCEER Joint Venture. (2002). *Comprehensive Specification for the Seismic Design of Bridges.* Washington, D.C.: National Academy Press.

5. Bonczar, C., & and Brena, S. (2005). Field Data and FEM Modeling of the Orange-Wendell Bridge. *Integral Abutment and Jointless Bridges (IAJB 2005)* (pp. 163-173). Baltimore: West Virginia University.

6. Bonczar, C., & Brena, S. (2005). Integral Abutment Pile Behavior and Design - Field Data and FEM Studies. *Integral Abutment and Jointless Bridges (IAJB 2005)* (pp. 174-184). Baltimore: West Virigina University.

7. Burdette, E. G., & Howard, S. C. (2005). Behavior of Pile Supported Integral Abutments. *Integral Abutment and Jointless Bridges (IAJB 2005)* (pp. 222-232). Baltimore: West Virginia University.

8. Chovichien, V. (2004). *The Behavior and Design of Piles for Integral Abutment Bridges.* West Lafayette: Purdue University.

9. CSI, Inc. (2004). SAP2000 version 9. Berkeley, CA: Computers and Structures (CSI) Inc.

10. Frankel, A. D., Petersen, M. D., Mueller, C. S., Haller, K. M., Wheeler, R. L., Leyendecker, E. V., et al. (2002). *Documentation for the 2002 Update of the National Seismic Hazard Maps.* United States Geologic Survey.

11. Frankel, A. (1995). Mapping Seismic Hazard in the Central and Eastern United States. *Seismological Research Letters , 66* (4), 8-21.

12. Frankel, A., Mueller, C., Barnhard, T., Perkins, D., Leyendecker, E. V., Dickman, N., et al. *National Seismic-Hazard Maps: Documentation June 1996.* Denver, CO: United States Geologic Survey.

13. Indiana Department of Transportation. (2005). Bridge Design Memorandum #05-07. *Inter-Department Communication* .

14. Indiana Department of Transportation. (1992). Bridge Design Memorandum #233. *Inter-Department Communication* .

15. Indiana Department of Transportation. (1992). Bridge Design Memorandum #243. *Inter-Department Communication* .

16. Johnston, A. C., & Shedlock, K. M. (1992). Overview of Research in the New Madrid Seismic Zone. *Seismological Research Letters , 63* (3), 193-208.
17. Kurama, Y., & Farrow, K. (2003). Ground motion scaling methods for different site conditions and structure characteristics. *Earthquake Engineering and Structural Dynamics* , 2425-2450.

18. Maruri, R., & Petro, S. (2004). Integral Abutments and Jointless Bridges (IAJB) 2004 Survey Summary. *Integral Abutment and Jointless Bridges (IAJB 2005)* (pp. 12-29). Baltimore: Constructed Facilities Center - West Virginia University.

19. Munson, P. J., Munson, C. A., Bleuer, N. K., & Labitzke, M. D. (1992). Distribution and Dating of Prehistoric Earthquake Liqufaction in the Wabash Valley of the Central U.S. *Seismological Research Letters , 63* (3), 337-342.

20. Obermeier. (1998). Liquefaction Evidence for Strong Earthquakes of Holocene and Latest Pleistocene Ages in the States of Indiana and Illinois, USA. *Engineering Geology , 50,* 227-254.

21. Obermeier, S. F., Munson, P. J., Munson, C. A., Martin, J. R., Frankel, A. D., Youd, T. L., et al. (1992). Liquefaction Evidence for Strong Holocene Earthquakes in the Wabash Valley of Indiana-Illinois. *Seismological Research Letters , 63* (3), 321-335.

22. Wasserman, E., & Walker, J. (1996). *Integral Abutments for Steel Bridges.* Tennessee Department of Transportation. American Iron and Steel Institute.

23. Wesnousky, S. G., & Leffler, L. M. (1992). On the Search for Paleoliquefaction in the New Madrid Region. *Seismological Research Letters , 63* (3), 343-348.